Synthetic and Structural Studies of Polyoxometalates as Versatile All-Inorganic Catalysts

Dissertation

Zur Erlangung der naturwissenschaftlichen Doktorwürde

(Dr. sc. nat.)

vorgelegt der

Mathematisch-naturwissenschaftlichen Fakultät

der

Universität Zürich

von

Kim Dimuth von Allmen

von Lauterbrunnen BE

Promotionskomitee

Prof. Dr. Greta R. Patzke (Vorsitz)

Prof. Dr. Jürg Hutter

Prof. Dr. Roland K. O. Sigel

To my Family

Acknowledgements

The research done during my four years of PhD would not have been possible without the help of many people, who supported me with ideas, technical support and encouragement. I am very grateful and would like to express my gratitude to all of them.

First of all I would like to thank my supervisor Prof. Dr. Greta R. Patzke who gave me the opportunity to work in her group and supported my thesis with many good ideas and suggestions. Thank you for the freedom you gave me to explore my own ideas, for all the constructive discussions and the generous support.

I am indebted to Prof. Dr. Roland K. O. Sigel and Prof. Dr. Jürg Hutter for their work as co-referees of this thesis. Thank you for all of the productive meetings over the years.

I would like to thank all former and present group members. Dr. Roman Kontic, Dr. Georg Geisberger, Dr. Lubin Ni, Dr. Min Sheng, Dr. Franziska Conrad, Dr. René Moré, Dr. Yáng Zhèn, Dr. Pierre-Emmanuel Car, Roger Jacot, Dr. Fabio Evangelisti, Dr. Hongfei Liu, Michael Olah, Robin Güttinger, Matteo Croce, Rafael Müller, Fangyuan Song, Simona Conti, Karla Lienau, Peter Bösiger, Mauro Schilling, Adria Garcia and Patrick Felder. Thank you for your help and the great times we had inside and outside of the Lab.

Many people have contributed to this work, with technical and administrative support. I am very thankful to Prof. Dr. Anthony Linden, Prof. Dr. Bernhard Spingler and Dr. Olivier Blacque for their help with theoretical and practical aspects of crystallography. I am thankful to PD. Dr. Laurent Bigler, Urs Stalder and Dr. Thomas Fox who helped me to perform mass spectrometry and NMR experiments. I am grateful to Dr. Ferdinand Wild, Hanspeter Stalder, Heinz Spring, Manfred Jöhri and Ramona Erni, Nathalie Melunsky-Fichter and Dr. Sabine Stockhause for their support with many different technical and administrative problems. Thank you all for your time and for supporting my thesis with your expertise.

Different projects and strategies have been followed during this thesis. I am thankful for the support of many different collaboration partners. I would like to thank Prof. Dr. Roger Alberto, Dr. Benjamin Probst and Dr. Cyril Bachmann, for their help with H_2 evolution measurements and interesting discussions in context of the UFSP and Sinergia research projects. I am thankful to Joaquín Soriano-López for his help with DFT calculations. I would like to thank Dr. Georg Meseck for an interesting collaboration on the topic of Si-

nanofilament functionalization and Dr. Hudson Wallace Pereira de Carvalho for his efforts to solve the structure of the POM-PS complex from EXAFS measurements.

I am particularly thankful to my family who consequently supported me and I would like to thank my parents Philippe and Simone von Allmen for their encouragement to pursue my studies in chemistry. I am very grateful to my twin sister and my brother in law Noémie and Sebastian Gentsch as well as to my brother Vasco de Matos Pinto.

Finally I would like to express my gratitude to all my friends which I have met across my studies and who supported me. Dominik Sommerhalder, Cédric Jost, Florian Gerber, Mirko Münger, Irene Rösle, Anna Senn, Olivier Sallin, Family Gyger, Team Uni Basel and Team EPFL. Thank you for all the good times!

I would like to acknowledge the University of Zurich and the graduate school of Chemical and Molecular Sciences Zurich (CMSZH) for the allocation of an impeccable research environment and financial support.

This work was supported by the Swiss National Science foundation (SNSF Professorship PP002_114711/1, PP00P2_133483/1) and the Sinergia Grant number (CRSII2_136205/1).

Abbreviations

ACN	Acetonitrile
ADP	Atomic Displacement Parameter
ATP	Adenine Triphosphate
BVS	Bond Valence Sum Analysis
DMF	Dimethylformamide
CIF	Crystallographic Information File
DFT	Density Functional Theory
DLS	Dynamic Light Scattering
EDX	Electron Dispersive X-ray
EXAFS	Extended X-ray Absorption Spectroscopy
FTO	Fluorine Tin Oxide
GC	Gas Chromatography
HR-ESI MS	High Resolution Electrospray Ionization Mass Spectrometry
ICSD	Inorganic Crystal Structure Database
IR	Infrared
IPA	Isopolyanion
IUCR	International Union of Crystallography
LightCheC	Light to Chemical energy Conversion
M	1^{st}, 2^{nd} row d and f-block, 13^{th}-15^{th} group metals
NHE	Normal Hydrogen Electrode
NMR	Nuclear Magnetic Resonance
NPD	Non Positive Definite
NPs	Natural Photosynthesis
OEC	Oxygen Evolving Complex
POM	Polyoxometalate
PXRD	Powder X-ray Diffraction
SAR	Structure-Activity Relationship
SEM	Scanning Electron Microscopy
SNF	Swiss National Science Foundation
TEOA	Triethanolamine
TGA	Thermogravimetric Analysis
THF	Tetrahydrofurane
TMSPs	Transition Metal Substituted Polyoxometalate
UFSP	Universitärer Forschungsschwerpunkt
UV/Vis	Ultraviolet / Visible
SEM	Scanning Electron Microscopy
SMM	Single Molecular Magnets
WOC	Water Oxidation Catalyst
WRC	Water Reduction Catalyst

Publications

The following parts of this PhD thesis have been published or are currently prepared for publication.

Tuning the Composition of the Transition Metal Core in Krebs-type Photocatalysts by HR-ESI Mass Spectrometry (Chapter 1 §1.16 and Chapter 2, §2-2.7)
Kim D. von Allmen, H. Grundmann, U. Stalder, A. Linden, G. R. Patzke,
In preparation for publication

Multidimensional Architectures of Copper Substituted Tungstobismuthates – Structural Analogues of Water Oxidation Catalysts (Chapter 3, §3-3.4)
Kim D. von Allmen, Henrik Grundmann[†], Anthony Linden, Greta R. Patzke*
Prepared for submission

Nickel-containing Keggin-type Polyoxometalates as Hydrogen Evolution Catalysts: Photochemical Structure Activity Relationships (Chapter4, §4-4.9)
Kim von Allmen[†], René Moré[†], Rafael Müller, Joaquín Soriano-López, Anthony Linden and Greta R. Patzke* ChemPlusChem, **2015**, 80 (9), 1389-1398. DOI: 10.1002/cplu.201500074
† = Equal contribution

Structure and Properties of New Gallium-containing Polyoxotungstates with Hexanuclear and Tetranuclear Cores (Chapter 5, §5-5.9)
Kim von Allmen, Pierre-Emmanuel Car, Olivier Blacque, Thomas Fox, Rafael Müller, Greta R. Patzke. Zeitschrift für Anorganische und Allgemeine Chemie, **2014**, 640 (5), 781. DOI: 10.1002/zaac.201300669

Chapter 1

Introduction

1 Introduction

Polyoxometalates (POMs) are an important class of inorganic metal oxygen clusters. The synthesis and the properties of these clusters have been studied in detail in the context of this thesis. As catalysts for artificial photosynthesis (AP) POMs have shown promising results, which are the starting point for the development of a new POM-based system for photocatalytic H_2 production. This introduction illustrates how POMs are used in photocatalytic systems for AP and which issues are crucial for their synthesis and photocatalysis. This introduction covers relevant topics for the understanding of natural and artificial photosynthesis (§) and relates this work to the search for new renewable energy technologies (§). Furthermore a detailed introduction to the field of POM chemistry (§1.10), the synthesis of POMs (§1.11) and their characterization (§1.13) gives an impression of the challenges which were encountered in the course of this project.

1.1 Research Environment and Strategy

This PhD thesis was conducted in the context of the Swiss National Science foundation (SNF) Sinergia project 136205 entitled “Homogeneous photocatalytic water splitting” which and aims to find ways to mimic natural photosynthesis. Research groups involved in the Sinergia project have later been combined with further groups from the University of Zurich and two external groups to the University Research Priority Program (URPP). These research groups work on a project which is entitled Light to Chemical Energy Conversion (LightChEC). The skills of different research groups have been combined to integrate preparative, physico-chemical and theoretical expertise. The Sinergia project was originally divided in four subprojects, a structure that has been retained for the LightChEC project. Subproject 1 is focused on H_2 evolution and the development of new WRCs. Subproject 2 is focused on the investigation of O_2 evolution and the development of new water oxidation catalysts (WOCs). Subproject 3+4 give insights in the reaction mechanism of the water oxidation process through spectroscopic investigations and by computational chemical investigation.

This PhD thesis started from subproject 2 and its initial aim was to answer the question:

What is the potential of Mn substituted POMs as catalysts for water oxidation?

- First a series of Mn-substituted polyanions with systematic structural variations were targeted and tested for photocatalytic water oxidation.
- The second goal was the optimization of selected polyanions according to the determined structure-activity relationships.
- Mechanistic investigations and the combination of O_2 and H_2 evolution half reactions were defined as long-term goals.
- Co containing tungstobismuthates. The instability of this precursor in aqueous solutions made the selective phase pure preparation and crystallization of new tungstobismuthates difficult. Synthetic protocols with Mn(II) were studied in more detail in order to crystallize a pure Mn_4 core for the Krebs-type POMs $[Mn_{(2+x)}(H_2O)_4(WO_2)_{(1-x)}(B\text{-}\beta\text{-}BiW_9O_{33})_2]^{n-}$. In the reaction with Cu(II) a variety of 0D-3D structures were characterized by single crystal X-ray diffraction. As a consequence of the obtained wide structural diversity, the formation of these polyanions was studied in more detail.
- Project 2: H_2-evolution was studied for the series of Ni substituted Keggin-type polyanions $[Ni(H_2O)(XW_{11}O_{39})]^{n-}$ (X = Si, Ge, P; n = 5 for P, 6 for Ge and Si).
- Project 3: The reaction of Ga(III) with tungsten precursors was studied with special emphasis on the reaction of the lacunary Keggin precursor $[\alpha\text{-}SiW_9O_{34}]^{10-}$ with $Ga(NO_3)_3$.

1.2 Today's Energy Supply – and its Consequences for Society

A turnaround in energy policy is the subject of many debates. The reasons why the current sources of energy need to be replaced are miscellaneous. Environmental, political and economic aspects play an important role. Three crucial points are briefly discussed and should illustrate the necessity for further development of renewable energy technologies and energy storage technologies.

CO_2 and the Greenhouse Effect: Only a negligibly small fraction (14 %) of the total consumed energy is renewable, whereas the lions share releases large amounts of CO_2 into the atmosphere (Figure 1.1, left).[1–7] Reducing the emission of CO_2, the main greenhouse gas,[8] is

crucial. It was shown that the levels of CO_2 and the average global temperature are associated (Figure 1.1, right).[9,10] As population and economic growth will continue, the global energy consumption will increase from 14 TW today to 28 TW in 2050.[11,12] If this energy demand is covered by fossil fuels, the increase of CO_2 levels and the associated greenhouse effect will have a drastic impact on the world climate and ecosystem.[13–15] The average global temperature has increased by 0.85 °C from 1860 to 2015 already and is expected to increase by 2.7 °C in 2100.[7] The rising sea-level is only one example how climate change will become problematic for our society (Figure 1.2, left).[16,17,14]

Safety Aspects of Nuclear Technology: The production of energy with nuclear energy technologies does not produce CO_2. Tragic accidents in Chernobyl in 1986[18–22] or in Fukushima in 2009[23,24] however, have shown, that this technology is not safe against unexpected accidents.[25] Furthermore no final solution for the storage of radioactive nuclear waste has been found yet[26–30] and the acquisition of nuclear fuels is highly problematic.[5,6]

Political Aspects and Dependency: Most of the fossil and nuclear fuels consumed in Switzerland and the European Union originate from foreign countries. This dependency questions the sovereignty of Switzerland as well as the European Union in political circumstances.[5,6,31,32]

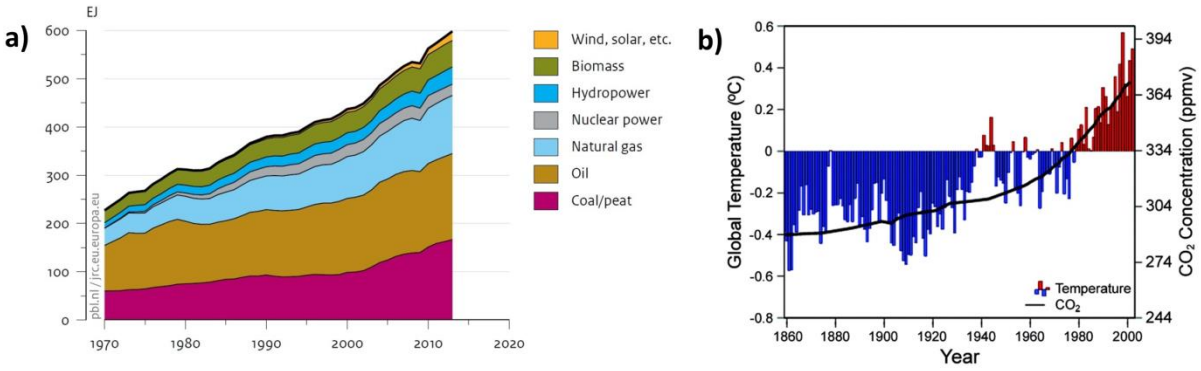

Figure 1.1 (a) Composition of the energy supply of the European Union.[1] **(b)** CO_2 concentration in the atmosphere (solid curve) and the temperature deviation from the mean global temperature of 14 °C (red and blue bars).[10]

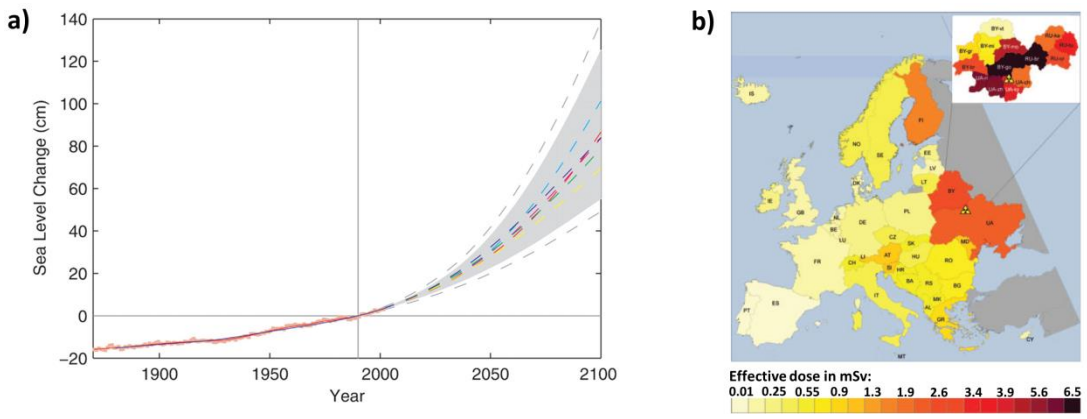

Figure 1.2. (a) Past sea level and sea-level projections from 1990 to 2100, based on global mean temperature projections. The grey uncertainty range spans a temperature increase from 1.4-5.8 °C.[16] **(b)** Country specific radiation dose in mSv after the Chernobyl accident (bright yellow = 0.01 mSv, dark red = 6.5 mSv).[22]

Renewable energy sources such as wind and geothermal energy, hydropower, wave energy from the oceans, the conversion of solar energy and the use of biofuels are CO_2 neutral, i.e. they do not release additional CO_2 into the atmosphere.[33] A failure of these technologies does not represent the same threat as a nuclear meltdown and no nuclear waste is produced. Some renewable energy technologies are already in use, other are investigated for their potential to replace fossil and nuclear fuels as primary energy source.[34,35] Carbon sequestration[33,36] may be a temporary solution to reduce CO_2 emissions and recent advances in the field of nuclear fusion have come with promising solutions. However, it will still take a considerable number of years until these technologies are ready to use.[37] Today none of the renewable energy technologies can compete with fossil fuels or nuclear energy in terms of price, accessibility and energy density. Solar energy conversion however has the potential to do so, considering that 120 000 TW of light strike the surface of the earth which is equivalent to 8500 times todays energy demand.[38,39]

1.2.1 Energy Storage

Today's energy infrastructure is based on fossil fuels and nuclear energy. Oil and enriched uranium can easily be stored and used upon request. Alternative energy technologies like solar or wind are Variable Renewable Energy Sources (VRES).[40] They do not provide a steady supply of energy, which is considered as major drawback.[41] A variety of energy storage technologies have been explored which store energy either mechanically (pumped hydro, compressed air, flywheels, superconducting magnets, capacitors and supercapacitors)

or chemically (H_2-storage or batteries).[41] Hydrogen production and storage[42] is particularly interesting considering a future hydrogen economy, where H_2 replaces conventional fuels.[43,44] The concept of artificial photosynthesis (AP) converts solar energy directly into a storable chemical compound. In AP H_2 is often considered as the compound with the highest potential for chemical energy storage. Combining light absorption and H_2 evolution would allow integrating both processes in a single device. This is considered as the main advantage over separated systems and makes APs a particularly interesting approach for solar energy conversion.

1.3 Natural Photosynthesis

Natural photosynthesis (NP) is the process by which nature converts light into chemical energy. It is essential for all life on Earth.[45–47] In this process, which occurs in green plants, bacteria and algae, carbon dioxide and water are transformed, through energy rich intermediates, into oxygen and glucose (eq. 1.1). Glucose molecules may then be transformed to larger structures of carbohydrates which represent chemical compounds in which solar energy is stored.

$$6\ CO_2 + 6\ H_2O + h\nu \rightarrow C_6H_{12}O_6 + 6\ O_2 \qquad \text{(eq. 1.1)}$$

Organisms which capture light to acquire energy are called photoautotrophs. In all photoautotrophs light to energy conversion follows almost the same steps (Figure 1.5). Photosynthesis is separated in light-dependent and dark (light-independent) reactions. Light-dependent reactions take place in photosystem II (PSII) and photosystem I (PSI) where photons are absorbed by chlorophyll and other light-absorbing antenna molecules. Electrons are further excited in PSI in a second light absorption process and the energy is ultimately used to transform nicotinamide adenine dinucleotide phosphate (NADP) to its protonated form (NADPH). Relayed electrons are replaced as H_2O is oxidized.

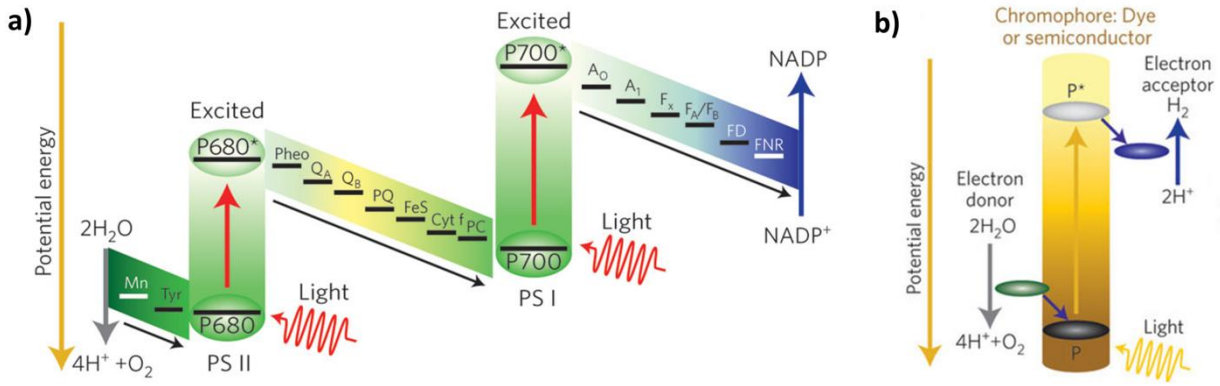

Figure 1.3. (a) Schematic representation of the charge-separation process in natural photosynthesis (light-dependent reactions).[48] **(b)** Schematic representation of an artificial system known as the Z-Scheme.[48]

Oxidation of H_2O molecules occurs at the $\{CaMn_4O_5\}$ cluster in the Kok-cycle. Thereby O_2, H^+ and electrons are generated which create a proton gradient by accumulation of protons between the inside of the membrane known as thylakoid lumen and the outside known as chloroplast stroma. This proton gradient provides the energy to transform adenine diphosphate (ADP) to adenine triphosphate (ATP) by the enzyme ATP synthase. NADPH and ATP are chemical compounds that temporarily store the energy which originates from the photons of sunlight. In a subsequent process, known as Calvin-cycle,[49] CO_2 fixation takes place. CO_2 and ribulose-1,5-bisphosphat (RuBP) react to glycerinaldehyde-3-phosphate (PGAL), thereby using the energy stored in NADPH and ATP. This process is catalyzed by the enzyme RuBisCo. PGAL reacts in an ultimate step to glucose, which serves as building blocks for other carbohydrates.[49]

1.3.1 The Structure of Photosystem II

Since water oxidation takes place in PSII, its structure will be discussed in more detail in the following section. PSII is a membrane protein complex with a molecular weight of 650 kDa. It is located in the thylakoid membranes of oxygenic photosynthetic organisms. The structure of this protein has been studied by X-ray crystallography, X-ray spectroscopy, electron paramagnetic resonance (EPR) and other biochemical methods.[50,51] Since the first single crystal X-ray structure of PSII at a resolution of ~3.8 Å was published in 2001,[52] it has improved to a resolution of 1.9 Å[53] and recently a structure of 1.95 Å was obtained by using X-ray, free electron laser pulses.[54]

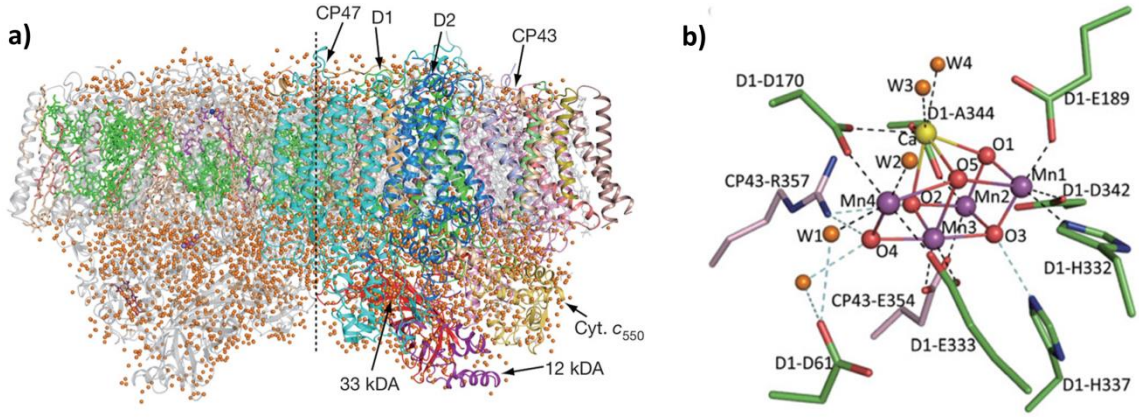

Figure 1.4. (a) Overall structure of the PSII dimer from T. vulcanus at a resolution of 1.9 Å with individually colored subunits.[53] Color Code of subunits: D1 = green, CP43 = pink. **(b)** Structure of the Mn_4O_5Ca cluster.[53] Color code of atoms: Mn = purple, Ca = yellow, O = red.

The catalytically active center for water oxidation is embedded in the protein subunit D1 of PSII. This subunit contains the oxygen evolving complex (OEC) in form of the Mn_4CaO_5 cluster. The structure of this cluster has been revealed step by step with methods including EPR, NMR and X-ray absorption spectroscopy techniques (extended x-ray absorption fine structure (EXAFS) and x-ray absorption near edge spectroscopy (XANES)). The OEC is constituted by three Mn atoms and a Ca atom, which are connected by four oxygen atoms. They represent the cubane-like-motif of the OEC. An external Mn atom is connected with an additional O atom (Figure 1.4, right).[50,51] For our studies this is considered a promising structural feature to store the four oxidizing equivalents, which are necessary for the oxidation of water.

1.4 Artificial Photosynthesis

NP is a highly complex process, which involves different fine-tuned steps of light absorption and charge separation. Active centers and photosensitizers are embedded in large protein complexes. Charge recombination is avoided by rapid and spatial separation of the electron from the photosensitizer. Due to its complexity, NP cannot be considered as blue print for an artificial system. Nevertheless, efforts have been made to design systems that perform water oxidation according to the same basic principles.[55,39] Photosynthesis can be mimicked with a single step reaction which involves only 1 light absorption process (Z-Scheme). Alternatively a 2-step reaction could be used, which involves two light absorption processes, one for the water oxidation step and one for the water reduction step.[48] In this study water splitting half

reactions were investigated according to the Z-Scheme, aiming for transition metal substituted POMs (TMSPs) as OEC mimics.[56]

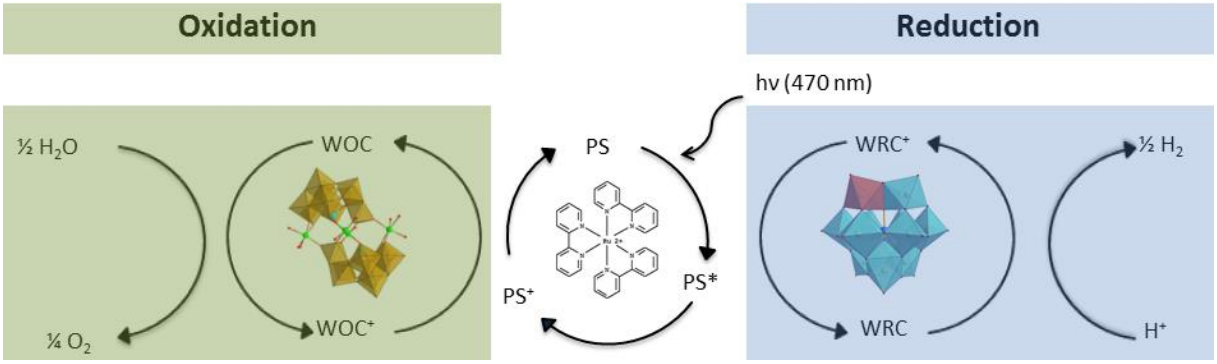

Figure 1.5. Z-Scheme representation of the artificial water-splitting process using $[Ru(bpy)_3]^{2+}$ as photosensitizer. Both half-reactions are driven by a POM catalyst; (**green**) water oxidation half-reaction, (**blue**) water reduction half reaction.

To split water at least 237 kJ mol^{-1} are required (eq. 1.2).[57] The O_2 evolution half-reaction is summarized in eq. 1.3, the H_2 evolution reaction is summarized in eq. 1.4.

$$H_2O \rightarrow H_2 + ½\ O_2 \qquad \Delta G = 237\ kJ\ mol^{-1} \qquad \text{(eq. 1.2)}$$

$$2\ H^+ + 2e^- \rightarrow H_2 \qquad E° = 0\ V\ vs.\ RHE \qquad \text{(eq. 1.3)}$$

$$2\ H_2O \rightarrow O_2 + 4\ H^+ + 4e^- \qquad E° = 1.23\ V\ vs.\ RHE \qquad \text{(eq. 1.4)}$$

An artificial system for O_2 evolution has to fulfill different requirements to perform this task in a single step. The excited state reduction potential of the photosensitizer ($[Ru(bpy)_3]^{2+*}$) has to be more positive than the water oxidation potential (+0.82 V vs. NHE at pH = 7). The excited state oxidation potential has to be more negative than the H_2 evolution potential (+0.41 V vs. NHE at pH = 7).[48] After light absorption by photosensitizer molecules, excited electrons are transferred to an electron acceptor or water reduction catalyst (WRC) and used to reduce protons to hydrogen. This leads to oxidized photosensitizer molecules which are subsequently reduced and thereby brought back to their initial state by the WOC. In a final step the oxidized WOC recovers by oxidizing water to O_2 and H^+.

1.4.1 Established Photochemical Assays

The imitation of the entire photocatalytic water splitting process as it is illustrated in Figure 1.5 has not been achieved to date. To test the performance of photocatalysts for a particular half-reaction, the other half of the reaction needs to be mimicked. To test a WOC, an electron acceptor is required to replace the electron consuming H_2 evolution reaction. To test a WRC it is necessary to provide electrons which, in an operating system, would come from splitting of the O-H bonds.

O_2 Evolution

Sodium persulfate ($Na_2S_2O_8$) is an established electron acceptor and has been used to characterize the water oxidation activity of many promising WOCs.[58,59] This sacrificial electron acceptor was used for almost all photocatalytic water oxidation tests done in this work.

$$[Ru(bpy)_3]^{2+} + [S_2O_8]^{2-} \rightarrow [SO_4]^{2-} + [SO_4]^{-\cdot} + [Ru(bpy)_3]^{3+} \qquad \text{(eq. 1.5)}$$

$$[Ru(bpy)_3]^{2+} + [SO_4]^{-\cdot} \rightarrow [SO_4]^{2-} + [Ru(bpy)_3]^{3+} \qquad \text{(eq. 1.6)}$$

In this process two electrons are accepted by one molecule of sodium persulfate (eq. 1.5). Two molecules of sodium persulfate are used to generate 4 equivalents of oxidized $[Ru(bpy)_3]^{3+}$ sensitizer. The reduction potential of $[S_2O_8]^{2-}$ is approximately 2.0 V vs. NHE but despite its strong thermodynamic driving force, it is kinetically stable. The sulfate radical $[SO_4]^{-\bullet}$ which is formed in this step has a reduction potential of approximately 2.4 V vs. NHE. It accepts an electron from the photosensitizer, the WOC or directly from water (eq. 1.6).[60] When sodium persulfate is used, it is necessary to ensure that this sacrificial electron acceptor is stable under the used reaction conditions. Although its reaction with water is exothermic, this compound is kinetically stable under the commonly used conditions for catalytic water oxidation.[61–63]

Alternative electron acceptors are Ce(IV) in the form of cerium ammonium nitrate (CAN) or $[Ru(bpy)_3]^{3+}$ which can be isolated and used as electron acceptor at low pH. Iron nitrate can also be used in acidic environments.[64–67] Potassium peroxymonosulfate ($KHSO_5$) known as Oxone® and sodium periodate ($NaIO_4$) are used in basic environments. For a full overview of sacrificial electron acceptors and their application see the review article by Brudvig et al.[60]

The analogue of the chlorophyll sensitizer in PSII is an artificial photosensitizer that absorbs light and thereby creates photoexcited electrons. The photosensitizer tris(2,2′-bipyridyl)dichlororuthenium(II) ($[Ru(bpy)_3]^{2+}$) used in this work is based on a precious metal. This widely used compound is considered as standard component for AP test systems.[68] Development of photosensitizers based on cheaper and more abundant transition metals is a general topic of current interest in AP.

Besides the photosensitizer and the electron acceptor, the solvent in which photocatalytic tests are performed is crucial for catalytic activity. Photocatalytic tests with POMs are usually performed in aqueous buffer systems at concentrations between 50 mM and 100 mM depending on the required buffer capacity. In this work borate (H_3BO_3/NaOH) buffers were used in the pH range 8-9,[69] phosphate buffers (Na_2HPO_4/NaH_2PO_4) in the pH range 7-8 and acetate buffers (HOAc/NaOAc) in the pH range 4.75-6.50.

H_2 Evolution

To test the activity of WRCs, the water oxidation half-reaction needs to be substituted which requires an electron donor. In this work, all H_2 evolution tests were done in an ascorbate buffer system ($AscOH/AscO^-$), where ascorbate is oxidized to dehydroascorbic acid (DHA).[70] This system provides both, an electron donor and a buffer, which is a major advantage over other systems. Other electron donors have frequently been used, for instance triethanolamine (TEOA), methanol, isopropanol, triethylamine or zinc powder. A list of POM WRCs and different test setups is provided in Table 4.1.

While $[Ru(bpy)_3]^{2+}$ is the standard photosensitizer for O_2 evolution, the organic dye EOSIN, and transition metal complexes such as $[ReBr(CO)_3bpy]$ or $[Ir(ppy)_2(dtbbpy)]^+$ are frequently used for H_2 evolution.[71]

Co-catalysts are often required in combination with POM WRCs to observe catalytic activity (in this context Co does not refer to cobalt). Pt or Te nanoparticles or cobalt containing compounds are frequently used for this purpose. The application of co-catalysts is problematic, since a clear attribution of the WRC activity is not possible anymore. Photocatalytic tests with WRCs are done in aqueous solutions usually at low pH. To increase the solubility of the WRC mixtures of organic solvents and water are often used. The highest turnover number (TON) ever reported for a POM-based WRC was reported in a mixture of dimethylformamide (DMF) and acetonitrile (ACN) using TEOA as electron donor.[72]

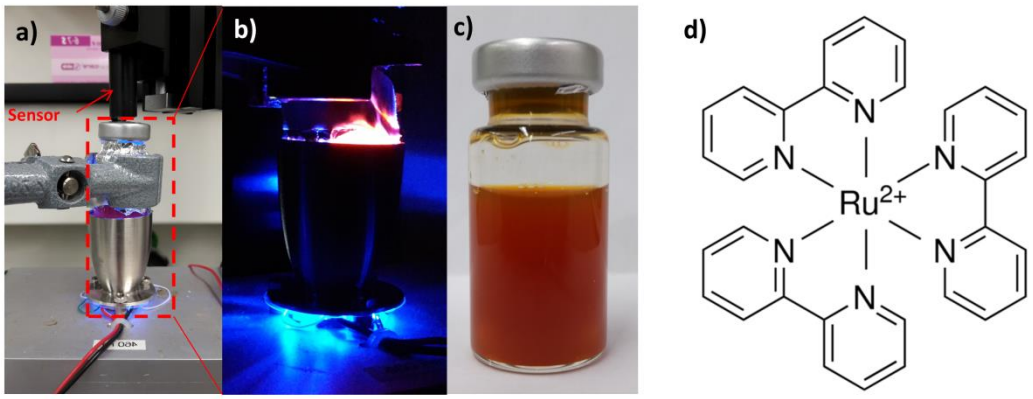

Figure 1.6. (**a**) Setup for measuring H_2 evolution with a H_2 sensitive sensor or O_2 evolution with an O_2 sensitive Clark electrode. (**b**) Irradiation of a test-vial with a blue LED at 470 nm and 4650 LUX. (**c**) Photocatalytic test with a dark precipitate of the POM-PS complex, after catalysis in a gas-tight headspace vial. (**d**) Structure of the photosensitizer $[Ru(bpy)_3]^{2+}$.

1.5 The Availability of Metals – The Bottleneck for Industrial Applications

Catalyst development for this research project has been done with the aim to find active compounds for artificial photosynthesis, which could be scaled up and used in large scale industrial applications. This restricts the number of available metals to those that are abundant in the earth's crust and are available in sufficient amounts for industrial applications. The elements W, Mn and Co which are in the focus of this thesis fulfill these conditions.[73–75] The photosensitizer $[Ru(bpy)_3]^{2+}$ however, contains the precious metal ruthenium and is only used as working model.

1.6 POM Water Oxidation Catalysts for Photocatalysis

The most prominent POM-based WOCs are the sandwich-type Co containing structures $[Co_4(H_2O)_2(B\text{-}\alpha\text{-}PW_9O_{34})_2]^{10-}$ and the Ru based sandwich POM $[Ru_4O_5(OH)(H_2O)_4(\gamma\text{-}PW_{10}O_{36})_2]^{10-}$ with a cubane-like $\{Ru_4O_5\}$ core.[58] Both POMs are formed from lacunary Keggin structures. The publication of these all-inorganic structures as WOCs has launched a search for related structures exhibiting water oxidation activity. Hence, many different polyanions have successfully been tested for water oxidation to date and the results have been recently summarized.[76] Catalytic activity has been reported for Keggin-type polyanions substituted with Co, Ni, Ru, and Mn transition metal cores under standard conditions in the field of photocatalytic water oxidation (§1.4.1).

1.7 $[\{Mn^{III}_3Mn^{IV}O_3(OAc)_3\}(A\text{-}\alpha\text{-}SiW_9O_{34})]^{6-}$ – The First Mn-POM WOC

To the best of our knowledge, the first manganese containing POM WOC was reported in 2014 by Al-Oweini et al.[77,78] It is based on a lacunary $[A\text{-}\alpha\text{-}SiW_9O_{34}]^{10-}$ ligand and has a manganese core $\{Mn^{III}_3Mn^{IV}O_3(OAc)_3\}$ in which the Mn atoms are found in the oxidation states III and IV. The structural arrangement of the four Mn atoms resembles the OEC in PSII with the sole difference that the Ca atom is replaced by Mn.

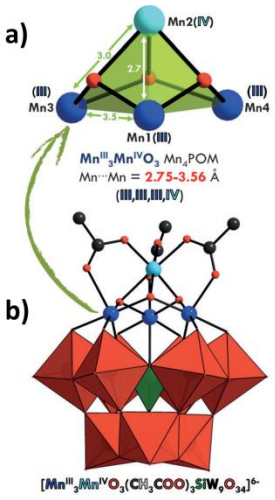

Figure 1.7. (a) Detailed view of the Mn-core of the POM WOC. **(b)** Combined polyhedral ball-and stick representation of the Mn_4 WOC.[77]

Water oxidation was reported in silicate buffer ($NaHCO_3/Na_2SiF_6$, 50 mM, pH = 5.2) with $Na_2S_2O_8$ as electron acceptor and $[Ru(bpy)_3]^{2+}$ as photosensitizer (1 mM). The catalyst concentration was varied from 6.3 µM–50 µM and the sample was irradiated with a tungsten lamp, equipped with a cutoff filter at 375 nm. Evidence for photocatalytic water oxidation has been given by the traces of a FOXY-R-AF probe. This technique detects O_2 by measuring its quenching effect on a fluorescent dye.[79] Between 0.4 and 1.4 µmol of O_2 form after 70 min of irradiation, depending on the catalyst concentration. This amount of O_2 seems to be too low for quantification by gas chromatography (GC). In the reported study the reaction mechanism was investigated by laser flash photolysis experiments. The recovery of the oxidized dye was measured as function of catalyst concentration (eq. 1.7).

$$[Ru(bpy)_3]^{3+} + POM \rightarrow [Ru(bpy)_3]^{2+} \qquad \text{(eq. 1.7)}$$

Recovery experiments were performed under first order conditions with concentrations of $[Mn^{III}_3Mn^{IV}O_3(OAc)_3(A\text{-}\alpha\text{-}SiW_9O_{34})]^{6-}$ much higher than the concentration of the oxidized

sensitizer. This yields a quantitative recovery of the $[Ru(bpy)_3]^{2+}$ species, which follows a mono-exponential law. The resulting second order rate constant for the process $S_0 \rightarrow S_1$ has been determined at $k = (4.6 \pm 0.6) \times 10^6\ M^{-1}s^{-1}$.

While this study shows interesting results for a Mn-based POM WOC, it also illustrates that specific points need to be carefully investigated in future studies. Powder x-ray diffraction (PXRD) or electrospray ionization mass spectrometry (ESI-MS) are generally recommended to ensure phase purity of the starting materials. The stability of polyanions under catalytic conditions needs to be studied in detail, e.g. through stability tests in solution by UV/Vis-spectroscopy or other methods. As the formation of solid POM-PS-complexes has been reported in many studies (§1.9.1), the assumption of a completely homogeneous system is not valid anymore. For a better comparability of POM catalysts, it is necessary to quantify O_2 evolution by conventional methods such as gas chromatography.

1.8 POM Water Reduction Catalysts for Photocatalysis

POMs have been investigated in depth as electrocatalysts for electrochemical H_2 evolution.[80] Later their potential as photocatalysts was investigated in different photocatalytic setups. In some of these setups Pt nanoparticles are used as Co-catalysts. The highest TON was reported for the Ni substituted sandwich-type polyphosphotungstate $[Ni_4(H_2O)_2(PW_9O_{34})_2]^{8-}$. TEOA was used as electron donor and $[Ir(ppy)_2(dtbbpy)]$ as photosensitizer in a mixture of DMF and H_2O. A TON as high as 6500 could be reached under these conditions.[72] For an overview of currently known POM-based WRCs and a comparison of their efficiency and the catalytic test conditions, see Table 4.1.

1.9 Homogeneous or Heterogeneous Catalysis – POM Stability

It is of fundamental interest whether catalysis occurs homogeneously or heterogeneously.[81–83] Nanoparticles which form prior to catalysis may subsequently catalyze the reaction. This issue was studied in particular for Ir based metal complexes, which are powerful WOCs.[84] In general this question is brought up when catalysis is stated to occur homogeneously. Polyanions are considered to be insensitive towards oxidative decomposition. Nevertheless, it has been suggested that the polyanion is not the active catalyst. This has led to a heated debate on the mechanism of POM water oxidation catalysis.[58,81,85,86] Nanoparticles may form prior to catalysis by two different processes. One of these processes is related to the stability of polyanions. Leaching of transition metals cations from the core has been considered as source of Co(II).[85] Under the oxidative conditions during photocatalysis Co(II) cations have been

assumed to be oxidized and form cobalt oxide nanoparticles, a species for which catalytic activity has been reported earlier.[87] Metal cation leaching has been investigated for $[Co_4(H_2O)_2(PW_9O_{34})_2]^{10-}$ – the most prominent example of a POM WOC.[85,88,58] Another process was observed under the catalytic test conditions where (nano)particles form by electrostatic interactions of the polyanion with the positively charged photosensitizer molecules. This process is described in more detail in §1.9.1.

1.9.1 Formation of the POM-PS Complex

The formation of an insoluble precipitate has been observed for almost all polyanions tested for water oxidation. This precipitate was denoted as POM-PS complex. In contrast to a classic transition metal complex, it is formed by electrostatic interactions between positively charged $[Ru(bpy)_3]^{2+}$ cations and the negatively charged polyanions. This solid immobilizes the catalyst and can be collected by filtration, which allows an easy recovery of the catalyst after the reaction. It has been speculated that the POM-PS complex rather than the pristine polyanion represents the true active catalyst.[89,90] This compound was therefore studied in more detail by us and other research groups.

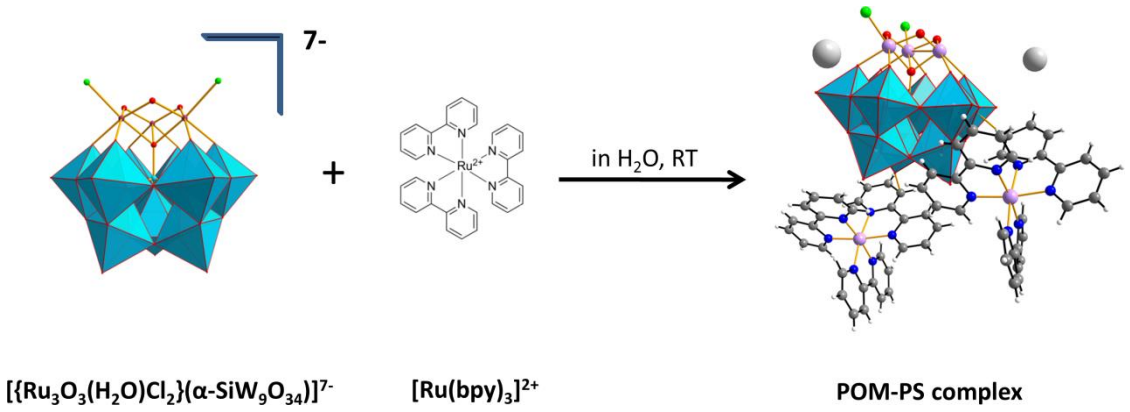

Figure 1.8. Schematic representation of the formation of the POM-PS complex for $[\{Ru_3O_3(H_2O)Cl_2\}(\alpha\text{-}SiW_9O_{34})]^{7-}$ with $[Ru(bpy)_3]^{2+}$ (unpublished results).

Due to the strong electrostatic interactions, this solid forms very quickly. Long range ordering of the POM and sensitizer molecules may be very difficult as confirmed by PXRD patterns which all show characteristics of an amorphous compound. To the best of our knowledge, single crystal X-ray structures have only been reported for POM-PS complexes of spherical Keggin-type isopolyanions $[XW_{12}O_{40}]^{n-}$ to date.[91,92] Crystallization of the POM-PS complex requires special crystallization conditions which enable slow diffusion of a solution of

$[Ru(bpy)_3]^{2+}$ in a solution of the polyanion. In this work, crystals of a Mn substituted TMSP POM-PS complex could be grown after several crystallization tests (§2.6).

As this solid can be precipitated easily from solution it can functionalize a variety of surfaces. With the goal to deposit isolated nanoparticles on silicon nanofilaments a diluted solution of $[Ru(bpy)_3]Cl_2$, was added dropwise to a solution of $[\{Ru_3O_3(H_2O)Cl_2\}(\alpha\text{-}SiW_9O_{34})]^{7-}$. A glass slide functionalized with Si-nanofilaments was thereby immersed in the solution. According to scanning electron microscopy (SEM) no nanoparticles were formed. Compared to TiO_2 which deposits on filaments as discrete nanoparticles,[93] the POM-PS complex deposited uniformly and filled up cavities between the single fibers of the filament (Figure 1.9).

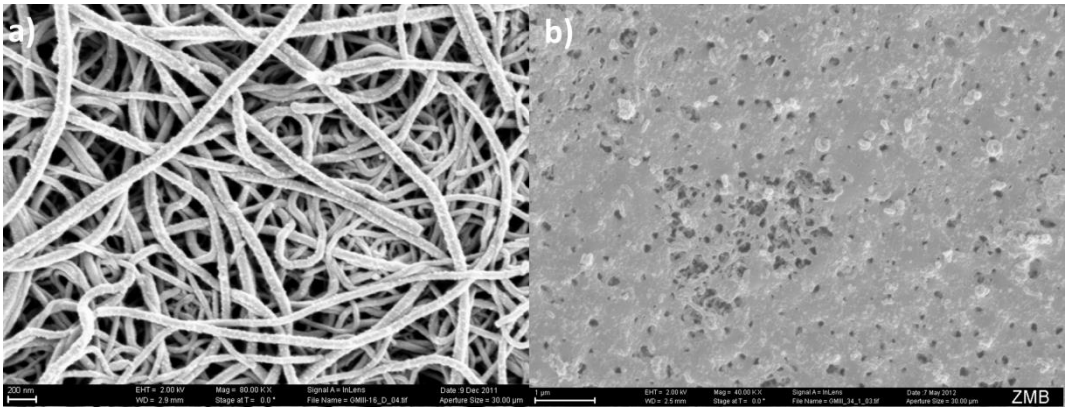

Figure 1.9. (a) Uncoated Si-Nanofilaments, scale bar = 200 nm. **(b)** Si-Nanofilaments after coating attempts with the POM-PS complex, scale bar = 1 µm. (Collaboration with Dr. Georg Meseck, unpublished results)

The formation of the POM-PS complex has been observed consequently for all tested POMs in the following studies. Its formation may depend on the polyanion concentration, but the strong electrostatic interaction between the polyanion and the sensitizer renders it unlikely that the anion remains dissolved. This transformation of the homogeneous catalyst into a heterogeneous species makes mechanistic or spectroscopic studies difficult.[94,95] In order to investigate the POM-PS complex by flash photolysis experiments, attempts have been made to prepare well-defined nanoparticles and to prevent their agglomeration. Through systematic variation of the POM/photosensitizer ratio a parameter window could be found where nanoparticles form in solution. Nanoparticle formation and size-distribution was monitored by dynamic light scattering (DLS). In a second step, the role of the $[Ru(bpy)_3]^{2+}$ counter-cation in the POM-PS-complex was investigated. For this purpose metal complexes, isostructural with $[Ru(bpy)_3]^{2+}$ ($[M(bpy)_3]^{2+}$ (M = Cu, Ni, Co, Os[96]) have been synthesized. Nanoparticles

prepared from $[\{Ru_3O_3(H_2O)Cl_2\}(\alpha\text{-}SiW_9O_{34})]^{7-}$ and the tris-bipyridine metal complexes can reveal the role of the $[M(bpy)_3]^{2+}$ counter-cation. Flash photolysis experiments can reveal differences in the recovery time of $[Ru(bpy)_3]^{2+}$ as a function of the counter-cation type. In combination with promising results of electrochemical studies on the solid POM-PS complex (§1.14.1) this compound remains of great interest for further studies.

1.10 Polyoxometalates – A Short Introduction

Polyoxometalates (POMs) are a class of negatively charged, water soluble metal oxides, mainly formed from tungsten (+VI), molybdenum (+VI), vanadium (+V) and less commonly tantalum (+V) and niobium (+V) in their highest oxidation states.[97–105] The ability to undergo polycondensation is a characteristic feature of metals of the 5th and 6th group and it is more pronounced for heavier atoms. All these metals form MO_6 octahedra, which condensate into larger polyanions. The structures of stable polyanions that can be isolated may slightly differ, depending on the metal type. Isopolyanions (IPA) only consist of a single metal type and oxygen atoms. Heteropolyanions (HPA) contain an additional heteroatom, which allows a different arrangement of the MO_6 (M = W, Mo, V, Ta, Nb) octahedra. The most often encountered IPA within this work is $[H_2W_{12}O_{42}]^{10-}$, also known as paratungstate B. A schematic overview of the most important known polyanion structures to date can be found in Figure 1.10.[105,106]

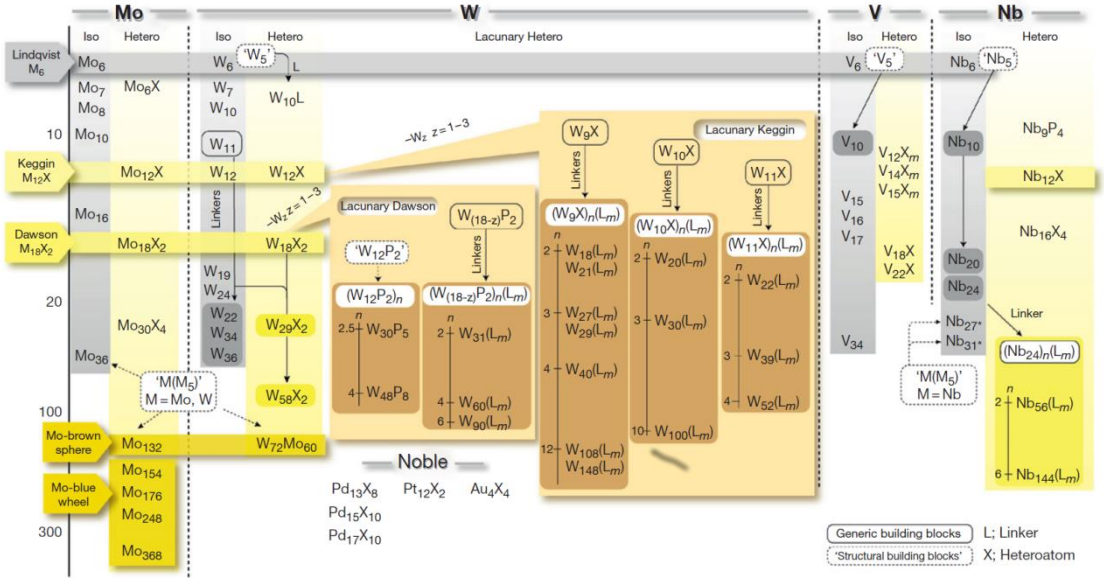

Figure 1.10: A classification of known POM building blocks. **Black lines:** POMs isolated as stable clusters. **Dashed lines**: POM building blocks that could not be isolated to date. Isopolyanion are shown in grey, heteropolyanions are colored.[105,106]

Different heteropolyanions (HPA) have been used in this thesis, such as $[PW_{12}O_{40}]^{3-}$ $[GeW_{12}O_{40}]^{4-}$ or the lacunary precursor $[SiW_9O_{40}]^{10-}$. Target structures of this thesis were tungsten based POMs, also called polyoxotungstates. Lacunary precursors arise from removal of one, two or three WO_6 octahedron from the Keggin structure $[XW_{12}O_{40}]^{n-}$ or the Wells-Dawson structure $[X_2W_{18}O_{62}]^{n-}$ (X = heteroatom, n = depends on X). The term polyanion in

general refers to the negatively charged metal oxygen cluster, while the term polyoxometalate is used to denote the polyanion, its counter-cations and crystal water molecules. Rules for correct nomenclature have been established but are rarely applied due to their complexity.[107] An overview of lacunary building blocks is given in Figure 1.10.[105] Almost all new POMs reported in this work have been prepared from lacunary tungsten based compounds through the reaction with transition metals. Transition metal functionalized POMs are also referred to as TMSPs.

1.10.1 Structural Features of Transition Metal Substituted POMs

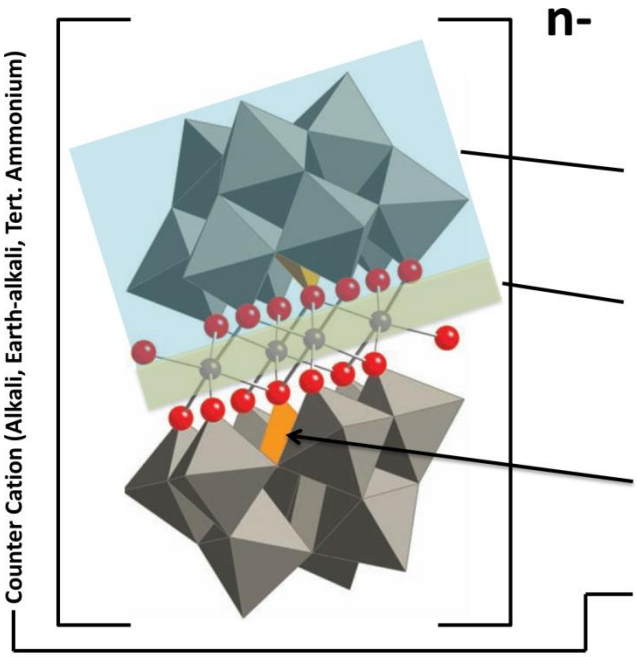

Charge: All polyanions in solution have a high negative charge with n depending on X and M.

Ligand: Cluster of WO_6, MoO_6 or VO_6 octahedra. Lacunary ligands of tungstates arise from removal of 1-3 WO_6 octahedra. 1-4 lacunary ligands assemble with M cations to form complex TMSPs.

Transition metal M: 1st and 2nd row d-block and f block metals, metals from main groups III and IV.

Heteroatom X: X_aO_4 or X_bO_3 atom (X_a = Si, P, Ge, Zn, Co, Ti, Al, Ga, B, As; X_b = Bi, Sb, As, Te).

Cations C: In the solid state the charge of polyanions is often balanced with alkali/earth alkali cations or quaternary ammonium cations.

Figure 1.11. Polyhedral ball and stick representation of a sandwich-type, TMSP of the type $[M_4(H_2O)_2(B\text{-}\alpha\text{-}XW_9O_{34})_2]^{n-}$.

For a better understanding of TMSPs, their most important structural features are briefly discussed here. Heteropolyanions can be prepared with a wide variety of heteroatoms X. The most common are silicon and phosphorous, followed by various metals and non-metals, which can be incorporated as heteroatom in polyoxotungstates (Figure 1.11). Heteroatoms are either three fold coordinated (X_b = Bi, Sb, As, Te) or four fold coordinated with oxygen (X_a = Si, P, Ge, Zn, Co, Ti, Al, Ga, As). The latter configuration can be considered as XO_4 tetrahedron and two types of lacunary structures can be derived, namely the A- and B-types. For three fold coordinated heteroatoms (XO_3) only structures of the B-type are possible.

Structural differences of Keggin-type polyanions are illustrated in Figure 1.12. Polyoxotungstates of the A-type are obtained by removing three edge sharing octahedra, while structures of the B-type are obtained by removing three corner sharing octahedra. In lacunary structures of the A-type, all oxygen atoms of the heteroatom are part of a W-O bond. In structures of the B-type one oxygen atom of the tetrahedral heteroatom X can coordinate to the transition metal core.

The Keggin structure can described as follows: Four so-called triads with the structural formula $[W_3O_{13}]$ coordinate to a heteroatom XO_4/XO_3. Each triad thereby shares one oxygen atom with the heteroatom, also called axial oxygen atom. Each of the four triads can be described with 3 connected WO_6 octahedra, which share oxygen atoms. Lacunary Keggin-type building blocks can be prepared and isolated as starting material with 9, 10 and 11 WO_6 octahedra. The number of possible structures is even larger when we consider that each of the triads can be rotated by 60° around the axis X-O_{ax} to the heteroatom. Rotation of the first triad leads to the *β* isomer and rotation of a second triad to the γ isomer. Rotation of the third and fourth triad would give the δ and ε isomer (Figure 1.12).

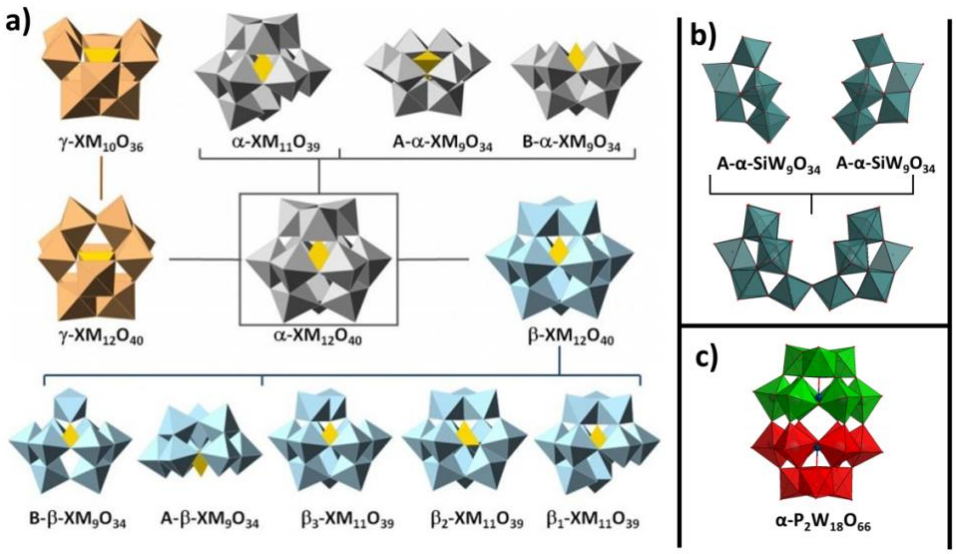

Figure 1.12. (**a**) Polyhedral representation of lacunary Keggin-type polyanion.[108] **(b**) Schematic formation of an open Wells-Dawson structure. (**c**) Wells-Dawson structure with highlighted lacunary Keggin-type moieties.

The ε isomer only exist for non-lacunary structures ($[XW_{12}O_{40}]^{n-}$) and has only been reported for an Al-based POM $[Al_{13}O_4(OH)_{24}(H_2O)_{12}]^{7+}$ which was synthesized in the solid state as a rather unusual compound.[109] From solution the thermodynamically unstable ε isomer is

hardly accessible. For the same reason the δ isomer is rare, and only recently first crystallizations have been reported.[110] The Wells-Dawson structure can be considered as condensation of two Keggin-type structures of the $[\alpha\text{-A-}XW_9O_{34}]^{n-}$ type (Figure 1.12, c). Open Wells-Dawson structures can be isolated when additional transition metal cations are incorporated.[111,112] Starting from the precursor $[\alpha\text{-A-}XW_9O_{34}]^{n-}$ the lacunary Wells-Dawson structures can be obtained. Besides the well-studied Keggin and Wells-Dawson structures other structural types of tungstates are known, but they remain rather rare. Some of them can be functionalized with additional transition metals. The following structures have been reported: Anderson $[MW_6O_{24}]^{n-}$,[113] Weakley-Yamase $[MW_{10}O_{32}]^{n-}$,[114,115] Dexter-Silverton $[MW_{12}O_{42}]^{n-}$,[116] and Lindqvist $[W_6O_{19}]^{2-}$,[117] structures.

1.10.1.1 Hybrid structures

Hybrid structures are formed from the reaction of polyanions with organic molecules or with transition metal complexes. The result is a covalent bond between the polyanion and the organic moiety. The analytical investigation of hybrid structures remains challenging. However, they bear the potential to combine all the components required for artificial photosynthesis in one single compound where the POM is linked to the photosensitizer and the sensitizer to the WRC [POM-Sensitizer-WRC].[118–120] Polyoxometalate based open-frameworks (POM-OFs) may belong to this class of compounds.[121]

1.10.1.2 POM-Based Nanoparticles and Materials

POM-based nanoparticles and materials have been studied in detail, as shown by the large number of review articles of this field. In contrast to hybrid materials where a covalent bond between the organic component and the polyanion is the key feature, hybrid materials are formed by coulombic interactions between positively charged polymers and the negatively charged polyanions. However a distinct delineation between the two types of materials is difficult.[122] The interaction of polyanions with (bio)-polymers such as chitosan, agarose or PMMA was studied in detail.[123,124] Nanoparticles can be prepared from POMs[102,125] or POMs can be used to coat nanoparticles prepared from another material.[103]

1.10.1.3 Multidimensional Structures

Multidimensional structures are formed from bridged polyanionic monomers. Bridging can occur either by 1st and 2nd row d-and f-block metals, as well as metals of the 13th-15th main group or with organic linkers. Isolated polyanions or polyanionic monomers are sometimes referred to as having no dimension (0D). It is important to notice that there is no generally

accepted definition how bridging between different polyanions has to occur in a multidimensional structure. Sometimes alkali metal cations of the 1st and 2nd group are considered as bridging and part of the structure. In this work only non-alkali metal cations are considered as bridging - and only when they directly connect two polyanions. Bridging can either occur at the transition metal core via M_a-O-M_b where M_a and M_b are transition metal cations from the cores of the two connected polyanions. Bridging can also occur via terminal oxygen atoms W_a-O-M_b where a terminal oxygen atom coordinates to the transition metal cores of a second polyanion. Alternatively polyanions can be connected via organic linkers.[118] Inorganic polymers or a 1D chain of polyanions with additional transition metal cations M between the chains lead to a 2D layer of interconnected polyanions. These layers may be connected with further transition metal cations M into 3D structures. The occurrence of multidimensional structures seems to be higher for 1st and 2nd row d-block metal cations which can undergo Jahn-Teller distortion. In this thesis multidimensional structures have been observed for Mn and Cu containing tungstobismuthates (§2.3 and §3).

1.11 Synthesis and Crystallization

A characteristic feature of the tungstate ion is its ability to form condensed, complex isopolytungstate ions in acidic media (Figure 1.13).[74,75] A variety of different tungsten-based isopoly and heteropolyanions are known. Lacunary heteropolyanions can be prepared, isolated and used as starting materials for the synthesis of larger transition-metal substituted structures. The synthesis of these lacunary precursors is in general well reproducible and they can be prepared on a large scale, especially from well-known literature protocols, see section 1.17.1 for an overview. An exception is the lacunary tungstobismuthate $Na_9[BiW_9O_{33}]\cdot 19.5H_2O$, whose synthesis turned out to be very unreliable, frequently giving rise side products (§2.2.3).

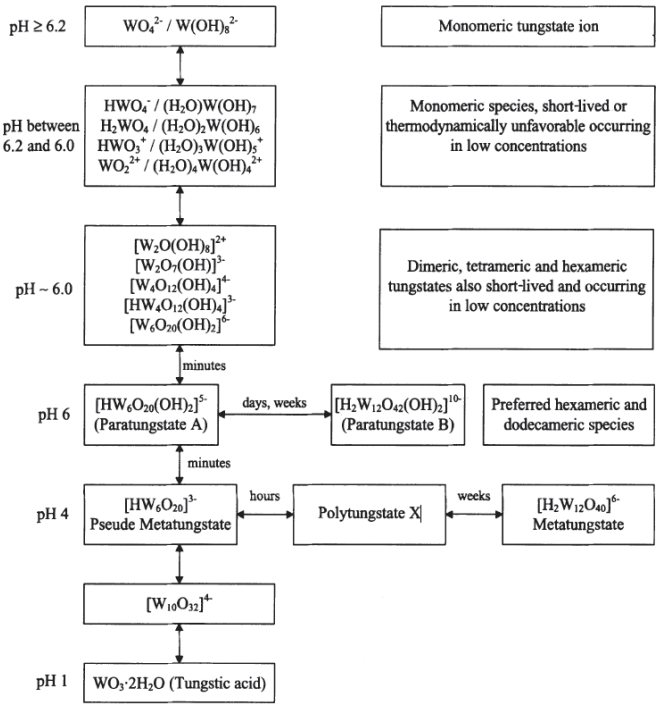

Figure 1.13. Overview of tungstates in aqueous solution.[126]

The distribution of V, Mo, and W polyanions has been described earlier, and reviewed by Cruywagen.[127] Distributions have been calculated from experimentally determined formation constants. The monomeric tungsten ion $[W(OH)_8]^{2-}$ or WO_4^{2-} is only stable at pH ≥ 6.2. At pH 1 highly polymeric amorphous tungstic acid precipitates. This white solid is usually observed during POM synthesis when concentrated acids are added too rapidly to a solution of sodium tungstate so that the local pH is too low for the formation of tungstic acid. Solid tungstic acid partially re-dissolves when the pH increases again (very slow dropwise addition of acid under vigorous stirring helps to avoid this). POMs assemble through a process referred to as polycondensation, referring to the reaction of anionic species and protons. The general overall tungstate polycondensation reaction is summarized in (eq. 1.8):

$$2\ WO_4^{2-} + 2H^+ \rightarrow W_2O_7^{2-} + H_2O \qquad \text{(eq. 1.8)}$$

At first glance, it is rather unlikely that two negatively charged species react with each other, but this process can be explained as follows: cationic and anionic tungsten species are in equilibrium. Upon acidifying the reaction mixture, the amount of positively charged species increases by releasing a hydroxyl group. This species can react with some remaining anions and thereby form large polyoxotungstates. The nature of the monomeric tungstate in an

aqueous solution is not precisely known. Although it is commonly referred to as $[WO_4]^{2-}$ it is most likely present in solution in the hydrated form $[W(OH)_8]^{2-}$.[75]

$$[W(OH)_8]^{2-} + 4H^+ \rightarrow [W(OH)_4(H_2O)_4]^{2+}$$
$$[WO_4]^{2-} + 4H^+ \rightarrow [WO_2]^{2+} + 2H_2O$$

Step 1. Acidification of the reaction mixture leads to positively charged species.

$$2[W(OH)_8]^{2-} + [W(OH)_4(H_2O)_4]^{2+} \rightarrow$$

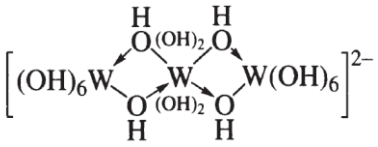

$$2[WO_4]^{2-} + [WO_2]^{2+} \rightarrow [O_3W{-}O{-}WO_2{-}O{-}WO_3]^{2-}$$

Step 2. The reaction of a negative and a positive species results in the formation of polyoxotungstates.

1.11.1 Lacunary Starting Materials

Large polyanion structures can be obtained from the reaction of lacunary POM ligands with 1st and 2nd row d and f-block metals, as well as from metals of the 13th-15th main group herein referred to as M^+. Almost all tungstates are based on Keggin or Wells-Dawson frameworks from which a certain number of WO_6 octahedra are missing. These so-called lacunary tungsten ligands can coordinate via negatively charged oxygen atoms to a large number of cations M^+, thereby forming TMSPs. For an overview of possible lacunary ligands based on the Keggin-structure, see Figure 1.12. The presence of M^+ cations can influence the equilibrium of the different polyanion species in solution. Heteroatoms present in the solution can shift the polycondensation process to more alkaline pH.[126] The distribution of polyanion species in solution in the presence of a heteroatom X and metal cations M^+ has been less intensely studied to date.

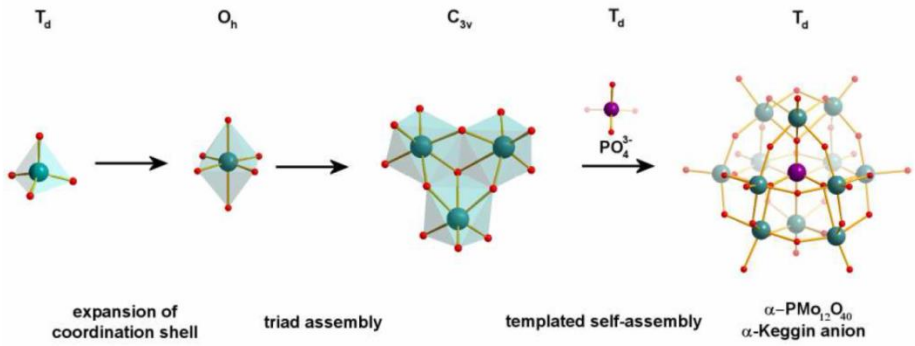

Figure 1.14. Schematic representation of the formation of heteropolyanions.[128]

The synthesis and characterization of lacunary precursors has been described in detail.[129] In this work most experiments were performed with the lacunary Keggin-type precursors [*α/β*-$SiW_9O_{34}]^{10-}$,[130] [*α/β*-$GeW_9O_{34}]^{10-}$,[131] [$BiW_9O_{33}]^{9-}$,[132] [B-*α*-$PW_9O_{33}]^{9-}$,[133] [A-$PW_9O_{34}]^{9-}$ [134,133] and [$SbW_9O_{33}]^{9-}$.[135] Lacunary Wells-Dawson precursors have been used as well, preferably the phosphorus containing precursor [*α*-$P_2W_{15}O_{56}]^{12-}$,[133,136] which was prepared from the Wells-Dawson POM [$P_2W_{18}O_{66}]^{6-}$,[136] and [*α*-$As_2W_{15}O_{56}]^{12-}$.[137] All of these precursors except for the Bi containing POM could easily be prepared according to reported procedures. Preparation of the lacunary starting material $Na_9[BiW_9O_{33}]\cdot 19.5\ H_2O$ was possible under adjusted reaction conditions, but its phase pure isolation was not always successful (§2.2.3).

1.11.2 Practical Aspects of the Synthesis and Crystallization of POMs

Synthesis of POMs reported in literature has turned out to be a challenging task in the course of this thesis. The reproduction of reported synthetic procedures often failed or the reported crystalline product could not be obtained. The same applies to polyoxometalate structures that have been synthesized herein. Some of them could be isolated phase pure once but attempts to reproduce the synthesis failed or resulted in different structures.

It is important to realize that at different pH values a broad range of structurally different isopolyanion species are found in solution at equilibrium.[138,139,127] While the distribution of the different polyanion species in the reaction mixture has been studied for isopolyanions,[127] little is known about the distribution of TMSPs species. Attempts to precipitate a specific polyanion by addition of counter-cations are usually made without prior knowledge of the polyanion distribution in solution. As result, a mixture of products can crystallize from the reaction mixture. The POM that crystallizes first may not be the most abundant polyanion in

solution. Depending on the countercation mixture the POM that crystallizes first may vary.[140] The arrangement of countercations in the crystal structure may be neglected, as long as no specific 1D-3D structure needs to be reproduced and no M^+ is amongst the countercations.

These difficulties are illustrated by the following example. The polyanion $[\{Ga_4(H_2O)_2\}(VWO_{34})_2]^{6-}$ was chosen as synthetic target and prepared according to a published procedure for a H_2 evolution catalyst with a Mn_4 core.[141] The structure of the compounds obtained from this procedure was determined by single crystal structure analysis. The quality of the diffraction data was sufficient to determine the structures of the polyanions. In the first synthesis, the 2D compound 2D-V$[GaW_{12}O_{40}]$ was isolated in phase pure form instead of the target compound.

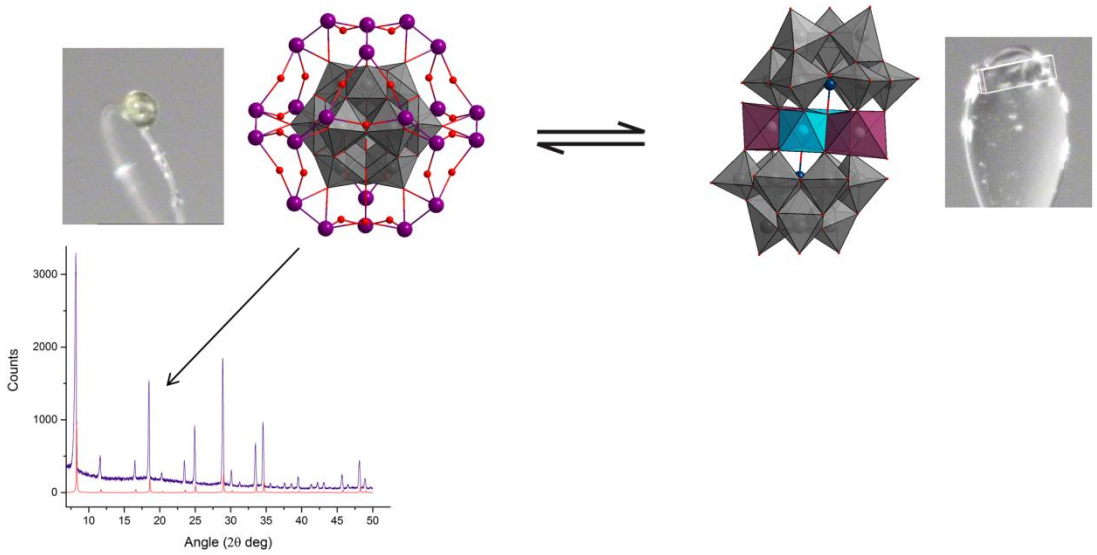

Figure 1.15. Equilibrium of 2D-V$[GaW_{12}O_{40}]$ with the sandwich type compound $[\{V_2Ga_2(H_2O)_2\}(VWO_{34})_2]^{6-}$. Color code: WO_6 = grey, GaO_6 = blue, VO_6 = purple, Na = purple sphere. (Unpublished results)

Despite several attempts to repeat this synthesis according to precise experimental records, this compound could not be isolated in phase pure form again. In subsequent batches, crystals of a different shape were present. Crystal structure analysis revealed the formation of a polyanion of the type $[\{V_2Ga_2(H_2O)_2\}(VWO_{34})_2]^{6-}$. This indicates that the Keggin and the Sandwich structure are in equilibrium, or that a slow transformation occurs.

Difficulties Related to the Synthesis

- The presence of a polyanion species in solution does not necessarily imply that it can be isolated by crystallization. The main species present in solution may not be the one that crystallizes.[140]
- Purification of POMs by recrystallization may only be possible for structures, in which the arrangement of countercations is not essential.
- Impurities in the starting material can be present in small amounts below PXRD detection limits.[142]
- Polyanions that are structurally very different from the starting material or contain different tungstate fragments may arise from complex pathways which are difficult to reproduce.

Difficulties Related to Analytical Methods

- The purity of POMs is usually verified by elemental analysis (EA). EA complements other techniques which are used to investigate the purity of the bulk material. Structurally different compounds may have almost the same EA results.
- XRD is a good method to verify the purity of bulk material given that the compound is crystalline and diffracts well under the experimental conditions. In a mixture of different compounds one species may not diffract as good as the other and can therefore not be detected. However, the crystal structures of all different polymorphs need to be known (§1.16.1.6).
- There is no convenient way reaction control strategy for POM formation to date, which renders optimizing the reaction conditions difficult. Consequently initial conditions are chosen randomly and the reaction is stopped at a random point. The distribution of different species in solution at this time is unknown.

It is crucial to point out that the synthesis of POMs, unlike organic synthesis, is a self-assembly process. Precursors may undergo unexpected transformations upon dissolution depending on pH and countercations. The isolated compounds may only represent a small fraction of all polyanions in solution that are in equilibrium with each other. Even if present in solution, polyanions may only be isolated as crystals in presence of the right (mixture) of countercations. Studies where POMs are applied should focus on well-described structures that can easily be crystallized, characterized and purified by recrystallization. Larger

structures with complex M^+ metal core may be not reproducible or impossible to obtain in phase pure form.

1.12 Applications of Polyoxometalates

The broad application spectrum of POMs can be distinguished into homo- and heterogeneous setups, and the following survey summarizes some highlights.[143]

1.12.1 Application Options in Solution

POMs in solution have been investigated as compounds with a great potential for biomedical applications.[144,145] They have been tested for their antiviral, and antitumoral[146] properties or as versatile enzyme inhibitors.[144] Nanoparticles prepared with the negatively charged polyanions and positively charged biopolymers (e.g. chitosan) pave the way to overcoming the long-standing problem of POM cytotoxicity for anticancer and antiviral therapy.[147–151] A variety of organic reactions can be catalyzed with POMs and the potential of these compounds has been investigated in detail. POMs have been successfully used as homogeneous[152,153] and heterogeneous[154,155] catalysts for organic reactions. Chiral polyanions have been of particular catalytic interest as a new way to introduce chirality in organic synthesis.[156,157] As discussed in more detail in §1.6-1.8 POMs are investigated for their promising properties as WOCs[58,158] and WRCs[159] for artificial photosynthesis. Electrocatalytic POM applications encompass organic catalysis[80] or water splitting.[80,160,161]

1.12.2 Solid State POM Applications

The use of POMs as crystallization agents for the crystallization of proteins has been reviewed by Bijelic et al.[162] The Wells-Dawson polyanion $[P_2W_{18}O_{62}]^{6-}$ was used to crystallize the small ribosomal subunit of Thermus thermophiles. While POMs have mainly been used for phasing reasons, they also enhance the crystalline arrangement of macromolecules. Electrostatic interactions reduce their flexibility and thereby facilitate crystallization. In addition, improved rigidity enhances the diffraction intensity of protein crystals. A different potential application is the sensing of organic molecules. This was investigated with electrodes functionalized with a layer of POMs which were tested for sensing in solution and in the gas phase.[163] POMs represent a source of unusual spin topologies and are therefore investigated intensively for their magnetic properties, especially their potential as single molecular magnets (SMM), which can retain magnetization at low temperature.[164–167] This property makes them interesting synthetic targets for high density

data storage. A rather unusual application of POMs is their use in rewritable paper. Their ability to undergo reversible electron transfers is exploited. The color change triggered by applying a reducing agent to polyanions stains the paper blue, which can be reversed with an oxidant.[168]

Besides the application of polyanions in solution and in the solid state, these large structures represent a challenge for computational chemists and allow them to test and improve new computational methods.[169]

1.13 Structural Investigations on Polyoxometalates

POMs can be characterized by a broad variety of analytical methods. All of them add another piece of information to the final structural model. The most important methods applied for the structural characterization of new POMs presented in this thesis are briefly summarized below. As the presented analytical work is mainly focused on single crystal/PXRD, mass spectrometry and electroanalytical methods, they are discussed in more detail (§1.14-0).

Elemental analysis (EA) is the most fundamental method to confirm the purity of POM compounds. However, this analytical method is not suitable for discriminating between compounds with a similar composition or between different isomers. An EA requires at least one backup method to confirm purity.

Infrared (IR) and Raman spectroscopy are important methods for the characterization of as-synthesized pure POM compounds. Crucial information on W-O or X-O vibrations are obtained.[170,117] Although IR spectra of POMs are dominated by vibrations of the W-O framework, X-O vibrations can be distinguished, e.g. for P-O vibrations. M-O vibrations in TMSPs may not result in significant peaks. The IR spectra of Keggin-type polyanions of the type [α/β-$XW_{12}O_{40}$] (X = Si, Ge, P, As, B) have been studied in detail.[171] Vibrations have been assigned after normal mode analysis, thereby cation-anion[170] and anion-anion[117] interactions have been taken into account. These methods can be useful for detecting α-β isomerization or the transformation from A-type to B-type.[133] We have observed that IR spectra of phase pure compounds obtained in different batches agree very well and peak-shifts are negligible. Mixtures of similar structures or impurities, however, may not be detected without a reference spectrum of the phase pure compound at hand.

UV/Vis spectroscopy is used for characterization of new POMs and is a standard technique to investigate the stability of POMs in solution. However, if decomposition occurs on a very fast timescale, e.g. upon dissolution, the POM could be wrongly assigned as stable.

Nuclear magnetic resonance spectroscopy (NMR) requires a NMR active nucleus and a compound that is free of paramagnetic cations. For the characterization of the new POMs presented in this work ^{183}W,[172] ^{31}P, ^{71}Ga, and ^{209}Bi NMR experiments have been performed. ^{71}Ga and ^{209}Bi have a quadrupole moment which results in very broad signals, thus requiring solid state NMR methods. ^{31}P is very sensitive and such spectra are frequently recorded,[173,174] especially to confirm the purity of phosphotungstates.[142] ^{183}W NMR provides the most detailed information about the solution structure of polyanions.[175] All chemically different W atoms have a different chemical shift, which makes it possible to confirm the presence of a certain polyanion structure in solution. The drawback of ^{183}W NMR spectroscopy is that the ^{183}W isotope is rare, has a low sensitivity and a long relaxation time. Therefore, it takes a long time to measure a good ^{183}W NMR spectrum.[172] ^{183}W NMR spectra cannot be measured in the solid state.

Thermogravimetric Analysis (TGA) is applied routinely, in order to determine the number of crystal water molecules in POM structures. There is no commonly accepted definition of whether crystal water molecules coordinating to the TM-cores are part of the crystal water content that is supposed to evaporate or not. Crystal water molecules may evaporate already upon sample preparation. The accuracy of this technique is not sufficiently high to draw any conclusion about the origin of remaining electron density in a crystal structure arising from disordered crystal water molecules or from background noise. Routinely, samples should be dried under high vacuum prior to elemental analysis.

1.14 Electrochemistry of Polyoxometalates

Electrochemical properties of POMs have been investigated widely by means of cyclic voltammetry (CV),[80] mostly to measure redox potentials of dissolved molecular species. From this information, electron transfer kinetics and subsequent reactions can be studied.[176] An electrolyte is used in order to facilitate electron transfer between the dissolved species and the electrodes. Electron transfer processes from the working electrode to the dissolved molecular species and vice versa are probed by applying a potential between the working electrode and a counter electrode. The current which is observed when electrons are transferred is plotted against the potential. This results in the characteristic plots of cyclic

voltammograms (Figure 1.16). A detailed study of cyclic voltammograms of polyanions has been presented earlier by Launay et al.[177,85] and others.[178,80,179,180] They tested electrochemical properties of polyanions and assigned the waves which are observed in cyclic voltammograms to specific electron-transfer processes. The potential at which an electron transfer process takes place can be determined under specific conditions (pH, additives, buffers) and be used to predict if a reaction may take place or not (§1.14).

1.14.1 Electrochemical Water Oxidation with POMs/POM-Composite Materials

POMs have been investigated extensively as homogeneous[80,181] and heterogeneous electrocatalysts for O_2 and H_2 evolution. O_2 evolution was observed for functionalized FTO glass surfaces or for carbon paste functionalized electrodes.[160,182,161] H_2 evolution at solid electrodes has been investigated for the Keggin-type anion $[SiW_{12}O_{40}]^{6-}$, which was used as the redox-mediator between a solid electrode and the WRC.[183]

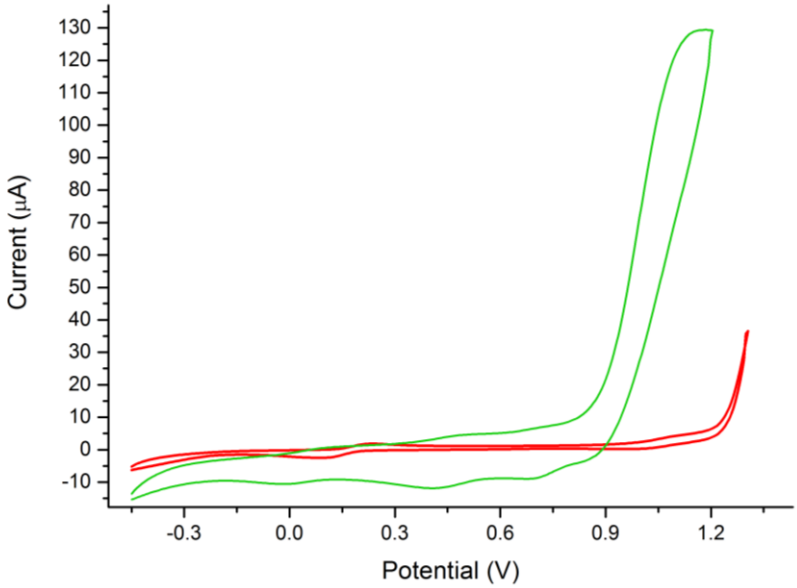

Figure 1.16. CVs measured with POM-PS complex functionalized carbon paste electrodes vs. Ag/AgCl, in acetate buffer (pH = 4.75, 0.1 M), 50 mV/s;
red: $Na_n[Ru(bpy)_3]_{(10-2n)}[Co_4(H_2O)_2(PW_9O_{34})_2]$; green: $[Ru(bpy)_3]_2K_3[\{Ru_3O_3(H_2O)Cl_2\}(\alpha\text{-}SiW_9O_{34})]$ (unpublished results).

In the context of a sub-project of this thesis, the POM-PS complex $[Ru(bpy)_3]_2K_3[\{Ru_3O_3(H_2O)Cl_2\}(\alpha\text{-}SiW_9O_{34})]$ was prepared in larger amounts and its electrochemical properties were characterized by cyclic voltammetry of the POM-PS complex material in carbon paste electrodes. The observed waves indicate that the electrochemical

properties of this solid can be measured. At approx. +0.82 V the onset of an electrocatalytic wave can be observed which most likely corresponds to catalytic water oxidation. Later a similar study has been published by Hill et al., who studied the electrochemical properties of the POM-PS complex $Rb_4[Ru^{II}(bpy)_3]_5[\{Ru^{III}{}_4O_4(OH)_2(H_2O)_4\}(\gamma\text{-}SiW_{10}O_{36})_2]$ in carbon paste electrodes (Figure 1.16).[184,185] Other electrochemical studies have been reported where compounds prepared from polyanions with positively charged cations have been used as electrocatalysts.[186–189]

1.15 High Resolution Mass Spectrometry

Mass spectrometry has become a valuable tool to study the self-assembly process of polyanions. The topic was reviewed by Ohlin who focused on early ESI-MS studies of isopolyanions.[190] Later studies have been extended to more complex TMSPs and new techniques of mass spectrometry have been used to study complex mixtures of polyanions.[191–193] This technique has proven very useful to describe the equilibrium of polyanions in solution.[140,194] To date a large number of studies on the formation of polyoxotungstates[195–204], polyoxomolybdates,[205,206,113,207–210] polyoxovanadates,[211,212] polyoxniobates[213,214] and polyoxotantalates[213] have been reported. In the context of this thesis high resolution mass spectrometry (HR-ESI MS) was used to confirm the identity of new polyanions. Single crystals can be selected from solution and measured by HR-ESI MS. While the structure of polyanions with a non-disordered TM core could be confirmed (Figure 6.7), this is more ambiguous for polyanions with a disordered TM core (Figure 2.9). Because of overlapping peaks a clear identification of polyanions with a specific core composition is not always possible.

1.16 Investigation of POMs with X-ray Radiation

Most POMs are crystalline solids, which permits structure determination by single crystal X-ray diffraction. This method has therefore become the most important tool for studying the structure of POMs in the solid state. Structure determination from single-crystal diffraction data is convenient and one of the oldest methods for structural investigation of these compounds. For paramagnetic or multidimensional POMs (§1.10.1.3), single crystal X-ray diffraction is the only reliable method for structure determination. Powder X-ray diffraction (PXRD) is not yet used in POM chemistry on a regular basis, although it is crucial to provide evidence of a phase pure product. Synchrotron radiation was used in this work to probe the coordination environment and oxidation state of different POM structural elements with EXAFS and XANES.

1.16.1 Single Crystal X-ray Diffraction

Approximately 110 data sets from polyoxometalate crystals have been collected during this thesis. Data collection was done on an Xcalibur diffractometer from Oxford Diffraction equipped with a four circle goniometer, a Ruby135 mm CCD detector and a Mo sealed X-ray tube ($\lambda = 0.71073$ Å).

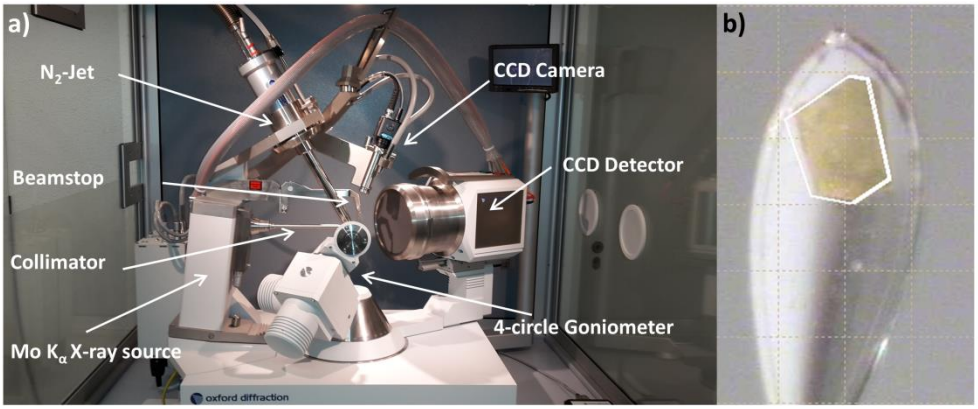

Figure 1.17. (a) Xcalibur diffractometer from Oxford Diffraction at the Department of Chemistry of the University of Zurich; **(b)** Mn-POM crystal mounted inside of a glass fiber loop with oil.

Attempts have been made to collected datasets with a resolution of 0.8-0.6 Å, at an average redundancy of 5 with a signal to noise ratio I/I_σ of at least 20:1. Crystals were mounted on top or inside a glass fiber loop with the help of Infineon or Paraton oil depending on whether the

crystals are sensitive to crystal water evaporation. Crystals were placed in an N_2 stream, usually at 183 K, provided by a Cryojet cooling system from Oxford Instruments.

1.16.1.1 Structure Solution and Refinement

The CrysAlisPro software package was used for data reduction and to perform an analytical absorption correction.[215] The software package WINGX was used for data analysis. Structure solution was done with different programs; initial structure solutions were usually obtained with SIR97[216] or SHELXT[217] and in some cases with SHELXS-2013.[218] The positions of the tungsten atoms were located with direct methods. For structure refinement, SHELXL-2014 was used. Once all tungsten atoms were located, the structure could be assembled step by step from successive difference Fourier maps. Hydrogen atoms were not routinely included in the models as they could not be localized. PLATON[219] was used for structure validation, and ORTEP[220] was used to visualize the solved structure and to check on appropriate atomic displacement parameter (ADPs). Crystallographic information files (CIF) were prepared for publication with EnCIFer 1.5.[221]

Crystal structure solution of POMs is usually performed in two steps. First the tungsten oxygen framework of the polyanion is refined and the transition metal core is assigned and checked for an eventual M/W disorder. While this step is rather simple for structures with low symmetry, it turned out to be surprisingly difficult for structures with a higher symmetry. In crystal systems with a high symmetry the choice of the correct space group is often ambiguous and only a very small fraction of all atoms is found in the asymmetric unit. This renders the assignment of structural features difficult. Once the atoms of the polyanion are found, crystal water molecules and counter-cations need to be added carefully to the model. It is important to do a preliminary analytical absorption correction before this step with the approximate unit cell content. An analytical absorption correction is necessary because POMs have rather high absorption coefficients around ~26.00 mm^{-1} for Mo X-rays. This step has to be repeated at the end of the refinement process once that the entire unit cell content is known. The corrected data has much less contribution of artificial electron density which makes the distinction between crystal water molecules and cations easier. In the structures reported in this thesis, attempts have been made to refine all atoms anisotropically. In published structures, crystal water molecules and counter-cations are often refined isotropically. Finding a model that is in optimal agreement with charge balance, the measured

elemental analysis and structural information from other experimental techniques, e.g. the number of crystal water molecules from TGA or information from HR-ESI MS, can become very difficult. This renders the second step very time consuming. POM structures may have large voids, filled with disordered solvent molecules and counter-cations.[222] Crystal water molecules and counter-cations have been refined explicitly in all of the solved crystal structures. Often they are found on disordered positions and partially occupied. If this disorder is too extensive, SQUEEZE can be applied to remove the contribution of this blurred electron density. It may look exaggerated to spend a lot of time on the correct assignment of counter-cations and crystal water molecules, considering that the polyanion is the structure of interest. However, this final step remains crucial and helps to avoid errors with the entire polyanion model. Furthermore, it is necessary to ensure that only alkali metal cations are part of the structure and no M^{n+} transition metal cations. Such free Co^{2+} countercations can form CoO_x particles in solution, which may act as active catalysts in water oxidation.[85,223] To avoid this source of error, careful analysis of all refined countercations in the crystal structure is mandatory.

1.16.1.2 Structure Validation and CIF preparation

Structure validation is a crucial part of crystal structure analysis. In this step the structural model is checked for possible problems, which could indicate the assignment of a wrong atom type or occupancy of a particular site. Various criteria are considered for the correctness of a crystal structure.[224] A few points which are often encountered in crystal structures of POM are briefly discussed below.

- Voids: The model is checked with PLATON for possible voids. While voids in POM structures are common,[222] there are different possibilities for adressing this problem, such as SQUEEZE.[219]
- Interatomic Distances and Occupancies have to be physically meaningful. They need to be checked carefully and brought into agreement. It may be quite difficult to achieve this in disordered structures.
- Oxidation State of Cations: Bond valence sum (BVS) analysis was used as an additional information to check whether the oxidation state of metal cations (W, Mn, Co, Ga) is correctly assigned.[225] BVS analysis on oxygen atoms usually does not allow for a clear statement on the oxidation state of oxygen atoms. While crystal water molecules can be distinguished, the distinction between hydroxyl- and oxo-groups is more difficult.

- Protonation: As a consequence of ambiguous BVS values for oxygen atoms, their exact protonation state often remains unknown. It may not be possible to achieve charge balance between the expected charge of the polyanion and the number of countercations found in the refinement process.
- Residual Electron Density: Residual electron density peaks as high as 2.35-4.34 $e^{-}A^{-3}$, were even found for structures with good quality datasets. However, these values are in agreement with other published POM structures.[226–228] An analytical absorption correction can help to reduce residual electron density peaks outside of the polyanion cluster. In the ideal case, approximately 15-20 of the highest electron density peaks are found close to the heavy metal atoms.
- Charge Balance: The charge of the polyanion needs to be balanced by a matching number of countercations to maintain electroneutrality. As already mentioned, residual electron density peaks may have values in the range of disordered countercations. In combination with the unknown protonation state, a definitive solution may not be found. Polyanions in low symmetry space groups with an asymmetric unit that contains half or an entire sandwich-type polyanion (9-18 W atoms) often contain partially occupied countercations and crystal water molecules. In these structures, the occupancies of the countercations can be refined with more flexibility, which makes it possible to match the expected charge. A wrong charge balance may be an indication of an entirely wrong structure model (see §1.16.1.5).
- checkCIF: The checkCIF tool of the International Union of Crystallography (IUCr) may be considered as final validation of a CIF which is obtained after the structure refinement process.[229–231] The test procedure is designed to detect errors within the structural model, as well as errors regarding data collection and data treatment processes. Errors are categorized by their severity and lead to alerts with a different degree of relevance. A- and B-alerts are considered as serious and need to be eliminated or their cause should be explained. Frequently encountered alerts in POM structures are excessively high residual electron density peaks or voids in the structure. Depending on their magnitude this leads to an A- or B-alert. The threshold values which lead to critical A- or B-alerts may turn out rather low for large POM structures containing many heavy metal atoms.

1.16.1.3 Disorder

Disorder is a frequently encountered phenomenon in organic and inorganic crystal structures. Three types of disorder are commonly observed (dynamic disorder, static disorder in the form of elemental disorder and solvent disorder).[232]

Disordered Solvent and Counter-Cations: Many POM crystal structures contain large cavities filled with crystal water molecules and countercations. Larger polyanions may face similar problems to those observed in macromolecular protein crystallography.[233] Often more than one arrangement of the counter-cations is possible. In the extreme case, none of the refined cation positions is fully occupied. The occupancy of each cation can be refined slightly different without ADPs becoming unreasonable (up to ± 30%). The refined charge can thereby be varied in a certain range and no conclusion can be drawn anymore on the exact oxidation states of the cations in the transition metal core. Furthermore, countercations and crystal water molecules are often found to be disordered across several positions, and sometimes three or four different positions have been refined in this work. This leaves a certain ambiguity about the nature of the remaining electron density peaks. They could be modeled as cations, oxygen atoms or simply be interpreted as background noise.

Elemental Disorder: This type of disorder, where two or more elements occupy a single crystallographic site in a model, is frequently encountered in POM chemistry and it is likely to be overlooked. It can, for example, occur for cations of different elements with the same coordination geometry[234,235] which are integrated into the W-O framework through replacing a WO_6 octahedron. This was observed for the W/Ni disorder in Nickel-Keggin POMs (§1.16.1.5). In other structures, disorder is restricted to the transition metal core, e.g. in the transition metal core of copper-containing tungstobismuthates of the B-α type where extensive Cu/K disorder was observed (§3.2.2.2). In this work, elemental disorder was investigated in particular for tungstobismuthates of the B-β type with a W/M (M = Mn, Co) disordered transition metal core. Attempts were made to reduce the disorder by modification of the reaction conditions where $[HWO_4]^-$, as a source of additional tungsten, is present in solution. It arises from partial decomposition of the lacunary precursor $[BiW_9O_{33}]^{9-}$. In polyanions of the type $[\{M_1(H_2O)_3\}_2\{Bi_2M_2W_{18}O_{66}(OH)_4\}]^{n-}$ (n = depends on the occupation of M_1 and M_2) the positions M_1 and M_2 can either be occupied with W or M. The resulting polyanions are isostructural but display a different W/M composition of the transition metal cores. A crystal can be considered as a 3D macroscopic object which is composed of a large number of stacked unit cells. It is unknown whether polyanions with a distinct transition metal

core (however being isostructural) are distributed in these unit cells with a regular pattern or whether their distribution is random. Consideration of Bragg intensities only, as usual practice in conventional X-ray crystallography, does not permit further conclusions about an eventual regular pattern. Diffraction at the sites of the transition metal core arises from elements with different scattering powers. Conventional X-ray crystallography only permits measurements of the average electron density and refinement with a certain ratio of both elements. This was possible for the structures reported in this thesis, because the scattering powers of W and Mn or Co are fairly different. The percentage occupation by W/M (M = Mn, Co, Cu) is thus obtained from the refinement. This type of disorder is indicated by ADPs which become non positive definite (NPD) for a 100 % occupation of either of the elements. The consequences of W/M disorder for the structure of the polyanion is illustrated by examples 1 (§1.16.1.4) and 2 below (§1.16.1.5).

1.16.1.4 Example 1 - W/Mn Disorder in a 1D-Tungstobismuthate

Implications of elemental disorder on the effective structure of the transition metal core of polyanions were studied for the self-assembly process of the lacunary precursor $[BiW_9O_{33}]^{9-}$ with Mn, Cu and Co cations (§2.3).

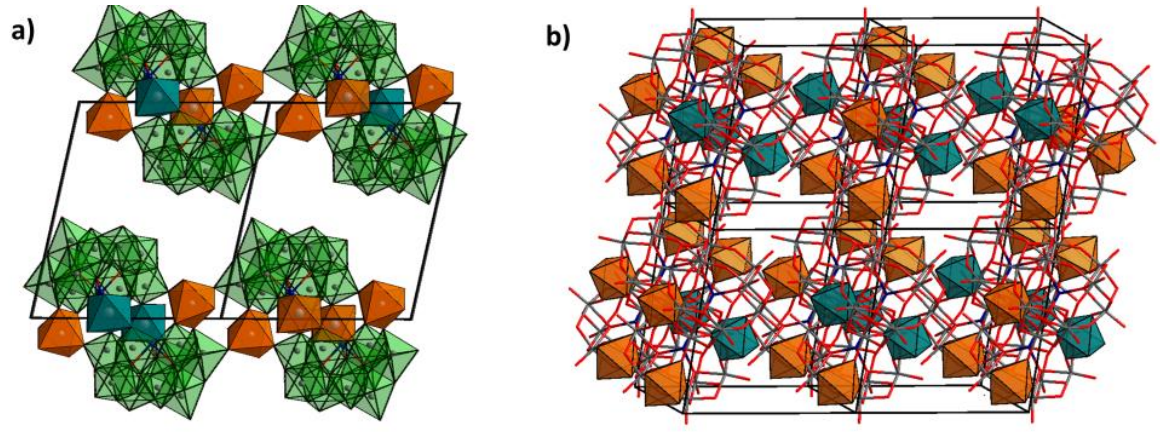

Figure 1.18. Polyhedral ball-and stick representation of the 1D polyanion **Mn-1** with a Mn/W disordered transition metal core. Two unit cells are shown. Counter-cations were omitted for clarity. **(a)** View along the b-axis. **(b)** View perpendicular to the ab-plane. The polyanion **Mn-1** is shown in the wire-frame representation, the transition metal core is represented by a polyhedron. Color code: green = WO_6, orange = MnO_6, dark green = $MnO_4(H_2O)_2/WO_6$.

The knowledge of the exact composition of the transition metal core is crucial for establishing SAR. The core composition has a significant influence on the catalytic activity as reported earlier for Co-containing tungstobismuthates.[235] The crystal structure of the polyanion 1D-$[\{A(H_2O)_3\}_2(B(H_2O)_2)\ (C(H_2O)_2)(BiW_9O_{33})_2]_n^{(10n)-}$ with a W/Mn disordered transition metal core was solved by conventional crystallography (Figure 1.18). The ratio of W/Mn for the positions A in the tungstobismuthate was refined to 0:100 and to 37:63 for the positions B and C.In this example the POM crystallized in the triclinic space group $P\bar{1}$. The transition metal core is completed by the inversion symmetry from which the two remaining positions are created (A → D and B → C). The general description of a the transition metal core is {A, B, C, D} in which each position can be occupied independently. In all the structures characterized in this thesis, the outer positions A and D are fully occupied by Mn which simplifies the core composition to {Mn, B, C, Mn}. Conventional X-ray crystallography does not permit to distinguish between the two positions B and C as only an average value for the electron density can be observed which leads to B = C, which is the reason for the observed inversion symmetry. When considering the local structure, the positions B and C can be distinguished and either occupied by Mn or W, and their ratio was refined. Three different core compositions are possible, {Mn, Mn, Mn, Mn}, {Mn, W, W, Mn} and {Mn, Mn, W, Mn} which is identical with {Mn, W, Mn, Mn}. Probabilities for the distinct polyanions were calculated assuming a stochastically independent distribution of Mn and W in the transition metal core (Figure 1.19).

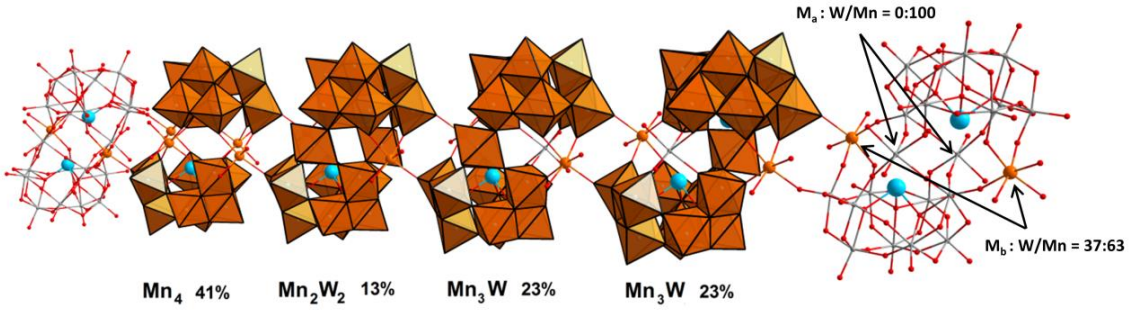

Figure 1.19. Polyhedral ball-and stick representation of a hypothetical local structure of the transition metal core. The probabilities of a specific transition metal core have been calculated assuming a stochastically independent distribution of Mn/W.

Stochastic independency means that the inclusion of the first element in the transition metal core {Mn, X, X, Mn} happens with a probability of 50 % for both elements, the same applies

to the second inclusion. Despite efforts made for further structure analysis by HR-ESI MS, proof of existence of the suggested polyanions and quantification of different species in the measured POM crystals could only partially be established (§2.4.1).

1.16.1.5 Example 2 - Disordered Keggin-type POM

The following example illustrates the importance of a careful consideration of charge balance and disorder for successful structure determination. The Keggin-type germanotungstate $K_4[GeW_{12}O_{40}]$ was prepared as reference compound for catalytic H_2 evolution tests (§4.3). The polyanion crystallizes with potassium countercations in the cubic space group $P\bar{4}3m$ and was assumed to be $K_4[GeW_{12}O_{40}]$ (according to the synthetic procedure).[236] Only a small fraction of the entire Keggin polyanion is found in the asymmetric unit $\{K_2GeWO_4{\cdot}H_2O\}$. Careful refinement of the cations in the crystal structure shows eight potassium counter-cations, which is twice the expected number. A reduction of the occupancy of the K^+ positions did not lead to physically meaningful Atomic Displacement Parameters (ADPs) and the K^+ content could not be reduced below 7 K^+ cations without their ADPs turning negative. The figures of merit for this structure (R1 = 5.24 %, wR2 = 0.1313) are in agreement with figures of merit observed for other polyoxometalate structures and do not indicate obvious errors in the structural model. Surprisingly, neither the elemental analysis nor the HR-ESI MS analysis data (which were both obtained from phase pure material) were in agreement with the structural model of $K_4[GeW_{12}O_{40}]$.

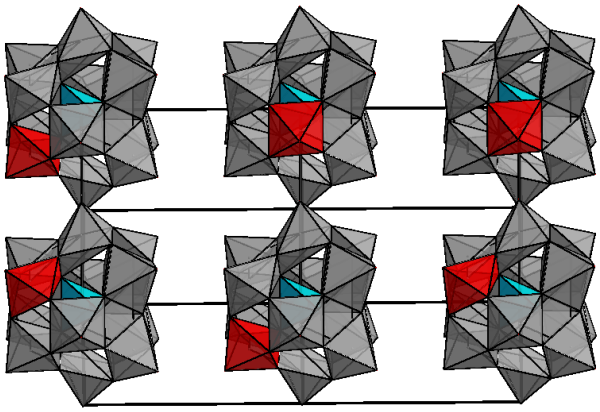

Figure 1.20. Polyhedral ball-and stick representation of the disorder in the crystal structure of $K_8[GeW_{11}O_{39}]$, red octahedra visualize missing $KO_5(H_2O)$ octahedra (counter-cations are omitted for clarity, two unit cells are shown).

Both methods indicated a lacunary structure with one missing WO_6 octahedron (Figure 1.20). As a consequence, the structural model had to be re-investigated. Data refinement with the structural model of the lacunary Keggin $K_8[GeW_{11}O_{39}]$ with a potassium tungsten disorder (K/W, 1:11) led to significantly enhanced figures of merit (R1 = 3.08 %, wR2 = 0.0652). $[GeW_{11}O_{39}]^{8-}$ polyanions can also be described as $[GeKW_{11}O_{39}]^{7-}$, which could be considered approximately as spherical. Thereby the incorporated K^+ cation may substitute any of the twelve WO_6 octahedra. The K^+ cation is most likely found in a $KO_5(H_2O)$ coordination environment (Figure 1.20).

For lacunary Keggin-type structures with the general formula $[GeW_{11}O_{39}]^{8-}$, four different structural isomers are possible, namely $[\alpha\text{-}GeW_{11}O_{39}]^{8-}$, $[\beta_1\text{-}GeW_{11}O_{39}]^{8-}$, $[\beta_2\text{-}GeW_{11}O_{39}]^{8-}$ or $[\beta_3\text{-}GeW_{11}O_{39}]^{8-}$. Crystal structure determinations showed that the POM is present in the solid state as the α-isomer.[234,181] For the α isomer, there is only one possibility to realize the missing octahedron. For this position an extra 16.7 e^- would be refined if a $[GeW_{12}O_{40}]^{12-}$ polyanion were wrongly assumed (electron density of (⅓ [W(VI)-K(I)] = 16.7 e^-).[234] In order to check our assumption, a ^{183}W NMR spectrum of this polyoxotungstate in D_2O was recorded. The spectrum shows 12 lines (Figure 1.21). For α, β_1 and β_3, which all have C_s symmetry, a 6 line ^{183}W-NMR spectrum is expected. Considering that the original compound is the α-isomer, the measured NMR spectrum could be explained as a mixture of the α and β_1-isomers in equilibrium. Each isomer shows 6 lines, which results in a total of 12 lines.

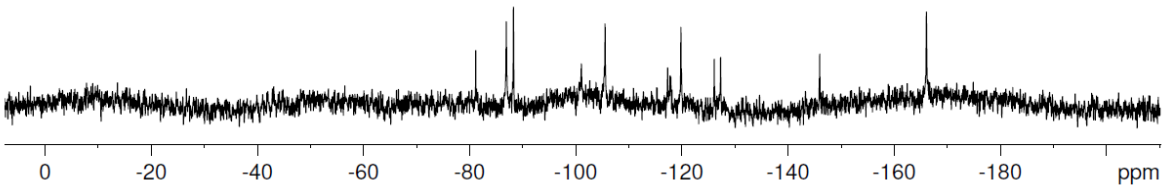

Figure 1.21. ^{183}W-NMR of $[\alpha\text{-}GeW_{11}O_{39}]^{8-}$ and $[\beta_1\text{-}GeW_{11}O_{39}]^{8-}$ (in D_2O, 500 MHz).

This example shows that even after careful X-ray structure refinement a complementary analytical method may still be requested.

1.16.1.6 Polymorphism/Solvates

Polymorphism is an important field with many practical consequences in the pharmaceutical industry.[237–240] Polyanions crystallize from solution with different countercations and a varying number of crystal water molecules. Slight variations in the composition of the crystallization medium can afford crystals with different unit cell parameters. These crystals

do not fulfill the IUCr definition of a polymorph, as their chemical composition usually differs either by the number and/or type of countercations or by containing a different number of crystal water molecules. However, the structure and chemical composition of the polyanion is maintained. The term polymorph refers to a crystal with unit cell parameters that are different from the ones in which the POM was originally published. In a polymorph, **the same polyanion** crystallizes with a different packing of the same countercations and crystal water molecules. This type of polymorph is also known as pseudo-polymorph.

Example: if the crystallization medium contains two different types of countercations, e.g. K^+ and Na^+, and a polyanion with 10^- charge, it could in principle crystallize with 10 different ratios of Na/K. This may result in 10 different crystal structures, herein referred to as polymorphs. The general connection between a particular ratio of countercations and the formation of stable crystals has not been investigated in detail so far. Selective preparation of only one polymorph may be impossible in some cases. The crystallization of different polymorphs from the reaction mixture usually does not represent a problem or requires purification, as long as there are no undesired 1st and 2nd row d or f-block metals amongst the countercations. Therefore, it is crucial to identify and determine the structures of all polymorphs and to assure that only alkali countercations are present in the structure (§1.16.1.7). Furthermore, the identification and characterization of polymorphs through their single crystal X-ray structure is an inevitable part of POM chemistry. Furthermore, it is essential to check for phase purity by powder x-ray diffraction (PXRD) (see §1.16.1.3). In the course of the preparative work of this thesis, polymorphs of different manganese, cobalt and gallium substituted POMs have been characterized by their single crystal X-ray structure. This phenomenon is illustrated for the well-studied POM WOC $[Co_4(H_2O)_2(B\text{-}\alpha\text{-}PW_9O_{34})_2]^{10-}$, which was found to form a particularly large number of different types of polyanions and polymorphs with Na^+ when following the reported preparative procedure. In this one-pot synthesis the polyanion is prepared from scratch. The mixture of Na_2HPO_4 and Na_2WO_4 in the presence of $Co(NO_3)_2$ in H_2O is refluxed and sodium chloride is added. Microscopic analysis of the crystalline reaction products revealed crystals with different morphologies and colors. Besides the Co containing polyanions $[((Co(H_2O)Co_2(PW_9O_{34})_2(PW_6O_{26})]^{17-}$ and $[Co_3(H_2O)Na(H_2O)_2(A\text{-}\alpha\text{-}PW_9O_{34})_2]^{12-}$ which should be considered as impurities, two polymorphs of the reported POM structure $Na_{10}[Co_4(H_2O)_2(A\text{-}\alpha\text{-}PW_9O_{34})_2]$ (ICSD 422958) have been observed to crystallize with Na^+ counter-cations in the triclinic space group $P\bar{1}$ (Figure 1.22). In both new crystal structures, the same polyanion $[Co_4(H_2O)_2(A\text{-}\alpha\text{-}$

$PW_9O_{34})_2]^{10-}$ is found with Na^+ counter-cations (with a different PXRD pattern for each crystal structure). Example 3 (§1.16.1.7) illustrates that POM synthesis does not generally result in the selective formation of only one polyanion structure: polyanions often crystallize as polymorphic structures. In this example, three polymorphic structures could already be observed in the presence of only sodium counter-cations. This number may be much higher in the presence of two or three different types of counter-cations.

1.16.1.7 Example 3 - Three Polymorphs of $[Co_4(H_2O)_2(A\text{-}\alpha\text{-}PW_9O_{34})_2]^{10-}$

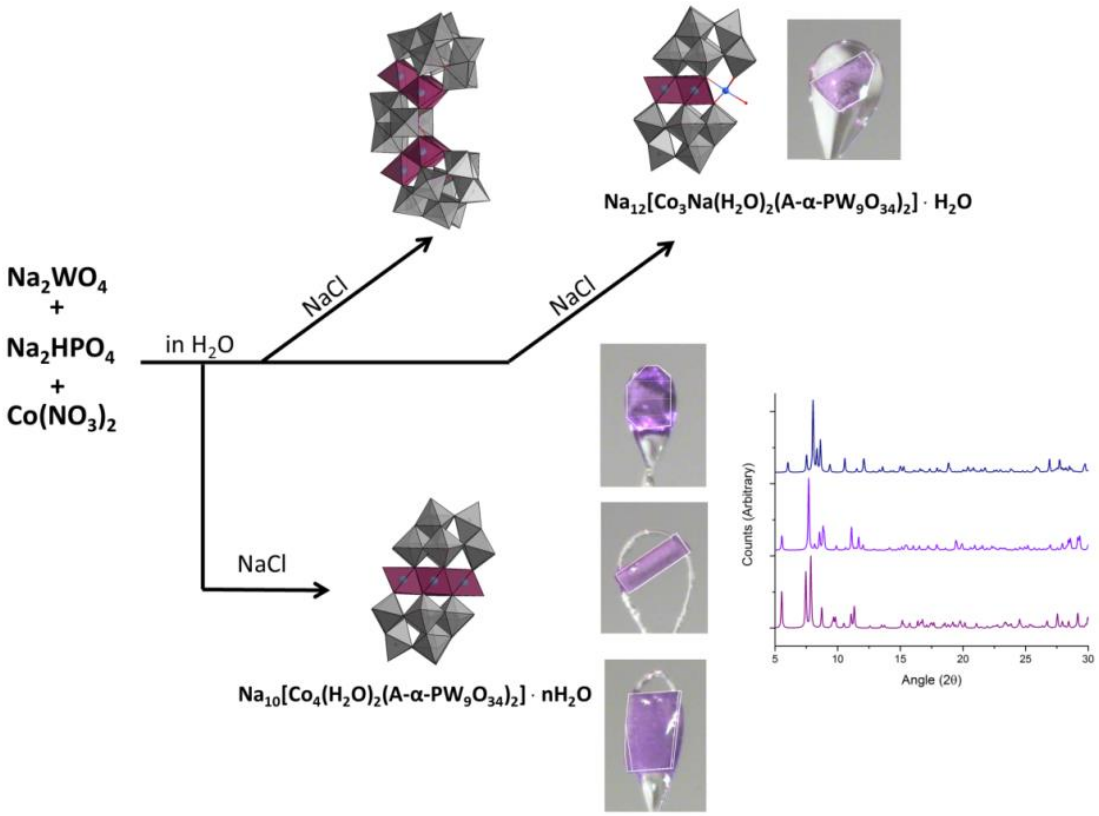

Figure 1.22. Analysis of the crystalline products in the reaction of sodium tungstate, sodium phosphate and Co(III) with Na^+ counter-cations. Different crystals from the reaction mixture were analyzed by single crystal X-ray diffraction (unpublished results).

Table 1.1. Unit cell parameters for different polymorphs of $Na_{10}[Co_4(H_2O)_2(A\text{-}\alpha\text{-}PW_9O_{34})_2]$.

	Triclinic, P-1 (421465-ICSD)	**Triclinic, P-1** (this work)	**Triclinic, P-1** (this work)
a	11.539(3)	11.5069(2)	12.9120(3)
b	12.807(4)	12.3195(2)	13.3435(4)
c	17.259(5)	16.0930(3)	15.5073(4)
α	98.019(4)	82.9290(15)	93.644(2)
β	106.639(4)	88.9316(14)	105.309(2)
γ	111.205(4)	75.6884(16)	115.859(3)

1.16.2 Powder X-ray Diffraction

Powder x-ray diffraction (PXRD) is one of the most powerful tools for the study of crystalline solids.[241] It is routinely used to confirm the identity and phase purity of crystalline material. PXRD was used to investigate the phase purity of new POMs in the present study. For some POMs, the measured powder pattern and the simulated pattern from the solved crystal structure match perfectly (Figure S5.4). However, a well-matching powder pattern may not be sufficient proof of a phase pure compound, as amorphous impurities may be present. This may be examined by visual and microscopic inspection of a compound in the first place. The Co-containing tungstobismuthate $Na_{10}[\{(Co(H_2O)_3)_2(Co(H_2O))_{1.87}(WO_2)_{0.13}\}(B\text{-}\beta\text{-}BiW_9O_{33})_2]\cdot 25H_2O$ serves as an instructive example (Figure S2.4). The PXRD pattern of the first batch was in good agreement with the calculated one, while EA showed the presence of an additional Co containing species. In subsequent batches, a pure compound could be obtained. PXRD diffraction patterns are usually measured at room temperature (~293 K) and datasets for single crystals collected at 183 K (in our lab). The unit cell of the crystal at 183 K is expected to be slightly smaller than that at room temperature. Significant peak shifts between the calculated and measured patterns, which may be due to the larger unit cells at room temperature, have never been observed in this work.

The loss of crystallinity cannot exclusively be explained by the evaporation of crystal water molecules. Crystals can diffract very well in the presence of a large amount of crystal water molecules. Furthermore, transformations of the crystalline structure can occur, as observed for the Mn containing POM $K_{10}[\{Mn_4(H_2O)_2\}(PW_9O_{34})_2]\cdot 20H_2O$,[242] for which the PXRD pattern significantly changes over the course of 6 h (Figure 1.23).

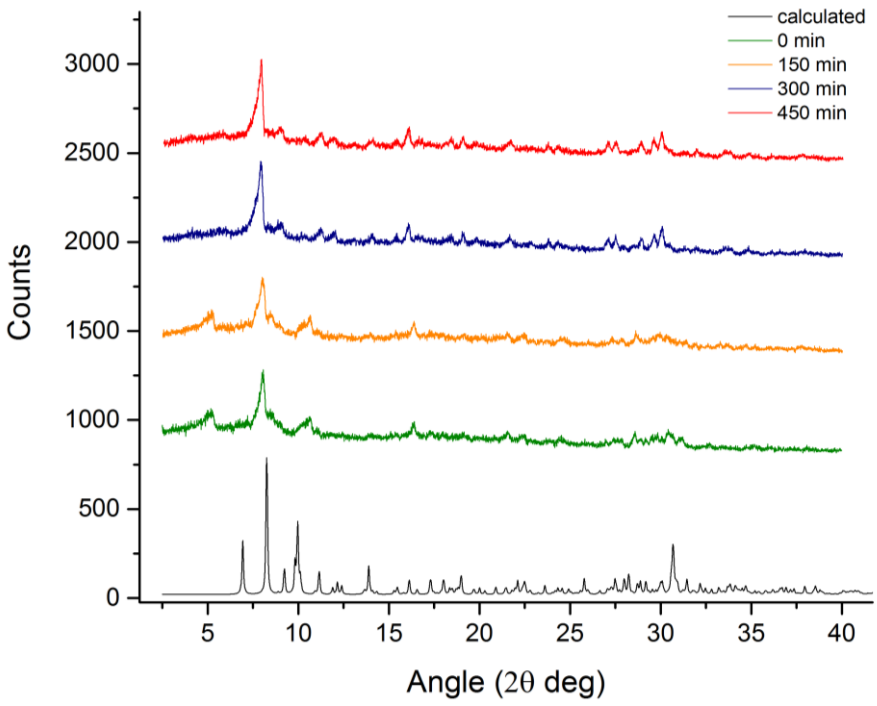

Figure 1.23. PXRD pattern recorded from a single crystal of $K_{10}[Mn_4(H_2O)_2(B\text{-}\alpha\text{-}PW_9O_{34})_2]\cdot 20H_2O$ at intervals of 150 min ($CuK_{\alpha 1}$ $\lambda = 1.54056$ Å).

In order to avoid the physical destruction of the crystals or the evaporation of crystal water molecules, XRD samples were kept in solution as long as possible and were only isolated from the reaction mixture for sample preparation. A few crystals were removed from the reaction mixture with a pipette and put on a glass slide or a mortar. The excess of mother liquor was removed with a paper towel and the product was placed between two pieces of adhesive tape (near-amorphous with low background). The sample preparation method used herein may still be optimized for further data treatment, e.g. Rietveld refinement, because anisotropic crystals may adopt a preferential orientation, which changes the intensity of certain Bragg reflections. However, phase purity was reliably detected, and the sample remained in a humid environment.

PXRD patterns were recorded on STOE STADI P diffractometers in transmission mode. The first machine was equipped with $CuK_{\alpha 1}$ X-ray source at $\lambda = 1.540562$ Å (Ge monochromator, operated at 40 kV and 40 mA). The second diffractometer was equipped with a $MoK_{\alpha 1}$ X-ray source ($\lambda = 0.71069$ Å) (Si monochromator, operated at 50 kV, 40 mA). A position sensitive detector (PSD) was used, which was later replaced by a state-of-the-art Mythen K detector. Flat sample holders were used for sample preparation. The use of Cu radiation seems to be favorable for POMs over Mo radiation due to the higher intensity and the better resolution of

the Bragg peaks. Mn or Co in the amounts present in the transition metal core did not result in a high background due to X-ray fluorescence.

To check the phase purity of a solid that is obtained by crystallization or by precipitation from the reaction mixture, it is crucial to know whether the desired crystals diffract under the applied conditions. We could **not** measure good matching PXRD patterns for all POM samples where good single crystal data sets were obtained. This may be related directly to the data collection temperature. For example, powder samples prepared from large single crystals, for which a perfectly matching pattern was expected, did not diffract (Figure 5.4). PXRD patterns of newly synthesized POMs frequently resemble the pattern of $K_{10}[Mn_4(H_2O)_2(PW_9O_{34})_2]$ 20 H_2O[243] shown in Figure 1.23 (sample prepared from single crystals).

All in all, it is crucial to report whether PXRD patterns can be recorded for POM crystals. If a sample does not diffract under certain conditions, this may still be an inherent POM property and does not necessarily indicate an impure or wrongly assigned compound.

1.17 Experimental

1.17.1 Chemicals and Reagents

Chemical starting materials for the preparation of POMs have been purchased either from Sigma Aldrich or from ABCR. $Na_2WO_4 \cdot 2H_2O$ (≥ 99 %), $Co(NO_3)_2 \cdot 6H_2O$ (≥ 98 %), $MnOAc \cdot 4H_2O$, $Mn(NO_3)_2 \cdot H_2O$, $Ni(NO_3)_2$, GeO_2, $Ru(bpy)_3Cl_2 \cdot 6H_2O$ (99.95 %), $Ga(NO_3)_3 \cdot 6H_2O$ (molecular weight 255.73 g/mol). All chemicals were used without further purification.

The lacunary precursors $[\alpha\text{-}SiW_9O_{34}]^{10-}$,[130] $[\beta\text{-}SiW_9O_{34}]^{10-}$,[130] $[\alpha/\beta\text{-}GeW_9O_{34}]^{10-}$,[131] $[B\text{-}\alpha\text{-}PW_9O_{33}]^{9-}$,[133] $[A\text{-}PW_9O_{34}]^{9-}$,[134,133] and $[SbW_9O_{33}]^{9-}$,[135] have been prepared and purified according to published literature procedures. $[BiW_9O_{33}]^{9-}$,[132] was obtained through a modified procedure (§2.5.5.2). The lacunary Wells-Dawson precursor $[\alpha\text{-}P_2W_{15}O_{56}]^{12-}$,[133,136] and $[\alpha\text{-}As_2W_{15}O_{56}]^{12-}$ [137] have been prepared according to the published synthesis procedure. The Wells-Dawson POM $[P_2W_{18}O_{66}]^{6-}$,[136] was used to prepare lacunary Well-Dawson phosphotungstate species.

1.17.2 Instrumentation

Thermogravimetric Analysis (TGA) was performed on a Netzsch STA 449 F3 Jupiter from 30 to 500 °C with a heating rate of 10 K/min under a Ar flow (20 mL/min).

Cyclic Voltammograms (CV) were recorded on a Metrohm 797 VA computrace, and solutions were purged prior to the measurement with N_2. A polished glassy carbon electrode was used as working electrode (Metrohm AG, 3 mm) and Ag/AgCl was used as a reference electrode (Metrohm AG).

Fourier Transform Infrared Spectroscopy (FT-IR) was performed on a Bruker Vertex 70 spectrometer equipped with an ATR accessory and a diamond crystal.

^{183}W-Nuclear Magnetic Resonance (NMR) spectra were recorded on a Bruker AV3-500 spectrometer, in D_2O/H_2O (1:1), at 20.8 MHz, relatively to Na_2WO_4 in water.

Ultraviolet/visible (UV/vis) spectra were recorded on a Lambda 650 S Perkin Elmer UV-visible spectrometer in the range 300-800 nm using a Quartz SUPRASIL precision cell (10 mm).

Raman spectra were recorded on a Renishaw Ramascope spectrometer equipped with a diode Laser (785 nm) for analysis of the POM PS complex and with an Ar^+-Ion laser (514 nm) for the analysis of pristine POMs.

High Resolution Electrospray Ionization Mass Spectra (HR-ESI MS) were recorded on a Bruker maXis HR-MS. Samples were dissolved in an appropriate solvent at a concentration of around 1 µmol/mL and measured at continuous flow at 3 µL/min. The mass spectrometer was operated in the negative electrospray ionization mode at 4,000 V capillary voltage, -500 V endplate offset, with a N_2 nebulizer pressure of 0.8 bar and dry gas flow of 4 L min^{-1} at 180 °C. MS acquisitions were performed in the mass range from m/z 50 to 2'000 at 20'000 resolution (full width at half maximum) and 1.0 Hz spectra rate. Masses were calibrated between m/z 158 and 1450 or 2721 prior to analysis below 2 ppm accuracy, with a 2 mM solution of sodium formate or with a Fluka electrospray calibration solution (Sigma-Aldrich, Buchs, Switzerland) that was 100-fold diluted with acetonitrile, respectively.

Magnetization measurements were conducted on a 7 T Quantum Design MPMS XL SQUID at a magnetic field of 1.0 T in the temperature range 2−200 K in both zero field and field cooling modes. The mass susceptibility was calculated according to $\chi = M/(H \cdot m)$ (M: magnetization, H: field strength, m: sample mass).

Hydrogen evolution (H_2) was measured with a hydrogen sensitive needle sensor (H2-N) from Unisense.

Oxygen evolution (O_2) was measured with a hydrogen sensitive needle sensor (OX-N) from Unisense.

Elemental Analyses (EA) of metals were carried out by Mikroanalytisches Labor Pascher, An der Pulvermühle 1, 53424 Remagen, Germany. CHN elemental analysis was done by the analytical service of the University of Zurich (Department of Zurich).

X-ray Absorption Near Edge Spectroscopy (XANES) and Extended X-ray Absorption Fine-structure Spectroscopy (EXAFS) were measured at the European Synchrotron Facility (ESRF) in Grenoble at the Swiss-Norwegian beamline (SNBL).

1.18 References

[1] J. G. Olivier, G. Janssens-Maenhout, M. Muntean, J. A. Peters, *Trends in global CO2 emissions. 2014 Report*, PBL Netherlands Environmental Assessment Agency, The Hague.

[2] International Energy Agency (IEA), *World Energy Outlook*, **2010**.

[3] International Energy Agency (IEA), *Energy and Climate Change. World Energy Outlook Special Report*, http://www.iea.org/bookshop/700-World_Energy_Outlook_2015.

[4] International Energy Agency (IEA), *Key World Energy Statistics 2015*.

[5] J.-C. Victor, *Die Energieversorgung der EU (1/2)*, Arte France, **2011**.

[6] J.-C. Victor, *Die Energieversorgung der EU (2/2)*, Arte France, **2011**.

[7] J.-C. Victor, *2037 – Eine CO2-neutrale Welt?*, Arte France, **2015**.

[8] P. Falkowski, R. J. Scholes, E. Boyle, J. Canadell, D. Canfield, J. Elser, N. Gruber, K. Hibbard, P. Högberg, S. Linder, F. T. Mackenzie, B. Moore, T. Pedersen, Y. Rosenthal, S. Seitzinger, V. Smetacek, W. Steffen, *Science* **2000**, *290*, 291–296.

[9] R. B. Alley, P. U. Clark, P. Huybrechts, I. Joughin, *Science* **2005**, *310*, 456–460.

[10] T. R. Karl, K. E. Trenberth, *Science* **2003**, *302*, 1719–1723.

[11] P. Nejat, F. Jomehzadeh, M. M. Taheri, M. Gohari, M. Z. A. Majid, *Renew. Sust. Energ. Rev.* **2015**, *43*, 843–862.

[12] N. S. Lewis, D. G. Nocera, *P. Natl. Acad. Sci. USA* **2006**, *103*, 15729–15735.

[13] G. A. Meehl, W. M. Washington, W. D. Collins, J. M. Arblaster, A. Hu, L. E. Buja, W. G. Strand, H. Teng, *Science* **2005**, *307*, 1769–1772.

[14] A. Grinsted, S. Jevrejeva, R. Rem, D. Dahl-Jensen, *Clim. Res.* **2015**, *64*, 15–23.

[15] G.-R. Walther, E. Post, P. Convey, A. Menzel, C. Parmesan, T. J. C. Beebee, J.-M. Fromentin, O. Hoegh-Guldberg, F. Bairlein, *Nature* **2002**, *416*, 389–395.

[16] S. Rahmstorf, *Science* **2007**, *315*, 368–370.

[17] R. J. Nicholls, A. Cazenave, *Science* **2010**, *328*, 1517–1520.

[18] L. R. Anspaugh, R. J. Catlin, M. Goldman, *Science* **1988**, *242*, 1513–1519.

[19] L. Devell, H. Tovedal, U. Bergstrom, A. Appelgren, J. Chyssler, L. Andersson, *Nature* **1986**, *321*, 192–193.

[20] Y. E. Dubrova, V. N. Nesterov, N. G. Krouchinsky, V. A. Ostapenko, R. Neumann, D. L. Neil, A. J. Jeffreys, *Nature* **1996**, *380*, 683–686.

[21] D. Williams, *Nat. Rev. Cancer* **2002**, *2*, 543–549.

[22] V. Drozdovitch, A. Bouville, N. Chobanova, V. Filistovic, T. Ilus, M. Kovacic, I. Malátová, M. Moser, T. Nedveckaite, H. Völkle, E. Cardis, *Rad. Prot. Dosim.* **2007**, *123*, 515–528.

[23] K. Buesseler, M. Aoyama, M. Fukasawa, *Environ. Sci. Technol.* **2011**, *45*, 9931–9935.

[24] A. Stohl, P. Seibert, G. Wotawa, D. Arnold, J. F. Burkhart, S. Eckhardt, C. Tapia, A. Vargas, T. J. Yasunari, *Atmos. Chem. Phys.* **2012**, *12*, 2313–2343.

[25] E. Cardis, D. Krewski, M. Boniol, V. Drozdovitch, S. C. Darby, E. S. Gilbert, S. Akiba, J. Benichou, J. Ferlay, S. Gandini, C. Hill, G. Howe, A. Kesminiene, M. Moser, M. Sanchez, H. Storm, L. Voisin, P. Boyle, *Int. J. Cancer* **2006**, *119*, 1224–1235.

[26] G. Neuenschwander, O. Sallin, K. D. von Allmen, *Le stockage des déchets hautement radioactifs en couches géologiques profondes*, **2010**.

[27] P. Slovic, J. H. Flynn, M. Layman, *Science* **1991**, *254*, 1603–1607.

[28] K.-J. Röhlig, H. Geckeis, K. Mengel, *Chem. Unserer Zeit* **2012**, *46*, 140–149.
[29] H. Geckeis, K.-J. Röhlig, K. Mengel, *Chem. Unserer Zeit* **2012**, *46*, 282–293.
[30] K. Mengel, K.-J. Röhlig, H. Geckeis, *Chem. Unserer Zeit* **2012**, *46*, 208–217.
[31] Aldo Spanjer, *Energ. Policy* **2007**, *35*, 2889–2898.
[32] Andreas Goldthau, *Energ. Policy* **2008**, *36*, 686–692.
[33] L. Brennan, P. Owende, *Renew. Sust. Energ. Rev.* **2010**, *14*, 557–577.
[34] J. Twidell, T. Weir, *Renewable energy resources*, Routledge, **2015**.
[35] H. Tüysüz, C. K. Chan (Eds.) *Topics in Current Chemistry*, Springer International Publishing, **2016**.
[36] P. Styring, K. Armstrong, *Front. Energy Res.* **2015**, *3*.
[37] F. Close, *Too Hot to Handle*, **2014**, Princeton University Press.
[38] A. Kleidon, L. Miller, F. Gans in *Topics in Current Chemistry* (Eds.: H. Tüysüz, C. K. Chan), Springer International Publishing, **2016**.
[39] T. Grewe, M. Meggouh, H. Tüysüz, *Chem.-Asian J.* **2016**, *11*, 22–42.
[40] H. Holttinen, *PhD thesis*, Aalto University (Aalto, Finnland), **2004**.
[41] M. Beaudin, H. Zareipour, A. Schellenberglabe, W. Rosehart, *Energy. Sustain. Dev.* **2010**, *14*, 302–314.
[42] S. Niaz, T. Manzoor, A. H. Pandith, *Renew. Sust. Energ. Rev.* **2015**, *50*, 457–469.
[43] G. W. Crabtree, M. S. Dresselhaus, M. V. Buchanan, *Physics Today* **2004**, 39–45.
[44] G. W. Crabtree, M. S. Dresselhaus, *MRS Bulletin* **2008**, *33*, 421–428.
[45] V. Krewald, M. Retegan, D. A. Pantazis (Eds.: H. Tüysüz, K. C. Chan), Springer International Publishing, Cham, **2016**.
[46] H. Dau, I. Zaharieva, *Accounts Chem. Res.* **2009**, *42*, 1861–1870.
[47] J. Barber, *Chem. Soc. Rev.* **2009**, *38*, 185–196.
[48] Y. Tachibana, L. Vayssieres, J. R. Durrant, *Nat. Photonics* **2012**, *6*, 511–518.
[49] C. A. Raines, *Photosynth. Res.* **2003**, *75*, 1–10.
[50] V. K. Yachandra, K. Sauer, M. P. Klein, *Chem. Rev.* **1996**, *96*, 2927–2950.
[51] J. Yano, V. K. Yachandra, *Chem. Rev.* **2014**, *114*, 4175–4205.
[52] A. Zouni, H.-T. Witt, J. Kern, P. Fromme, N. Krauss, W. Saenger, P. Orth, *Nature* **2001**, *409*, 739–743.
[53] Y. Umena, K. Kawakami, J.-R. Shen, N. Kamiya, *Nature* **2011**, *473*, 55–60.
[54] M. Suga, F. Akita, K. Hirata, G. Ueno, H. Murakami, Y. Nakajima, T. Shimizu, K. Yamashita, M. Yamamoto, H. Ago, J.-R. Shen, *Nature* **2015**, *517*, 99–103.
[55] V. Balzani, A. Credi, M. Venturi, *ChemSusChem* **2008**, *1*, 26–58.
[56] F. Evangelisti, R. Moré, F. Hodel, S. Luber, G. R. Patzke, *J. Am. Chem. Soc.* **2015**, *137*, 11076–11084.
[57] H. Dau, C. Limberg, T. Reier, M. Risch, S. Roggan, P. Strasser, *ChemCatChem* **2010**, *2*, 724–761.
[58] Q. Yin, J. M. Tan, C. Besson, Y. V. Geletii, D. G. Musaev, A. E. Kuznetsov, Z. Luo, K. I. Hardcastle, C. L. Hill, *Science* **2010**, *328*, 342–345.
[59] S. M. Barnett, K. I. Goldberg, J. M. Mayer, *Nat. Chem.* **2012**, *4*, 498–502.
[60] A. R. Parent, R. H. Crabtree, G. W. Brudvig, *Chem. Soc. Rev.* **2013**, *42*, 2247–2252.
[61] C. U. Singh, K. Venkatarao, *J. Inorg. Nucl. Chem.* **1976**, *38*, 541–543.

[62] R. L. Johnson, P. G. Tratnyek, R. O. Johnson, *Environ. Sci. Technol.* **2008**, *42*, 9350–9356.
[63] I. M. Kolthoff, I. K. Miller, *J. Am. Chem. Soc.* **1951**, *73*, 3055–3059.
[64] N. W. Barnett, B. J. Hindson, S. W. Lewis, S. D. Purcell, P. Jones, *Anal. Chem. Acta* **2000**, *421*, 1–6.
[65] G. P. McDermott, P. Jones, N. W. Barnett, D. N. Donaldson, Paul S. Francis, *Anal. Chem.* **2011**, *83*, 5453–5457.
[66] P. K. Ghosh, B. S. Brunschwig, M. Chou, C. Creutz, N. Sutin, *J. Am. Chem. Soc.* **1984**, *106*, 4772–4783.
[67] R. D. Gerardi, N. W. Barnett, P. Jones, *Anal. Chem. Acta* **1999**, *388*, 1–10.
[68] P. A. Lay, A. M. Sargeson, H. Taube, M. H. Chou, C. Creutz in *Inorganic Syntheses*, John Wiley & Sons, Inc, **2007**.
[69] Y. P. Perelygin, D. Y. Chistyakov, *Russ. J. Appl. Chem+.*, *79*, 2041–2042.
[70] C. Bachmann, M. Guttentag, B. Spingler, R. Alberto, *Inorg. Chem.* **2013**, *52*, 6055–6061.
[71] B. Probst, M. Guttentag, A. Rodenberg, P. Hamm, R. Alberto, *Inorg. Chem.* **2011**, *50*, 3404–3412.
[72] H. Lv, W. Guo, K. Wu, Z. Chen, J. Bacsa, D. G. Musaev, Y. V. Geletii, S. M. Lauinger, T. Lian, C. L. Hill, *J. Am. Chem. Soc.* **2014**, *136*, 14015–14018.
[73] S.R. Taylor, *Geochim. Cosmochim. Ac.* **1964**, *28*, 1273–1285.
[74] E. Lassner, W.-D. Schubert (Eds.) *Tungsten. Properties, Chemistry, Technology of the Element, Alloys, and Chemical Compounds*, Springer US, Boston, MA, **1999**.
[75] E. Lassner, W.-D. Schubert, E. Lüderitz, H. U. Wolf in *Ullmann's Encyclopedia of Industrial Chemistry*, Wiley-VCH Verlag GmbH & Co. KGaA, **2000**.
[76] J. M. Sumliner, J. W. Vickers, H. Lv, Y. V. Geletii, C. L. Hill in *Molecular Water Oxidation Catalysis*, John Wiley & Sons, Ltd, **2014**.
[77] R. Al-Oweini, A. Sartorel, B. S. Bassil, M. Natali, S. Berardi, F. Scandola, U. Kortz, M. Bonchio, *Angew. Chem. Int. Ed.* **2014**, *53*, 11182–11185.
[78] B. Schwarz, J. Forster, M. K. Goetz, D. Yücel, C. Berger, T. Jacob, C. Streb, *Angewandte Chemie International Edition* **2016**.
[79] Ocean Optics, *OOISensors Fiber Optic Sensors. System Installation and Operation Manual*. Document Number FOXY-AL300-000-02-0207.
[80] M. Sadakane, E. Steckhan, *Chem. Rev.* **1998**, *98*, 219–238.
[81] J. A. Widegren, R. G. Finke, *J. Mol. Catal. A-Chem.* **2003**, *198*, 317–341.
[82] V. Artero, M. Fontecave, *Chem. Soc. Rev.* **2013**, *42*, 2338–2356.
[83] R. H. Crabtree, *Chem. Rev.* **2012**, *112*, 1536–1554.
[84] T. J. Meyer, *Nat Chem* **2011**, *3*, 757–758.
[85] J. J. Stracke, R. G. Finke, *J. Am. Chem. Soc.* **2011**, *133*, 14872–14875.
[86] J. J. Stracke, R. G. Finke, *ACS Catal.* **2014**, *4*, 909–933.
[87] M. Anbar, I. Pecht, *Trans. Faraday Soc.* **1968**, *64*, 744–750.
[88] J. W. Vickers, H. Lv, Jordan M. Sumliner, G. Zhu, Z. Luo, D. G. Musaev, Y. V. Geletii, C. L. Hill, *J. Am. Chem. Soc.* **2013**, *135*, 14110–14118.
[89] J. J. Stracke, R. G. Finke, *ACS Catal.* **2014**, *4*, 79–89.

[90] P.-E. Car, M. Guttentag, K. K. Baldridge, R. Alberto, G. R. Patzke, *Green. Chem.* **2012**, *14*, 1680–1688.
[91] J. Song, Z. Luo, H. Zhu, Z. Huang, T. Lian, A. L. Kaledin, D. G. Musaev, S. Lense, K. I. Hardcastle, C. L. Hill, *Inorg. Chim. Acta.* **2010**, *363*, 4381–4386.
[92] J. Gao, S. Cao, Q. Tay, Y. Liu, L. Yu, K. Ye, P. C. S. Mun, Y. Li, G. Rakesh, S. C. J. Loo, Z. Chen, Y. Zhao, C. Xue, Q. Zhang, *Sci. Rep.* **2013**, *3*, 1853–1858.
[93] G. R. Meseck, R. Kontic, G. R. Patzke, S. Seeger, *Adv. Funct. Mater.* **2012**, *22*, 4433–4438.
[94] M. K. Seery, L. Guerin, R. J. Forster, E. Gicquel, V. Hultgren, A. M. Bond, A. G. Wedd, T. E. Keyes, *J. Phys. Chem. A* **2004**, *108*, 7399–7405.
[95] M. K. Seery, N. Fay, T. McCormac, E. Dempsey, R. J. Forster, T. E. Keyes, *Phys. Chem. Chem. Phys.* **2005**, *7*, 3426–3433.
[96] N. Fay, E. Dempsey, T. McCormac, *Electrochim. Acta.* **2005**, *51*, 281–288.
[97] M. T. Pope, A. Müller, *Angew. Chem. Int. Ed.* **1991**, *30*, 34–48.
[98] M. T. Pope in *Comprehensive Coordination Chemistry 5II6* (Ed.: J. A. Meyer), Pergamon, Oxford, **2003**.
[99] C. L. Hill in *Comprehensive Coordination Chemistry 5II6* (Eds.: J. A. Meyer, T. J. McCleverty), Pergamon, Oxford, **2003**.
[100] J.-F. Lemonnier, S. Duval, S. Floquet, E. Cadot, *Isr. J. Chem.* **2011**, *51*, 290–302.
[101] P. Hermosilla-Ibanez, P.-E. Car, A. Vega, J. Costamagna, F. Caruso, J.-Y. Pivan, E. Le Fur, E. Spodine, D. Venegas-Yazigi, *CrystEngComm* **2012**, *14*, 5604–5612.
[102] A. Müller, P. Gouzerh, *Chem. Soc. Rev.* **2012**, *41*, 7431–7463.
[103] Y. Wang, I. A. Weinstock, *Chem. Soc. Rev.* **2012**, *41*, 7479–7496.
[104] M. Hinz, C. Näther, W. Bensch, *Z. anorg. allg. Chem.* **2013**, *639*, 2482–2486.
[105] D.-L. Long, R. Tsunashima, L. Cronin, *Angew. Chem. Int. Ed.* **2010**, *49*, 1736–1758.
[106] M. Hutin, M. H. Rosnes, D.-L. Long, L. Cronin in *Comprehensive Inorganic Chemistry II (Second Edition)* (Ed.: J. R. K. Poeppelmeier), Elsevier, Amsterdam, **2013**.
[107] Y. P. Jeannin, *Chem. Rev.* **1998**, *98*, 51–76.
[108] P. Aroa, "Lacunary species from Keggin type heteropolyanions.", to be found under http://mappingignorance.org/2015/04/01/.
[109] P. Billik, B. Horváth, *Inorg. Chem. Commun.* **2008**, *11*, 1125–1127.
[110] H. Sartzi, H. N. Miras, L. Vilà-Nadal, D.-L. Long, L. Cronin, *Angew. Chem.-Ger. Edit.* **2015**, *127*, 15708–15712.
[111] L. Ni, F. Hussain, B. Spingler, S. Weyeneth, G. R. Patzke, *Inorg. Chem.* **2011**, *50*, 4944–4955.
[112] K. D. von Allmen, P.-E. Car, O. Blacque, T. Fox, R. Müller, G. R. Patzke, *Z. anorg. allg. Chem.* **2014**, *640*, 781–789.
[113] Y.-F. Song, D.-L. Long, S. E. Kelly, L. Cronin, *Inorg. Chem.* **2008**, *47*, 9137–9139.
[114] D. C. Duncan, C. L. Hill, *Inorg. Chem.* **1996**, *35*, 5828–5835.
[115] W. G. Klemperer in *Inorganic Syntheses*, John Wiley & Sons, Inc, **2007**.
[116] K. Bhattacharjee, K. K. Chattopadhyay, G. C. Das, *J. Phys. Chem. C.* **2015**, *119*, 1536–1547.
[117] C. Rocchiccioli-Deltcheff, M. Fournier, R. Franck, R. Thouvenot, *Inorg. Chem.* **1983**, *22*, 207–216.

[118] M.-P. Santoni, G. S. Hanan, B. Hasenknopf, *Coord. Chem. Rev.* **2014**, *281*, 64–85.
[119] S. Berardi, M. Carraro, A. Sartorel, G. Modugno, M. Bonchio, *Isr. J. Chem.* **2011**, *51*, 259–274.
[120] A. Proust, B. Matt, R. Villanneau, G. Guillemot, P. Gouzerh, G. Izzet, *Chem. Soc. Rev.* **2012**, *41*, 7605–7622.
[121] H. N. Miras, L. Vilà-Nadal, L. Cronin, *Chem. Soc. Rev.* **2014**, *43*, 5679–5699.
[122] M. Carraro, S. Gross, *Materials* **2014**, *7*, 3956.
[123] Y.-F. Song, R. Tsunashima, *Chem. Soc. Rev.* **2012**, *41*, 7384–7402.
[124] W. Qi, L. Wu, *Polymer International* **2009**, *58*, 1217–1225.
[125] T. Zhang, J. Brown, R. J. Oakley, C. F. Faul, *Curr. Opin. Colloid. In.* **2009**, *14*, 62–70.
[126] E. Lassner, W.-D. Schubert in *Tungsten. Properties, Chemistry, Technology of the Element, Alloys, and Chemical Compounds* (Eds.: E. Lassner, W.-D. Schubert), Springer US, Boston, MA, **1999**.
[127] J.J. Cruywagen, *Adv. Inorg. Chem.* **1999**, *49*, 127–182.
[128] C. Streb, *PhD Thesis*, Uniersity of Glasgow (Glasgow, Schottland), **2008**.
[129] W. G. Klemperer in *Inorganic Syntheses*, John Wiley & Sons, Inc, **2007**.
[130] A. Tézé, G. Hervé, R. G. Finke, D. K. Lyon (Eds.) *α-, β-, and γ-Dodecatungstosilicic Acids: Isomers and Related Lacunary Compounds*.
[131] G. Hervé, A. Tézé, *Inorg. Chem.* **1977**, *16*, 2115–2117.
[132] B. Botar, T. Yamase, E. Ishikawa, *Inorg. Chem. Commun.* **2000**, *3*, 579–584.
[133] W. J. Randall, M. W. Droege, N. Mizuno, K. Nomiya, T. J. R. Weakley, R. G. Finke, N. Isern, J. Salta, J. Zubieta, 167–185.
[134] P. J. Domaille, G. Hervé, A. Tézé in *Inorganic Syntheses*, John Wiley & Sons, Inc, **2007**.
[135] M. Bösing, I. Loose, H. Pohlmann, B. Krebs, *Chem. Eur. J.* **1997**, *3*, 1232–1237.
[136] R. Contant, W. G. Klemperer, O. Yaghi in *Inorganic Syntheses*, John Wiley & Sons, Inc, **2007**.
[137] R. Contant, R. Thouvenot, *Can. J. Chemistry* **1991**, *69*, 1498–1506.
[138] F. J. C. Rossotti, H. Rossoti, *Acta Chem. Scand.* **1956**, *10*, 957–984.
[139] N. Ingri, I. Andersson, L. Pettersson, A. Yagasaki, L. Andersson, K. Holmstrom, *Acta Chem. Scand.* **1996**, *50*, 717–734.
[140] L. Fan, J. Cao, C. Hu, *RSC Adv* **2015**, *5*, 83377–83382.
[141] H. Lv, J. Song, Z. Haiming, Y. V. Geletii, J. Bacsa, Z. Chongchao, T. Lian, D. G. Musaev, C. L. Hill, *J. Catal.* **2013**, *307*, 48–54.
[142] W. W. Laxson, S. Özkar, R. G. Finke, *Inorg. Chem.* **2014**, *53*, 2666–2676.
[143] D. E. Katsoulis, *Chem. Rev.* **1998**, *98*, 359–388.
[144] H. Stephan, M. Kubeil, F. Emmerling, C. E. Müller, *Eur. J. Inorg. Chem.* **2013**, *2013*, 1585–1594.
[145] J. T. Rhule, C. L. Hill, D. A. Judd, R. F. Schinazi, *Chem. Rev.* **1998**, *98*, 327–358.
[146] T. Yamase in *Progress in Molecular and Subcellular Biology* (Eds.: W. E. G. Müller, X. Wang, H. C. Schröder), Springer Berlin Heidelberg, **2013**.
[147] G. Geisberger, E. Besic Gyenge, C. Maake, G. R. Patzke, *Carbohyd. Polym.* **2013**, *91*, 58–67.

[148] G. Geisberger, E. B. Gyenge, D. Hinger, P. Bosiger, C. Maake, G. R. Patzke, *Dalton Trans* **2013**, *42*, 9914–9920.
[149] Georg Geisberger, Emina Besic Gyenge, Doris Hinger, Andres Käch, Caroline Maake, Greta R. Patzke, *Biomacromolecules* **2013**, *14*, 1010–1017.
[150] G. Geisberger, S. Paulus, E. B. Gyenge, C. Maake, G. R. Patzke, *Small* **2011**, *7*, 2808–2814.
[151] G. Geisberger, S. Paulus, M. Carraro, M. Bonchio, G. R. Patzke, *Chemistry – A European Journal* **2011**, *17*, 4619–4625.
[152] S.-S. Wang, Guo-Yu Yang, *Chem. Rev.* **2015**, *115*, 4893–4962.
[153] C. L. Hill, C. M. Prosser-McCartha, *Coord. Chem. Rev.* **1995**, *143*, 407–455.
[154] I. V. Kozhevnikov, *Chem. Rev.* **1998**, *98*, 171–198.
[155] N. Mizuno, M. Misono, *Chem. Rev.* **1998**, *98*, 199–218.
[156] W.-L. Chen, H.-Q. Tan, E.-B. Wang, *J. Coord. Chem.* **2012**, *65*, 1–18.
[157] B. Hasenknopf, K. Micoine, E. Lacôte, S. Thorimbert, M. Malacria, R. Thouvenot, *Eur. J. Inorg. Chem.* **2008**, *2008*, 5001–5013.
[158] H. Lv, Y. V. Geletii, C. Zhao, J. W. Vickers, G. Zhu, Z. Luo, J. Song, T. Lian, D. G. Musaev, C. L. Hill, *Chem. Soc. Rev.* **2012**, *41*, 7572–7589.
[159] K. D. von Allmen, R. Moré, R. Müller, J. Soriano-López, A. Linden, G. R. Patzke, *ChemPlusChem* **2015**, *80*, 1389–1398.
[160] S. Goberna-Ferrón, J. Soriano-López, J. R. Galán-Mascarós, *Inorganics* **2015**, *3*, 332.
[161] J. Soriano-López, S. Goberna-Ferrón, L. Vigara, J. J. Carbó, J. M. Poblet, J. R. Galán-Mascarós, *Inorg. Chem.* **2013**, *52*, 4753–4755.
[162] A. Bijelic, A. Rompel, *Coord. Chem. Rev.* **2015**, *299*, 22–38.
[163] M. Ammam, *J. Mater. Chem. A* **2013**, *1*, 6291–6312.
[164] B. Keita, U. Kortz, L. R. Brudna Holzle, S. Brown, L. Nadjo, *Langmuir* **2007**, *23*, 9531–9534.
[165] U. Kortz, A. Müller, J. van Slageren, J. Schnack, N. S. Dalal, M. Dressel, *Coord. Chem. Rev.* **2009**, *253*, 2315–2327.
[166] S.-T. Zheng, G.-Y. Yang, *Chem. Soc. Rev.* **2012**, *41*, 7623–7646.
[167] M. Vonci, C. Boskovic, *Aust. J. Chem.* **2014**, *67*, 1542–1552.
[168] H. Sun, N. Gao, J. Ren, X. Qu, *Chem. Mater.* **2015**, *27*, 7573–7576.
[169] J. M. Poblet, X. López, C. Bo, *Chem. Soc. Rev.* **2003**, *32*, 297–308.
[170] R. Thouvenot, M. Fournier, R. Franck, C. Rocchiccioli-Deltcheff, *Inorg. Chem.* **1984**, *23*, 598–605.
[171] C. Rocchiccioli-Deltcheff, R. Thouvenot, R. Franck, *Spectrochimica Acta Part A: Molecular Spectroscopy* **1976**, *32*, 587–597.
[172] Y.-G. Chen, Jian Gong, L.-Y. Qu, *Coord. Chem. Rev.* **2004**, *248*, 245–260.
[173] M. Pascual-Borras, X. López, J. M. Poblet, *Phys. Chem. Chem. Phys.* **2015**, *17*, 8723–8731.
[174] M. J. Potrzebowski, S. Kaźmierski, H. Kassassir, B. Miksa in *Annual Reports on 5NMR6 Spectroscopy* (Ed.: G. Webb), Academic Press, **2010**.
[175] N. N. Sveshnikov, M. T. Pope, *Inorg. Chem.* **2000**, *39*, 591–594.
[176] J. Heinze, *Angew. Chem. Int. Ed.* **1984**, *23*, 831–847.
[177] J. P. Launay, *J. Inorg. Nucl. Chem.* **1976**, *38*, 807–816.

[178] B. Keita, Y. W. Lu, L. Nadjo, R. Contant, *Eur. J. Inorg. Chem.* **2000**, 2463–2471.
[179] H. El Moll, W. Zhu, E. Oldfield, L. M. Rodriguez-Albelo, P. Mialane, J. Marrot, N. Vila, I.-M. Mbomekallé, E. Rivière, C. Duboc, A. Dolbecq, *Inorg. Chem.* **2012**, *51*, 7921–7931.
[180] B. Keita, I.-M. Mbomekallé, L. Nadjo, R. Contant, *Electrochem. Commun.* **2001**, *3*, 267–273.
[181] F. Song, Y. Ding, B. Ma, C. Wang, Q. Wang, X. Du, S. Fu, J. Song, *Energ. Environ. Sci.* **2013**, *6*, 1170–1184.
[182] S. Goberna-Ferrón, L. Vigara, J. Soriano-López, J. R. Galán-Mascarós, *Inorg. Chem.* **2012**, *51*, 11707–11715.
[183] B. Rausch, M. D. Symes, G. Chisholm, L. Cronin, *Science* **2014**, *345*, 1326–1330.
[184] S.-X. Guo, Y. Liu, C.-Y. Lee, A. M. Bond, J. Zhang, Y. V. Geletii, C. L. Hill, *Energ. Environ. Sci.* **2013**, *6*, 2654–2663.
[185] S.-X. Guo, C.-Y. Lee, J. Zhang, A. M. Bond, Y. V. Geletii, C. L. Hill, *Inorg. Chem.* **2014**, *53*, 7561–7570.
[186] V. M. Hultgren, A. M. Bond, A. G. Wedd, *J. Chem. Soc. Dalton* **2001**, 1076–1082.
[187] S. Ogo, S. Moroi, T. Ueda, K. Komaguchi, S. Hayakawa, Y. Ide, T. Sano, M. Sadakane, *Dalton Trans.* **2013**, *42*, 7190–7195.
[188] N. Fay, V. M. Hultgren, A. G. Wedd, T. E. Keyes, R. J. Forster, D. Leane, A. M. Bond, *Dalton Trans.* **2006**, 4218–4227.
[189] M. Goral, T. McCormac, E. Dempsey, D.-L. Long, L. Cronin, A. M. Bond, *Dalton Trans.* **2009**, 6727–6735.
[190] C. A. Ohlin, *Chemistry – An Asian Journal* **2012**, *7*, 262–270.
[191] H. N. Miras, E. F. Wilson, L. Cronin, *Chem. Commun.* **2009**, 1297–1311.
[192] H. N. Miras, L. Cronin in *New Strategies in Chemical Synthesis and Catalysis*, Wiley-VCH Verlag GmbH & Co. KGaA, **2012**.
[193] M. J. Deery, O. W. Howarth, K. R. Jennings, *J. Chem. Soc., Dalton Trans.* **1997**, 4783–4788.
[194] H. N. Miras, J. Yan, D.-L. Long, L. Cronin, *Chem. Soc. Rev.* **2012**, *41*, 7403–7430.
[195] D.-L. Long, C. Streb, Y.-F. Song, S. G. Mitchell, L. Cronin, *J. Am. Chem. Soc.* **2008**, *130*, 1830–1832.
[196] Alessandro Trovarelli, Richard G. Finke, *Inorganic Chemistry* **1993**, *32*, 6034–6039.
[197] Michelle T. Ma, Tom Waters, Karin Beyer, Rosemary Palamarczuk, Peter J. S. Richardt, Richard A. J. O'Hair, Anthony G. Wedd, *Inorganic Chemistry* **2009**, *48*, 598–606.
[198] Q. Zheng, L. Vilà-Nadal, C. Busche, J. S. Mathieson, D.-L. Long, L. Cronin, *Angew. Chem. Int. Ed.* **2015**, *54*, 7895–7899.
[199] P. J. Robbins, A. J. Surman, J. Thiel, D.-L. Long, L. Cronin, *Chem. Commun.* **2013**, *49*, 1909–1911.
[200] C. R. Mayer, C. Roch-Marchal, H. Lavanant, R. Thouvenot, N. Sellier, J.-C. Blais, F. Sécheresse, *Chem. Eur. J.* **2004**, *10*, 5517–5523.
[201] C. Lydon, C. Busche, H. N. Miras, A. Delf, D.-L. Long, L. Yellowlees, L. Cronin, *Angew. Chem.-Ger. Edit.* **2012**, *124*, 2157–2160.

[202] C. P. Pradeep, D.-L. Long, C. Streb, L. Cronin, *J. Am. Chem. Soc.* **2008**, *130*, 14946–14947.
[203] Ross S. Winter, Jamie M. Cameron, Leroy Cronin, *Journal of the American Chemical Society* **2014**, *136*, 12753–12761.
[204] J. Yan, D.-L. Long, E. F. Wilson, L. Cronin, *Angew. Chem.-Ger. Edit.* **2009**, *121*, 4440–4444.
[205] E. F. Wilson, H. N. Miras, M. H. Rosnes, L. Cronin, *Angew. Chem. Int. Ed.* **2011**, *50*, 3720–3724.
[206] L. Vilà-Nadal, E. F. Wilson, H. N. Miras, A. Rodríguez-Fortea, L. Cronin, J. M. Poblet, *Inorg. Chem.* **2011**, *50*, 7811–7819.
[207] I. Nakamura, H. N. Miras, A. Fujiwara, M. Fujibayashi, Y.-F. Song, L. Cronin, R. Tsunashima, *J. Am. Chem. Soc.* **2015**, *137*, 6524–6530.
[208] S. J. Veen, *Dissertation* (University of Utrecht).
[209] J. Cao, C. Xu, Y. Fan, L. Fan, X. Zhang, C. Hu, *Journal of The American Society for Mass Spectrometry* **2013**, *24*, 884–894.
[210] D. K. Walanda, R. C. Burns, G. A. Lawrance, E. I. von Nagy-Felsobuki, *J. Chem. Soc., Dalton Trans.* **1999**, 311–322.
[211] Daud K. Walanda, Robert C. Burns, Geoffrey A. Lawrance, Ellak I. von Nagy-Felsobuki, *Inorganic Chemistry Communications* **1999**, *2*, 487–489.
[212] T. McGlone, J. Thiel, C. Streb, D.-L. Long, L. Cronin, *Chem. Commun.* **2012**, *48*, 359–361.
[213] Frans Sahureka, Robert C. Burns, Ellak I. von Nagy-Felsobuki, *Inorganica Chimica Acta* **2003**, *351*, 69–78.
[214] Frisch, G. W. Trucks, H. B. Schlegel, G. E. Scuseria, M. A. Robb, J. R. Cheeseman, G. Scalmani, V. Barone, B. Mennucci, G. A. Petersson, H. Nakatsuji, M. Caricato, X. Li, H. P. Hratchian, A. F. Izmaylov, J. Bloino, G. Zheng, J. L. Sonnenberg, M. Hada, M. Ehara, K. Toyota, R. Fukuda, J. Hasegawa, M. Ishida, T. Nakajima, Y. Honda, O. Kitao, H. Nakai, T. Vreven, J. A. Montgomery Jr., J. E. Peralta, F. Ogliaro, M. Bearpark, J. J. Heyd, E. Brothers, K. N. Kudin, V. N. Staroverov, R. Kobayashi, J. Normand, K. Raghavachari, A. Rendell, J. C. Burant, S. S. Iyengar, J. Tomasi, M. Cossi, N. Rega, J. M. Millam, M. Klene, J. E. Knox, J. B. Cross, V. Bakken, C. Adamo, J. Jaramillo, R. Gomperts, R. E. Stratmann, O. Yazyev, A. J. Austin, R. Cammi, C. Pomelli, J. W. Ochterski, R. L. Martin, K. Morokuma, V. G. Zakrzewski, G. A. Voth, P. Salvador, J. J. Dannenberg, S. Dapprich, A. D. Daniels, O. Farkas, J. B. Foresman, J. V. Ortiz, J. Cioslowski, D. J. Fox, *Gaussian 09, Revision A.02*.
[215] Agilent Technologies, *CrysAlis PRO and CrysAlis RED. Agilent Technologies, Yarnton, Oxfordshire, England.*
[216] A. Altomare, G. Cascarano, G. Giacovazzo, A. Guagliardi, M. C. Burla, G. Polidori, M. Camalli, *J. Appl. Cryst.* **1994**, *27*, 435.
[217] G. M. Sheldrick, *Acta Crystallogr. A.* **2015**, *71*, 3–8.
[218] G. M. Sheldrick, *Acta Crystallogr. A.* **2008**, *64*, 112–122.
[219] A. L. Spek, *Acta Crystallogr. C.* **2015**, *71*, 9–18.
[220] L. J. Farrugia, *J. Appl. Cryst.* **2012**, *45*, 849–854.

[221] F. H. Allen, O. Johnson, G. P. Shields, B. R. Smith, M. Towler, *J. Appl. Cryst.* **2004**, *37*, 335–338.
[222] B. K. Nicholson, C. J. Clark, S. G. Telfer, T. Groutso, *Dalton Trans.* **2012**, *41*, 9964–9970.
[223] Andrew M. Ullman, Yi Liu, Michael Huynh, D. Kwabena Bediako, Hongsen Wang, Bryce L. Anderson, David C. Powers, John J. Breen, Héctor D. Abruña, Daniel G. Nocera, *J. Am. Chem. Soc.* **2014**, *136*, 17681–17688.
[224] A. L. Spek, *J. Appl. Cryst.* **2003**, *36*, 7–13.
[225] I. D. Brown, D. Altermatt, *Acta Crystallogr. B.* **1985**, *41*, 244–247.
[226] Delina Barats-Damatov, L. J. W. Shimon, Y. Feldman, Tatyana Bendikov, R. Neumann, *Inorg. Chem.* **2015**, *54*, 628–634.
[227] R. S. Winter, L. De-Liang, L. Cronin, *Inorg. Chem.* **2015**, *54*, 4151–4155.
[228] K.-Y. Wang, Z. Lin, B. S. Bassil, X. Xing, A. Haider, B. Keita, G. Zhang, C. Silvestru, U. Kortz, *Inorg. Chem.* **2015**, *54*, 10530–10532.
[229] IUCR, *A Guide to CIF for Authors*, **1995**.
[230] S. R. Hall, F. H. Allen, I. D. Brown, *Acta Crystallogr. A.* **1991**, *47*, 655–685.
[231] A. L. Spek, *Acta Crystallographica Section D* **2009**, *65*, 148–155.
[232] M. Neuburger, Universität Basel (Basel), **2012**.
[233] C. X. Weichenberger, P. V. Afonine, K. Kantardjieff, B. Rupp, *Acta Crystallogr. D.* **2015**, *71*, 1023–1038.
[234] Y. Mastai (Ed.) *Advanced Topics in Crystallization. Syntheses and X-Ray Crystal Structures of Magnesium- Substituted Polyoxometalates*, **2015**.
[235] F. Evangelisti, P.-E. Car, O. Blacque, G. R. Patzke, *Catal. Sci. Technol.* **2013**, *3*, 3117–3129.
[236] T. J. R. Weakley, S. A. Malik, *J. Inorg. Nucl. Chem.* **1967**, *29*, 2935–2944.
[237] *Polymorphism*, Wiley-VCH Verlag GmbH & Co. KGaA, **2006**.
[238] U. J. Griesser in *Polymorphism*, Wiley-VCH Verlag GmbH & Co. KGaA, **2006**.
[239] P. Ochsenbein, K. J. Schenk in *Polymorphism*, Wiley-VCH Verlag GmbH & Co. KGaA, **2006**.
[240] P. H. Stahl, B. Sutter in *Polymorphism*, Wiley-VCH Verlag GmbH & Co. KGaA, **2006**.
[241] A. Le Bail et al., *Powder Diffraction. Theory and Practice*, The Royal Society of Chemistry, **2008**.
[242] C. J. Gomez-Garcia, E. Coronado, P. Gomez-Romero, N. Casan-Pastor, *Inorg. Chem.* **1993**, *32*, 3378–3381.
[243] C. J. Gomez-Garcia, J. J. Borras-Almenar, E. Coronado, L. Ouahab, *Inorg. Chem.* **1994**, *33*, 4016–4022.

Chapter 2

Manganese Containing Polyoxometalates for Artificial Photosynthesis

2 Manganese Containing Polyoxometalates for Artificial Photosynthesis

Mn substituted POM catalysts have been the initial research focus of this thesis. Their synthesis and catalytic activity was studied in detail. As the transition metal core of polyanions can adopt a broad variety of different structures, most recently transition metal cores were isolated which are structurally very close to the oxygen evolving complex of PSII (§1.3.1). Numerous manganese containing polyanions have been reported to date. They differ by the structure of their tungsten ligands (A-*α*, A-*β*, B-*α*, B-*β*, *α*, β_1, β_2, β_3 or *γ*), or by their heteroatom, or they display different structural arrangements of the Mn(II) or Mn(III) cations in the transition metal core. Polyanions with a pure Mn transition metal core have been reported in the literature, as well as polyanions with mixed-metal transition metal cores. After an extensive literature search for reported Mn containing polyoxotungstates (Table 2.1-Table 2.8) attempts were made synthesize a series of isostructural compounds with a systematic variation of the heteroatom. In the first place, the goal was to optimize the structure of the tungsten ligand once the best performing heteroatom was determined. Small POMs of the Keggin-type $[Mn_y(H_2O)_y(XW_{12-y}O_{40-y})]^{n-}$ (y = 1-3, X = Si, P, Ge, P, As, n = depends on y and X) were synthesized and X was varied systematically. However, analysis of the synthesized products by PXRD and FT-IR often indicated the formation of impure products which rendered catalytic tests unreasonable (§1.11). The formation of the POM-PS complex was observed during photocatalytic tests for all Mn-POMs, and attempts were made to crystallize these compounds (§1.9.1). After several trials, crystals of a the arsenotungstate $[Mn_3(H_2O)_3(AsW_9O_{33})_2]^{12-}$ with $[Ru(bpy)_3]^{2+}$ cations were obtained (§2.6). Further research with Mn-POMs was focused on the synthesis and the catalytic properties of Krebs-type tungstobismuthates (§2.2). In previous studies a Mn-containing tungstobismuthate was not active, while its Co-containing structural analogue displayed activity. This was ascribed to the degree of W/M disorder in the transition metal core and investigated in further detail (§2.2.1).

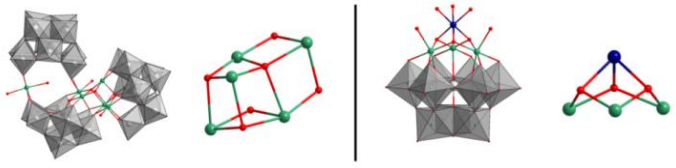

Figure 2.1. Polyhedral ball-and stick representation of polyoxotungstates with a cubane-like Mn_4O_4 core motif.[1–3] Color code: grey octahedra = WO_6, green = Mn, red = O.

2.1 Manganese Substituted POMs for Photocatalytic Water Oxidation

Table 2.1-Table 2.8 summarize Mn-containing POMs reported in the literature. They were considered as potential bio-inspired catalysts for water oxidation. POMs highlighted in green are structures which were isolated in phase pure form and tested as WOC. For POMs highlighted in red the proof of phase purity could not be established.

Table 2.1. Literature overview of reported Mn substituted Keggin-type monomers.

Keggin-type Structures (Monomers)	Ligand	Core	X	# Mn	Ref.
$[\{Mn(H_2O)\}_3(A\text{-}\alpha\text{-}SiW_9O_{37})]^{8-}$	A-α	$\{Mn_3(H_2O)_3\}$	Si	3	[4,5]
$[\{Mn^{II}_3(OH)_3(H_2O)_3\}(A\text{-}\alpha\text{-}SiW_9O_{34})]^{7-}$	A-α	$\{Mn^{II}_3(OH)_3(H_2O)_3\}$	Si	3	[1]
$[\{Mn^{III}_3(OH)_3(H_2O)_3\}(A\text{-}\alpha\text{-}SiW_9O_{34})]^{4-}$	A-α	$\{Mn^{III}_3(OH)_3(H_2O)_3\}$	Si	3	[1]
$[\{Mn^{III}_3Mn^{IV}O_3(CH_3COO)_3\}(A\text{-}\alpha\text{-}SiW_9O_{34})]^{6-}$	A-α	$\{Mn^{III}_3Mn^{IV}O_3(CH_3COO)_3\}$	Si	4	[1,2]
$[\{Mn^{III}_3(OH)_3(H_2O)_3\}(A\text{-}\beta\text{-}SiW_9O_{34})]^{4-}$	A-β	$\{Mn^{III}_3(OH)_3(H_2O)_3\}$	Si	3	[1]
$[\{Mn^{III}_3Mn^{IV}O_3(CH_3COO)_3\}(A\text{-}\beta\text{-}SiW_9O_{34})]^{6-}$	A-β	$\{Mn^{III}_3Mn^{IV}O_3(CH_3COO)_3\}$	Si	4	[1]
$[\{Mn^{II}(H_2O)\}(\alpha\text{-}AlW_{11}O_{39})]^{7-}$	α	$\{Mn^{II}\}$	Al	1	[6]
$[\{Mn^{III}(H_2O)\}(\alpha\text{-}AlW_{11}O_{39})]^{6-}$	α	$\{Mn^{III}\}$	Al	1	[6]
$[\{Mn^{IV}(H_2O)\}(\alpha\text{-}AlW_{11}O_{39})]^{5-}$	α	$\{Mn^{IV}(H_2O)\}$	Al	1	[6]
$[\{Mn_2\}GeW_{10}O_{38})_3Rb]^{17-}$	α	{(W/Mn)$_6$Rb}disordered	Ge	6	[7]
$[\{Mn(H_2O)\}_3(\alpha\text{-}SiW_9O_{37})]^{10-}$	α-Not specified	$\{Mn(H_2O)\}_3$	Si	3	[8]
$[\{Mn(H_2O)\}_3(\beta\text{-}SiW_9O_{37})]^{10-}$	β-Not specified	$\{Mn(H_2O)\}_3$	Si	3	[8]
$[(\{Mn_2(OH)_2(N_3)_{0.5}(H_2O)_{0.5}\}(\gamma\text{-}SiW_{10}O_{36}))_2(\mu\text{-}1,3\text{-}N_3)]^{10-}$	γ	2 x $\{Mn_2(OH)_2(N_3)_{0.5}(H_2O)_{0.5}\}$	Si	2 x 2	[9]
$[Mn^{III}(N_3)(\beta_3\text{-}PW_{11}O_{39})]^{5-}$	β_3	$\{Mn(N_3)\}$	P	1	[10]
$[Mn^{III}(H_2O)(\beta_3\text{-}PW_{11}O_{39})]^{4-}$	β_3	$\{Mn(H_2O)\}$	P	1	[10,11]

Keggin-type Structures (Monomers)	Ligand	Core	X	# Mn	Ref.
$[\{Mn(H_2O)\}(XW_{11}O_{39})]^{n-}$ (X = B, Zn, P, Si, Ge)	Not specified	$\{Mn(H_2O)\}$	P, Si Ge	1	[12–14,5,15]
$[(\{Mn(OH)\}(\beta_2\text{-}SiW_{11}O_{38}))_3]^{15-}$	β_2	$\{Mn_3\}$	Si	1	[16]
$[\{Mn_3(OH)_3(H_2O)_3\}(SiW_9O_{34})]^{4-}$	Not specified	$\{Mn_3(OH)_3(H_2O)_3\}$	Si	3	[8]
$[\{Mn(OH)\}(ZnW_{11}O_{39})]^{7-}$	Not specified	$\{Mn(OH)\}$	Zn	1	[17]
$[\{Mn(H_2O)\}(SiW_7Mo_4O_{39})]^{6-}$	Not specified	$\{Mn(H_2O)\}$	Si	1	[18]
$Ln_2[\{Mn(H_2O)\}(BW_9{}^{VI}W^{V}{}_2O_{39})]^{3-}$	Not specified	$\{Mn(H_2O)\}$	B	1	[19]
$Ln_2[\{Mn(H_2O)\}(BW_{11}O_{39})]^{-}$	Not specified	$\{Mn(H_2O)\}$	B	1	[19]
$[\{Mn^{III}{}_2(H_2O)\}_2(\gamma\text{-}SiW_{10}O_{40})]^{6-}$	γ	$\{Mn^{III}{}_2(H_2O)\}_2$	Si	2	[20]
$[\{Mn^{III}{}_{10}Mn^{II}{}_6O_6(OH)_6(PO_4)_4\}(A\text{-}\alpha\text{-}SiW_9O_{34})_4]^{28-}$	A-α	$\{Mn^{III}{}_{10}Mn^{II}{}_6O_6(OH)_6(PO_4)_4\}$	Si	16	[21]
$[\{Mn^{III}{}_4Mn^{II}{}_{12}(OH)_{12}(PO_4)_4\}(A\text{-}\alpha\text{-}SiW_9O_{34})_4]^{28-}$	A-α	$\{Mn^{III}{}_4Mn^{II}{}_{12}(OH)_{12}(PO_4)_4\}$	Si	16	[21]

Table 2.2. Literature overview of reported Mn substituted Wells-Dawson-type monomers.

Wells-Dawson-type Structures (Monomers)	Ligand	Core	X	# Mn	Ref.
$[Mn^{III}(\alpha_2\text{-}P_2W_{17}O_{61})]^{8-}$	α_2	$\{Mn\}$	P	1	[22,5]
$[\{Mn^{III}{}_3Mn^{IV}O_3(OAc)_3\}(\alpha\text{-}P_2W_{15}O_{56})]^{8-}$	α	$\{Mn^{III}{}_3Mn^{IV}O_3(OAc)_3\}$	P	4	[23]
$[\{[Mn(H_2O)](\mu\text{-}H_2O)_2K[Mn(H_2O)_4]\}(Si_2W_{18}O_{66})]^{11-}$		$\{[Mn(H_2O)](\mu\text{-}H_2O)_2K[Mn(H_2O)_4]\}$	Si	2	[24]

Table 2.3. Literature overview of reported Mn substituted Keggin-type sandwich structures.

Keggin-type Structures (Sandwich-type)	Ligand	Core	X	# Mn	Ref.
$[\{M_2Mn_4(OH)_2\}(A\text{-}\alpha\text{-}SiW_9O_{34})_2]^{n-}$ (M = Fe, Co, Ni, Cu, Ga, Mn)	A-α	$\{M_2Mn_4(OH)_2\}$	Si	4,6	[25]
$[\{Mn(H_2O)_2\}(\gamma\text{-}SiW_{10}O_{35})_2]^{10-}$	γ	$\{Mn(H_2O)\}$	Si	1	[26,27]
$[\{Mn_4(H_2O)_2\}(B\text{-}\alpha\text{-}PW_9O_{34})_2]^{10-}$	B-α	$\{Mn_4(H_2O)_2\}$	P	4	[28–30]
$[\{Mn^{II}{}_2ZnW\}(ZnW_9O_{34})_2]^{12-}$	Not specified	$\{Mn^{II}{}_2ZnW\}$	Zn	2	[31–34]
$[\{Mn^{III}{}_2ZnW\}(B\text{-}\alpha\ ZnW_9O_{34})_2]^{10-}$	B-α	$\{Mn^{III}{}_2ZnW\}$	Zn	2	[35]
$[\{Mn_4(H_2O)_2\}(B\text{-}\alpha\text{-}VW_9O_{34})_2]^{10-}$	B-α	$\{Mn_4(H_2O)_2\}$	V	4	[36]
$[\{W_2Mn_2(H_2O)_2\}(B\text{-}\alpha\text{-}ZnW_9O_{34})_2]^{8-}$	B-α	$\{Mn_2(H_2O)_2W_2\}$	Zn	2	[37]
$[\{Mn(H_2O)\}_2WO(H_2O)(B\text{-}\alpha\text{-}AsW_9O_{33})_2]^{10-}$	B-α	$\{Mn_2(H_2O)_2WO(H_2O)\}$	As	2	[38]
$[\{Mn^{III}{}_2ZnW\}(B\text{-}\alpha\text{-}ZnW_9O_{34})_2]^{10-}$	B-α	$\{Mn_2ZnW\}$	Zn	1	[39,40]
$[\{Mn_4(H_2O)_2\}(B\text{-}\alpha\text{-}AsW_9O_{34})_2]^{10-}$	B-α	$\{Mn_4(H_2O)_2\}$	As	4	[41]
$[\{Mn^{II}{}_4(H_2O)_2\}(B\text{-}\alpha\text{-}As^{V}W_9O_{34})_2]^{10-}$	B-α	$\{Mn_4(H_2O)_2\}$	As(V)	4	[42]
$[\{Mn^{III}{}_4(H_2O)_2\}(B\text{-}\alpha\text{-}GeW_9O_{34})_2]^{8-}$	B-α	$\{Mn^{III}{}_4(H_2O)_2\}$	Ge	4	[43]
$[\{Mn^{III}{}_4Mn^{II}{}_2O_4(H_2O)_4\}(B\text{-}\alpha\text{-}GeW_9O_{34})_2]^{8-}$	B-α	$\{Mn^{III}{}_4Mn^{II}{}_2O_4(H_2O)_4\}$	Ge	6	[44]
$[\{Mn^{III}{}_4Mn^{II}{}_2O_4(H_2O)_4\}(B\text{-}\alpha\text{-}SiW_9O_{34})_2]^{12-}$	B-α	$\{Mn^{III}{}_4Mn^{II}{}_2O_4(H_2O)_4\}$	Si	6	[44]

Table 2.4. Literature overview of reported Mn substituted Wells-Dawson-type sandwich-structures.

Wells-Dawson-type Structures (Sandwich type)	Ligand	Core	X	# Mn	Ref.
$[\{Mn_4(H_2O)_2\}(P_2W_{15}O_{56})_2]^{16-}$		$\{Mn_4\}$	P	4	[45–47]
$[\{Mn^{II}(OH)_2)_2Fe^{III}{}_2\}(\alpha\beta\beta\alpha\text{-}P_2W_{15}O_{56})_2]^{14-}$	αββα	$\{Mn^{II}(OH)_2)_2Fe^{III}{}_2\}$	P	2	[48]
$[\{Mn^{III}{}_6Mn^{IV}O_6(H_2O)_6\}(\alpha\text{-}P_2W_{15}O_{56})_2]^{14-}$		$\{Mn^{III}{}_6Mn^{IV}O_6(H_2O)_6\}$	P	7	[23]
$[\{(Mn^{II}OH_2)_2Mn^{II}{}_2\}(\alpha\beta\beta\alpha\text{-}As_2W_{15}O_{56})_2]^{16-}$	αββα	$\{(Mn^{II}OH_2)_2Mn^{II}{}_2\}$	As	4	[49]
$[\{Na_2(H_2O)_2Mn^{II}{}_2\}\ (As_2W_{15}O_{56})_2]^{18-}$		$\{Mn^{II}{}_2Na_2(H_2O)_2\}$	As	2	[50]
$[Na_2(H_2O)_2Mn^{III}{}_2(As_2W_{15}O_{56})_2]^{16-}$		$\{Mn^{III}{}_2Na_2(H_2O)_2\}$	As	2	[50]
$[Na(H_2O)_2Mn^{II}(H_2O)Mn^{II}{}_2(As_2W_{15}O_{56})_2]^{17-}$		$\{Mn^{II}{}_2(H_2O)Mn^{II}{}_2\}$	As	3	[50]

Table 2.5. Literature overview of reported Mn substituted POMs formed based on the lacunary precursor $[H_2P_2W_{12}O_{46}]^{12-}$.

Monomers (P_8W_{48})	Ligand	Core	X	# Mn	Ref.
$[Mn_8(H_2O)_{26}(P_8W_{48}O_{184})]^{24-}$		$\{Mn_8\}$	P	8	[51]
$[Mn_6(H_2O)_{22}(WO_2(H_2O)_2)_{1.5}(P_8W_{48}O_{184})]^{25-}$		$\{Mn_4W_4\}\{Mn_2\}$	P	6	[51]
$[Mn_4(H_2O)_{16}(WO_2(H_2O)_2)_2(P_8W_{48}O_{184})]^{28-}$ [b]		$\{Mn_4W_2\}$	P	4	[52]
$[Mn^{II}{}_8(H_2O)_{48}(P_8W_{48}O_{184})]^{24-}$		$\{Mn_8\}$	P	8	[53]
$[Mn^{II}{}_{14}(H_2O)_{30}(P_8W_{48}O_{184})]^{12-}$		$\{Mn_{14}\}$	P	14	[53]

Table 2.6. Literature overview of reported Mn substituted Krebs-type POMs.

Krebs (Sandwich-type)	Ligand	Core	X	# Mn	Ref.
$[\{Mn(H_2O)\}_3(B\text{-}\alpha\text{-}BiW_9O_{33})_2]^{12-}$	B-α	$\{Mn_3\}$	Bi	3	[54]
$[\{Mn^{II}(mim)\}_3(B\text{-}\alpha\text{-}BiW_9O_{33})_2]^{12-}$	B-α	$\{Mn_3(mim)_3\}$	Bi	3	[55]
$[\{Mn(H_2O)\}_3(B\text{-}\alpha\text{-}AsW_9O_{33})_2]^{12-}$	B-α	$\{Mn_3\}$	As	3	[56]
$[\{Mn(H_2O)(WO)_2\}(B\text{-}\alpha\text{-}AsW_9O_{33})_2]^{8-}$	B-α	$\{Mn(H_2O)W_2(H_2O)_2\}$	As	1	[57]
$[\{Mn^{II}(H_2O)Mn_2\}(B\text{-}\alpha\text{-}AsW_9O_{33})_2]^{12-}$	B-α	$\{Mn^{II}(H_2O)Mn_2\}$	As	3	[58]
$[\{(Mn^{III}(H_2O))_{2.25}(WO(H_2O))_{0.75}\}(B\text{-}\alpha\text{-}AsW_9O_{33})_2]^{8.25-}$	B-α	$\{(Mn_3(H_2O))_{2.25}(WO(H_2O))_{0.75}\}$[a]	As	2.25	[58]
$[\{Mn^{III}(H_2O)_3\}(B\text{-}\alpha\text{-}SbW_9O_{33})_2]^{9-}$	B-α	$\{Mn^{III}(H_2O)_3\}$	Sb	3	[58,47]
$[\{Mn^{II}(H_2O)\}_3(B\text{-}\alpha\text{-}SbW_9O_{33})_2]^{12-}$	B-α	$\{Mn_3\}$	Sb	3	[59]
$[\{Mn(Sn_2(OAc)_2\}(B\text{-}\alpha\text{-}GeW_9O_{34})_2]^{12-}$	B-α	$\{(MnSn(OAc))_2\}$	Ge	2	[60]
$[\{Mn^{II}(H_2O)_3\}_2(WO_2)_2(B\text{-}\beta\text{-}BiW_9O_{33})_2]^{10-}$	B-β	$\{Mn_2W_2\}$[c]	Bi	2-4	[59]
$[\{(Mn(H_2O)_3)_{1.3}(WO_2)_{0.7}(Mn(H_2O)_2)_{0.2}(WO_2)_{1.8}\}(B\text{-}\beta\text{-}BiW_9O_{32}(OH))_2]^{6-}$	B-β	$\{(Mn(H_2O)_3)_{1.3}(WO_2)_{0.7}(Mn(H_2O)_2)_{0.2}(WO_2)_{1.8}\}$	Bi	1.5	[61]
$[\{Mn(H_2O)_3\}_2\{Sn(OAc)\}_2(B\text{-}\beta\text{-}BiW_9O_{33})_2]^{10-}$	B-β	$\{Mn_2Sn_2\}$	Bi	2	[62]
$[\{Mn(H_2O)_3\}_2(W(OH)_2)_2(B\text{-}\beta\text{-}BiW_9O_{33})_2]^{8-}$	B-β	$\{Mn_2W_2\}$	Bi	2	[63]
$[\{Mn(CO)_3(WO_2)_2\}(B\text{-}\beta\text{-}XW_9O_{33})_2]^{12-}$ (X = Bi, Sb)	B-β	$\{Mn_2(CO)_3(WO_2)_2\}$	Bi, Sb	2	[64]
$[\{Mn_2(H_2O)_6(WO_2)_2\}(B\text{-}\beta\text{-}SbW_9O_{33})_2]^{10-}$	B-β	$\{Mn_2(H_2O)_6(WO_2)_2\}$	Sb	2	[65]
$[\{Mn^{II}(imc)(H_2O)\}_2(WO_2)_2(B\text{-}\beta\text{-}SbW_9O_{33})]^{12-}$	B-β	$\{Mn^{II}{}_2(imc)_4W_2\}$	Sb	2	[66]
$[\{Mn^{II}(H_2O)_3\}_2\{Mn^{II}(H_2O)_2\}_2(B\text{-}\beta\text{-}TeW_9O_{33})_2]^{8-}$	B-β	$\{Mn_4\}$	Te	4	[59]
$[\{Mn^{II}(imc)(H_2O)\}_2(WO_2)_2(B\text{-}\beta\text{-}TeW_9O_{33})_2]^{10-}$	B-β	$\{Mn^{II}{}_2(imc)_4W_2\}$	Te	2	[66]

Krebs (Sandwich-type)	Ligand	Core	X	# Mn	Ref.
$[\{(Ce(H_2O)_2)_2Mn_2\}(B\text{-}\beta\text{-}GeW_9O_{33})_2]^{8-}$	B-β	$\{(Ce(H_2O)_2)_2Mn_2\}$	Ge	2	[67]
[a] = Disordered TM core					

Table 2.7. Literature overview of reported Mn substituted POMs formed from different types of tungsten ligands.

Other Structures (Different Tungsten Fragments)	Ligand	Core	X	# Mn	Ref.
$\{[Mn(H_2O)_3]_2[Mn(H_2O)_2][(B\text{-}\beta\text{-}SiW_9O_{33}(OH))\text{-}Mn_3(H_2O)(B\text{-}\beta\text{-}SiW_8O_{30}(OH))]_2\}^{18-}$	B-β, B-β	$\{Mn_3\}\{Mn_3\}\{Mn_3\}$	Ge	9	[68]
$[Mn_{19}(OH)_{12}(SiW_{10}O_{37})_6]^{34-}$	Not specified	$\{Mn_{19}(OH)_{12}\}^{26+}$	Si	19	[69]
$[NaH_2Mn^{IV}(OH)W_{17}F_6O_{55}]^{8-}$	Not specified	{Mn(IV)}	NaF_6	1	[70]
$[NaH_2Mn^{III}(H_2O)W_{17}F_6O_{55}]^{8-}$	Not specified	{Mn(III)}	NaF_6	1	[70]
$[\{Mn(H_2O)Mn_2\}_2(\gamma\text{-}PW_6O_{26})(B\text{-}\alpha\text{-}PW_9O_{34})_2]^{17-}$	γ, B-α	2 x $\{Mn(H_2O)Mn_2\}$	P	6	[71]
$[Ni_4Mn_2P_3W_{24}O_{94}(H_2O)_2]^{17-}$ [(a)]	Not specified	$\{PW_6Mn_2Ni_4\}$	P	2	[72]
$[Mn^{III}{}_{13}Mn^{II}O_{12}(PO_4)_4(B\text{-}\alpha\text{-}PW_9O_{34})_4]^{31-}$	B-α	$\{Mn^{III}{}_{13}Mn^{II}\}$	P	14	[73]
$[(P_8W_{48}O_{184})\{(P_2W_{14}Mn_4O_{60})(P_2W_{15}Mn_3O_{58})_2\}_4]^{144-}$	Not specified	$\{Mn_4\}$ / $\{Mn_3\}$	P	40	[74]
$[\{(Mn^{II}(H_2O))_2Mn^{III}{}_4\}(\gamma\text{-}SiW_6O_{26})(B\text{-}\alpha\text{-}SiW_9O_{34})_2]^{16-}$	γ, B-α	$\{(Mn^{II}(H_2O))_2Mn^{III}{}_4\}$	Si	6	[43]
$[Mn^{II}{}_2\{Mn^{II}(H_2O)_5Mn^{III}{}_3(H_2O)(B\text{-}\beta\text{-}SiW_9O_{34})(B\text{-}\beta\text{-}SiW_6O_{26})\}_2]^{18-}$	B-β	$\{Mn_3(H_2O)_2]$ / $\{Mn_2\}$ / $\{Mn_4(H_2O)_5\}$	Si	3 /2 /5	[75]
$[MnW_6O_{24}]^{8-}$	Anderson-Type	{Mn}	---	1	[76]
$[\{(Mn(H_2O))Mn_2\}_2(\gamma\text{-}GeW_6O_{26})(B\text{-}\alpha\text{-}GeW_9O_{34})_2]^{18-}$	γ/B-α	$\{GeW_6Mn_6\}$	Ge	6	[77]
$[\{Mn^{II}(H_2O)\}_2Mn^{III}{}_4(\gamma\text{-}SiW_6O_{26})(B\text{-}\alpha\text{-}SiW_9O_{34})_2]^{16-}$	γ/B-α	$\{Mn^{II}Mn^{III}{}_2\}$	Si	5	[43]
$[\{Mn^{III}{}_2Mn^{II}{}_4(\mu_3\text{-}O)_2(H_2O)_4\}(B\text{-}\beta\text{-}SiW_8O_{31})(B\text{-}\beta\text{-}SiW_9O_{34})(\gamma\text{-}SiW_{10}O_{36})]^{18-}$	B-β; B-β; γ	$\{Mn^{III}{}_2Mn^{II}{}_4(\mu_3\text{-}O)_2(H_2O)_4\}$	Si	6	[3]

Table 2.8. Literature overview of reported Mn substituted POMs with a 1D-3D network structure.

Multidimensional structures 1D to 3D	Ligand	Core	X	# Mn	Ref.
2D-$[\{Mn(H_2O)_3\}_2\{Mn(H_2O)_4\}_2(H_2W_{12}O_{42})]^{5-}$	Paratungstate B	{Mn}	---	4	[78]
1D-$[\{Mn(imi)(H_2O)\}\{H_4W_{12}O_{42}\}]^{6-}$	Paratungstate B	{Mn(imi)}[a]	---	1	[79]
2D-$[Mn_2(H_2O)_6(H_2W_{9.52}Mo_{2.48}O_{42})]^{6-}$	Paratungstate B	2.0 x {Mn}	---	2	[80]
1D-$[Mn_4(H_2O)_{14}(H_2W_{12}O_{42})]^{2-}$	Paratungstate B	4.0 x {Mn}	---	4	[80]
3D-$[Mn_4(H_2O)_{14}(H_2W_{12}O_{42})]^{2-}$	Paratungstate B	4.0 x {Mn}	---	4	[80]
1D-$[\{Mn^{II}(H_2O)Mn^{III}(OH)\}(\alpha\text{-}SiW_{10}O_{37})]^{6-}$	α	$\{Mn_2\}$	Si	2	[81]
1D-$[(Mn(en)_2)]_4[\{Mn_4(H_2O)_2\}(B\text{-}\alpha\text{-}PW_9O_{34})_2]^{2-}$	B-α	$\{Mn_4(H_2O)_2\}$	P	4	[82]
1D-$\{Ce(H_2O)_7\}_2[Mn_4[(B\text{-}\alpha\text{-}SiW_9O_{34}(H_2O))_2]^{6-}$	B-α	$\{Mn_4\}$	Si	4	[83]
2D-$Mn_2(H_2O)_{12}Mn_2(H_2O)_{10}[\{Mn_4(H_2O)_2\}(B\text{-}\alpha\text{-}XW_9O_{34})_2]^{4-}$ (X = Ge, Si)	B-α	$\{Mn_4(H_2O)_2\}$	Ge, Si	8	[84]
2D-$Mn_4(H_2O)_{18}[\{Mn_4(H_2O)_2\}(B\text{-}\alpha\text{-}XW_9O_{34})_2]^{4-}$ (X = Ge, Si)	B-α	$\{Mn_4(H_2O)_2\}$	Ge, Si	8	[84]
3D-$Mn_2(H_2O)_6[\{Mn_4(H_2O)_2\}(B\text{-}\alpha\text{-}SiW_9O_{34})_2]^{8-}$	B-α	$\{Mn_4(H_2O)_2\}$	Si	6	[84]
2D-$[Mn_{1.5}(H_2O)_4(W_{5.65}Mo_{1.35}O_{24})]^{3-}$	Not specified	1.5 x {Mn}	---	1.5	[80]
1D-$[\{Mn(H_2O)\}(\mu\text{-}H_2O)_2K\{Mn(H_2O)_4\}(XW_9O_{33})_2]^{11-}$ (X = Ge, Si)	Not specified	$\{Mn(H_2O)\}(\mu\text{-}H_2O)_2K\{Mn(H_2O)_4\}$	Ge, Si	2	[85]
1D-$[\{Mn_{3.5}(H_2O)_7W_{0.5}(H_2O)\}(B\text{-}\beta\text{-}SbW_9O_{33})_2]^{8-}$	B-β	$\{Mn_{3.5}W_{0.5}\}$ Disordered	Sb	3.5	[86]
[a] imi = imidazole					

2.2 Mn and Co Substituted Krebs-Type Tungstobismuthates

The term Krebs-type structure generally refers to sandwich-type polyanions which are formed from lacunary tungsten ligands with a B-*β* structure. Structures of this type have first been reported by Bernt Krebs and have been obtained with the heteroatoms Sb(III), Bi(III), Se(IV), Te(IV), Ge(III) and As(III). Krebs-type structures are based on the tungsten fragment {B-*β*-XW_9O_{33}} which remains hypothetical and to the best of our knowledge has not been isolated in its own right to date. Krebs-type structures are only known for heteroatoms which are threefold coordinated by oxygen (Figure 2.2). This is most likely due to the electrostatic repulsion which would occur between the oxygen atoms of a tetrahedrally coordinated oxygen atoms pointing to the transition metal core and the terminal oxygen atoms of the rotated W_3O_{13} triad. In case of Sb, Bi, Te, As(III) and Ge which have a lone pair rather than an oxygen atom at the respective position, electrostatic repulsion would be avoided. The lone-pair is therefore an important structure-determining factor and the reason for the distinct structure of Krebs-type polyanions.

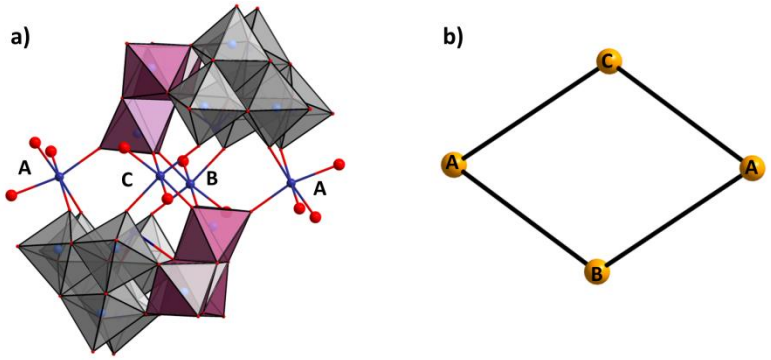

Figure 2.2. (a) Polyhedral ball-and stick representation of a Krebs-type polyanion $[\{(A(H_2O)_3)_2(B(H_xO)_2)C(H_xO)_2\}(B\text{-}\beta\text{-}BiW_9O_{33})_2]^{n-}$ (n = depends on A, B and C, x = depends on B and C). The rotated W_3O_{11} triad is displayed with purple octahedra. **(b)** Schematic representation of the transition metal core and with the three different positions (A, B and C).

Krebs-type POMs often crystallize with a W/M disordered transition metal core. W/M disorder can be observed at the inner and outer positions of the transition metal core (see §2.2.1). Tungstobismuthates in which W/M disorder is restricted to the inner positions of the transition metal core were in the focus of this thesis. The extent of disorder can be influenced and adjusted by the reaction conditions which were studied for Mn(II), Co(II) (§2.3), and Cu(II) (§3.2.1). Manganese containing Krebs-type polyanions have been reported earlier for Sb, Bi, Te, and Ge heteroatoms (see Table 2.6 and Table 2.8). A special property of Krebs-

type polyanions is their ability to undergo cross-linking into 1D inorganic chains, as reported for the Mn containing antimonate 1D-$[\{Mn_{3.5}(H_2O)_7W_{0.5}(H_2O)\}(B\text{-}\beta\text{-}SbW_9O_{33})_2]^{8-}$ or the Fe containing compound 1D-$[Fe(III)_4(H_2O)_8(SbW_9O_{33})_2]^{6-}$. These polyanions are isostructural to the herein reported Mn containing 1D structures **Mn-1** and **Mn-4**. Previous studies by our group have shown that the cobalt-containing polyanion $[\{Co(H_2O)_3\}_2\{CoBi_2W_{19}O_{66}(OH)_4\}]^{10-}$ is performing well as a WOC, while the isostructural cobalt and manganese containing tungstobismuthates $[\{Co_{2.5}(H_2O)_6\}_2\{Bi_2W_{19.5}(OH)_4\}]^{8-}$ were not active. This difference in activity was assigned to differences of the W/Co disorder in the transition metal core which appears to exert a tremendous impact on the catalytic activity.

2.2.1 W/M Disordered Transition Metal Cores of Krebs-Type Tungstobismuthates

The transition metal core of Krebs-type POMs has four distinct positions (see §1.16.1.4). In the context of this thesis, only structures are reported in which W/M disorder is restricted to the positions B and C of the transition metal core (Figure 2.3). The most general polyanion formula to describe the isolated tungstobismuthates is $[\{(A(H_2O)_3)_2(B(H_yO)_2)_x(C(H_yO)_2)_x\}(B\text{-}\beta\text{-}BiW_9O_{33})_2]^{n-}\cdot nH_2O$ (A = M; B and C = W or M, y = 0 for W, 2 for M, x is obtained from crystal structure refinement, n depends on A and B), and it was used to make the structure of the core more evident. The structure of the transition metal core is described in {} brackets. (Note that the same brackets are also used to denote a hypothetical polyanion.)

In the reaction of $[B\text{-}\alpha\text{-}BiW_9O_{33}]^{9-}$ with Cu(II) cations, Krebs-type polyanions were obtained in which the inner positions (B and C) are exclusively occupied by W and the outer positions (A, A) with Cu (§1.16.1.3). While the reaction of the lacunary precursor with Cu(II) led to the formation of polyanions of the B-α and B-β-type, the reaction with of Mn(II) and Co(II) cations exclusively led to the formation of polyanions with B-β structure. In the structures with an Mn(II) or Co(II) transition metal core, the inner positions may be W/M (M = Mn, Co) disordered.

Table 2.9. Composition of the transition metal core of transition metal substituted tungstobismuthates based on the hypothetical {B-β-BiW_9O_{33}} fragment.

Structure	Inner Position (W/M)	Outer Position (W/M)	
Mn-1	36:64	0:100	§2.3.1.2
Mn-2	14:86	0:100	§2.3.1.1
Mn-3	100:0	0:100	§2.3.1.3
Mn-4	2 distinct positions [a]	0:100	§2.3.1.2
Mn-5	0:100	0:100	§2.3.1.1
BiW_9-2	100:0	100:0	§2.2.3.2
Co-1	6:94	0:100	§2.3.2
Co-2	0:100	0:100	§2.3.2
Cu-1	100:0	0:100	§3.2.1
Cu-2	100:0	0:100	§3.2.1
Cu-3	100:0	0:100	§3.2.1

[a] The inner positions of Mn-3 are occupied with 1 Mn and 1 W atom which are not disordered.

2.2.2 Influence of Crystallographic Disorder on the Transition Metal Core

The Mn containing polyanion $[Mn_{1.5}(H_2O)_6\{Bi_2W_{20.5}O_{68}(OH)_2\}]^{6-}$ was obtained from the lacunary precursor $[B\text{-}\alpha\text{-}BiW_9O_{33}]^{9-}$, and phase pure products emerge from heating of the reaction mixture or in acidic conditions. Crystals of this compound show disorder at the inner position and outer position of the transition metal core. The resulting crystals may contain polyanions with up to nine different transition metal cores. The W/Mn ratio at the inner position was refined to be 90:10 and at the outer position to 35:65, respectively. Assuming a stochastically independent distribution (§1.16.1.3), the probability to obtain polyanions with a specific core composition was calculated (Figure 2.15). The probability for polyanions with a pure Mn_4 transition metal core is only 0.12 %. This low value may account for the absence of WOC activity.

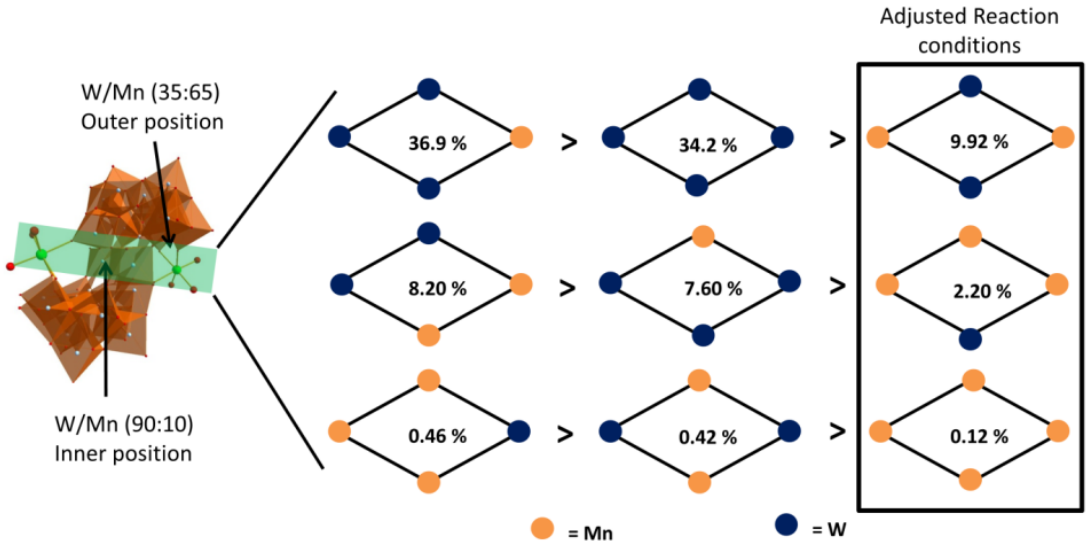

Figure 2.3. Possible permutations of the transition metal core of the Mn substituted tungstobismuthate $Na_6[Mn_{1.5}(H_2O)_6\{Bi_2W_{20.5}O_{68}(OH)_2\}]\cdot 36H_2O$. The probabilities for the different polyanions were calculated assuming a stochastically independent distribution of Mn and W.

2.2.3 Synthesis and Solution Stability of the Lacunary Precursor [B-α-BiW_9O_{33}]$^{9-}$

The reason for the broad distribution of transition metal substituted polyanion species which form crystals with a W/M disordered transition metal core may be related to the low stability of the lacunary precursor [B-α-BiW_9O_{33}]$^{9-}$ in solution. The phase pure preparation of this precursor from literature procedures always turned out to be challenging and was only possible after modification of the reported procedure (§2.5.5.2). The sodium salt Na_9[B-α-BiW_9O_{33}]$\cdot 19.5H_2O$ was finally obtained in phase pure form. According to the PXRD pattern, the material is free of sodium tungstate residues, and the low background indicates that no amorphous impurities contaminate the product (Figure 2.4). Despite the modified procedure the preparation of this compound remained to be very sensitive to small variations of the reaction conditions and alternatively results in the formation of paratungstate B or $Na_{14}[\{(WO_3)_2(WO_2)_2\}(BiW_9O_{33})_2]\cdot 47H_2O$ (**BiW_9-2**). In the end, it was not possible to determine the key synthetic parameters for a reproducible phase pure synthesis. Similar difficulties have been reported for the lacunary Wells-Dawson phosphotungstate precursor $Na_{12}[\alpha$-$P_2W_{15}O_{56}]$. The authors claim that the precursor is metastable and precipitation at a well-defined pH only results in ~90 % pure starting material. A similar situation may be encountered in the synthesis of [B-α-BiW_9O_{33}]$^{9-}$. Judging from the number crystal structures

reported in the ICSD with a W/M disordered transition metal core for the isostructural lacunary tungstoantimonates $[B\text{-}\alpha\text{-}SbW_9O_{33}]^{9-}$ or for $[B\text{-}\alpha\text{-}TeW_9O_{33}]^{9-}$ moieties, these precursor are less prone to decomposition. The synthesized precursor material was analyzed by PXRD and by IR spectroscopy.

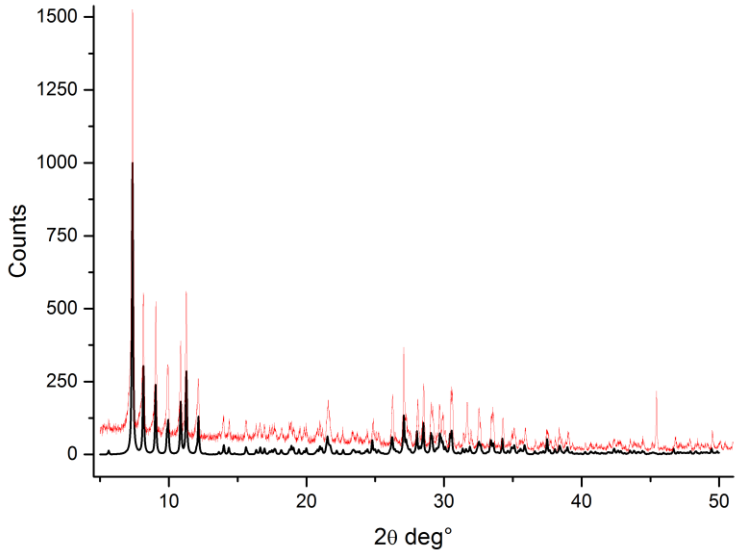

Figure 2.4. PXRD pattern of the lacunary precursor **$[B\text{-}\alpha\text{-}BiW_9O_{33}]^{9-}$** (red) vs. calculated (black).

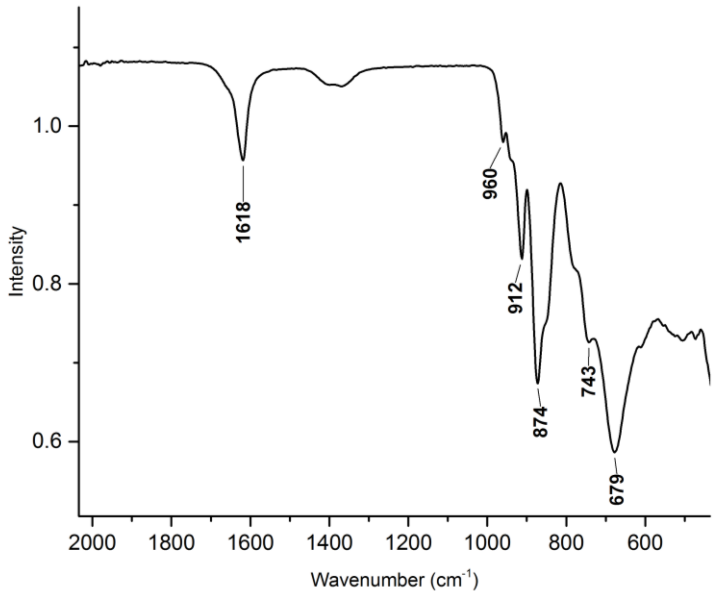

Figure 2.5. FT-IR spectrum of the lacunary precursor $Na_9[B\text{-}\alpha\text{-}BiW_9O_{33}]\cdot 19.5\ H_2O$.

Crystals of different polyanions have been obtained from the reaction mixture during the preparation of the lacunary precursor. Aiming for higher yield of the lacunary precursor [B-α-

$BiW_9O_{33}]^{9-}$, the pH was screened in the range between 6–8. Analysis of the unit cell parameters confirmed the presence of different polymorphs of $Na_{10}[H_2W_{12}O_{42}]$ and of $Na_{14}[\{(WO_3)_2(WO_2)_2\}(BiW_9O_{33})_2]\cdot 47H_2O$ (**BiW_9-2**). These polyanions have been obtained regularly in larger amounts. Crystals of the target compound occurred rather rarely, because $[B\text{-}\alpha\text{-}BiW_9O_{33}]^{9-}$ may remain dissolved in solution. A similar observation was made earlier by Fan et al during the preparation of the target compound paratungstate B ($[H_2W_{12}O_{42}]^{10-}$). They have observed that paratungstate A ($[W_7O_{24}]^{6-}$) which crystallizes first from the reaction mixture is not the main polyanion species. The target compound paratungtate B as main species may remain dissolved. Only one single crystal of $Na_{14}[WO_2(BiW_8O_{29.5})_2]\cdot 35.5H_2O$ **(BiW_9-1)** occurred as a rather unusual tungstobismuthate and most likely an intermediate (Figure 2.6). To understand the impact of the different reaction parameters on the distribution of polyanions in the reaction mixture the synthesis was monitored with HR-ESI MS.

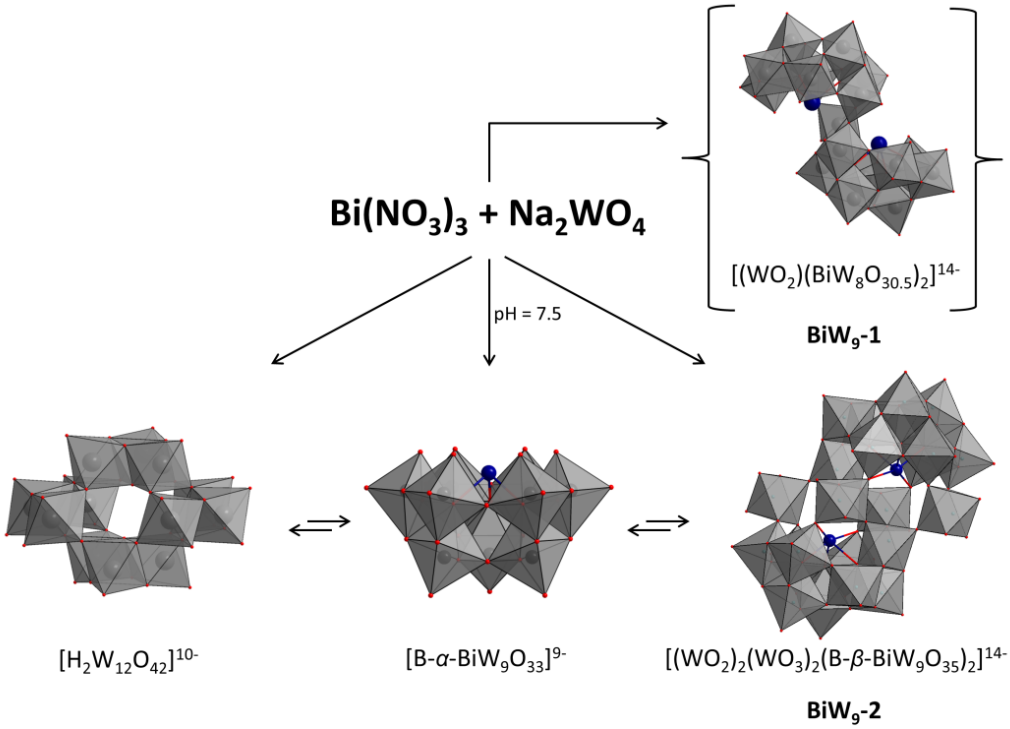

Figure 2.6. Polyhedral ball-and stick representation of polyanion species which were characterized as single crystals and obtained during the preparation of the lacunary precursor $Na_9[BiW_9O_{33}]\cdot 19.5\ H_2O$.

2.2.3.1 Structure of $Na_{14}[WO_2(BiW_8O_{29.5})_2]\cdot 35.5H_2O$ (BiW_9-1)

When using sodium tungstate from different supplies (ABCR (99 %) instead of Sigma Aldrich (≥ 99 %)) under the same reaction conditions, the formation of minor amounts of a new compound was observed. $Na_{14}[\{WO_2\}(BiW_8O_{29.5})_2]\cdot 35.5H_2O$ (**BiW_9-1**) crystallizes in the triclinic space group $P\bar{1}$.

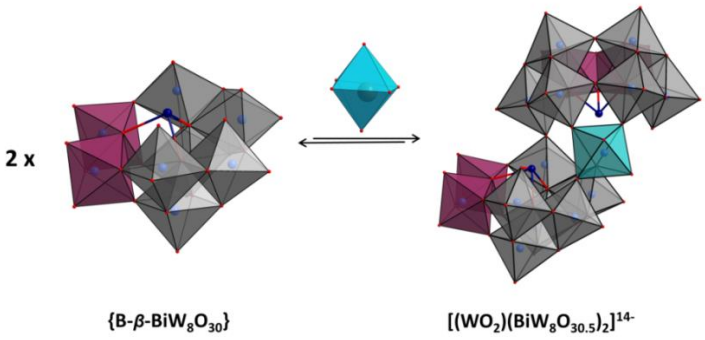

Figure 2.7. Schematic formation process of $[\{WO_2\}(BiW_8O_{30.5})_2]^{14-}$ from two hypothetical $\{B\text{-}\beta\text{-}BiW_8O_{30}\}$ and an additional WO_6 octahedron.

The structure of this polyanion is particularly interesting as it may represent an intermediate in the decomposition and isomerization process which the $[B\text{-}\alpha\text{-}BiW_9O_{33}]^{9-}$ precursor undergoes upon dissolution. Only one single crystal of this compound was observed amongst crystals of paratungstate B as the main product. This new polyanion is constituted of two condensed $\{B\text{-}\beta\text{-}BiW_8O_{30}\}$ lacunary ligands which coordinate to an additional W atom in the transition metal core. The lacunary ligand displays B-β geometry and is lacking one WO_6 octahedron from the rotated $\{W_3O_{11}\}$ triad (Figure 2.7, left). Terminal oxygen atoms coordinate to sodium counter-cations.

2.2.3.2 Structure of $Na_{14}[\{(WO_3)_2(WO_2)_2\}(BiW_9O_{33})_2]\cdot 47\ H_2O$ (BiW_9-2)

$Na_{14}[\{(WO_3)_2(WO_2)_2\}(BiW_9O_{33})_2]\cdot 47H_2O$ (**BiW_9-2**) crystallizes in the triclinic space group $P\bar{1}$. It has a pure $\{(WO_3)_2(WO_2)_2\}$ transition metal core and therefore represents a HPA. A similar polyanion with a disordered transition metal core $[H_{(2-x)}Bi_2W_{20}O_{70}(HWO_3)_x]^{12-}$ was reported earlier and is formed under similar reaction conditions. The disorder in this earlier reported crystal structure indicates that the polyanions $[\{(WO_2)_2\}(B\text{-}\beta\text{-}BiW_9O_{33})_2]^{14-}$, $[\{(WO_2)Na(H_2O)_2\}(B\text{-}\beta\text{-}BiW_9O_{33})_2]^{15-}$ and $[\{(WO_3)_2(WO_2)_2\}(B\text{-}\beta\text{-}BiW_9O_{33})_2]^{14-}$ most likely co-exist in solution. The absence of disorder in the crystal structure of **BiW_9-2** may be

considered as an indication that the respective crystals were formed from a pure solution of $[\{(WO_3)_2(WO_2)_2\}(B\text{-}\beta\text{-}BiW_9O_{33})_2]^{14-}$. If polyanions with missing WO_6 octahedra would have been found in solution under the same reaction conditions most likely crystals with a W/Na disordered transition metal core would have been obtained. The polyanion $[\{(WO_2)_2\}(B\text{-}\beta\text{-}BiW_9O_{33})_2]^{14-}$ can be considered as lacunary species from which polyanions with a transition metal core of the type $[\{M(H_2O)_3)_2(WO_2)_2\}(B\text{-}\beta\text{-}BiW_9O_{33})_2]^{n-}$ can be obtained, as this was observed for **Mn-3**. This polyanion could also be described as combination of two lacunary fragments of $\{BiW_{11}O_{41}\}$ (Figure 2.15). The W–O bond lengths of the tungsten atoms at the outer site of the transition metal core are 1.732(2) Å, 1.927(6) Å, and 1.746(7) Å. They are in the range of terminal and axial oxygen atoms and have been assigned as oxo groups. The same accounts for the tungsten atoms at the inner site of the transition metal core with W–O bond lengths of 1.740(6) Å and 1.720(6) Å which indicates the presence of oxo groups. All four positions of the transition metal core are fully occupied by W(VI) cations which adds another non-disordered transition metal core to the series of Krebs-type tungstobismuthates.

2.2.4 Reaction Control During the Preparation of $[B\text{-}\alpha\text{-}BiW_9O_{33}]^{9-}$

The large number of different polyanions which form during the preparation of the lacunary precursor $[B\text{-}\alpha\text{-}BiW_9O_{33}]^{9-}$ even in the absence of transition metal cations renders the isolation of this lacunary precursor in phase pure form challenging.

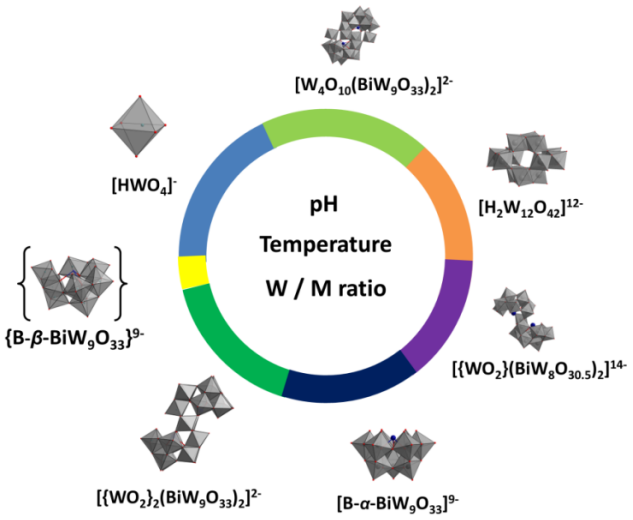

Figure 2.8. Hypothetical distribution of polyanion species in solution, during the synthesis of $[B\text{-}\alpha\text{-}BiW_9O_{33}]^{9-}$. Different colors are used to estimate the percentage of a particular polyanion of the total tungsten content. Quantification of the different species is the subject of ongoing work.

Describing the composition of the reaction mixture by identification of different POMs by single crystal structure determination does not permit quantification of the different species. However, a rough idea of stable polyanions can be obtained from which hypothetical fragments may be derived. In order to find reaction conditions under which the yield of [B-α-BiW_9O_{33}]$^{9-}$ can be maximized and to study the influence of different reaction parameters on the polyanion distribution in the reaction mixture, the reaction was monitored by HR-ESI MS and ^{183}W NMR spectroscopy.

The polyanion distribution was monitored by HR-ESI MS during the preparation of the lacunary precursor (§2.5.5.2) through sampling at different points of the reaction: during the addition of the solution of $Bi(NO_3)_3$ in HCl, before and after heating, and at different pH values. The recorded mass spectra show that there are much more polyanion species present in solution than expected (as well as their respective Na^+ and K^+ adducts). A list of plausible polyanions and polyanion-fragments is shown in Table 2.10. Due to the complexity of the measured HR-ESI MS spectra, evaluation of this work is still in progress.

Table 2.10. Polyanion fragments that may be present in the reaction mixture during the preparation of the lacunary precursor [B-α-BiW_9O_{33}]$^{9-}$.

Polyanions or Polyanion Fragments	**m**
$\{BiW_8O_{30}\}/\{Bi_2W_{16}O_{59}\}$	2159.70/4302.40
$\{BiW_{10}O_{37}\}$	2639.38
$\{BiW_{11}O_{41}\}$	2887.22
$[\{(WO_2)Na(H_2O)_2\}(B\text{-}\beta\text{-}BiW_9O_{33})_2]^{15-}$	5105.93
$[H_2W_{12}O_{42}]^{10-}$	2880.09
$[\{(WO_3)_2(WO_2)_2\}(BiW_9O_{33})_2]^{14-}$	5678.44
$[\{(WO_2)_2\}(BiW_9O_{33})_2]^{14-}$	5214.75
$[B\text{-}\alpha\text{-}BiW_9O_{33}]^{9-}$	2391.54

It is very important to identify all the parameters that influence the self-assembly of the lacunary precursor in order to increase the yield. However, it is equally important to understand how a phase pure sample of the lacunary precursor can be stabilized in aqueous solution and how its decomposition can be avoided. The mass spectrum of a freshly prepared solution of a phase pure sample of the lacunary precursor Na_9[B-α-BiW_9O_{33}] shows mass peaks of different polyanions (Figure 2.9).

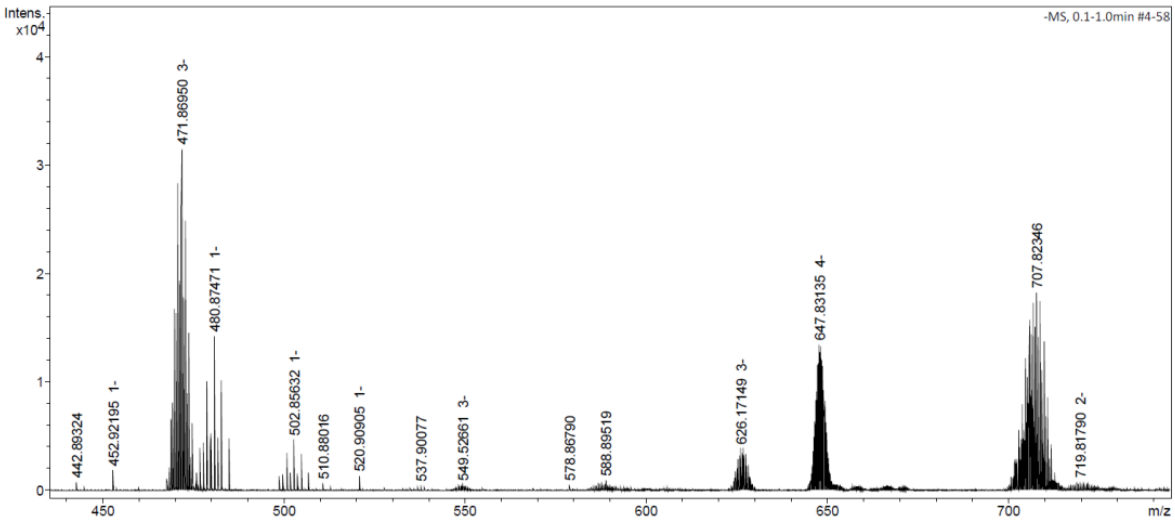

Figure 2.9. High resolution mass spectrum of a phase pure sample of the lacunary precursor $Na_9[B\text{-}\alpha\text{-}BiW_9O_{33}]$ in H_2O + 0.1 % HCOOH, diluted in H_2O.

Furthermore, the solution stability of this precursor was investigated by ^{183}W NMR spectroscopy (Figure 2.10). The low abundance of ^{183}W and its long relaxation times are difficult prerequisites to monitor the time-dependent transformation of the lacunary precursor. Therefore, the NMR experiment was run for 14 d. In contrast to the high number of tungsten species which were observed by HR-ESI MS, the ^{183}W NMR spectrum only shows three peaks. Over time, a single stable species with a high symmetry seems to form, which is still under structural investigation.

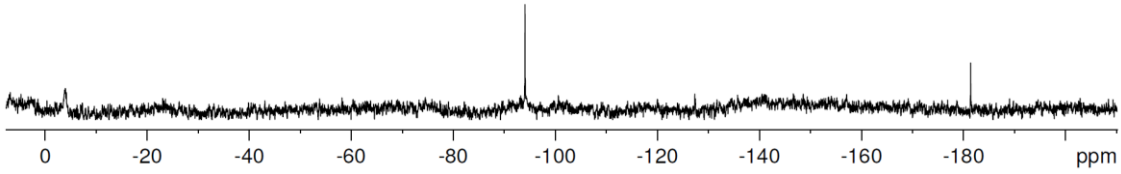

Figure 2.10. ^{183}W NMR of the lacunary precursor $Na_9[B\text{-}\alpha\text{-}BiW_9O_{33}]$ in D_2O after 14 d.

Table 2.11. Crystallographic and structural refinement data for (**BiW_9-1**), and (**BiW_9-2**).

	(BiW_9-1)	**(BiW_9-2)**
Empirical formula	$Bi_2H_{71}Na_{14}O_{96.5}W_{17}$	$Bi_2H_{94}Na_{14}O_{123}W_{22}$
Formula weight ($g \cdot mol^{-1}$)	5480.57	6847.00
Temperature	183(2)	183(2)
Wavelength (λ/Å)	0.7107	0.7107
Crystal system	Triclinic	Triclinic
Space group	$P\bar{1}$	$P\bar{1}$
a (Å)	13.0936(2)	12.8018(4)
b (Å)	17.1934(4)	13.3489(5)
c (Å)	21.1324(4)	17.8481(6)
α (°)	79.8520(17)	106.798(3)
β (°)	89.7348(16)	98.413(3)
γ (°)	71.1695(18)	104.499(3)
V ($Å^3$)	4427.87(18)	2747.12(17)
Z	2	1
ρ_{calc} (g/cm^{-3})	4.086	4.139
Crystal size	0.05 x 0.20 x 0.33	0.04 x 0.12 x 0.40
Reflections collected/unique	93720/30361	34643/18356
Unique observed reflections	21089	15623
θ range (°)	2.388-33.466	2.311-32.949
F(000)	4842	3026
Data/restraints/parameters	30361/2349/1180	18356/1044/745
Goodness-of-fit	1.040	1.091
R_1[a] [I>2σ(I)]	0.0631	0.0400
wR_2[b]	0.1428	0.0912
R_1[a] [I>2σ(I)] (all data)	0.1023	0.0502
wR_2[b] (all data)	0.1653	0.1053

2.3 Mn- and Co-Substituted Tungstobismuthates

The polyoxometalate precursor $Na_9[BiW_9O_{33}] \cdot 19.5H_2O$ was applied in the reaction with manganese(II) and cobalt(II) salts. In order to isolate polyanions with low or no W/M exchange, mild reaction conditions were adjusted. Despite these special reaction conditions, a broad variety of 0D, 1D and even 2D structures crystallized, which were characterized by single crystal X-ray diffraction (Figure 2.11). Two 0D Mn containing polyanions were obtained: $Na_{10}[\{Mn(H_2O)_6(Mn(H_2O)_2)_{1.72}(WO_2)_{0.28}\}(B\text{-}\beta\text{-}BiW_9O_{33})_2] \cdot 27.56H_2O$ (**Mn-2**)

shows W/Mn disorder at the inner position of the transition metal core, while the 0D structure motif of $Na_6Mn_2[\{(Mn(H_2O)_3)_2(Mn(H_2O)_2\}(B\text{-}\beta\text{-}BiW_9O_{33})_2]\cdot 46H_2O$ (**Mn-5**) displays a transition metal core that is free of W/Mn disorder and fully occupied with manganese. However, two Mn(II) cations are present in **Mn-5** amongst the counter-cations, which rendered this polyanion useless for further catalytic testing. In addition to the 0D structures, two 1D-chains could be characterized. The structure 1D-$Na_{10}[\{(Mn(H_2O)_3)_2(Mn(H_2O)_2)_{1.27}(WO_2)_{0.73}\}(B\text{-}\beta\text{-}BiW_9O_{33})_2]\cdot 35H_2O$ (**Mn-1**) could be isolated in phase pure form and shows W/Mn disorder at the inner position of the transition metal core. The $[\{(Mn(H_2O)_3)_2(Mn(H_2O)_2)_{1.27}(WO_2)_{0.73}\}(B\text{-}\beta\text{-}BiW_9O_{33})_2]^{10-}$ units are bridged by Mn-O-Mn bonds forming the 1D chain.

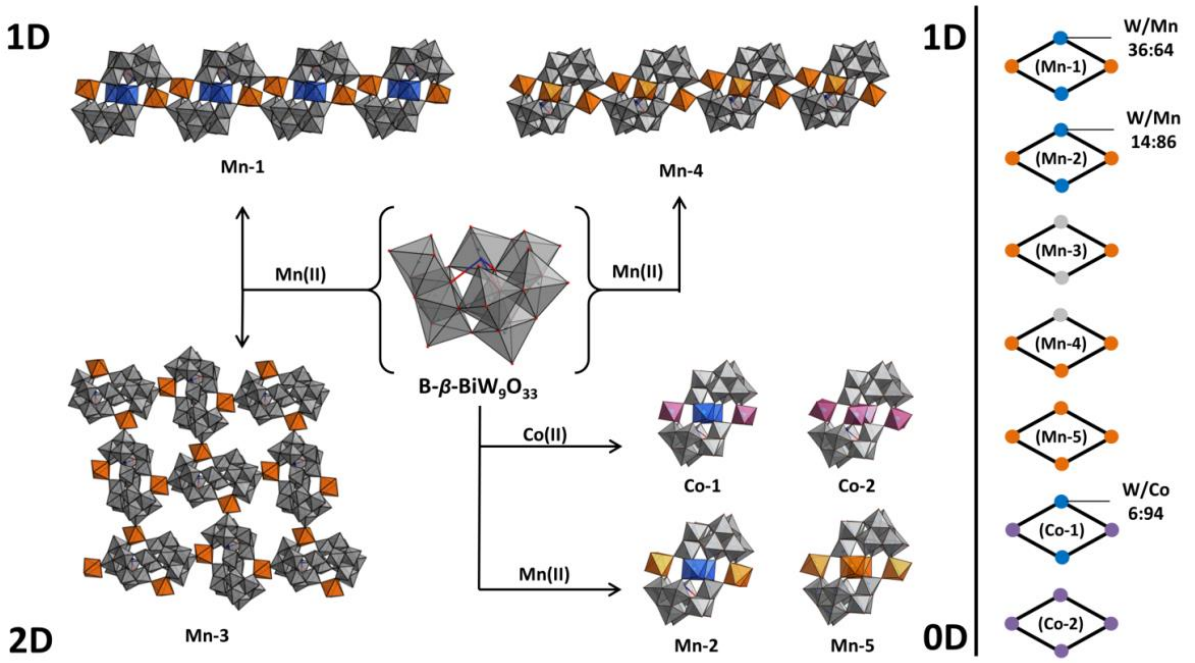

Figure 2.11. Polyhedral ball-and stick representation of polyanions obtained in the reaction of $[BiW_9O_{33}]^{9-}$ with Mn(II) and Co(II) cations (color code: grey octahedral = WO_6, orange = $MnO_4(H_2O)_2$, purple = $Co_4(H_2O)_2$, blue = disordered $WO_6/MO_4(H_2O)_2$ (M = Mn, Co)).

After applying slightly different reaction conditions (§2.4.1), two different compounds were formed. In 1D-$Na_{10}[\{(Mn(H_2O)_2)_2(Mn(H_2O)_2)(WO_2)\}(B\text{-}\beta\text{-}BiW_9O_{33})_2]\cdot 31.3H_2O$ (**Mn-4**) the monomeric units are connected in the same way as observed for **Mn-1**, with the difference that the $\{(Mn(H_2O)_2)_2WO_2(Mn(H_2O)_2\}$ transition metal core is non-disordered. From the same reaction mixture that afforded **Mn-4** crystals, 2D-$Na_{10}[\{(Mn(H_2O)_2)_2(WO_2)_2\}(B\text{-}\beta\text{-}$

$BiW_9O_{33})_2]\cdot 32H_2O$ (**Mn-3**) was also isolated. **Mn-3** has a non-disordered $\{Mn_2(H_2O)_6(WO_2)_2\}$ transition metal core.

Although the reaction conditions for analogous cobalt-based systems have not been screened to the same extent as for manganese, the observed structural diversity was smaller and restricted to 0D structures. $Na_{10}[\{(Co(H_2O)_3)_2(Co(H_2O))_{1.87}(WO_2)_{0.13}\}(B\text{-}\beta\text{-}BiW_9O_{33})_2]\cdot 25 H_2O$ (**Co-1**) has a disordered transition metal core, while $Co_2Na_6[\{(Co(H_2O)_3)_2(Co(H_2O)_2)_2\}(B\text{-}\beta\text{-}BiW_9O_{33})_2]\cdot 36H_2O$ (**Co-2**) exhibits a pure Co_4 core. As seen for **Mn-5**, Co(II) cations are amongst the counter-cations, which rendered further catalytic tests impossible.

2.3.1 Structure of New Mn and Co-Containing Tungstobismuthates

All of the polyanions **Mn-1**–**Mn-5** as well as the polyanions in **Co-1** and **Co-2** are sandwich-type structures. They can be considered as being based on a hypothetical $\{B\text{-}\beta\text{-}BiW_9O_{33}\}$ precursor which coordinates to four metal centers. Through applying mild reaction conditions, the W/M disorder in the transition metal core could be restricted to the inner positions of the transition metal core, while the outer positions are fully occupied with the transition metal The lacunary structure $\{B\text{-}\beta\text{-}BiW_9O_{33}\}$ is essentially isostructural in all of these compounds. Crystals with disordered transition metal cores are formed from three different type of polyanions which co-exist in solution. It was assumed that polyanions with a disordered transition metal core (**Mn-1**, **Mn-2** and **Co-1**) contain the following polyanions: $[(M(H_2O)_3)_2(Mn(H_2O)_2(B\text{-}\beta\text{-}BiW_9O_{33})_2]^{10-}$, $[(M(H_2O)_3)_2(M(H_2O)(WO_2)(B\text{-}\beta\text{-}BiW_9O_{33})_2]^{10-}$ and $[(M(H_2O)_3)_2(WO_2)_2(B\text{-}\beta\text{-}BiW_9O_{33})_2]^{10-}$ (M = Mn for **Mn-1** and **Mn-2**, Co for **Co-1**). The oxidation state of metal cations on the disordered position cannot be determined reliably. The same applies to nature of the oxygen atoms in their coordination sphere. It remains unknown whether these are water ligands, oxo or hydroxo groups. The oxidation state and nature of the oxygen atoms of Mn and W atoms were derived from crystal structures with a non-disordered transition metal core (**Mn-3**, **Mn-4**, **BiW_9-2**) which may be a reasonable assumption.

2.3.1.1 0D Structures

The 0D structure $Na_{10}[\{Mn(H_2O)_6(Mn(H_2O)_2)_{1.72}(WO_2)_{0.28}\}(B\text{-}\beta\text{-}BiW_9O_{33})_2]\cdot 27.56H_2O$ (**Mn-2**) crystallizes in the monoclinic space group $P2_1/n$. **Mn-2** shows W/Mn disorder at the inner position of the transition metal core which was refined to a W/Mn ratio of 14:86. Assuming a stochastically independent distribution of W and Mn (§1.16.1.3), the probability for polyanions with a pure $\{(Mn_2(H_2O)_3)_2(Mn(H_2O)_2)_2\}$ core is 74 %, for polyanions with a $\{Mn_2(H_2O)_6(WO_2)Mn(H_2O)_2\}$ core, 24 % and for polyanions with a $\{Mn_2(H_2O)_6(WO_2)_2\}$ core only 2 %. The interatomic distances within the transition metal core were refined to 5.6872(23) Å between the inner positions, 10.1734(25) Å between the outer positions, and to 5.8191(21) Å between the inner and outer position. A total of 10 sodium counter-cations was refined to fulfill charge balance in **Mn-2**. 7 partially occupied sodium positions have been located in the asymmetric unit. The second Mn containing 0D POM observed in this series is $Na_6Mn_2[\{(Mn(H_2O)_3)_2(Mn(H_2O)_2\}(B\text{-}\beta\text{-}BiW_9O_{33})_2]\cdot 46H_2O$ (**Mn-5**). It crystallizes in the triclinic space group $P\bar{1}$. The transition metal core of this compound could be refined without W/Mn disorder and represents phase pure non-disordered $\{Mn_2(H_2O)_6(WO_2)Mn(H_2O)_2\}$ as a major target for bio-inspired WOC tests. The interatomic distances between the Mn atoms in the transition metal core have been refined to 5.6510(29) Å between the inner positions, to 10.1001(42) Å between the outer positions, and to 5.8852(22) Å between the inner and outer position. The charge of the polyanion is compensated with six counter-cations which were located on four distinct positions in the asymmetric unit. In addition to the sodium counter-cations, two Mn(II) cations an octahedral $Mn(H_2O)_6$ coordination environment are present, which do not bridge single polyanions. Unfortunately, this intrinsic free Mn(II) impurity remains in the way of further WOC tests.

2.3.1.2 1D Structures

The inorganic polymer $1D\text{-}Na_{10}[\{(Mn(H_2O)_3)_2(Mn(H_2O)_2)_{1.27}(WO_2)_{0.73}\}(B\text{-}\beta\text{-}BiW_9O_{33})_2]\cdot 35H_2O$ (**Mn-1**) crystallizes in the triclinic space group $P\bar{1}$. The polyanion monomers $[\{(Mn(H_2O)_3)_2(Mn(H_2O)_2)_{1.27}(WO_2)_{0.73}\}(B\text{-}\beta\text{-}BiW_9O_{33})_2]^{10-}$ are bridged into a 1D chain via the Mn atoms at the outer position of the transition metal core by sharing the terminal oxygen atom of the WO_6 octahedron of the next polyanion. The W/Mn ratio of the transition metal core in this particular polyanion was refined to 36:64. The probability for polyanions with a pure Mn_4 core was calculated to 41 %, for polyanions with a $\{Mn_2(H_2O)_6(WO_2)Mn(H_2O)_2\}$ core to 46 %, and for polyanions with a $\{Mn_2(H_2O)_6(WO_2)_2\}$

core to only 13 %. The probabilities for polyanions with a pure Mn core are 33 % lower compared to transition metal core of **Mn-2**. The interatomic distances between atoms of the transition metal core have been refined to 5.8178(28) Å between the inner positions, to 10.1236(39) Å between the outer positions and to 5.7862(29) Å between the inner and outer position in the transition metal core. 7 distinct and partially occupied sodium positions have been refined in the asymmetric unit, and a total of 10 sodium atoms were refined in order to compensate the negative polyanion charge of 10-.

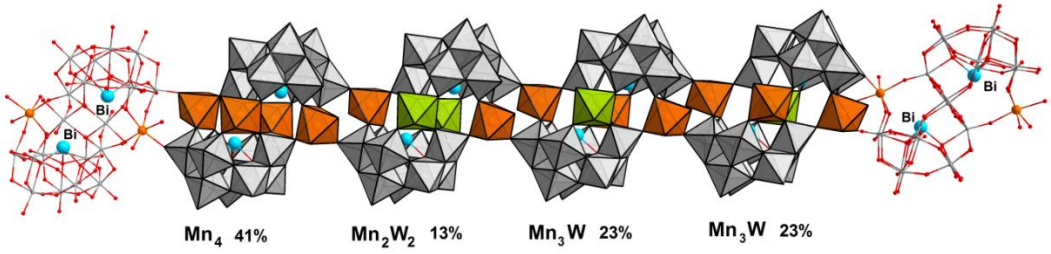

Figure 2.12. Exemplary sequence of the **Mn-1** polyanion monomer units in the chain and their probability, assuming a stochastically independent distribution (color code: orange octahedra = MnO_6; green polyhedra = $WO_6/MnO_4(H_2O)_2$; grey polyhedra = non-disordered WO_6).

The 1D chain 1D-$Na_{10}[\{(Mn(H_2O)_2)_2(Mn(H_2O)_2)(WO_2)\}(B\text{-}\beta\text{-}BiW_9O_{33})_2]\cdot 31.3H_2O$ (**Mn-4**) with a non-disordered transition metal core crystallizes in the triclinic space group $P\overline{1}$. (Z = 2). In contrast to other polyanions which crystallize in this space group, the inversion center is not within the polyanion. Bridging of the single $[\{(Mn(H_2O)_2)_2(Mn(H_2O)_2)(WO_2)\}(B\text{-}\beta\text{-}BiW_9O_{33})_2]^{10-}$ polyanion monomers occurs in the same way as outline above for **Mn-1.** The transition metal core of this polyanion could be refined without W/Mn disorder to $\{(Mn(H_2O)_2)_2(Mn(H_2O)_2)(WO_2)\}$. The Mn cations at the external sites of the polyanion share a terminal oxygen atom of a WO_6 octahedron of the subsequent polyanion. Two of these Mn–O–W connections link subsequent polyanions. Distances inside the core of **Mn-1** are 5.774(19) Å between the Mn and W atom at the inner position of the transition metal core, while the distance between the Mn atoms of the outer positions is 10.0748(28) Å. As sole exception of all polyanions in this series, the core positions of **Mn-4** are crystallographically independent, i.e. one position is occupied with Mn (100 %) and the other with W (100 %). The distances between the Mn atom at the inner core position and the Mn atom at the outer

core position are 5.8180(28) Å and 5.8143(27) Å. Bond lengths between the W atom at the inner core position and the Mn atom at the outer core position are 5.881(2) Å and 5.714(2) Å. A total of 10 Na^+ counter-cations were refined on 14 distinct positions of the transition metal core, and six of these positions are only partially occupied.

2.3.1.3 2D Structures

The 2D network 2D-$Na_{10}[\{(Mn(H_2O)_2)_2(WO_2)_2\}(B\text{-}\beta\text{-}BiW_9O_{33})_2]\cdot 32H_2O$ (**Mn-3**) crystallizes in the monoclinic space group $P2_1/n$. The polyanion monomer $[\{(Mn(H_2O)_2)_2(WO_2)_2\}(B\text{-}\beta\text{-}BiW_9O_{33})_2]^{10-}$ show a non-disordered transition metal core with the inner core positions fully occupied by W (100 %) and the outer core positions occupied by Mn (100 %). They crystallize into a 2D structure where the polyanions are linked via the Mn cation at the outer position of the transition metal core and a terminal oxygen atom of the subsequent polyanion, which is rotated with respect to the first one (Figure 2.13). While bridging of two polyanions in the 1D structures **Mn-1** and **Mn-4** occurs via two Mn–O(–W) bonds, two polyanions are connected by only one Mn–O(–W) bond in the 2D network of **Mn-3**. Each polyanion is surrounded by 4 polyanions connecting via Mn–O(–W) bonds.

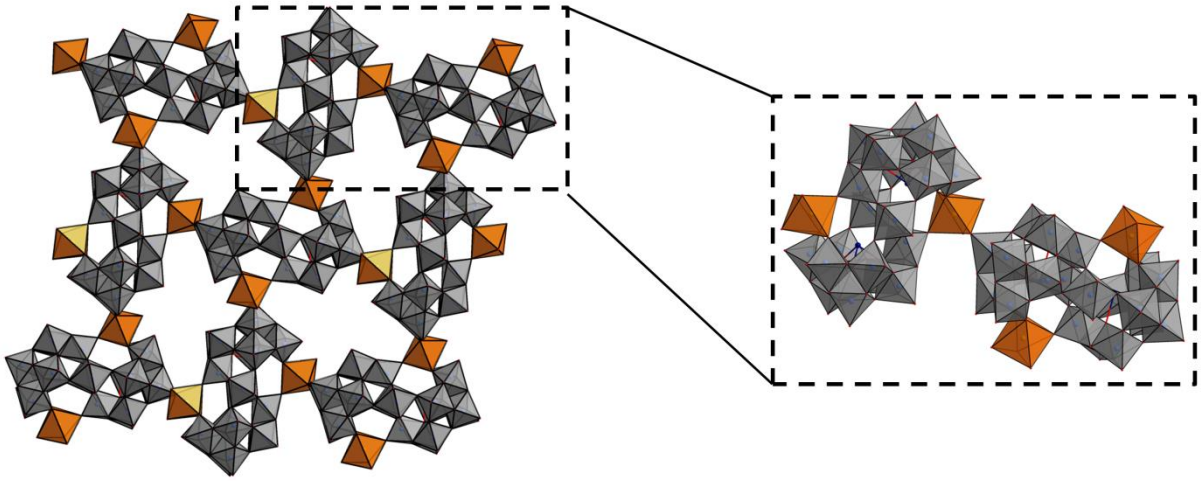

Figure 2.13. Polyhedral ball and stick representation of the 2D layer of **Mn-3**. Inset: repeating unit of the 2D structure and connectivity between the two polyanions.

This structure is particularly interesting, given that the connection between two polyanions occurs directly via the transition metal core and not through an additional Mn(II) linker. Furthermore, the transition metal core $\{(Mn(H_2O)_2)_2(WO_2)_2\}$ is not disordered. The interatomic distances between the W atoms on the inner positions were found at 5.8552(24)

Å, the Mn atoms on the outer positions at 10.3119(15) Å and the Mn atom at the outer position and the W atom at the inner position at a distance of 5.9404(36) Å. The 2D network crystallizes with Na^+ counter-cations, and to maintain charge neutrality a total of 10 Na^+ cations was refined.

2.3.2 New Co-Containing Tungstobismuthates

Two 0D structures were obtained through replacing Mn(II)- with Co(II) salts under the same reaction conditions. The 0D POM $Na_{10}[\{(Co(H_2O)_3)_2(Co(H_2O))_{1.87}(WO_2)_{0.13}\}(B\text{-}\beta\text{-}BiW_9O_{33})_2]\cdot 25H_2O$ (**Co-1**) crystallizes in the monoclinic space group $P2_1/n$. The W/Co disorder in the transition metal core of this compound is lower than observed in the isostructural compound **Mn-2**. It was refined to a ratio of 94:6. The probability for a pure Co_4 core is as high as 88 %, for polyanions with a $\{Co_2(H_2O)_6(WO_2)Co(H_2O)_2\}$ core it is 5.64 % and for polyanions with a $\{Co_2(H_2O)_6(WO_2)_2\}$ core the probability is only 0.36 %. The interatomic distances between the Co atoms in the transition metal core have been refined to 5.5471(34) Å between the inner positions, to 10.0769(45) Å between the outer positions and to 5.6841(36) Å between the inner and outer position. Six distinct Na^+ positions are located in the asymmetric unit. A total of 10 sodium counter-cations was included in the model.

The second structure which was obtained with Co(II) sources is the 0D POM $Co_2Na_6[\{(Co(H_2O)_3)_2(Co(H_2O)_2)_2\}(BiW_9O_{33})_2]\cdot 36H_2O$ (**Co-2**), which crystallizes in the triclinic space group $P\bar{1}$ and is isostructural to **Mn-5**. No disorder was refined in the Co-transition metal core, strongly pointing to a pure $\{(Co(H_2O)_3)_2(Co(H_2O)_2)_2\}$ (100 %) core. The interatomic distances between the Co atoms in the transition metal core have been refined to 5.5472(27) Å between the inner positions, 10.0768(22) Å between the outer positions and 5.8180(18) Å between the inner and outer position. Two Co(II) cations were found amongst the counter-cations, and the remaining charge of 6- is compensated by six sodium cations. In the asymmetric unit 5 distinct partially occupied Na^+ sites were located. A total of 10 Na^+ cations was refined for charge neutrality to be fulfilled.

2.4 Structural Considerations on Mn and Co Containing Tungstobismuthates

Crystal structure analysis of the new Mn and Co containing tungstobismuthates shows that all of them are isostructural and differ only with respect to their transition metal cores. The most important interatomic distances of the transition metal cores are summarized in Table 2.12.

Table 2.12. Summary of interatomic distances in the transition metal cores of **Mn-1 – Mn-5**, **Co-1** and **Co-2**.

Compound	I-I (Å)[a]	O-O (Å)[b]	I-O (Å)[c]
Mn-1	5.8178(28)	10.1236(39)	5.7862(29)
Mn-2	5.6872(23)	10.1734(25)	5.8191(21)
Mn-3	5.8552(24)	10.3119(15)	5.9404(36)
Mn-4	5.774(19)	10.748(28)	W-Mn: 5.881(2), 5.714(2) Mn-Mn: 5.8180(28),5.8143(27)
Mn-5	5.6510(29)	10.1001(42)	5.8852(22)
Co-1	5.5471(34)	10.0769(45)	5.6841(36)
Co-2	5.5472(27)	10.0768(22)	5.8180(18)

[a] I-I = Distance between the inner positions. [b] O-O = Distance between the outer positions. [c] I-O = Distance between the inner and outer position.

Table 2.13. Crystallographic and structural refinement data for (**Mn-1**), (**Mn-2**), (**Mn-3**), (**Mn-4**) and (**Mn-5**).

	Mn-1	**Mn-2**	**Mn-3**	**Mn-4**	**Mn-5**
Empirical formula	$Bi_2Mn_{3.27}H_{87}Na_{10}O_{109}W_{18.73}$	$Bi_2H_{69.44}Mn_{3.72}Na_{10}O_{103}W_{18.28}$	$Bi_2H_{72}Mn_2Na_{10}O_{106}W_{20}$	$Bi_2Mn_3H_{74.6}Na_{10}O_{105.3}W_{19}$	$Bi_2Mn_6H_{96}Na_6O_{114}W_{18}$
Formula weight ($g \cdot mol^{-1}$)	6102.42	5912.32	6203.05	6065.52	6115.30
Temperature	183(2) K	183(2) K	183(2)	183(2)	183(2)
Wavelength (λ/Å)	0.71069	0.71069	0.71069	0.71069	0.71069
Crystal system	triclinic	monoclinic	monoclinic	triclinic	triclinic
Space group	$P\bar{1}$ (2)	$P2_1/n$ (14)	$P2_1/n$ (14)	$P\bar{1}$ (2)	$P\bar{1}$ (2)
a (Å)	12.3521(3)	12.5299(3)	13.2203(3)	13.9754(2)	12.5858(3)
b (Å)	13.3042(4)	12.7741(2)	17.7877(4)	16.7771(3)	13.3264(3)
c (Å)	16.0349(4)	29.5144(6)	19.4182(5)	23.3375(5)	18.9243(5)
α (°)	98.995(2)	90	90	87.246(2)	86.844(2)
β (°)	108.293(2)	101.007(2)	94.964(2)	86.403(2)	75.685(2)
γ (°)	99.144(2)	90	90	78.5020(10)	63.811(2)
V ($Å^3$)	2409.61(12)	4637.12(17)	4549.23(19)	5347.96(17)	2754.44(13)
Z	1	2	2	2	1
ρ_{calc} (g/cm^{-3})	4.202	4.262	4.529	3.767	3.687
Crystal size	0.07 x 0.10 x 0.25	0.05 x 0.11 x 0.18	0.06 x 0.06 x 0.18	0.03 x 0.04 x 0.22	0.06 x 0.17 x 0.45
Reflections collected/unique	42943/11980	111610/19596	76594/15909	98680/27543	70726/19004
Unique observed reflections	10100	14623	12332	21370	16601
θ range (°)	2.316-29.573	2.299-35.177	2.290-32.954	2.5480-30.0480	2.395-32.923
F(000)	2703	5230	5452	5348	2722
Data/restraints/parameters	11980/1035/687	19596/1446/705	15909/1155/649	27543/2310/1310	19004/1026/694
Goodness-of-fit	1.172	1.109	1.061	1.065	1.078
R_1[a] [I>2σ(I)]	0.0407	0.0436	0.0584	0.0436	0.0324
wR_2[b]	0.0980	0.0967	0.1455	0.1075	0.0810
R_1[a] [I>2σ(I)] (all data)	0.0537	0.0705	0.0822	0.0646	0.0400
wR_2[b] (all data)	0.1118	0.1168	0.1615	0.1239	0.0853

Table 2.14. Crystallographic and structural refinement data for (**Co-1**) and (**Co-2**).

	Co-1	**Co-2**
Empirical formula	$Bi_2Co_{3.76}H_{65.7}Na_{10}O_{101}W_{18.13}$	$Bi_2Co_6H_{92}Na_6O_{112}W_{18}$
Formula weight ($g \cdot mol^{-1}$)	5884.59	6103.24
Temperature	183(2) K	183(2) K
Wavelength (λ/Å)	0.71069	0.71069
Crystal system	monoclinic	triclinic
Space group	$P2_1/n$ (14)	$P\bar{1}$ (2)
a (Å)	12.5150(4)	12.6718(2)
b (Å)	12.7149(3)	13.4201(3)
c (Å)	29.3394(6)	18.7288(5)
α (°)	90	89.724(2)
β (°)	101.797(3)	75.4832(19)
γ (°)	90	61.892(2)
V ($Å^3$)	4570.1(2)	2695.60(11)
Z	2	1
ρ_{calc} (g/cm^{-3})	4.258	3.760
Crystal size	0.05 x 0.12 x 0.25	0.03 x 0.18 x 0.38
Reflections collected/unique	76331/15982	51791/18232
Unique observed reflections	11391	13999
θ range (°)	2.308- 32.908	2.322-32.815
F(000)	5186	2714
Data/restraints/parameters	15982/984/677	18232/1047/676
Goodness-of-fit	1.060	1.061
R_1[a] [I>2σ(I)]	0.0555	0.0509
wR_2[b]	0.1117	0.1238
R_1[a] [I>2σ(I)] (all data)	0.0910	0.0762
wR_2[b] (all data)	0.1282	0.1405

2.4.1 Synthesis and Crystal Engineering of Mn-1 – Mn-5 and Co-1 - Co-2

The reaction of the lacunary precursor [B-*α*-BiW_9O_{33}]$^{9-}$ with Mn(II) and Co(II) transition metal cations was studied in detail as outlined above. Considering the difficulties which were encountered during the preparation of the lacunary precursor [B-*α*-BiW_9O_{33}]$^{9-}$ it was not surprising that the preparation of Mn and Co functionalized tungstobismuthates led to the formation of a variety of different polyanions which only differ by the composition of their transition metal cores. It is remarkable that the precursor maintained its original B-*α* conformation in none of these characterized structures. HR-ESI mass spectra of the phase pure precursor have shown the presence of numerous different tungstate species in solution (Figure 2.9). After the reaction with Co(II) and Mn(II) cations sandwich-type polyanions crystallize consecutively, some of them simultaneously from the same reaction mixture. The preparation of transition metal substituted tungstobismuthates is accompanied with the

precipitation of numerous solids and crystals. Figure 2.14 aims to clarify the identity of all the observed precipitates as far as they are known. The structure of all polyanions was determined from single crystal structure analysis only and may not be representative for the composition of the reaction mixture.

The reaction of Mn(II) cations with the precursor $[B\text{-}\alpha\text{-}BiW_9O_{33}]^{9-}$ results in the formation of different crystalline solids that precipitate consecutively from the reaction mixture. The addition of the Mn(II) cations in form of a solution of manganese acetate to a solution to the solution of the lacunary precursor first yields a pale yellow solid of which no single crystals could be obtained. This solid is crystalline and could be characterized by PXRD (Figure S2.1). From the same saturated reaction mixture three different solid can be crystallized. 1D-$Na_{10}[\{(Mn(H_2O)_3)_2(Mn(H_2O)_2)_{1.27}(WO_2)_{0.73}\}(B\text{-}\beta\text{-}BiW_9O_{33})_2]\cdot 35H_2O$ (**Mn-1**) is obtained as yellow crystalline powder after the addition of a saturated solution of solution of NaCl. The identity of this precipitate was confirmed by PXRD (Figure S2.2). Single crystals of **Mn-1** are obtained from the mother liquor first. Crystals of the monomer $Na_{10}[\{Mn(H_2O)_6(Mn(H_2O)_2)_{1.72}(WO_2)_{0.28}\}(B\text{-}\beta\text{-}BiW_9O_{33})_2]\cdot 27.56H_2O$ (**Mn-2**) crystallize from the mother liquor simultaneously with crystals of **Mn-1.** Given that the Mn content in **Mn-2,** which crystallizes next from the reaction mixture, is higher, the polyanion $[\{(Mn(H_2O)_3)_2(Mn(H_2O)_2\}(B\text{-}\beta\text{-}BiW_9O_{33})_2]^{10-}$ may have a higher solubility. This is most likely a concentration dependent effect and the subject of ongoing studies. **Mn-2** was obtained phase pure at lower $[B\text{-}\alpha\text{-}BiW_9O_{33}]^{9-}$ concentrations (Figure S2.3). Both **Mn-1** and **Mn-2** have a disordered transition metal core which indicates the presence of up to three different polyanion species in solution. From the same reaction mixture from which crystals of **Mn-1** and **Mn-2** formed after the addition of NaCl, yellow crystals of the polyanion $Na_6Mn_2[\{(Mn(H_2O)_3)_2(Mn(H_2O)_2\}(B\text{-}\beta\text{-}BiW_9O_{33})_2]\cdot 46H_2O$ **(Mn-5)** are obtained upon diffusion of THF into the reaction mixture. Crystal structure refinement showed the formation of a polyanion with a non-disordered Mn_4 transition metal core as evidence that the initial $\{Mn_4\}$ target compound can be formed in principle. However, it crystallizes with two Mn(II) counter-cations under the present conditions, which renders it useless for further WOC tests. Furthermore, proof of phase purity by PXRD could not be established for this compound.

While the structures **Mn-1**, **Mn-2** and **Mn-3** can be obtained from the same reaction mixture, 2D-$Na_{10}[\{(Mn(H_2O)_2)_2(WO_2)_2\}(B\text{-}\beta\text{-}BiW_9O_{33})_2]\cdot 32H_2O$ (**Mn-3**) and 1D-$Na_{10}[\{(Mn(H_2O)_2)_2(Mn(H_2O)_2)(WO_2)\}(B\text{-}\beta\text{-}BiW_9O_{33})_2]\cdot 31.3H_2O$ (**Mn-4**) are obtained from a reaction mixture which contains a lower concentration of $Mn(OAc)_2$ and [B-α-

$BiW_9O_{33}]^{9-}$. Yellow crystals of both compounds formed simultaneously at room temperature after addition of a small amount of NaCl. At higher NaCl concentrations crystals of **Mn-1** were formed.

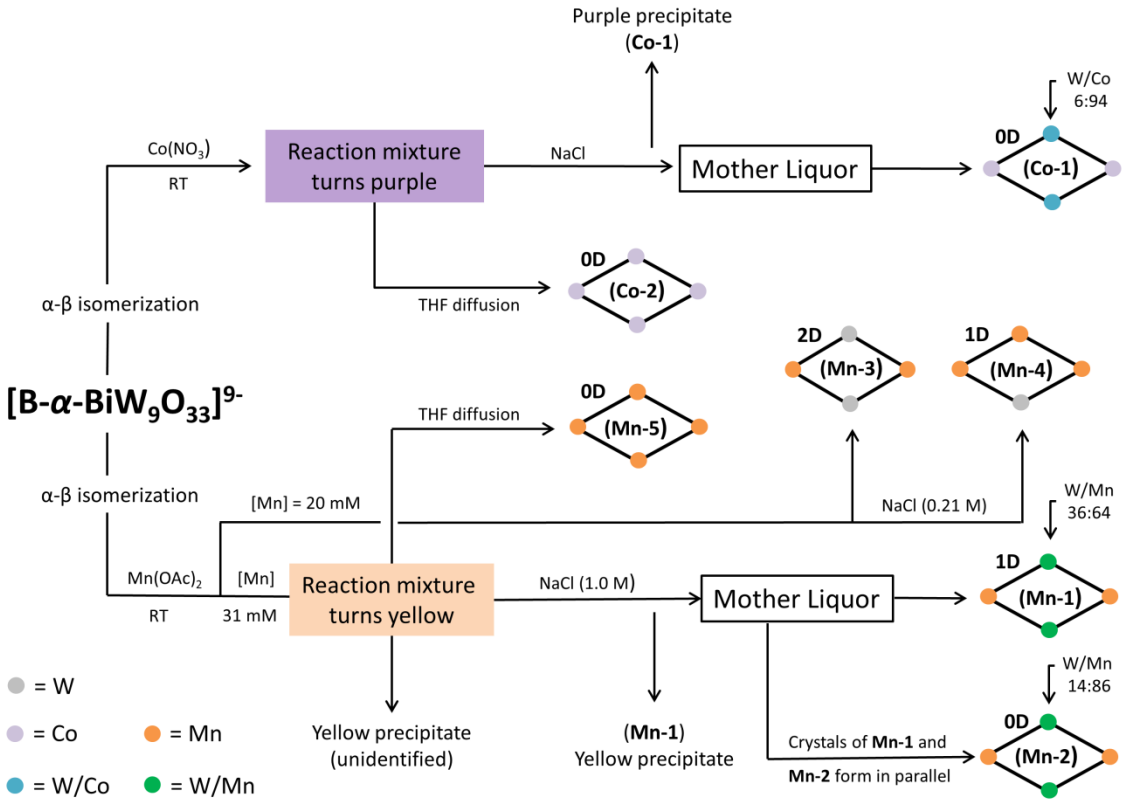

Figure 2.14. Crystallization scheme of $[B\text{-}\alpha\text{-}BiW_9O_{33}]^{9-}$ with Co(II) and Mn(II) cations at room temperature.

Cobalt functionalized compounds can be prepared by the same procedures as used for Mn compounds. $Na_{10}[\{(Co(H_2O)_3)_2(Co(H_2O))_{1.87}(WO_2)_{0.13}\}(B\text{-}\beta\text{-}BiW_9O_{33})_2]\cdot 25\ H_2O$ (**Co-1**) with W/Co disordered core precipitates phase pure from a reaction mixture saturated with $[B\text{-}\alpha\text{-}BiW_9O_{33}]^{9-}$ and Co(II) after addition of a saturated solution of NaCl. Phase purity of the isolated solid by PXRD could be established (Figure S2.4). From the mother liquor purple single crystals of **Co-1** are obtained. An isostructural compound to **Mn-5** is formed upon diffusion of THF into the saturated reaction mixture of $[B\text{-}\alpha\text{-}BiW_9O_{33}]^{9-}$ and Co(II) cations. $Co_2Na_6[\{(Co(H_2O)_3)_2(Co(H_2O)_2)_2\}(B\text{-}\beta\text{-}BiW_9O_{33})_2]\cdot 36H_2O$ (**Co-2**) crystallizes as purple single crystals with a pure Co_4 core. This compound crystallizes with two Co(II) counter-cations, which excludes significant WOC tests. PXRD analysis of crystals of **Co-2** was not applicable to establish purity of this compound.

2.4.2 Monitoring the Formation of Mn, Co and Cu Substituted Tungstobismuthates

The phase pure preparation of Mn and Co substituted tungstobismuthates was particularly challenging. The adjustment of the reaction conditions for the preparation of a pure M_4 core resulted in the formation of a variety of different polyanion structures with distinct transition metal cores. To study the influence of the reaction conditions (pH, temperature, counter-cation concentration) during the preparation of Mn and Co substituted polyanions, the reaction was monitored by HR-ESI MS.

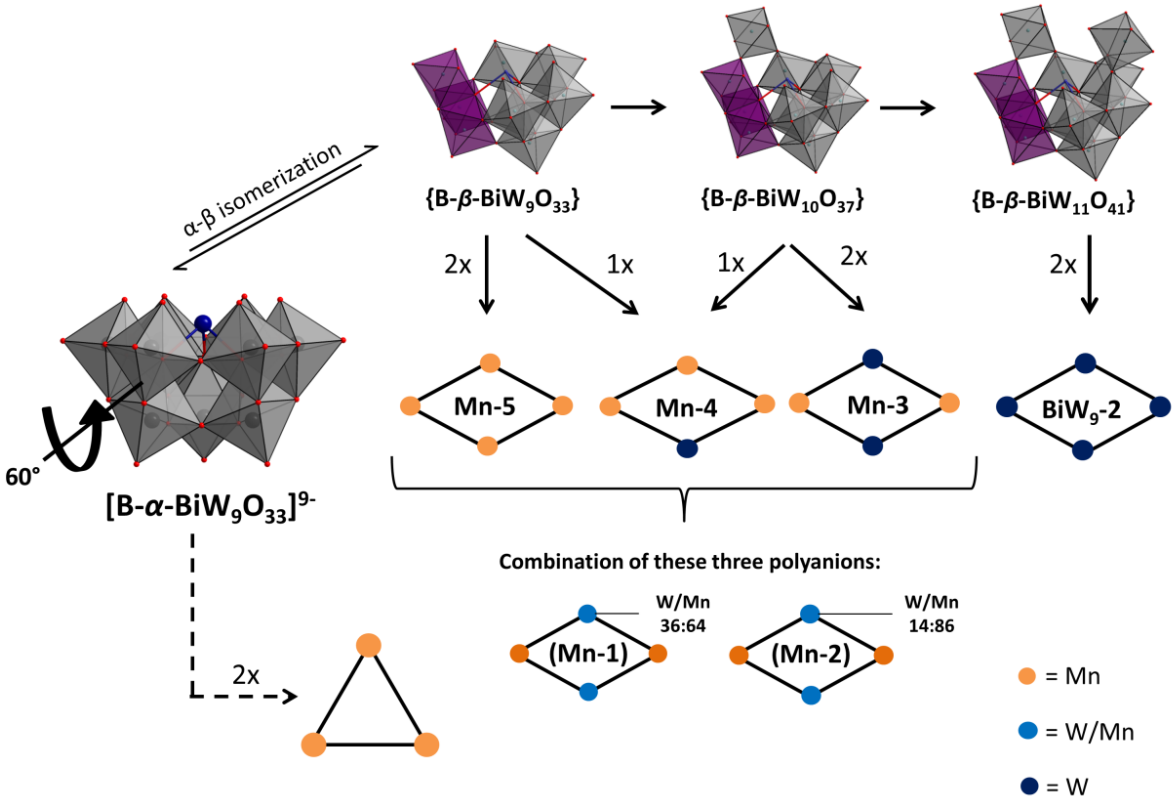

Figure 2.15. Hypothetical formation of transition metal functionalized Krebs-type polyanions with distinct transition metal cores.

Polyanions with a specific transition metal core may be formed via intermediate fragments which only exist in solution and remain hypothetical as they were not isolated to date (Figure 2.15). A large number of different polyanions and polyanion fragments is expected to form upon addition of a transition metal cation to a solution of the lacunary precursor [B-α-BiW_9O_{33}]$^{9-}$ (Table 2.15). These polyanions fragments may co-exist in solution and as soon as they are present in a specific ratio combine and crystallize to form the specific polyanions.

Table 2.15. Possible polyanion fragments in the reaction of the lacunary precursor [B-α-BiW_9O_{33}]$^{9-}$ with Mn(II) cations.

Polyanions or Polyanion Fragments
$\{BiW_9O_{33}Mn_3\}/\{BiW_9O_{33}Mn_2\}/\{BiW_9O_{33}Mn\}$
$[Mn_3(H_2O)_3(B\text{-}\alpha\text{-}BiW_9O_{33})_2]^{12-}$
$[\{(Mn(H_2O)_3)_2(Mn(H_2O)_2\}(B\text{-}\beta\text{-}BiW_9O_{33})_2]^{10-}$
$[\{(Mn(H_2O)_2)_2(Mn(H_2O)_2)(WO_2)\}(B\text{-}\beta\text{-}BiW_9O_{33})_2]^{10-}$
$[\{(Mn(H_2O)_3)_2(Mn(H_2O)_2\}(B\text{-}\beta\text{-}BiW_9O_{33})_2]^{10-}$

Attempts have been made to confirm the presence of different polyanion fragments. The reaction was monitored by HR-ESI MS by taking different samples in the course of the reaction. The identification of mass peaks of these polyanions amongst the numerous peaks in the HR-ESI MS spectra is the subject of ongoing studies.

The HR-ESI mass spectrum of a single crystal of **Mn-3** indicates that decomposition rapidly occurs after the dissolution of the crystal in H_2O as indicated by mass peaks of $[HWO_4]^-$.

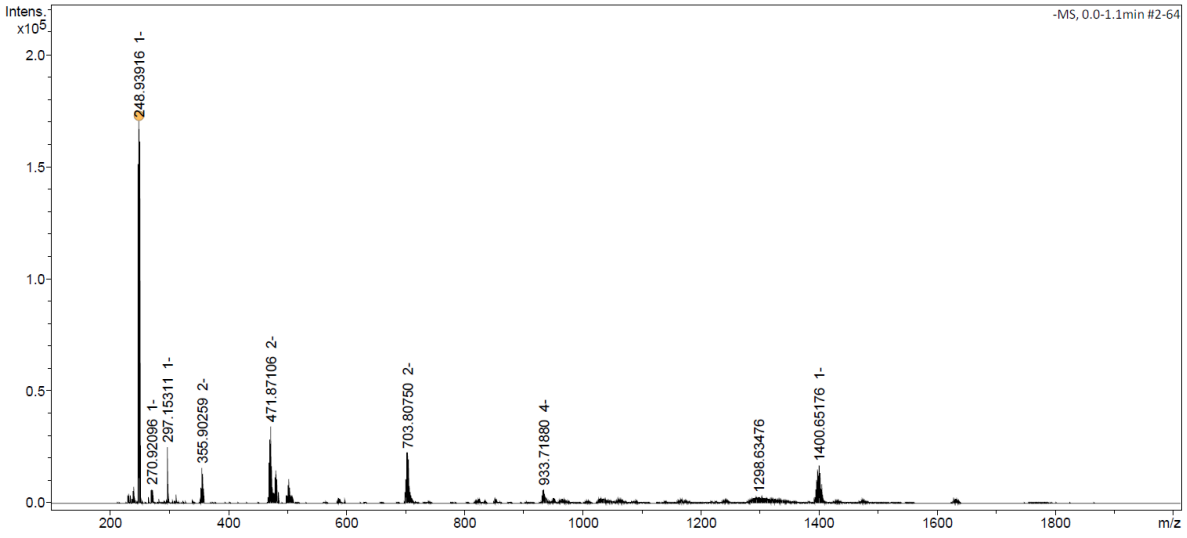

Figure 2.16. HR-ESI MS spectra of a single crystal of **Mn-3** dissolved in H_2O**.**

2.4.3 Tungstobismuthates as Catalysts for Artificial Photosynthesis

All polyanions that could be isolated in a phase pure form (**Mn-1**, **Mn-2**, and **Co-1)** were tested as visible-light-driven water oxidation catalysts. O_2 evolution was monitored with an oxygen sensitive Clark-electrode (see §1.4.1) and the amount of O_2 was quantified by GC. As

the probability of polyanions with a pure Mn_4 core could be highly increased for **Mn-1** and **Mn-2** compared to the previously reported polyanion $[Mn_{1.5}(H_2O)_6\{Bi_2W_{20.5}O_{68}(OH)_2\}]^{6-}$ they were expected to be more active for water oxidation catalysis.

2.4.3.1 O_2-Evolution

Visible light driven water oxidation tests were performed with a standard assay for photocatalytic water oxidation (§1.4). $[Ru(bpy)_3]^{2+}$ was used as photosensitizer (1 mM) and $Na_2S_2O_8$ as sacrificial electron acceptor (8.1 mM). The influence of the pH value on O_2 evolution activity was studied in different buffers. In NaPi (0.1 M, pH 7.0) and acetate buffer (0.1 M, pH 4.75) at a concentration of 75 µM **Mn-1** no activity was observed (Figure 2.17).

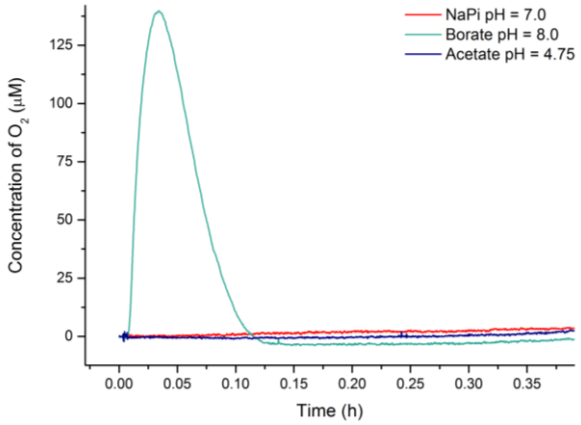

Figure 2.17. Oxygen evolution tests with **Mn-1** (75 µM) in different buffer media (acetate pH 4.75, NaPi pH 7.0 and borate pH 8.0).

O_2 evolution could only be observed in borate buffer (0.1 M, pH 8.0). Further catalytic tests to determine the influence of the catalyst concentration where thus performed in this buffer. The catalyst concentrations were screened in the concentration range from 12.5–150 µM. The highest efficiency was observed at low catalyst concentrations between 30 and 50 µM (Figure 2.18).

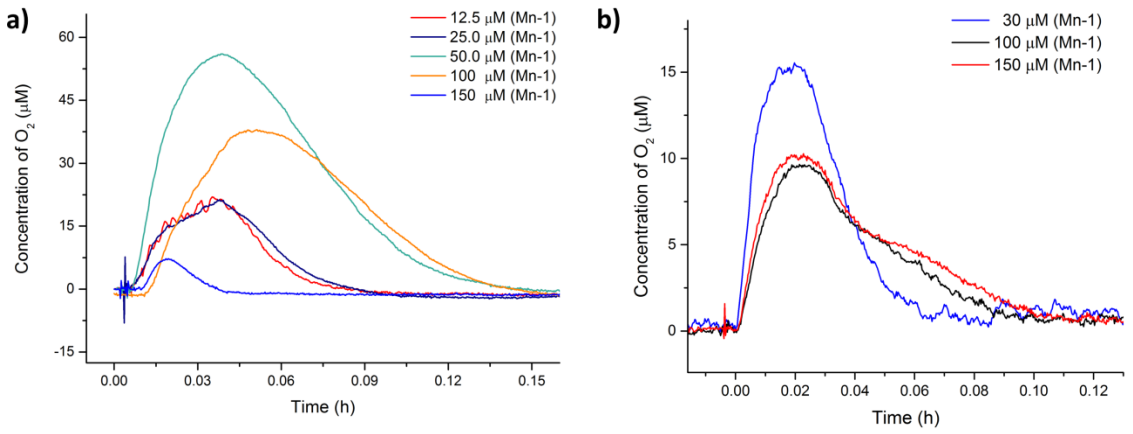

Figure 2.18. O_2 evolution of **Mn-1** in borate buffer (0.1 M, pH 8.0) at catalyst concentrations between **(a)** 12.5–150.0 µM (1st run) and **(b)** 50–150 µM (2nd run).

Clark traces which were monitored for **Mn-1** in aqueous borate buffer indicate that the reaction occurs very fast on a timescale of 7–10 min. The O_2 concentration in the buffer solution remains very low and rapidly equilibrates with gas in the headspace, so that it drops below the detection limit of the Clark sensor. No O_2 could be detected after analysis of the headspace. The amounts of O_2 which were detected by Clark electrode are beyond the detection limit of GC analysis and thus considered as negligibly small. Related effects were observed for catalytic tests of **Mn-2** which turned out inactive as well. The Co subsituted analogue **Co-1** showed a higher activity than **Mn-1** and **Mn-2**. However the amounts of O_2 produced are negligibly small compared with the amounts of O_2 produced by the WOC α-$K_6Na[\{Ru_3O_3(H_2O)Cl_2\}(SiW_9O_{34})]$.

2.4.3.2 H_2-Evolution

All new POMs obtained in this study were tested as H_2 evolution catalysts in an established photocatalytic assay (§1.4). H_2 evolution activity was observed for **Mn-1**, **Mn-2**, and **Co-1** at catalyst concentrations between 12.5–150 µM. All catalytic tests were performed in triplicate and were monitored with a H_2 sensitive sensor. The amounts of H_2 produced were quantified by GC and are higher than in reference experiments without POM catalysts. However, reference experiments with the lacunary precursor $[B\text{-}\alpha\text{-}BiW_9O_{33}]^{9-}$ showed that the activity of transition metal substituted POMs in general is lower than the activity of the non-functionalized lacunary precursor.

2.4.3.3 Formation of the POM-PS Complex

The formation of the solid POM-PS complex by the electrostatic interactions between negatively charged polyanions and positively charged photosensitizer molecules was observed in both O_2 and H_2 evolution tests (§1.9.1). EDX mapping of this solid (Figure 2.19) indicates that the compound is indeed composed of polyanion and phososensitizer. The formation of the POM-PS complex is inherent to all negatively charged polyanions in solutions which were tested in context of this project with positively charged photosensitizers, which renders further mechanistic studies very difficult.

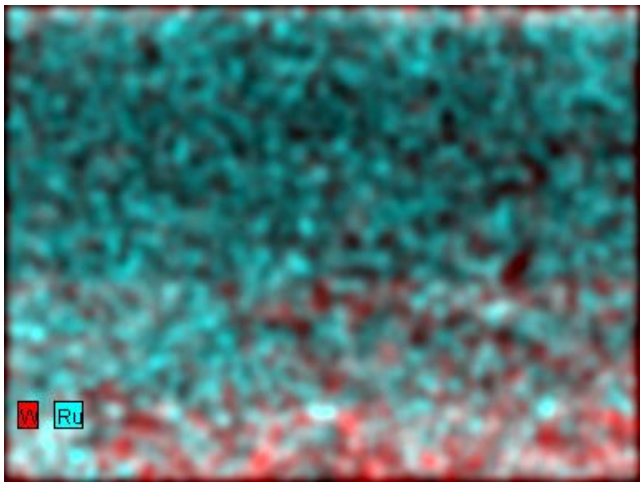

Figure 2.19. EDX mapping of a solid POM-PS complex formed from $[Ru(bpy)_3]^{2+}$ and **Mn-1** in a photocatalytic H_2 evolution test.

2.5 Appendix

2.5.1 Characterization and Properties of Mn- and Co-containing Tungstobismuthates

The solid which precipitates from the reaction mixture upon the addition of an excess of Mn(II) cations was characterized by PXRD (Figure 2.1).

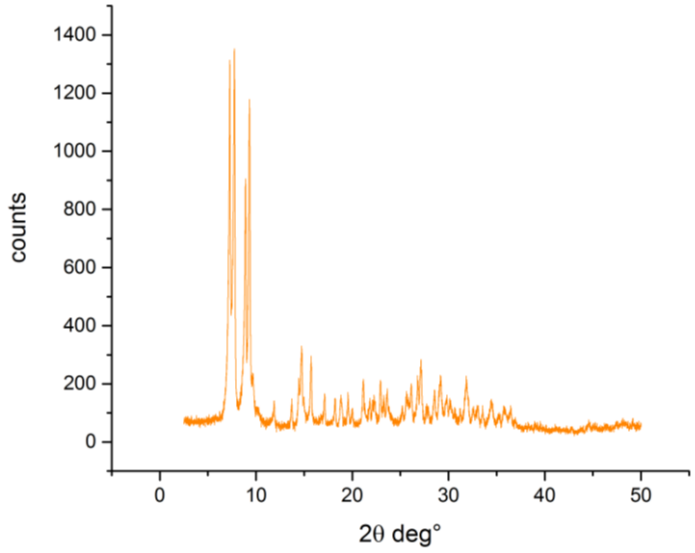

Figure S2.1. PXRD pattern of precipitate 0 zero formed immediately after the addition of Mn(II) to the precursor.

The phase purity of the three polyoxometalate **Mn-1**, **Mn-2** and **Co-1** could be established by PXRD (Figure S2.2 - Figure S2.4).

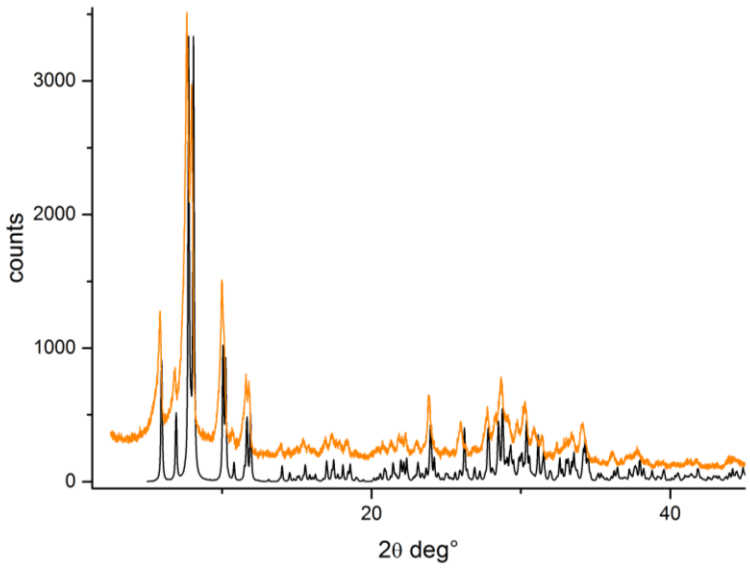

Figure S2.2. PXRD pattern of **Mn-1**(orange) vs. calculated pattern (black).

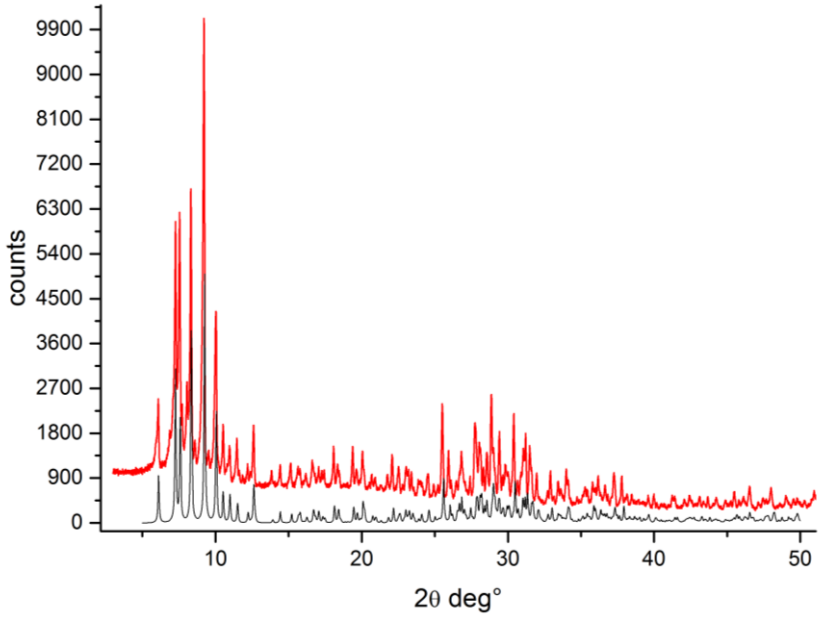

Figure S2.3. PXRD pattern of **Mn-2** (red) vs. calculated pattern (black).

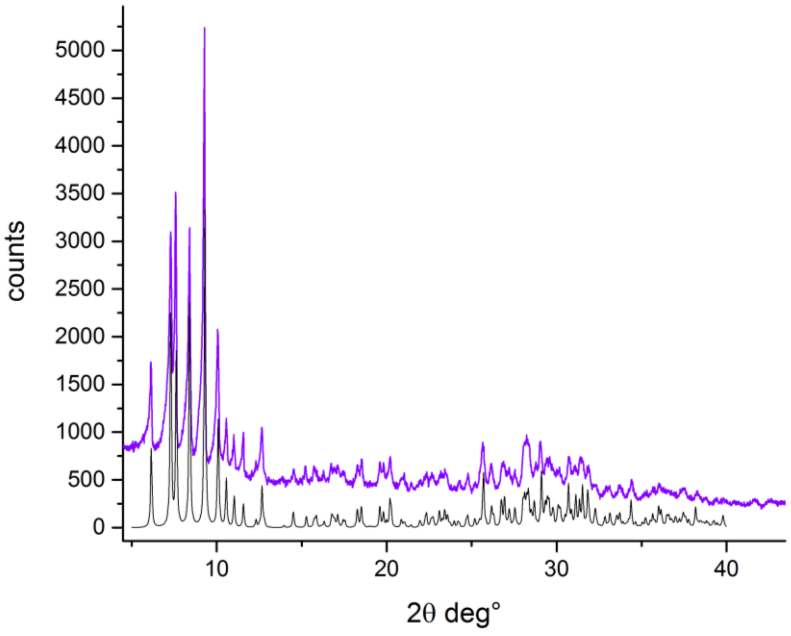

Figure S2.4. PXRD pattern of **Co-1** (purple) vs. calculated pattern (black).

2.5.2 Electrochemical Properties

The CV of **Mn-1** shows an irreversible reduction half-wave at -0.68 V (Figure S2.5). At lower potentials, an increase of the cathodic current was observed which is typical for polyoxometalates. Upon reversal of the potential, the CV shows oxidation waves that cannot be properly resolved. A broad oxidation half-wave is observed between -0.70-0.40 V. At -0.31 V an almost reversible redox wave is observed, which may be attributed to the reversible reduction/oxidation of the polyanion. For **Mn-1** an irreversible oxidation peak is observed at -0.04 V with a shoulder at -0.07 V. These irreversible oxidation waves are attributed to the oxidation of Mn(II) → Mn(III).

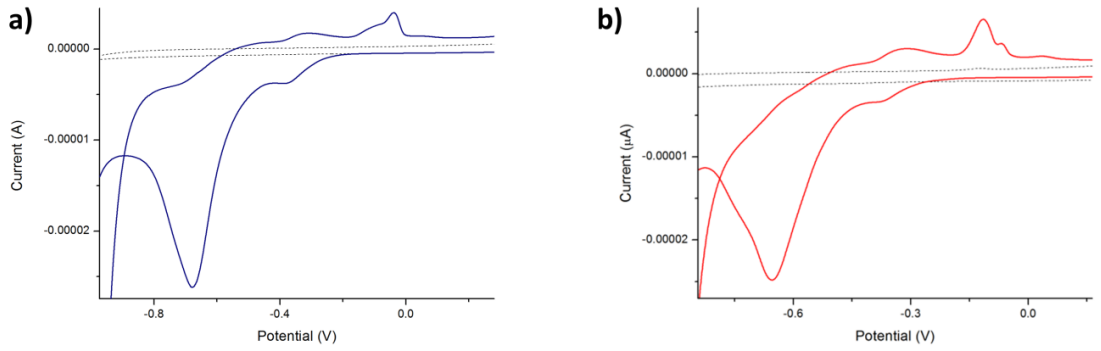

Figure S2.5. Cyclic voltammogram of **Mn-1** (a) and **Mn-2** (b) in 0.1 M HCl , pH 1.0 (blue), solvent (dashed).

The cyclic voltammogram of **Mn-2** shows similar redox waves as observed for **Mn-1**, albeit with different intensities. While the Mn_4 and Mn_3W cores are present in **Mn-1** with almost the same probability, the Mn_4 core in sample **Mn-2** is present to 74 % so that the more pronounced features in the CV may be assigned to this polyanion species

2.5.2.1 Spectroscopic Characterization of Mn-1, Mn-2, and Co-1

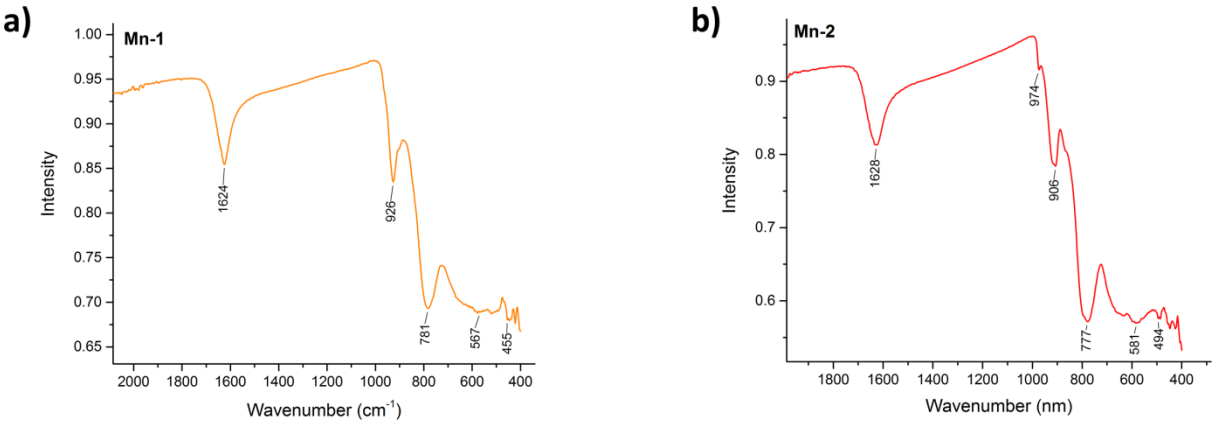

Figure S2.6. FT-IR spectra of 1D-$Na_{10}[\{(Mn(H_2O)_3)_2(Mn(H_2O)_2)_{1.27}(WO_2)_{0.73}\}(B\text{-}\beta\text{-}BiW_9O_{33})_2]\cdot 35\ H_2O$ **(Mn-1)** and $Na_{10}[\{Mn(H_2O)_6(Mn(H_2O)_2)_{1.72}(WO_2)_{0.28}\}(B\text{-}\beta\text{-}BiW_9O_{33})_2]\cdot 27.56\ H_2O$ **(Mn-2)**.

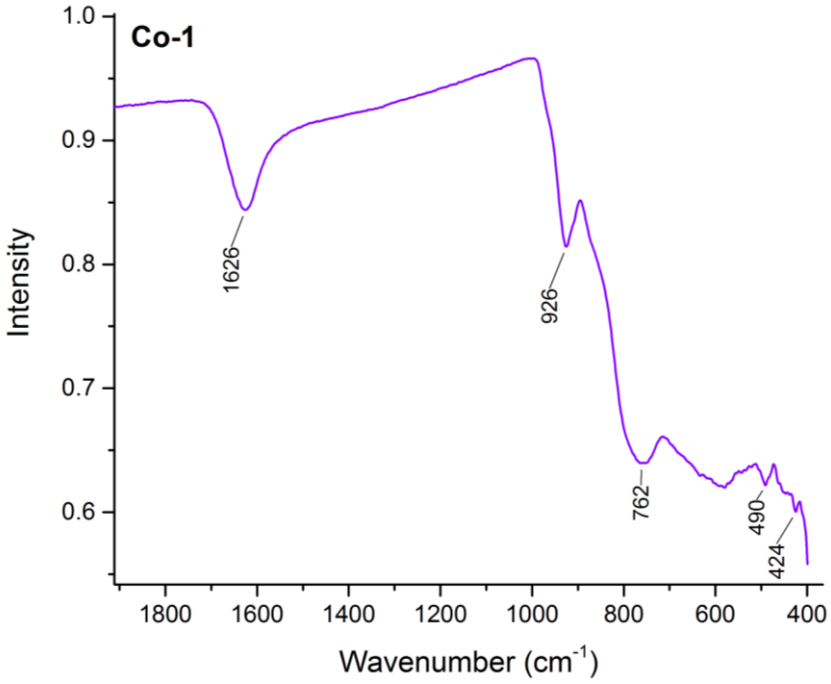

Figure S2.7. FT-IR spectra of $Na_{10}[\{(Co(H_2O)_3)_2(Co(H_2O))_{1.87}(WO_2)_{0.13}\}(B\text{-}\beta\text{-}BiW_9O_{33})_2]\cdot 25H_2O$ **(Co-1).**

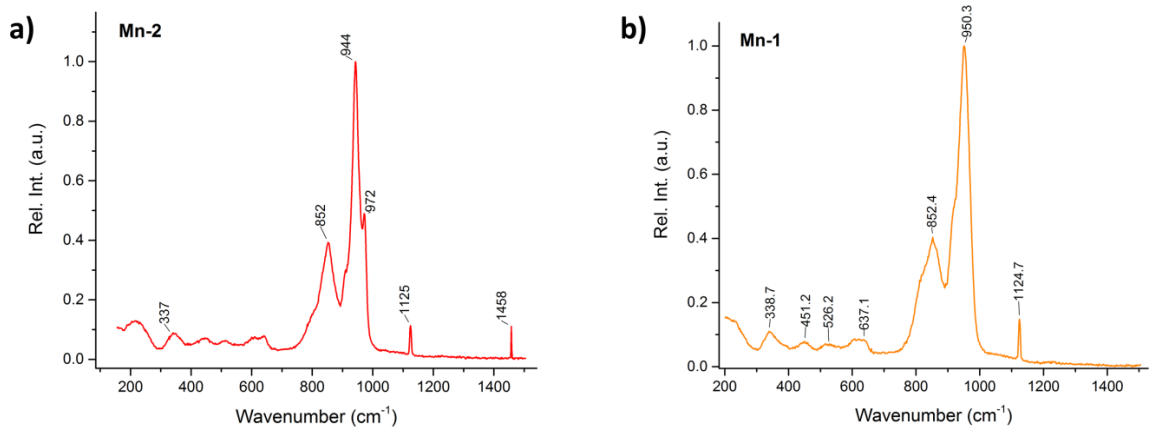

Figure S2.8. Raman spectra of (a) **Mn-1** and (b) **Mn-2**.

The IR spectra of **Mn-1**, **Mn-2**, and **Co-1** show different characteristic W–O vibrations of POMs between 400-1000 cm^{-1} (Figure S2.6 and Figure S2.7). An assignment of these vibrations, done for the Keggin structures in previous studies is beyond the scope of this project, as it would require normal mode analysis, and careful consideration of polyanion-polyanion and polyanion-cation interactions. The same applies for the measured Raman spectra of **Mn-1**, **Mn2** and **Co-1** which show the characteristic W–O bands expected for polyoxometalates between 800 and 1200 cm^{-1}.

2.5.3 UV/vis Absorption Spectroscopy

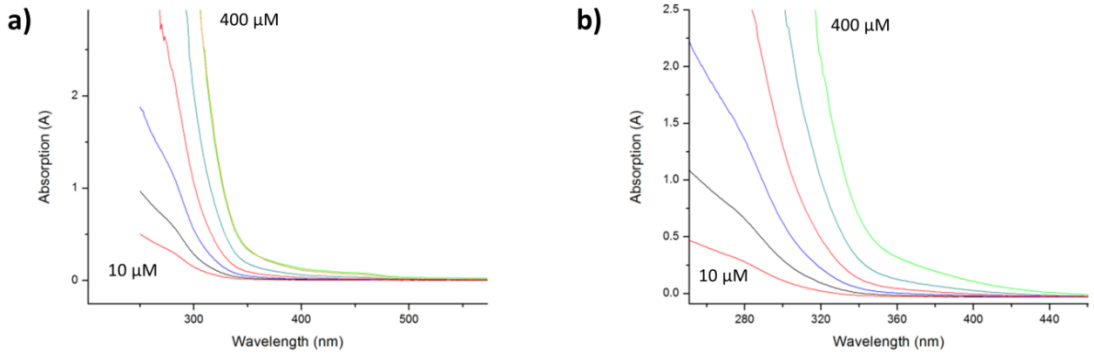

Figure S2.9. UV-Vis absorption spectra of (a) **Mn-1** and (b) **Mn-2** in acetate buffer at pH 4.75 at concentrations between 10-400 µM.

The slightly yellow solution absorbs visible light from ~440 nm onwards. No distinct absorption was observed at lower concentrations in the UV range. Absorption in the UV range is likely due to O→W charge transfer transitions.

2.5.3.1 UV/vis Stability Test of Co-1 at pH 4

The stability of **Co-1** in an aqueous sodium ascorbate solution at pH = 4 was monitored by UV/vis spectroscopy (Figure S2.10). The decreasing intensity below 540 nm indicates that this compound decomposes in the time-range of 30 min.

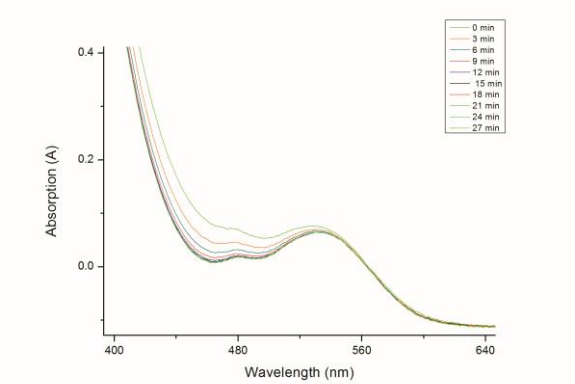

Figure S2.10. Stability of $Na_{10}[\{(Co(H_2O)_3)_2(Co(H_2O))_{1.87}(WO_2)_{0.13}\}(B\text{-}\beta\text{-}BiW_9O_{33})_2]\cdot 25\ H_2O$ **(Co-1)** in ascorbate buffer pH 4.

2.5.4 Thermal analysis of Mn-1, Mn-2, and Co-1

The content of crystal water was confirmed by thermal analysis (Figure S2.11).

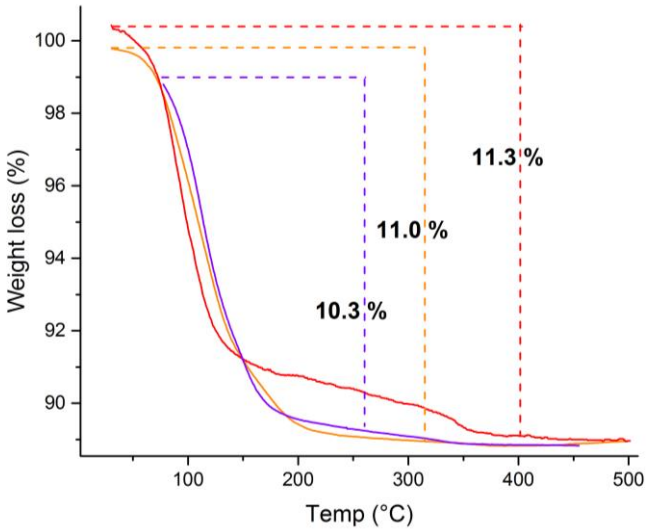

Figure S2.11. Thermal analysis of **Mn-1** (red), **Mn-2** (orange), and **Co-1** (purple) in the temperature range 300-500 °C.

2.5.5 Experimental Section

2.5.5.1 Reagents and Materials

The lacunary precursor $Na_9[BiW_9O_{33}]\cdot 19.5H_2O$ (M_{wt} = 2949.71 g/mol) was prepared from a modified literature procedure and characterized by FT-IR spectroscopy. $Na_2WO_4\cdot 2H_2O$, $MnOAc\cdot 4H_2O$, and $Co(NO_3)_2\cdot 6H_2O$ were obtained from Sigma Aldrich and used without further purification.

2.5.5.2 Modified Procedure for the Synthesis of $Na_9[BiW_9O_{33}]\cdot 19.5H_2O$

$Na_9[BiW_9O_{33}]\cdot 19.5H_2O$ was obtained by a modified literature procedure. A solution of $Bi(NO_3)_3\cdot 5H_2O$ (6.50 g, 13.4 mmol) in HCl (5 mL, 6 M) was added dropwise to a stirred solution of $Na_2WO_4\cdot 2H_2O$ (40.0 g, 0.12 mol) in H_2O (40 mL) at 80 °C. The formation of a white solid was observed which was removed by filtration over celite. The pH of the solution after the addition of the $Bi(NO_3)_3$ solution was 8.0, and it was adjusted to 7.5-7.8 with HCl (1.0 M). The reaction mixture was left in the fridge which led to the formation of an oil, which was removed. The volume was reduced at the rotary evaporator and the yellow solution was left at 5 °C. $Na_9[BiW_9O_{33}]\cdot 19.5\ H_2O$ crystallized as a white solid. (ATR FTIR cm^{-1}): 1618, 960, 912, 874, 743, 679.

General remark: The $Na_9[BiW_9O_{34}]\cdot 19.5H_2O$ precursor may contain a small amount of an insoluble impurity below the detection limits of IR or PXRD. It can be removed from the reaction mixture prior to the addition of the counter-cation by filtration over celite. Regarding the low stability of this precursor and the likelihood that it undergoes partial decomposition or *α-β* isomerization, this precursor cannot be purified by recrystallization.

2.5.5.3 Synthesis of 1D-$Na_{10}[\{(Mn(H_2O)_3)_2(Mn(H_2O)_2)_{1.27}(WO_2)_{0.73}\}(B\text{-}\beta\text{-}BiW_9O_{33})_2]\cdot 35H_2O$ (Mn-1)

A solution of $Na_9[BiW_9O_{33}]\cdot 19.5H_2O$ (5.00 g, 1.69 mmol) was prepared in demineralized H_2O (50 mL). The reaction mixture was sonicated until complete dissolution of the solid was achieved. A solution of $Mn(OAc)_2\cdot 4H_2O$ (15 mL, 0.16 M) was added dropwise to the vigorously stirred solution of the precursor. The colorless reaction mixture thereby turned yellow. During the addition a pale yellow precipitate formed which was removed by filtration over celite. A saturated solution of NaCl was added (10 mL) and the reaction mixture was stirred for 10 min. **Mn-1** formed as a yellow precipitate. It was collected by filtration and rinsed with water. High quality crystals for structure analysis were obtained overnight from

the mother liquor. PXRD confirmed phase purity of 1D-$Na_{10}[\{(Mn(H_2O)_3)_2(Mn(H_2O)_2)_{1.27}(WO_2)_{0.73}\}(B\text{-}\beta\text{-}BiW_9O_{33})_2]\cdot 35H_2O$ **(Mn-1)** (1.570 g, 25.2 %). Elemental analysis (%), calc. for $Bi_2Mn_{3.27}H_{87}Na_{10}O_{109}W_{18.37}$ (found): Bi 6.92 (6.92), Mn 2.98 (3.16), W 55.95 (54.70); Na 3.81 (3.98). (ATR FTIR cm^{-1}): 1625, 927, 779, 577, 518.

2.5.5.4 Synthesis of 2D-$Na_{10}[\{Mn(H_2O)_6(Mn(H_2O)_2)_{1.72}(WO_2)_{0.28}\}(B\text{-}\beta\text{-}BiW_9O_{33})_2]\cdot 27.56H_2O$ (Mn-2)

A solution of $Na_9[BiW_9O_{33}]\cdot 19.5H_2O$ (1.00 g, 0.34 mmol) was prepared in demineralized H_2O (60 mL). A solution of $Mn(OAc)_2\cdot 4H_2O$ (5 mL, 0.17 M) was added dropwise, the reaction mixture thereby turned yellow. The addition was continued until a precipitate formed. This precipitate was removed by filtration over celite, the pH of this solution was 6.5. A saturated solution of NaCl was added (5 mL). Yellow crystals of **Mn-2** formed overnight. They were collected by filtration and washed with H_2O. The identity of **Mn-2** was confirmed by PXRD (207 mg, 20.5 %). Elemental analysis (%): calc for $Bi_2H_{69.44}Mn_{3.72}Na_{10}O_{103}W_{18.28}$ (found): Bi 7.05 (6.72), Mn 3.45 (3.36), W 56.66 (55.0), Na 3.88 (3.12). (ATR FTIR cm^{-1}): 1624, 927, 781, 576, 422.

2.5.5.5 Preparation of crystals of 2D-$Na_{10}[\{(Mn(H_2O)_2)_2(WO_2)_2\}(B\text{-}\beta\text{-}BiW_9O_{33})_2]\cdot 32H_2O$ (Mn-3) and 1D-$Na_{10}[\{(Mn(H_2O)_2)_2(Mn(H_2O)_2)(WO_2)\}(B\text{-}\beta\text{-}BiW_9O_{33})_2]\cdot 31.3H_2O$ (Mn-4)

A solution of $Na_9BiW_9O_{33}\cdot 19.5\ H_2O$ (5.00 g, 1.69 mmol) was prepared in demineralized H_2O (50 mL). A solution of $Mn(OAc)_2\cdot 4H_2O$ (25 mL, 40.8 mM) was added dropwise. The colorless solution thereby turned yellow. The pH after complete addition of the $Mn(OAc)_2$ solution was 6.8. The reaction mixture was stirred for 20 min and divided into 5 parts of 15 mL each. Different amounts of a saturated NaCl solution were added. Yellow crystals of **Mn-3** and **Mn-4** formed in the vials where 0.5 and 1.5 mL saturated NaCl solution was added.

2.5.5.6 Synthesis of $Na_6Mn_2[\{(Mn(H_2O)_3)_2(Mn(H_2O)_2\}(B\text{-}\beta\text{-}BiW_9O_{33})_2]\cdot 46H_2O$ (Mn-5)

Crystals of **Mn-5** were obtained by a modified procedure for the synthesis of **Mn-1**.

A solution of $Na_9[BiW_9O_{33}]\cdot 19.5H_2O$ (5.00 g, 1.69 mmol) was prepared in demineralized H_2O (50 mL). The reaction mixture was sonicated until complete dissolution of the solid was achieved. A solution of $Mn(OAc)_2\cdot 4H_2O$ (15 mL, 0.16 M) was added dropwise to the vigorously stirred solution of the precursor. The colorless reaction mixture thereby turned yellow. During the addition a pale yellow precipitate formed which was removed by filtration

over celite. Slow diffusion of THF in the reaction mixture affords yellow crystals of **Mn-5**. PXRD analysis of this compound was not possible.

2.5.5.7 Synthesis of $Na_{10}[\{(Co(H_2O)_3)_2(Co(H_2O))_{1.87}(WO_2)_{0.13}\}(B\text{-}\beta\text{-}BiW_9O_{33})_2]\cdot 25\ H_2O$ (Co-1)

A solution of $Na_9[BiW_9O_{33}]\cdot 19.5H_2O$ (5.00 g, 1.69 mmol) was prepared in demineralized water (50 mL). A solution of $Co(NO_3)_3\cdot 6H_2O$ (25 mL, 75.6 mM) was added dropwise to the stirred solution of the lacunary precursor, whereupon the colorless solution turned to dark violet. The reaction mixture was stirred for 1 h, followed by the addition of a saturated solution of NaCl (10 mL). A purple solid precipitated and was collected by filtration. PXRD analysis confirms the formation of **Co-1** (1.18 g, 23.7 %). Single crystals of **Co-1** were obtained from the mother liquor at pH 7.00 as purple single crystals. (ATR FTIR cm^{-1}): 1625, 926, 763, 750, 490, 425. Elemental Analysis (%): calc. for $Bi_2Co_{3.76}H_{65.7}Na_{10}O_{101}W_{18.13}$ (found): Bi 7.10 (6.64), Co 3.77 (3.76), W 56.64 (54.3), Na 3.91 (3.91).

2.5.5.8 Synthesis of $Co_2Na_6[\{(Co(H_2O)_3)_2(Co(H_2O)_2)_2\}(B\text{-}\beta\text{-}BiW_9O_{33})_2]\cdot 36\ H_2O$ (Co-2)

A solution of $Na_9[BiW_9O_{33}]\cdot 19.5H_2O$ (5.00 g, 1.69 mmol) was prepared in demineralized water (50 mL). A solution of $Co(NO_3)_3\cdot 6H_2O$ (25 mL, 75.6 mM) was added dropwise to the stirred solution of the lacunary precursor. Thereby the colorless solution turned to dark violet. The reaction mixture was stirred for 1 h. Purple crystals of **Co-2** were obtained by slow diffusion of THF into the reaction mixture. Crystals of this compound did not diffract during PXRD analysis.

2.5.5.9 X-ray Diffraction Experiments

Crystal structure analysis was done by standard procedures, for a list of programs used see §1.16. Further details on the crystal structure investigations may be obtained from the Fachinformationszentrum Karlsruhe, D-76344 Eggenstein-Leopoldshafen, Germany (Fax: +49 7247 808 666; email crysdata@fiz-karlsruhe.de), by citing the depository numbers CSD-431274 (**BiW_9-1**), CSD-431275 (**BiW_9-2**), CSD-431279 (**Mn-1**), CSD-431277 (**Mn-2**) CSD-431278 (**Mn-3**), CSD-431276 (**Mn-4**), CSD-431281 (**Mn-5**), CSD-431280 (**Co-1**) and CSD-431273 (**Co-2**).

2.5.5.10 Instrumentation

For a list of instruments and procedures used for the characterization of the new the new tungstobismuthates see §1.17.2.

2.6 Crystal Structure of $[Ru(bpy)_3]_2Na_2[Mn_6(H_2O)_6(B\text{-}\alpha\text{-}AsW_9O_{33})_2]$

Polyanions form an insoluble precipitate with the photosensitizer (PS) $[Ru(bpy)_3]^{2+}$ or with other positively charged transition metal complexes. The formation of such a solid was observed during O_2 and H_2 evolution tests and denoted as POM-PS complex (§1.9.1). This solid was considered as the active species and has been investigated for this purpose[87] furthermore the photophysical properties have been studied in detail by Wedd et al.[88,89] Collecting the catalyst in this solid form allows the recovery of the catalyst.[90,61] However, very little is reported about the structure of POM-PS complex of TMSPs with the photosensitizer. The rapid formation kinetics in solution, as well as its low solubility renders it very difficult to obtain suitable POM-PS single crystals for X-ray diffraction experiments. Crystal structures of polyanions and $[Ru(bpy)_3]^{2+}$ have only been reported for spherical Keggin anions of the type $[XW_{12}O_{40}]^{n-}$.[91,92] Numerous crystallization experiments were necessary to overcome the mentioned difficulties associated with single crystal growth. Solvent layering techniques which separate the photosensitizer cation from the polyanion made the slow diffusion of both solutions possible. Crystals could be obtained from the Mn substituted arsenotungstate $[\{Mn_3(H_2O)_3\}(B\text{-}\alpha\text{-}AsW_9O_{33})_2]^{8-}$ and the photosensitizer $[Ru(bpy)_3]^{2+}$ and were characterized by single crystal X-ray diffraction.

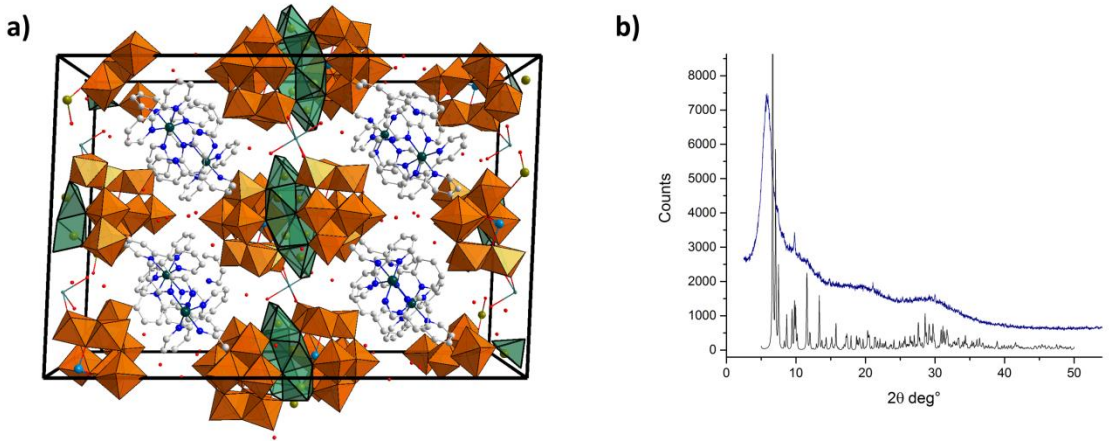

Figure 2.20. **(a)** Packing diagram of the POM-PS complex $[Ru(bpy)_3]_2Na_2[Mn_6(H_2O)_6(B\text{-}\alpha\text{-}AsW_9O_{33})_2]\cdot 14H_2O$; color code of octahedra: WO_6 = orange, $MnO_4(H_2O)$ = green, color code of atoms: Ru = blue. **(b)** PXRD pattern of the POM-PS complex which formed after fast mixing, calculated (black) measured (blue).

Table 2.16. Crystallographic and structural refinement data for (**Mn-6**).

	(Mn-6)[a]
Empirical formula	$C_{60}H_{88}As_2Mn_6Na_4N_{12}O_{86}Ru_2W_{18}$
Formula weight ($g \cdot mol^{-1}$)	6390.11
Temperature	293(2)
Wavelength (λ/Å)	1.54184
Crystal system	monoclinic
Space group	*C*2/*c*
a (Å)	37.4781(3)
b (Å)	14.1981(2)
c (Å)	25.0181(2)
α (°)	90
β (°)	92.5050(10)
γ (°)	90
V ($Å^3$)	13299.9(2)
Z	4
ρ_{calc} (g/cm^{-3})	3.088
Crystal size	0.03 x 0.08 x 0.20
Reflections collected/unique	49012/13819
Unique observed reflections	11922
θ range (°)	2.360-76.633
F(000)	11512
Data/restraints/parameters	13819/0/852
Goodness-of-fit	1.426
R_1[a] [I>2σ(I)]	0.0833
wR_2[b]	0.2477
R_1[a] [I>2σ(I)] (all data)	0.0939
wR_2[b] (all data)	0.2363

[a] The data quality did not fulfill the criteria of the IUCR for publication.

2.7 References

[1] R. Al-Oweini, B. S. Bassil, J. Friedl, V. Kottisch, M. Ibrahim, M. Asano, B. Keita, G. Novitchi, Y. Lan, A. Powell, U. Stimming, U. Kortz, *Inorg. Chem.* **2014**, *53*, 5663–5673.

[2] R. Al-Oweini, A. Sartorel, B. S. Bassil, M. Natali, S. Berardi, F. Scandola, U. Kortz, M. Bonchio, *Angew. Chem. Int. Ed.* **2014**, *53*, 11182–11185.

[3] S. G. Mitchell, P. I. Molina, S. Khanra, H. N. Miras, A. Prescimone, G. J. T. Cooper, R. S. Winter, E. K. Brechin, D.-L. Long, R. J. Cogdell, L. Cronin, *Angew. Chem. Int. Ed.* **2011**, *50*, 9154–9157.

[4] D. Dutta, A. D. Jana, M. Debnath, G. Mostafa, R. Clérac, J. G. Tojal, M. Ali, *Eur. J. Inorg. Chem.* **2010**, *2010*, 5517–5522.

[5] Z. Li, W. Li, X. Li, F. Pei, X. Wang, H. Lei, *J. Inorg. Biochem.* **2007**, *101*, 1036–1042.

[6] J. J. Cowan, A. J. Bailey, R. A. Heintz, D. Bao T, K. I. Hardcastle, C. L. Hill, I. A. Weinstock, *Inorg. Chem.* **2001**, *40*, 6666–6675.

[7] S. G. Mitchell, S. Khanra, H. N. Miras, T. Boyd, D.-L. Long, L. Cronin, *Chem. Commun.* **2009**, 2712–2714.

[8] J. Liu, F. Ortega, P. Sethuraman, D. E. Katsoulis, C. E. Costello, M. T. Pope, *J. Chem. Soc. Dalton* **1992**, 1901–1906.

[9] P. Mialane, C. Duboc, J. Marrot, E. Rivière, A. Dolbecq, F. Sécheresse, *Chem. Eur. J.* **2006**, *12*, 1950–1959.

[10] G. Izzet, E. Ishow, J. Delaire, C. Afonso, J.-C. Tabet, A. Proust, *Inorg. Chem.* **2009**, *48*, 11865–11870.

[11] K. Patel, P. Shringarpure, A. Patel, *Transition Met. Chem.* **2011**, *36*, 171–177.

[12] C. M. Tourné, Gilbert F. Tourné, S. A. Malik, T. J. R. Weakley, *J. Inorg. Nucl. Chem.* **1970**, *32*, 3875–3890.

[13] W. Adam, M. Herold, C. L. Hill, C. R. Saha-Möller, *Eur. J. Org. Chem.* **2002**, *2002*, 941–946.

[14] K. Patel, A. Patel, *Inorg. Chim. Acta.* **2012**, *382*, 79–83.

[15] M. Bösing, B. Krebs, B. Nestler, M. Seebach, R. Gerd, M. Wohlers, U. Dingerdissen, *Appl. Catal. A.* **1999**, *184*, 273–278.

[16] U. Kortz, S. Matta, *Inorg. Chem.* **2001**, *40*, 815–817.

[17] X.-Y. Zhang, M. T. Pope, M. R. Chance, G. B. Jameson, *Polyhedron* **1995**, *14*, 1381–1392.

[18] S.-R. Ye, Y.-K. Shan, M.-Y. He, L.-Y. Dai, *Z. Kristallogr. NCS* **2002**, *217*, 451–452.

[19] J. Liu, W.-J. Mei, A.-W. Xu, C.-P. Tan, S. Shi, L.-N. Ji, *Antivir. Res.* **2004**, *62*, 65–71.

[20] X.-Y. Zhang, C. J. O'Connor, G. B. Jameson, M. T. Pope, *Inorg. Chem.* **1996**, *35*, 30–34.

[21] A. Haider, M. Ibrahim, B. S. Bassil, A. M. Carey, A. N. Viet, X. Xing, W. W. Ayass, J. F. Miñam, R. Liu, G. Zhang, B. Keita, V. Mereacre, A. K. Powell, K. Balinski, A. T. N'Diaye, K. Küpper, H.-Y. Chen, U. Stimming, U. Kortz, *Inorg. Chem.* **2016**, *55*, 2755–2764.

[22] D. K. Lyon, W. K. Miller, T. Novet, P. J. Domaille, E. Evitt, D. C. Johnson, R. G. Finke, *J. Am. Chem. Soc.* **1991**, *113*, 7209–7221.

[23] X. Fang, P. Kögerler, M. Speldrich, H. Schilder, M. Luban, *Chem. Commun.* **2012**, *48*, 1218–1220.

[24] N. Leclerc-Laronze, J. Marrot, G. Hervé, *Inorg. Chem.* **2005**, *44*, 1275–1281.
[25] K. Suzuki, R. Sato, T. Minato, M. Shinoe, K. Yamaguchi, N. Mizuno, *Dalton Trans.* **2015**, *44*, 14220–14226.
[26] B. S. Bassil, M. H. Dickman, M. Reicke, U. Kortz, B. Keita, L. Nadjo, *Dalton Trans.* **2006**, 4253–4259.
[27] N. Leclerc-Laronze, J. Marrot, G. Hervé, *CR. Chimie* **2006**, *9*, 1467–1471.
[28] C. J. Gomez-Garcia, E. Coronado, P. Gomez-Romero, N. Casan-Pastor, *Inorg. Chem.* **1993**, *32*, 3378–3381.
[29] S. Goberna-Ferrón, J. Soriano-López, J. R. Galán-Mascarós, *Inorganics* **2015**, *3*, 332.
[30] X.-Y. Zhang, G. B. Jameson, C. J. O'Connor, M. T. Pope, *Polyhedron* **1996**, *15*, 917–922.
[31] R. Neumann, A. M. Khenkin, *Chem. Commun.* **1998**, 1967–1968.
[32] P. Liu, C. Wang, C. Li, *J. Catal.* **2009**, *262*, 159–168.
[33] W. Adam, Paul L. Alsters, R. Neumann, C. R. Saha-Möller, D. Seebach, A. K. Beck, R. Zhang, *J. Org. Chem.* **2003**, *68*, 8222–8231.
[34] J. Tang, X.-L. Yang, X.-W. Zhang, M. Wang, C.-D. Wu, *Dalton Trans.* **2010**, *39*, 3396–3399.
[35] B.-D. Revital, L. Weiner, R. Neumann, *J. Am. Chem. Soc.* **2002**, *124*, 8788–8789.
[36] H. Lv, J. Song, Z. Haiming, Y. V. Geletii, J. Bacsa, Z. Chongchao, T. Lian, D. G. Musaev, C. L. Hill, *J. Catal.* **2013**, *307*, 48–54.
[37] Y. Liu, J. Dou, D. Wang, X. Zhang, D. Li, Y. Jia, *J. Chem. Crystallogr.* **2011**, *41*, 186–191.
[38] U. Kortz, N. K. Al-Kassem, M. G. Savelieff, N. A. Al Kadi, M. Sadakane, *Inorg. Chem.* **2001**, *40*, 4742–4749.
[39] B.-D. Revital, L. Weiner, R. Neumann, *J. Am. Chem. Soc.* **2002**, *124*, 8788–8789.
[40] R. Neumann, M. Gara, *J. Am. Chem. Soc.* **1994**, *116*, 5509–5510.
[41] L.-H. Bi, R.-D. Huang, J. Peng, E.-B. Wang, Y.-H. Wang, C.-W. Hu, *J. Chem. Soc. Dalton* **2001**, 121–129.
[42] C. Roşu, D. C. Crans, Timothy J.R. Weakley, *Polyhedron* **2002**, *21*, 959–962.
[43] Z. Zhang, E. Wang, W. Chen, H. Tan, *Aust. J. Chem.* **2007**, *60*, 284–290.
[44] C. Ritchie, A. Ferguson, H. Nojiri, H. N. Miras, Y.-F. Song, D.-L. Long, E. Burkholder, M. Murrie, P. Kögerler, E. K. Brechin, L. Cronin, *Angew. Chem. Int. Ed.* **2008**, *47*, 5609–5612.
[45] C. J. Gomez-Garcia, J. J. Borras-Almenar, E. Coronado, L. Ouahab, *Inorg. Chem.* **1994**, *33*, 4016–4022.
[46] R. Sharma, J. Zhang, A. C. Ohlin, *Dalton Trans.* **2015**, *44*, 19068–19071.
[47] L. Han, P.-P. Zhang, H.-S. Liu, H.-j. Pang, Y. Chen, J. Peng, *J. Clust. Sci.* **2010**, *21*, 81–91.
[48] I.-M. Mbomekallé, B. Keita, L. Nadjo, W. A. Neiwert, L. Zhang, K. I. Hardcastle, C. L. Hill, T. M. Anderson, *Eur. J. Inorg. Chem.* **2003**, *2003*, 3924–3928.
[49] I.-M. Mbomekallé, B. Keita, L. Nadjo, P. Berthet, W. A. Neiwert, C. L. Hill, M. D. Ritorto, T. M. Anderson, *Dalton Trans.* **2003**, 2646–2650.
[50] M. Lebrini, I.-M. Mbomekallé, A. Dolbecq, J. Marrot, P. Berthet, J. Ntienoue, F. Sécheresse, J. Vigneron, A. Etcheberry, *Inorg. Chem.* **2011**, *50*, 6437–6448.

[51] S.-W. Chen, K. Boubekeur, P. Gouzerh, A. Proust, *J. Mol. Struct.* **2011**, *994*, 104–108.
[52] B. S. Bassil, M. Ibrahim, S. S. Mal, A. Suchopar, R. N. Biboum, B. Keita, L. Nadjo, S. Nellutla, J. van Tol, N. S. Dalal, U. Kortz, *Inorg. Chem.* **2010**, *49*, 4949–4959.
[53] S. G. Mitchell, T. Boyd, H. N. Miras, D.-L. Long, L. Cronin, *Inorg. Chem.* **2011**, *50*, 136–143.
[54] L. David, C. Crăciun, V. Chis, R. Tetean, *Solid State Commun.* **2002**, *121*, 675–678.
[55] H. Liu, L. Xu, G. Gao, F. Li, N. Jiang, *J. Mol. Struct.* **2008**, *878*, 124–130.
[56] P. Mialane, J. Marrot, E. Rivière, J. Nebout, G. Hervé, *Inorg. Chem.* **2001**, *40*, 44–48.
[57] C. Pichon, P. Mialane, E. Rivière, G. Blain, A. Dolbecq, J. Marrot, F. Sécheresse, C. Duboc, *Inorg. Chem.* **2007**, *46*, 7710–7712.
[58] D. Drewes, M. Piepenbrink, B. Krebs, *J. Clust. Sci.* **2006**, *17*, 361–374.
[59] M. Bösing, A. Nöh, I. Loose, B. Krebs, *J. Am. Chem. Soc.* **1998**, *120*, 7252–7259.
[60] X. Sang, J. Li, L. Zhang, Z. Wang, W. Chen, Z. Zhu, Z. Su, E. Wang, *ACS Appl. Mater. Interfaces* **2014**, *6*, 7876–7884.
[61] F. Evangelisti, P.-E. Car, O. Blacque, G. R. Patzke, *Catal. Sci. Technol.* **2013**, *3*, 3117–3129.
[62] Z.-J. Wang, L.-C. Zhang, Zai-Ming Zhu, W.-L. Chen, W.-S. You, E.-B. Wang, *Inorg. Chem. Commun.* **2012**, *17*, 151–154.
[63] L. Wang, B.-B. Zhou, K. Yu, Z.-H. Su, S. Gao, L.-L. Chu, Jia-Ren Liu, Guo-Yu Yang, *Inorg. Chem.* **2013**, *52*, 5119–5127.
[64] C. Zhao, C. S. Kambara, Y. Yang, A. L. Kaledin, D. G. Musaev, T. Lian, C. L. Hill, *Inorg. Chem.* **2013**, *52*, 671–678.
[65] M. Piepenbrink, E. M. Limanski, B. Krebs, *Z. anorg. allg. Chem.* **2002**, *628*, 1187–1191.
[66] B. Artetxe, S. Reinoso, L. San Felices, P. Vitoria, A. Pache, J. Martín-Caballero, J. M. Gutiérrez-Zorrilla, *Inorg. Chem.* **2015**, *54*, 241–252.
[67] S. Reinoso, J. R. Galán-Mascarós, *Inorg. Chem.* **2010**, *49*, 377–379.
[68] L. Chen, D. Shi, J. Zhao, Y. Wang, P. Ma, J. Wang, J. Niu, *Cryst. Growth. Des.* **2011**, *11*, 1913–1923.
[69] B. S. Bassil, M. Ibrahim, R. Al-Oweini, M. Asano, Z. Wang, J. van Tol, N. S. Dalal, K.-Y. Choi, R. Ngo Biboum, B. Keita, L. Nadjo, U. Kortz, *Angew. Chem. Int. Ed.* **2011**, *50*, 5961–5964.
[70] R. E. Schreiber, H. Cohen, G. Leitus, S. G. Wolf, A. Zhou, L. J. Que, R. Neumann, *J. Am. Chem. Soc.* **2015**, *137*, 8738–8748.
[71] M. D. Ritorto, T. M. Anderson, W. A. Neiwert, C. L. Hill, *Inorg. Chem.* **2004**, *43*, 44–49.
[72] I.-M. Mbomekallé, B. Keita, M. Nierlich, U. Kortz, P. Berthet, L. Nadjo, *Inorg. Chem.* **2003**, *42*, 5143–5152.
[73] Q. Wu, Y.-G. Li, Y.-H. Wang, E.-B. Wang, Z.-M. Zhang, R. Clérac, *Inorg. Chem.* **2009**, *48*, 1606–1612.
[74] X. Fang, P. Kögerler, Y. Furukawa, M. Speldrich, M. Luban, *Angew. Chem. Int. Ed.* **2011**, *50*, 5212–5216.
[75] S. G. Mitchell, H. N. Miras, L. De-Liang, L. Cronin, *Inorg. Chim. Acta.* **2010**, *363*, 4240–4246.

[76] A. L. Nolan, R. C. Burns, G. A. Lawrance, D. C. Craig, *Acta Crystallogr. C.* **2000**, *56*, 729–730.
[77] N. Jiang, F. Li, L. Xu, Y. Li, J. Li, *Inorg. Chem. Commun.* **2010**, *13*, 372–375.
[78] Q.-J. Kong, C.-J. Zhang, Y.-G. Chen, *J. Mol. Struct.* **2010**, *964*, 82–87.
[79] S. Gao, J. Zhao, B.-B. Zhou, K. Yu, Z. Su, L. Wang, Y. Yin, Z. Zhao, Yang Yu, Ying Chen, *Inorg. Chim. Acta.* **2011**, *379*, 151–157.
[80] X. Zhang, J. Dou, D. Wang, Y. Zhang, Y. Zhou, R. Li, S. Yan, Z. Ni, J. Jiang, *Cryst. Growth. Des.* **2007**, *7*, 1699–1705.
[81] P.-E. Car, B. Spingler, S. Weyeneth, J. Patscheider, G. R. Patzke, *Polyhedron* **2013**, *52*, 151–158.
[82] H. Liu, J. Peng, J. Sha, L. Wang, L. Han, D. Chen, Yan Shen, *J. Mol. Struct.* **2009**, *923*, 153–161.
[83] W. Chen, Y. Li, Y. Wang, E. Wang, *Eur. J. Inorg. Chem.* **2007**, *2007*, 2216–2220.
[84] Z. Zhang, S. Yao, E. Wang, C. Qin, Yanfei Qi, Y. Li, R. Clérac, *J. Solid State Chem.* **2008**, *181*, 715–723.
[85] C.-L. Wang, S.-X. Liu, C.-Y. Sun, L.-H. Xie, Y.-H. Ren, D.-D. Liang, H.-Y. Cheng, *J. Mol. Struct.* **2007**, *841*, 88–95.
[86] B.-W. Chen, W.-L. Chen, Y.-G. Li, E.-B. Wang, *J. Clust. Sci.* **2011**, *22*, 73–85.
[87] J. J. Stracke, R. G. Finke, *ACS Catal.* **2014**, *4*, 909–933.
[88] T. E. Keyes, E. Gicquel, L. Guerin, R. J. Forster, V. M. Hultgren, A. M. Bond, A. G. Wedd, *Inorg. Chem.* **2003**, *42*, 7897–7905.
[89] N. Fay, V. M. Hultgren, A. G. Wedd, T. E. Keyes, R. J. Forster, D. Leane, A. M. Bond, *Dalton Trans.* **2006**, 4218–4227.
[90] P.-E. Car, M. Guttentag, K. K. Baldridge, R. Alberto, G. R. Patzke, *Green. Chem.* **2012**, *14*, 1680–1688.
[91] J. Gao, S. Cao, Q. Tay, Y. Liu, L. Yu, K. Ye, P. C. S. Mun, Y. Li, G. Rakesh, S. C. J. Loo, Z. Chen, Y. Zhao, C. Xue, Q. Zhang, *Sci. Rep.* **2013**, *3*, 1853–1858.
[92] J. Song, Z. Luo, H. Zhu, Z. Huang, T. Lian, A. L. Kaledin, D. G. Musaev, S. Lense, K. I. Hardcastle, C. L. Hill, *Inorg. Chim. Acta.* **2010**, *363*, 4381–4386.

Chapter 3

New Copper Containing Tungstobismuthates

3 New Copper Containing Tungstobismuthates

3.1 Introduction

The exceptionally versatile structural chemistry of POMs gives rise to this inexhaustible reservoir of application options. POM dimensions range from low nuclearity to nanoscale clusters,[1] and single polyanions can be connected into 1D, 2D and even 3D networks.[2] Two classes of multidimensional structures can be distinguished through the different bridging modes between polyanion monomers: They can either be connected via organic linkers,[3–5] or through $1^{st}/2^{nd}$ row d-block or f-block transition metal ions, giving rise to extended, all-inorganic networks.[6]

$[\{(A(H_2O)_3)_2(B(H_2O)_2)_2\}(B\text{-}\beta\text{-}XW_9O_{33})_2]^{n-}$ polyanions with B-β type lacunary tungsten-oxygen frameworks are generally known as Krebs-type POMs. The two distinct positions A and B in the transition metal core can be occupied by transition metal or tungsten atoms. Prominent representatives with lower nuclearities are synthesized from lacunary precursors $[B\text{-}\alpha\text{-}XW_9O_{33}]^{9-}$ (X = As[7], Sb[8], Bi[9,10]). However, two different sandwich types can emerge from their reaction with 1^{st} and 2^{nd} row d-block metals, namely either $[M_3(H_2O)_3(B\text{-}\alpha\text{-}XW_9O_{33})_2]^{n-}$ or $[M_2(H_2O)_4(B\text{-}\beta\text{-}XW_{10}O_{35})_2]^{n-}$ (M = Mn, Co, Fe; X = Bi, Sb, As) after α-β isomerization. This well-known process provides access to a broad spectrum of polyoxotungstates.[8] α-β isomerization of the Krebs-type precursor $[B\text{-}\alpha\text{-}XW_9O_{33}]^{9-}$ is often accompanied by the incorporation of 2-4 additional $\{WO_6\}$ octahedra into the transition metal belt.[11–14] This frequently gives rise to mixtures of isostructural polyanions.

Our studies on active cobalt tungstobismuthates WOCs[11] in combination with recent reports on Cu-based WOCs[15,16] clearly suggest that Cu-substituted tungstobismuthates are new and attractive targets for structural and catalytic studies. Tetranuclear POMs such as $[\{Mn^{III}_3Mn^{IV}O_3(OAc)_3\}(A\text{-}\alpha\text{-}SiW_9O_{34})]^{6-}$,[17] $[Ru_4(\mu\text{-}O)_4(\mu\text{-}OH)_2(H_2O)_4(\gamma\text{-}SiW_{10}O_{36})_2]^{10-}$,[18,19] or $[Co_4(H_2O)_2(XW_9O_{34})_2]^{10-}$ (X = V[20], P[21]) have been in the focus of artificial photosynthesis research ever since their breakthrough discovery as all-inorganic WOCs. Previous reports on the reaction of the lacunary precursor $[B\text{-}\alpha\text{-}BiW_9O_{33}]^{9-}$ with Cu(II), however, pointed to their complex structure-synthesis relationships with a tendency towards the formation of bridged structures (Table S3.1), which leaves plenty of room for further explorations.

We report here on six new Cu-containing POMs covering a wide dimensionality spectrum from 0D to 3D structures. Special emphasis was placed on the 3D network 3D-$K_{6.89}Cu_{0.43}H_{0.93}[(Cu_3(H_2O)_2Cl)(K_{2.68}Cu_{0.32}(H_2O)_3(\alpha\text{-A-}BiW_9O_{33})_2]\cdot 13H_2O$ (**Cu-5**), which was characterized with a combined approach of crystallographic and spectroscopic methods. Furthermore, the magnetic properties of **Cu-5** were evaluated along with its catalytic performance in visible-light driven H_2 and O_2 evolution.

3.2 Results and Discussion

3.2.1 Overview of the Cu-POM family: Synthetic Strategy and Product Spectrum.

As $[Cu_4(H_2O)_{10}(B\text{-}\beta\text{-}BiW_9O_{33})_2]^{10-}$ with a Cu_4 core would combine the favorable WOC properties of tetranuclear POMs [17,22] with emerging trends on Cu-WOCs,[23,16,24,15] it was selected as the initial synthetic target. Mild room temperature reaction conditions were applied to avoid the formation of products with Cu/W disorder and the decomposition of $Na_9[B\text{-}\alpha\text{-}BiW_9O_{33}]\cdot 19.5H_2O$ (BiW_9). The reaction of BiW_9 with Cu(II) sources was conducted in water at pH 7. Crystals were obtained after addition of different alkali metal cations. Crystal structure analyses revealed the presence of three different structural types, i.e. partial decomposition of **BiW_9** could not be circumvented through careful adjustment of the reaction conditions.

Six new POM types could be structurally characterized (**Cu-1 – Cu-6**, **Figure 3.1**). Phase pure **Cu-5** was obtained in sufficient quantities for analytical and catalytic characterizations (cf. matching PXRD pattern in Figure S3.8), whereas crystals of **Cu-1 – Cu-4** and **Cu-6** are very sensitive to the evaporation of crystal water molecules and physical stress. Consequently, the corresponding batches could not be structurally identified with proper PXRD patterns.

However, this criterion remains crucial as is evident for the isolation of **Cu-2**, **Cu-3** and **Cu-4** from the same reaction mixture. Whereas both of the 2D architectures $Na_7K_3Cu_{0.5}Cl[Cu_2(H_2O)_4(B\text{-}\beta\text{-}BiW_{10}O_{35})_2]$ (**Cu-2)** and $Na_{5.5}K_{2.5}Cu[Cu_2(H_2O)_4(B\text{-}\beta\text{-}BiW_{10}O_{35})_2]$ (**Cu-3**) are formed in the presence of KCl, addition of RbCl leads to the formation of 0D $Na_6Rb_6[Cu_3(H_2O)_3(B\text{-}\alpha\text{-}BiW_9O_{33})_2]$ (**Cu-4)**. These different reaction pathways underscore the decisive role of counter-cations in POM crystallization. Whereas the structural motifs of **Cu-2** and **Cu-3** were obtained from single crystal analyses, attempts to quantify their respective amounts in the as-synthesized mixture by Rietveld analysis failed

due to its amorphous character. Apparently minor variations of the reaction conditions furthermore pave the way to the 0D polyanions. $Na_{12}[Cu_2(H_2O)_4\mathbf{Cl_2}(B\text{-}\beta\text{-}BiW_{10}O_{35})_2]$ (**Cu-1a**) and $Na_{10}[Cu_2(H_2O)_6(B\text{-}\beta\text{-}BiW_{10}O_{35})_2]$ (**Cu-1b**), which crystallize in the same unit cell without bridging Cu(II) cations so that they can be considered as independent polyanions. In contrast to previous reports on Mn[14,11,25] or Co[13,11,26] containing tungstobismutates, neither 0D POM showed Cu/W disorder, i.e. the inner positions of the transition metal belt are 100% occupied by W, and the two external positions are solely occupied by Cu(II). Noteworthy, partial decomposition of the lacunary precursor could not even be avoided under mild reaction conditions. Only **Cu-4** and **Cu-5** still display the $[B\text{-}\alpha\text{-}BiW_9O_{33}]^{9-}$ building block in combination with a $Cu_3(H_2O)_3$ core. While the space between the Cu(II) centers of the polyanions in **Cu-4** is occupied by Rb^+ cations, they are crosslinked into a 3D network in $3D\text{-}K_{6.89}Cu_{0.43}H_{0.93}[(Cu_3(H_2O)_2Cl)(K_{2.68}Cu_{0.32}(H_2O)_3(B\text{-}\alpha\text{-}BiW_9O_{33})_2]\cdot 13\ H_2O$ (**Cu-5)**. Other than on the **Cu-1** POMs, the transition metal belt of this structure displays extensive Cu/K disorder. Finally, a third structural type (**Cu-6**) emerged from completely decomposed precursor material which reassembles to the Bi-free $[H_2W_{12}O_{42}]^{10-}$ polyanion known as paratungstate B.[27,28] This corresponds with the ability of paratungstate B to form 1D-chains upon crystallization in the presence of d block transition metal ions (Table S3.1).

All in all, the new Cu-containing POMs **Cu-1** – **Cu-6** can be classified by their degree of precursor transformation. While $[B\text{-}\alpha\text{-}BiW_9O_{33}]^{9-}$ is fully retained in **Cu-4** and **Cu-5**, gradual α-β isomerization and decomposition generates the free tungsten atoms required for the building block $\{B\text{-}\beta\text{-}BiW_{10}O_{37}\}$ on which **Cu-1** – **Cu-3** are based. Without a source of tungsten cations, the formation of the polyanion fragment $\{B\text{-}\beta\text{-}BiW_{10}O_{37}\}$ is impossible and the structures **Cu-1** – **Cu-3** would not occur (Figure S3.1). None of the precursor features are maintained in paratungstate B-based **Cu-6**. Related transformations have been reported for $[A\text{-}\alpha\text{-}SiW_9O_{33}]^{9-}$[29,2] as a source for POMs with higher tungsten nuclearities.

Consequently, isolation of the initial target structure $[Cu_4(H_2O)_{10}(B\text{-}\beta\text{-}BiW_9O_{33})_2]^{10-}$ with an all-copper Cu_4 core would require the possibility of in situ addition of Cu(II) cations immediately after α–β isomerization, i.e. before any partial decomposition of $[B\text{-}\alpha\text{-}BiW_9O_{33}]^{9-}$.

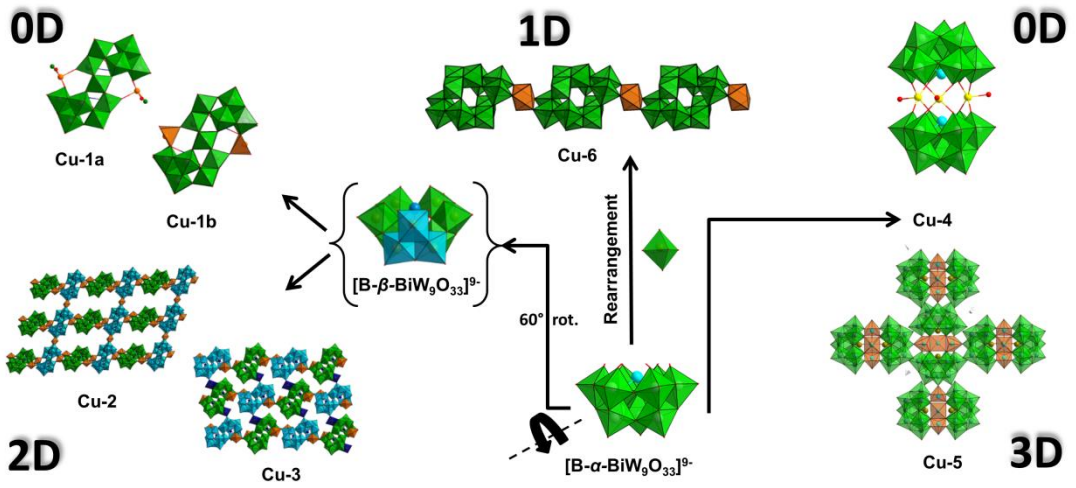

Figure 3.1. Survey of structural motifs emerging from the reaction of $[B\text{-}\alpha\text{-}BiW_9O_{33}]^{9-}$ with Cu(II) cations.

Generally, selective access to target POMs requires control over the precursor speciation, such as the isomerization and decomposition processes of **BiW_9** in the present case. However, precise quantification of the polyanionic species in solution remains a challenge in POM synthesis, giving rise to products with entirely different motifs than in the initial precursor. The main precursor species may remain in solution and might only be trapped in a narrow parameter window, such as for the particular $[B\text{-}\alpha\text{-}BiW_9O_{33}]^{9-}$ containing products **Cu-4** and **Cu-5** above.

Here, the hypothetical building block $\{B\text{-}\beta\text{-}BiW_{10}O_{37}\}$ of **Cu-1**, **Cu-2** and **Cu-3** can be interpreted as $\{B\text{-}\beta\text{-}BiW_9O_{33}\}$ with an incorporated tungsten center after partial decomposition of the $[B\text{-}\alpha\text{-}BiW_9O_{33}]^{9-}$ starting material. The high proportion of *β* type products obtained in this work clearly illustrates that *α*–*β* isomerization and tungsten uptake of the $[B\text{-}\alpha\text{-}BiW_9O_{33}]^{9-}$ occurs easily, even under non-acidic conditions at room temperature (Figure 3.1). However, to the best of our knowledge, neither $\{B\text{-}\beta\text{-}BiW_{10}O_{35}\}$ nor $\{B\text{-}\beta\text{-}BiW_9O_{33}\}$ have been isolated to date as lacunary precursors. Lastly, the Bi free compound **Cu-6** demonstrates the notable extent of complete **BiW_9** decomposition under mild conditions.

3.2.2 Structural Prerequisites for New Cu-POMs.

In addition to the above precursor speciation issues, the extraordinary structural diversity of copper-substituted tungstobismutates is also linked to the pronounced Jahn-Teller distortion effects of the Cu(II) centers. Most frequently, their axial L-Cu-L bonds are elongated in octahedral coordination environments.[30] This adds configurational flexibility to the Cu(II) centers with respect to connecting different polyanions whilst minimizing steric hindrance. The present structure family illustrates how this combination of precursor isomerization with versatile linker cations provides a rich source of structural motifs: **Cu-2** and **Cu-3** form their basic 1D chains through such elongated Cu–O(–W) bonds, whereas additional Cu(II) centers between these chains sustain the overall 2D networks of both POMs. The $[H_2W_{12}O_{42}]^{12-}$ polyanion in **Cu-6** displays a related bridging mode with 4 terminal oxygen atoms and 2 water ligands in its coordination sphere resulting in a distorted octahedral coordination environment. The water ligands are found in the equatorial positions. In contrast, the Cu(II) cations bridging the 3D network in **Cu-5** exhibit a square pyramidal coordination environment with the apical oxygen atoms belonging to adjacent monomers.

As illustrated above, the counter-cations are a third key parameter which can generate structural variations. However, their precise assignment during POM structure refinement processes often becomes challenging, especially for cations such as Na^+, NH_4^+ or Mg^{2+} which are quasi-isoelectronic with water and thus cannot be unambiguously assigned through their electron density or atomic displacement parameters.[31] Therefore, such atom types in the present study were assigned through careful consideration of Na–O, K–O or Cu–O and other bond lengths, as well as of their respective coordination environments in comparison with published structures. Nevertheless, the combination of notable crystallographic disorder with partial occupancy of countercation and water positions is frequently encountered in POM chemistry[32] and does not always permit their ultimate assignment. In the following, the structures of the newly obtained Cu-POMs are discussed in more detail.

3.2.2.1 Group 1: Krebs-Type Cu-POMs with $W_2O_4Cu_2(H_2O)_n$ Cores.

The connection of two {B-β-$BiW_{10}O_{35}$} fragments via two Cu(II) cations generates $[Cu_2(H_2O)_n(B\text{-}\beta\text{-}BiW_{10}O_{35})_2]^{n-}$ building blocks which constitute the POMs **Cu-1**, **Cu-2** and **Cu-3**. As mentioned above, this hypothetical lacunary tungstate precursor {B-β-$BiW_{10}O_{35}$} has not been isolated to date. All of these copper-substituted Krebs-type POMs with a $W_2O_4Cu_2(H_2O)_n$ core have an isostructural tungsten-oxygen framework in common. It is reasonable to assume that the Cu(II)/**BiW_9** ratio determines the final coordination

environment of the Cu(II) centers in the $[Cu_2(H_2O)_xCl_y(B\text{-}\beta\text{-}BiW_{10}O_{35})_2]^{10-}$ monomer, i.e. the formation of 0D or 2D motifs. **Cu-1** consists of two 0D polyanions, which co-crystallize in the same triclinic unit cell ($P\bar{1}$) in the presence of Na^+ counter-cations. Both polyanions are formed from two lacunary tungsten ligands $[B\text{-}\beta\text{-}BiW_9O_{33}]^{9-}$ which are connected by two W(VI) and two Cu(II) cations constituting the $\{W_2Cu_2\}$ transition metal core. The main structural difference between these two sandwich type POMs $[Cu_2(H_2O)_4Cl_2(B\text{-}\beta\text{-}BiW_{10}O_{35})_2]^{12-}$ (**Cu-1a**) and $[Cu_2(H_2O)_6(B\text{-}\beta\text{-}BiW_{10}O_{35})_2]^{10-}$ (**Cu-1b**) is the substitution of two water ligands which coordinate to the Cu-center of **Cu-1a** with two chloride anions in **Cu-1b**.

In line with the above hypothesis, 2D structures are obtained in the presence of excess Cu(II), namely **Cu-2** and **Cu-3** which also crystallize in the space group $P\bar{1}$. The asymmetric unit contains two halves of the $[Cu_2(H_2O)_4(B\text{-}\beta\text{-}BiW_{10}O_{35})_2]^{10-}$ monomer, which are completed into two entire polyanions through inversion symmetry. The two identical polyanion monomers display different geometrical orientations upon their connection into an 1D chain. These monomers are distinguished as monomers A (green) and B (blue), respectively (Figure 3.2). They are connected via two Cu–O(–W) bonds with the copper atom of the transition metal belt coordinating to the terminal oxygen atoms of the next polyanion.

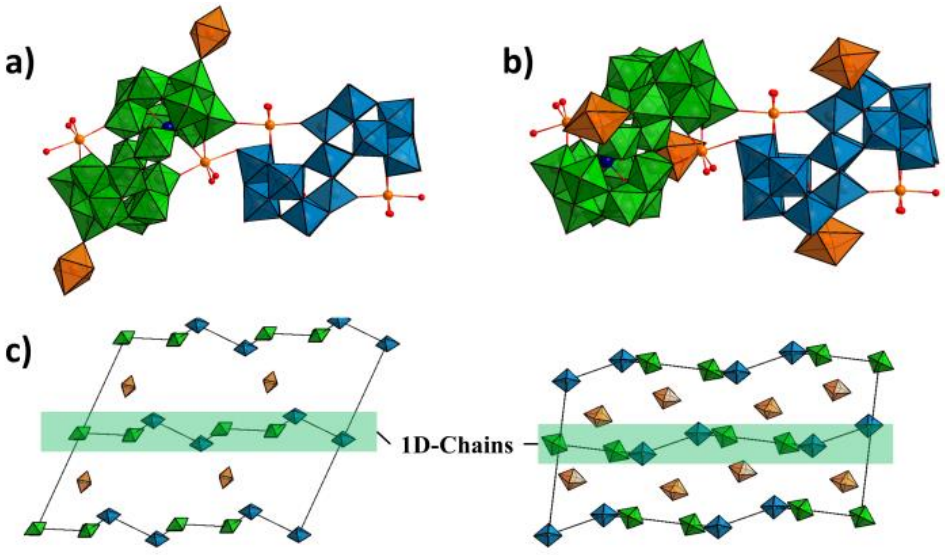

Figure 3.2. (top) Polyhedral ball-and stick representations of the repeating units of (a) **Cu-2** and (b) **Cu-3**: monomer A = green, monomer B = blue, chain-bridging CuO_6 octahedra = orange. **(c)** 2D-arrangement of Cu(II) cations (chain bridging CuO_6 octahedra = orange, monomeric CuO_6 = purple).

The B monomer is inclined and rotated relative to the A monomer. Interestingly, both forms crystallize in a different 2D network in the presence of excess Cu(II) cations, which bridge the 1D chains by coordinating to different terminal oxygen atoms of their repeating units. Chain bridging occurs via one Cu(II) cation in **Cu-2**, and via two centers in **Cu-3**. The different 2D networks result from bridging via terminal oxygen atoms of different tungsten atoms of the repeating unit in **Cu-2** and **Cu-3** (Figure 3.2). In both POM types, bridging to a 1D-chain occurs along the elongated O_{ter}–Cu–O_{ter} axis, which permits maximum distances between two monomers. Chain bridging Cu(II) atoms are expected to display the same trend by maximizing the interchain distance, such as the respective Cu(II) ion in **Cu-2**. Here, the elongation occurs along the O_{ter}-Cu–O_{ter} axis, whereas the chain-bridging in **Cu-3** is not located along the elongated axis. The resulting rotation of both polyanions with respect to each other may maximize the overall distance of the $[Cu_2(H_2O)_4(B\text{-}\beta\text{-}BiW_{10}O_{35})_2]^{10-}$ polyanions.

The overall distribution of Cu(II) cations in the 2D-networks of **Cu-2** and **Cu-3** is shown in Figure 3.2. The distance between the bridging Cu(II) ion and the Cu(II) ions of the polyanion range from 8.4217(1) Å to 10.6525(2) Å, while the Cu···Cu distances between the copper atoms located within the monomers units of **Cu-1**, **Cu-2** and **Cu-3** are between 10.0269(1) Å and 10.276(3) Å.

3.2.2.2 Group 2: POMs with a $Cu_3(H_2O)_3$ Core

The $\{B\text{-}\beta\text{-}XW_9O_{33}\}^{9-}$ subunit and the $[B\text{-}\alpha\text{-}XW_9O_{33}]^{9-}$ (X = Sb, As, Bi) precursor differ with respect to their coordination to Cu(II) cations.[33,34] POMs of the general type $[(Cu_3(H_2O)_3(M(H_2O)_2)_y(B\text{-}\alpha\text{-}BiW_9O_{33})_2]^{12-}$ (M = K, Rb, Cu) have been isolated herein as 0D and 3D structures. The structural formula of the 0D structure $Na_9Rb_3[(Cu_3(H_2O)_3(B\text{-}\alpha\text{-}BiW_9O_{33})_2]\ 20{\cdot}H_2O$ may alternatively be written as $Na_9[(Cu_3(H_2O)_3(Rb(H_2O)_2)_3(B\text{-}\beta\text{-}BiW_9O_{33})_2]{\cdot}20H_2O$. This takes into account that the voids between Cu(II) are filled with Rb^+ cations, which may be considered as part of the polyanion. **Cu-4** crystallizes in the monoclinic space group $P2_1/m$. While the synthesis and crystal structures of sodium salts of related polyanions have been reported earlier (Table S1), we present here the crystal structure of the mixed Na^+/Rb^+ salt. The two subunits $[B\text{-}\alpha\text{-}XW_9O_{33}]^{9-}$ are linked by three Cu(II) cations which form the transition metal belt. Cu(1) and Cu(2) are found in square pyramidal coordination environments with the apical positions occupied by a water ligand. The voids between the triangular Cu atoms are occupied by a Rb triad rotated by 60°.

A slight alteration of the reaction conditions leads to the formation of a 3D network. Detailed crystal structure analysis shows disorder for almost all of its counter cations and crystal water molecules (cf. description in the SI).

Disordered cations and crystal water molecules lead to similar residual electron density peaks. Thus, a certain ambiguity remains for the correct atom assignment and occupancy of such residual electron density peaks and their occupancy, giving rise to slightly different refinement options concerning counter-cations and crystal water molecules. The herein presented structural models have been completed so they agree with IR-Spectroscopy and elemental analysis data.

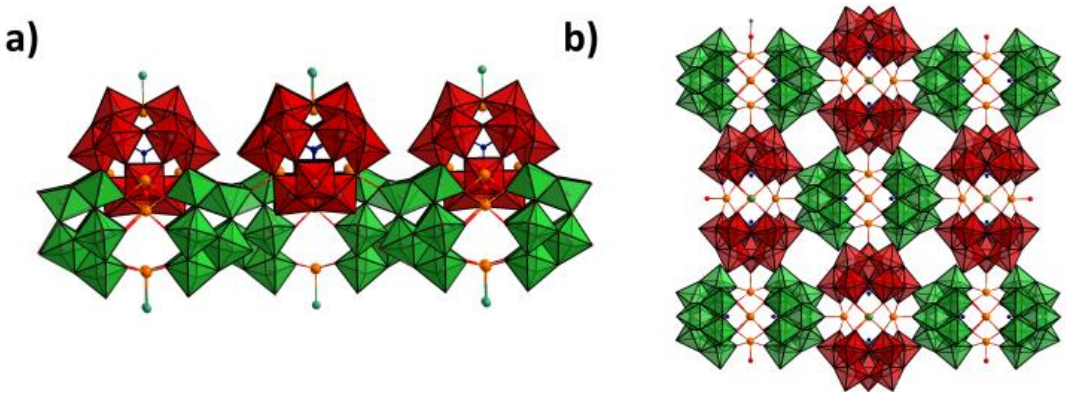

Figure 3.3. Polyhedral ball-and stick representation of **Cu-5**, side view (a), top view (b).

Cu-5 crystallizes in the tetragonal space group $P\bar{4}2_1m$. Structure refinement at the most detailed level possible reveals the presence of the 3D network 3D-$K_{6.89}Cu_{0.43}H_{0.93}[(Cu_3(H_2O)_2Cl)(K_{2.68}Cu_{0.32}(H_2O)_3(B\text{-}\alpha\text{-}BiW_9O_{33})_2]\cdot 13\ H_2O$ (**Cu-5)** based on the $[(Cu_3(H_2O)_3(B\text{-}\alpha\text{-}BiW_9O_{33})_2]^{9-}$ monomer. In **Cu-5**, the monomers crystallize into interconnected layers with alternating orientations of the polyanions within each layer. Monomers in layer A (green) are rotated by 90° relative to the monomers in layer B (red) (Figure 3.3), and they are bridged via the terminal oxygen atom of W(2) to Cu(1). This terminal oxygen atom is located in the apical position of the square-pyramidal coordination sphere Cu(1).

The polyanion of **Cu-5** is isostructural to that of **Cu-4**, with differences in the occupation of the cavity of the transition metal belt. The transition metal belt of **Cu-5** is formed by three Cu(II) ions, which connect the two **BiW_9** subunits in an analogous manner to **Cu-4.** As the transition metal belt of **Cu-5** shows a large extent of disorder, a certain ambiguity remains even after careful structure analysis (Supporting Information §3.3.4.2). We suggest that the

3D structure is formed from different polyanions, containing 3-5 Cu(II) atoms in the transition metal belt. Provided that the substitution of a 5th Cu(II) cation is stochastically independent of the preceding 4th cation and the substitution of a 6th Cu, the statistical probability of isolating the respective polyanions with different cores can be calculated as follows: 2.56 % of the monomers are $[Cu_5(H_2O)_4Cl(B\text{-}\alpha\text{-}BiW_9O_{33})_2]^{9-}$ and 16 % represent $[Cu_4(H_2O)_3ClK(H_2O)(B\text{-}\alpha\text{-}BiW_9O_{33})_2]^{10-}$ (Figure 3.4), compared to a rather small probability of 0.7% for the polyanion $[Cu_6(H_2O)_5Cl(B\text{-}\alpha\text{-}BiW_9O_{33})_2]^{7-}$. Whether this assumption is justified was further investigated by HR-ESI MS. Mass spectra, which were recorded from a phase pure sample of **Cu-5** show large numbers of different peaks, which cannot be assigned unambiguously due to the formation of K^+ and Na^+ adducts and the wide diversity of possible core compositions (Figure S3.9). Polyanions with a Cu_5 or Cu_6 core are indeed far less likely to be formed. Related network structures have been reported for the antimony containing analogue 3D-$[Cu_3(H_2O)_x(B\text{-}\beta\text{-}SbW_9O_{33})_2]^{12-}$ or for 3D-$[Cu_4K_2(H_2O)_8(B\text{-}\beta\text{-}AsW_9O_{33})_2]^{8-}$.[35,36]

3.2.2.3 Structure Analysis of 1D-Cu$[H_2W_{12}O_{42}]^{10-}$

(Cu-6). The Na^+/K^+ salt of **Cu-6** crystallizes in the monoclinic space group $P2_1/n$. Its 1D-chain is based on the paratungstate B anion $[H_2W_{12}O_{40}]^{10-}$ (cf. Table S3.1 for previous studies). Decomposition of the lacunary precursor $[BiW_9O_{33}]^{9-}$ and reassembly into Bi-free paratungstate B $[H_2W_{12}O_{42}]^{12-}$ has been reported earlier, and similar 1D structures could be isolated and characterized.[37,38] Charge balance is achieved by taking into account two hydrogen atoms coordinating to the oxygen atom O(15). The presence of these protons was confirmed previously by neutron diffraction studies.[39] Isolation of **Cu-6** strongly suggests that the $[BiW_9O_{33}]^{9-}$ precursor is not stable under the given mild reaction conditions, thus giving rise to a complex reaction system.

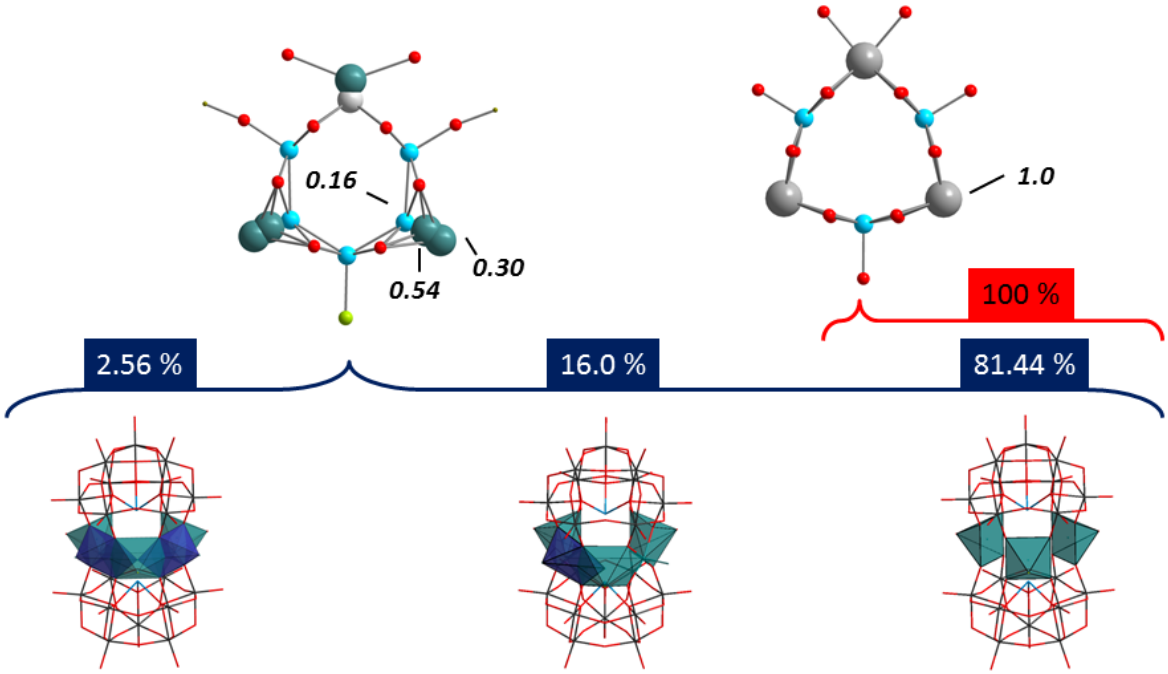

Figure 3.4. Top: Schematic representation of the transition metal belt of **Cu-4 (**top right**)** and **Cu-5 (**top left**) (**Rb = grey, Cu = blue, O = red, K = green). Bottom: Polyhedral ball-and stick representation of all three possible polyanion monomers and the probability of their occurrence (fully occupied Cu atoms = green polyhedra, partially occupied Cu positions = blue polyhedra).

3.2.3 Analytical and Photocatalytic Characterization of Cu-5.

The distinct star-like shape of the crystals of **Cu-5** allows visual discrimination from other morphologies observed for **Cu-1-Cu4** and **Cu-6** (Figure S3.4).

Spectroscopic analyses. The FT-IR spectrum of **Cu-5** (Figure 3.5) shows peaks at positions related to those of the [B-α-BiW_9O_{33}]$^{9-}$ starting material. This is a strong indication that the α-isomer is maintained in the structure of **Cu-5**. However, the comparison of the FT-IR spectrum of the starting material **BiW_9** with the spectrum of the product shows a significant shift of the peaks at 935 cm^{-1} and 692 cm^{-1} indicating that the functionalization of the starting material with Cu(II) was successful (Figure 3.5). In previous studies, FT-IR bands have been assigned for Keggin-type polyanions of the type [α/β-$XW_{12}O_{40}$] (X = B, Si, Ge, P, As) without transition metal substitution. Only after a detailed normal mode analysis,[40] and careful consideration of cation-polyanion[41] and polyanion-polyanion[42] interactions. As the structure of **Cu-5** is fundamentally different from single Keggin-POMs and consists of an

overlap of different polyanions due to disorder, assignment of W–O vibrations based on the earlier findings may not be sufficiently accurate.

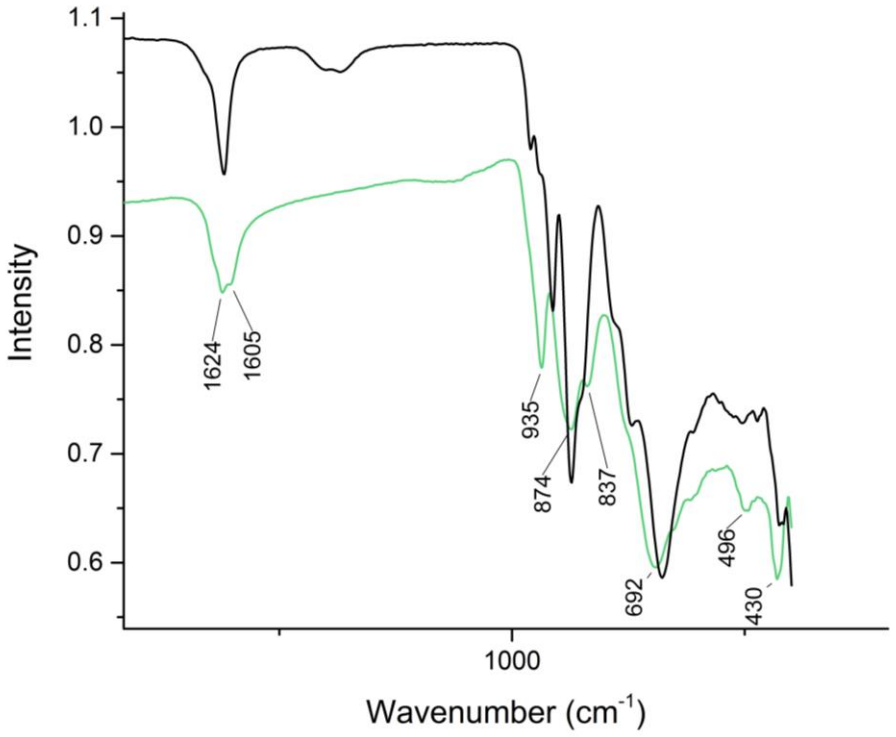

Figure 3.5. FT-IR spectrum of **Cu-5** (green) and the starting material $Na_9[B\text{-}\alpha\text{-}BiW_9O_{33}]\cdot 19.5H_2O$ (black).

Likewise, precise analysis of polyoxometalates with disordered transition metal cores by X-ray diffraction techniques remains challenging, i.e. the average structural model obtained from the structure refinement lacks information on the local structure. High resolution mass spectroscopy provides a direct option to discriminate between polyanions of different weights, so that a phase pure sample of **Cu-5** was selected for HR ESI-MS analysis (Supporting Information §3.3.7). Given the extensive crystallographic K/Cu disorder in the transition metal belt, **Cu-5** crystals may contain up to six structurally different polyanions, i.e. $[Cu_3(H_2O)_2ClCu_xK_{2-x}(H_2O)_2]$ (x = 0-2 (or 3)) with 3-6 Cu ions in the transition metal belt and the corresponding number of K^+ cations. Masses in the 5044.52 – 5234.45 u are expected, depending on the number of K and Na adducts. However, the observed broad peak distribution did not allow for an unambiguous identification of the rather weak signals of the individual polyanions (Figure S3.9).

3.2.4 Magnetic Measurements

The magnetic properties of 0D and 3D Cu substituted networks based on $[B\text{-}\alpha\text{-}XW_9O_{33}]^{n-}$ (X = Sb, As, Te, Se) keep attracting interest.[36,43] The temperature dependent molar magnetic susceptibility of a phase pure sample of **Cu-5** (14.5 mg) was measured at 500 Oe in the temperature range between 2 and 200K (Figure S3.6). Attempts to fit the data with a Curie-Weiss fit have shown large deviations at low temperatures. The data was fitted with a model that was previously applied on the magnetic behavior of a structurally related copper-based arsenotungstate $Na_9[Cu_3Na_3(H_2O)_9(B\text{-}\alpha\text{-}AsW_9O_{33})_2]$. The best last square fit is achieved with the spin-exchange factor J = -1.19228264 cm^{-1}, giving a Curie temperature θ = 0.17577707 K which is consistent with g = 2.67.

3.2.5 Conclusion

A series of new Cu-functionalized tungstobismutates was obtained from the lacunary precursor $[\alpha\text{-}BiW_9O_{34}]^{9-}$. Despite the mild reaction conditions, *α-β* isomerization and partial decomposition of the lacunary precursor afforded a variety of different Cu-containing POM motifs. The sandwich-type POMs **Cu-4** and **Cu-5** are based on the $[B\text{-}\alpha\text{-}BiW_9O_{33}]^{9-}$ subunit with a $Cu_3(H_2O)_3$ transition metal core. Single $[(Cu_3(H_2O)_3(B\text{-}\alpha\text{-}BiW_9O_{33})_2]^{12-}$ monomers are crosslinked into the 3D network of **Cu-5**. The sandwich-type POMs **Cu-1**, **Cu-2**, and **Cu-3** are based on the hypothetical $\{B\text{-}\beta\text{-}BiW_9O_{33}\}^{9-}$ precursor with $W_2O_4Cu_2(H_2O)_{6-x}Cl_x$ (x = 2 for **Cu-1**, 0 for **Cu-2** and **Cu-3**) cores. 2D structures (**Cu-2** and **Cu-3**) with a restructured building block emerge from cross-linking of 1D-$[Cu_2(H_2O)_4(B\text{-}\beta\text{-}BiW_{10}O_{35})_2]^{10-}$ chains with additional Cu(II) ions**.** Complete reassembly and bismuth loss of the lacunary precursor $[B\text{-}\alpha\text{-}BiW_9O_{33}]^{9-}$ results in the formation of paratungstate polyanions which are bridged by Cu(II) to give chains of 1D-$Na_4K_4Cu[H_2W_{12}O_{42}]$ (**Cu-6)**. The 3D-network of **Cu-5** was isolated in phase pure form for further spectroscopic and catalytic investigations. Careful refinement of the observed crystallographic disorder in the transition metal belt of **Cu-5** indicates that the polyanions $[Cu_5(H_2O)_4Cl(B\text{-}\alpha\text{-}BiW_9O_{33})_2]^{9-}$ and $[Cu_4(H_2O)_3ClK(H_2O)(B\text{-}\alpha\text{-}BiW_9O_{33})_2]^{10-}$ are in principle accessible. However, the direct synthesis of $[Cu_4(H_2O)_{10}(B\text{-}\beta\text{-}BiW_9O_{33})_2]^{10-}$ as an interesting Cu-analogue of POM-based water oxidation catalysts via the Cu(II)/$\{BiW_9O_{34}\}^{9-}$ species remained unachievable.

The properties of **Cu-5** as a catalyst for artificial photosynthesis, were investigated in detail with established photochemical assays. While no activity for O_2 evolution was observed, H_2 was formed upon irradiation. However, the precursor $[BiW_9O_{34}]^{9-}$ alone produces larger H_2

quantities, i.e. Cu-functionalization had no beneficial effect on photocatalytic water reduction under the given conditions.

All in all, the targeted access to Cu-containing tungstobismutates as potential catalysts for artificial photosynthesis from lacunary $[BiW_9O_{34}]^{9-}$ and copper sources posts major speciation challenges, namely control over α-β isomerization and restructuring of the $[B\text{-}\alpha\text{-}BiW_9O_{33}]^{9-}$ precursor in the presence of Cu(II) ions with strong Jahn-Teller effects. However, the precursor/copper ratio and the choice of counter-cations emerged as control parameters to access three specific Cu-POM types. Our investigations thus provide an interesting starting point for new strategies to achieve long sought-after predictable pathways to tailored and economic POM catalysts.

3.3 Appendix

3.3.1 Literature Survey

Table S3.1. Reported Cu substituted tungstobismuthates prepared from the $[BiW_9O_{33}]^{9-}$ precursor.

Polyoxometalate	Main structural motif	Ref.
$[Cu_3(H_2O)_3(\alpha\text{-}XW_9O_{33})_2]^{n-}$ (X = As, Sb, Se, Te, n = 10 for Te and Se, 12 for Sb, As)	$Cu_3(H_2O)_3O_3$	[34]
$Na_{12}[Cu_3(H_2O)_3(BiW_9O_{33})_2]\cdot 47H_2O$	$Cu_3(H_2O)_3O_3$	[44]
$Na_{12}[Cu_3(H_2O)_3(BiW_9O_{33})_2]$	$Cu_3(H_2O)_3O_3$[45]	[46]
$Na_{12}[Cu_3(H_2O)_3(BiW_9O_{33})_2]\cdot 29H_2O$	$Cu_3(H_2O)_3O_3$	[47]
2D-$Na_5(TEOA\text{-}H)_4[(Cu(H_2O))_3(BiW_9O_{33})_2]$	$Cu_3(H_2O)_3O_3$	[45]
$Na_{12}[\{Cu(H_2O)_2\}_3(BiW_9O_{33})_2]\cdot 42H_2O$	$Cu_3(H_2O)_3O_3$	[48]
2D-$[enH_2]_5[Cu^{II}(en)_2][Cu^{I}{}_2(WO_2)_2(\beta\text{-}SbW_9O_{33})_2]\cdot 16H_2O$	$Cu_2(H_2O)_2W_2O_4$	[45]
2D-$[enH_2]_5[Cu^{II}(en)_2][Cu^{I}{}_2(WO_2)_2(\beta\text{-}BiW_9O_{33})_2]\cdot 22H_2O$	$Cu_2(H_2O)_2W_2O_4$	[45]
$Na_{10}[Cu_4(H_2O)_2(BiW_9O_{33})_2]\cdot 43H_2O$	$Cu_2(H_2O)_2W_2O_4$	[47]
$Na_8[Bi_2W_{20}Cu_2O_{68}(OH)_2(H_2O)_6]\cdot 26H_2O$	$Cu_2(H_2O)_2W_2O_4$	[47]
$Na_6H_4[Bi_2Cu_2W_{20}O_{70}(H_2O)_6]\ 36H_2O$	$Cu_2(H_2O)_2W_2O_4$	[49]
$KNa_3[Cu(H_2O)_2\{Cu(H_2O)_3\}_2(H_2W_{12}O_{42})]\cdot 16H_2O$	$W_{12}O_{42}\text{-}M_x$	[50]
$\{Cu(H_2O)_4\}_2\{Cu_2(\mu\text{-}OH)_2(H_2O)_6\}(H_2W_{12}O_{42})]\cdot 10H_2O$	$W_{12}O_{42}\text{-}M_x$	[38]
$(NH_4)_8[Cu(H_2O)_2H_2W_{12}O_{42}]\cdot 10H_2O$	$W_{12}O_{42}\text{-}M_x$	[51]
$Na_8[Cu(H_2O)_2(H_2W_{12}O_{42})]\cdot 30H_2O$	$W_{12}O_{42}\text{-}M_x$	[52]
3D-$[Cu(H_2O)_6][\{Cu(H_2O)_2\}_2\{Cu(H_2O)_4H_4W_{12}O_{42}\}]\cdot 12H_2O$	$W_{12}O_{42}\text{-}M_x$	[53]
1D-$[Na_2(H_2O)_8][Na_8(H_2O)_{20}][Cu(en)_2][W_{12}O_{42}]\cdot 3H_2O$	$W_{12}O_{42}\text{-}M_x$	[37]
$Na_2Cu_3(CuOH)[W_{12}O_{40}(OH)_2]\cdot 32H_2O$	$W_{12}O_{42}\text{-}M_x$	[54]
$Na_{12}[(Na(H_2O)_2)_6(BiW_9O_{33})_2]$	Various	[10]
$[H_2bipy][Cu(bipy)(H_2O)_2][Cu(bipy)_3][H_3BiW_{18}O_{60}]\cdot H_2O$		[55]

3.3.2 Crystallographic and Structural Characterization

Crystal structure analysis was done by standard procedures, for a list of programs and instruments used see §1.16.1.

For structure solution of **Cu-1 – Cu-6** low angle reflections, attenuated by the beamstop, were omitted, as well as reflections above 55°. After subsequent assignment of residual electron density with partially occupied crystal water molecules, no more voids were observed. Residual electron density below 1 $e^{-}Å^{-3}$ was generally considered as noise. For the structurally related compounds **Cu-1**, **Cu-2** and **Cu-3**, an identical labelling scheme for W atoms was used. Rigid bond restraints (RIGU) have been applied in all refinements.

The three highest remaining electron density peaks in the structure **Cu-3** were located between 4.23 and 5.96 $e^{-}Å^{-3}$, at distances from W atoms of less than 1.0 Å. Despite several attempts to perform an analytical and Gaussian absorption correction, the sizes of these peaks could not be diminished. For the structures **Cu-1**, **Cu-2**, and **Cu-4** – **Cu-6** the highest remaining electron density peaks were between 1.3 and 3.0 e^{-} A^{-3}. This is in agreement with residual electron density peaks found for other reported polyoxometalate structures with characteristic values of 2.35-4.34 e^{-} A^{-3}.[56–58]

Details on the crystal structures as well as the crystallographic information files (CIF) may be obtained from the Fachinformationszentrum Karlsruhe, D-76344 Eggenstein-Leopoldshafen, Germany (Fax: +49 7247 808 666; email crysdata@fiz-karlsruhe.de), by citing the depository numbers CSD-431217 (**Cu-1**), CSD-431215 (**Cu-2**), CSD-431213 (**Cu-3**), CSD-431218 (**Cu-4**), CSD-431216 **(Cu-5)** and CSD-431214 **(Cu-6)**.

Table S3.2. Summary of the crystal structure refinements for **Cu-1 – Cu-6.**

	Cu-1	**Cu-2**	**Cu-3**	**Cu-4**	**Cu-5**	**Cu-6**
Empirical formula	$Bi_2ClCu_2H_{83}Na_{11}O_{11.5}$	$Bi_2Cu_{2.5}H_{66}K_3Na_7O_{103}$	$Bi_2Cu_3H_{43}K_{2.5}Na_{5.5}O_9$	$Bi_2Cu_3H_{48}Na_6O_{91}Rb_6$	$Bi_2ClCu_{3.82}H_{15.93}K_{9.18}$	$CuH_{26}K_4Na_4O_{66}W_{12}$
Formula weight (g mol^{-1})	6378.04	6289.80	6016.84	6072.76	5692.17	3600.12
Temperature (K)	183	183	183	183	183	183
Wavelength (λ/Å)	0.71073	0.71073	0.71073	0.71073	0.71073	0.71073
Crystal system	Triclinic	Triclinic	Triclinic	Monoclinic	Tetragonal	Monoclinic
Space group	$P\bar{1}$	$P\bar{1}$	$P\bar{1}$	$P2_1/m$	$P\bar{4}2_1m$	$P2_1/n$
a (Å)	13.0484(2)	12.1737(3)	11.5922(3)	13.2273(7)	16.6507(3)	13.1440(3)
b (Å)	17.4970(4)	18.8865(5)	17.4118(5)	19.3688(5)	16.6610(3)	11.5894(2)
c (Å)	23.2335(4)	22.3984(5)	20.5750(6)	18.1322(5)	13.7954(2)	19.0984(5)
α (°)	80.2569(17)	93.782(2)	95.335(2)	90	89.9885(13)	90
β (°)	89.1164(14)	95.696(2)	93.951(2)	98.083(3)	89.9890(12)	103.752(2)
γ (°)	71.4112(17)	99.016(2)	105.546(3)	90	89.9652(13)	90
V ($Å^3$)	4950.93(16)	5043.6(2)	3964.5(2)	4599.3(3)	3827.08(10)	2825.88(11)
Z	2	2	2	2	2	2
F(000)	5634	5493	5232	4966	4944	3258
M (mm-1)	27.289	26.987	34.374	30.187	33.192	25.138
ρ_{calc} (g/cm^{-3})	4.278	4.142	5.041	4.385	4.940	4.230
Crystal size (mm)	0.22 x 0.10 x 0.06	0.30 x 0.16 x 0.06	0.26 x 0.12 x 0.04	0.28 x 0.10 x 0.07	0.20 x 0.11 x 0.05	0.20 x 0.12 x 0.05
Reflections collected/unique	98674/22727	53429/23139	38976/18204	43254/10866	31680/4603	28159/6481
Unique observed reflections	18994	18536	13677	8254	4424	6002
θ range (°)	2.57-32.90	2.444-27.500	2.445-27.500	2.9090-30.5550	2.466-27.499	2.770-27.497
Data/restraints/parameters	22727/2295/1396	23139/2280/1420	18204/2076/1159	10866/1491/670	4603/774/342	6481/519/394
Goodness-of-fit	1.059	1.062	1.031	1.030	0.927	1.047
R_1[a] [I>2σ(I)]	0.0325	0.0410	0.0460	0.0610	0.0224	0.0236
wR_2[b] (all data)	0.0745	0.1058	0.1091	0.1712	0.0622	0.0641

[a] = R(F) [I > 2σ(I) reflections] ; [b] = wR(F^2) (all data)

Table S3.3. List of selected bond lengths for **Cu-1a** (left) and **Cu-1b** (right; ax. = axial, ter. = terminal, eq. = equatorial)

Cu-1a

Bond	d / Å	Bond	d / Å	Bond	d / Å
W(1A)-O(8A)$_{ax.}$	2.198(6)	W(4A)-O(1A)$_{ax.}$	2.250(6)	W(7A)-O(23A)$_{ax.}$	2.241(6)
W(1A)-O(17A)$_{ter.}$	1.732(6)	W(4A)-O(34A)$_{ter.}$	1.715(6)	W(7A)-O(30A)$_{ter.}$	1.717(6)
W(1A)-O(35A)$_{eq.}$	1.807(6)	W(4A)-O(31A)$_{eq.}$	1.944(6)	W(7A)-O(18A)$_{eq.}$	2.001(6)
W(1A)-O(32A)$_{eq.}$	1.814(6)	W(4A)-O(3A)$_{eq.}$	1.900(6)	W(7A)-O(19A)$_{eq.}$	2.024(7)
W(1A)-O(16A)$_{eq.}$	2.093(6)	W(4A)-O(10A)$_{eq.}$	1.898(7)	W(7A)-O(14A)$_{eq.}$	1.906(6)
W(1A)-O(9A)$_{eq.}$	2.024(6)	W(4A)-O(15A)$_{eq.}$	1.955(6)	W(7A)-O(22A)$_{eq.}$	1.799(7)
W(2A)-O(8A)$_{ax.}$	2.306(6)	W(5A)-O(1A)$_{ax.}$	2.228(6)	W(8A)-O(23A)$_{ax.}$	2.229(6)
W(2A)-O(26A)$_{ter.}$	1.714(7)	W(5A)-O(33A)$_{ter.}$	1.732(6)	W(8A)-O(25A)$_{ter.}$	1.740(6)
W(2A)-O(15A)$_{eq.}$	1.872(7)	W(5A)-O(3A)$_{eq.}$	2.016(6)	W(8A)-O(4A)$_{eq.}$	1.885(6)
W(2A)-O(13A)$_{eq.}$	2.026(6)	W(5A)-O(5A)$_{eq.}$	1.822(7)	W(8A)-O(6A)$_{eq.}$	1.947(6)
W(2A)-O(7A)$_{eq.}$	1.944(6)	W(5A)-O(14A)$_{eq.}$	1.917(6)	W(8A)-O(12A)$_{eq.}$	1.932(7)
W(2A)-O(16A)$_{eq.}$	1.837(6)	W(5A)-O(24A)$_{eq.}$	1.970(7)	W(8A)-O(18A)$_{eq.}$	1.910(6)
W(3A)-O(8A)$_{ax.}$	2.296(6)	W(6A)-O(1A)$_{ax.}$	2.196(6)	W(9A)-O(23A)$_{ax.}$	2.260(7)
W(3A)-O(29A)$_{ter.}$	1.716(7)	W(6A)-O(28A)$_{ter.}$	1.725(7)	W(9A)-O(21A)$_{ter.}$	1.711(7)
W(3A)-O(20A)$_{eq.}$	1.954(6)	W(6A)-O(10A)$_{eq.}$	2.010(6)	W(9A)-O(2A)$_{eq.}$	1.946(6)
W(3A)-O(6A)$_{eq.}$	1.894(6)	W(6A)-O(24A)$_{eq.}$	1.956(6)	W(9A)-O(20A)$_{eq.}$	1.894(6)
W(3A)-O(9A)$_{eq.}$	1.881(6)	W(6A)-O(2A)$_{eq.}$	1.869(6)	W(9A)-O(12A)$_{eq.}$	1.923(6)
W(3A)-O(7A)$_{eq.}$	1.931(6)	W(6A)-O(13A)$_{eq.}$	1.860(6)	W(9A)-O(19A)$_{eq.}$	1.904(6)
W(10A)-O(11A)$_{ter.}$	1.735(7)	Cu(1A)-O(17A)$_{ap.}$	2.195(6)	BI(1A)-O(8A)	2.144(6)
W(10A)-O(27A)$_{ter.}$	1.742(6)	Cu(1A)-O(36A)$_{ap.}$	2.9241(1)	BI(1A)-O(23A)	2.150(6)
W(10A)-O(31A)	1.949(6)	Cu(1A)-Cl(1A)	2.280(3)	BI(1A)-O(1A)	2.150(6)
W(10A)-O(4A)	2.004(6)	Cu(1A)-O(37A)	1.964(6)		
W(10A)-O(32A)	2.129(6)	Cu(1A)-O(22A)	1.929(7)		
W(10A)-O(35A)	2.121(6)	Cu(1A)-O(5A)	1.956(6)		

Cu-1b

Bond	d / Å	Bond	d / Å	Bond	d / Å
W(1B)-O(30B)$_{ax.}$	2.190(6)	W(4B)-O(11B)$_{ax.}$	2.248(6)	W(7B)-O(19B)$_{ax.}$	2.216(6)
W(1B)-O(18B)$_{ter.}$	1.731(6)	W(4B)-O(26B)$_{ter.}$	1.717(6)	W(7B)-O(28B)$_{ter.}$	1.732(6)
W(1B)-O(12B)$_{eq.}$	1.803(7)	W(4B)-O(9B)$_{eq.}$	1.880(7)	W(7B)-O(1B)$_{eq.}$	1.971(6)
W(1B)-O(17B)$_{eq.}$	2.052(6)	W(4B)-O(29B)$_{eq.}$	1.892(6)	W(7B)-O(4B)$_{eq.}$	1.960(6)
W(1B)-O(20B)$_{eq.}$	2.069(7)	W(4B)-O(2B)$_{eq.}$	1.937(7)	W(7B)-O(23B)$_{eq.}$	1.944(6)
W(1B)-O(8B)$_{eq.}$	1.811(6)	W(4B)-O(16B)$_{eq.}$	1.956(6)	W(7B)-O(10B)$_{eq.}$	1.817(7)
W(2B)-O(30B)$_{ax.}$	2.298(6)	W(5B)-O(11B)$_{ax.}$	2.206(6)	W(8B)-O(19B)$_{ax.}$	2.252(6)
W(2B)-O(24B)$_{ter.}$	1.713(7)	W(5B)-O(35B)$_{ter.}$	1.735(6)	W(8B)-O(22B)$_{ter.}$	1.727(6)
W(2B)-O(13B)$_{eq.}$	1.921(6)	W(5B)-O(3B)$_{eq.}$	1.787(7)	W(8B)-O(14B)$_{eq.}$	1.930(6)
W(2B)-O(20B)$_{eq.}$	1.873(7)	W(5B)-O(4B)$_{eq.}$	1.889(6)	W(8B)-O(5B)$_{eq.}$	1.876(7)
W(2B)-O(16B)$_{eq.}$	1.892(6)	W(5B)-O(6B)$_{eq.}$	2.013(7)	W(8B)-O(1B)$_{eq.}$	1.926(6)
W(2B)-O(25B)$_{eq.}$	1.972(6)	W(5B)-O(29B)$_{eq.}$	2.018(6)	W(8B)-O(7B)$_{eq.}$	1.944(7)
W(3B)-O(30B)$_{ax.}$	2.306(6)	W(6B)-O(11B)$_{ax.}$	2.283(7)	W(9B)-O(19B)$_{ax.}$	2.220(6)
W(3B)O(27B)$_{ter.}$	1.721(6)	W(6B)-O(32B)$_{ter.}$	1.713(7)	W(9B)-O(33B)$_{ter.}$	1.732(7)
W(3B)-O(13B)$_{eq.}$	1.937(7)	W(6B)-O(2B)$_{eq.}$	1.917(6)	W(9B)-O(15B)$_{eq.}$	1.884(6)
W(3B)-O(21B)$_{eq.}$	1.988(6)	W(6B)-O(6B)$_{eq.}$	1.913(6)	W(9B)-O(23B)$_{eq.}$	1.961(6)
W(3B)-O(14B)$_{eq.}$	1.886(7)	W(6B)-O(15B)$_{eq.}$	1.947(6)	W(9B)-O(21B)$_{eq.}$	1.846(6)
W(3B)-O(17B)$_{eq.}$	1.853(7)	W(6B)-O(25B)$_{eq.}$	1.889(6)	W(9B)-O(5B)$_{eq.}$	2.015(6)
W(10B)-O(31B)$_{ter.}$	1.736(7)	Cu(1B)-O(38B)$_{ap.}$	2.9303(1)	Bi(1B)-O(30B)	2.146(6)
W(10B)-O(34B)$_{ter.}$	1.755(6)	Cu(1B)-O(18B)$_{ap.}$	2.216(7)	Bi(1B)-O(11B)	2.157(6)
W(10B)-O(7B)	1.940(7)	Cu(1B)-O(37B)	1.973(6)	Bi(1B)-O(19B)	2.135(6)
W(10B)-O(8B)	2.098(6)	Cu(1B)-O(36B)	1.982(7)		
W(10B)-O(9B)	2.006(6)	Cu(1B)-O(10B)	1.934(6)		
W(10B)-O(12B)	2.152(7)	Cu(1B)-O(3B)	1.957(6)		

Table S3.4. List of selected bond lengths for **Cu-2** (ax. = axial, ter. = terminal, eq. = equatorial).

Cu-2A

Bond	d / Å	Bond	d / Å	Bond	d / Å
W(1A)-O(6A)$_{ax.}$	2.197(9)	W(4A)-O(18A)$_{ax.}$	2.244(9)	W(7A)-O(4A)$_{ax.}$	2.227(9)
W(1A)-O(28A)$_{ter.}$	1.733(9)	W(4A)-O(23A)$_{ter.}$	1.703(9)	W(7A)-O(17A)$_{ter}$	1.736(10)
W(1A)-O(1A)$_{eq.}$	2.069(9)	W(4A)-O(25A)$_{eq.}$	1.883(9)	W(7A)-O(10A)$_{eq.}$	1.959(9)
W(1A)-O(2A)$_{eq.}$	2.035(10)	W(4A)-O(8A)$_{eq.}$	1.964(9)	W(7A)-O(15A)$_{eq.}$	1.959(8)
W(1A)-O(19A)$_{eq.}$	1.823(8)	W(4A)-O(13A)$_{eq.}$	1.916(9)	W(7A)-O(20A)$_{eq.}$	1.801(9)
W(1A)-O(11A)$_{eq.}$	1.819(9)	W(4A)-O(29A)$_{eq.}$	1.924(9)	W(7A)-O(27A)$_{eq.}$	2.029(9)
W(2A)-O(6A)$_{ax.}$	2.288(9)	W(5A)-O(18A)$_{ax.}$	2.207(9)	W(8A)-O(4A)$_{ax.}$	2.266(8)
W(2A)-O(24A)$_{ter.}$	1.708(10)	W(5A)-O(14A)$_{ter.}$	1.716(9)	W(8A)-O(16A)$_{ter.}$	1.707(10)
W(2A)-O(2A)$_{eq.}$	1.872(9)	W(5A)-O(7A)$_{eq.}$	1.784(10)	W(8A)-O(15A)$_{eq.}$	1.906(9)
W(2A)-O(30A)$_{eq.}$	1.932(9)	W(5A)-O(10A)$_{eq.}$	1.922(9)	W(8A)-O(35A)$_{eq.}$	1.927(9)
W(2A)-O(26A)$_{eq.}$	1.971(9)	W(5A)-O(13A)$_{eq.}$	1.988(9)	W(8A)-O(12A)$_{eq.}$	1.939(10)
W(2A)-O(8A)$_{eq.}$	1.885(9)	W(5A)-O(22A)$_{eq.}$	2.013(10)	W(8A)-O(32A)$_{eq.}$	1.910(10)
W(3A)-O(6A)$_{ax.}$	2.328(9)	W(6A)-O(18A)$_{ax.}$	2.290(9)	W(9A)-O(4A)$_{ax.}$	2.255(8)
W(3A)-O(3A)$_{ter.}$	1.720(9)	W(6A)-O(31A)$_{ter.}$	1.750(10)	W(9A)-O(33A)$_{ter.}$	1.718(9)
W(3A)-O(1A)$_{eq.}$	1.854(9)	W(6A)-O(5A)$_{eq.}$	1.915(9)	W(9A)-O(5A)$_{eq.}$	1.878(9)
W(3A)-O(30A)$_{eq.}$	1.937(10)	W(6A)-O(22A)$_{eq.}$	1.903(10)	W(9A)-O(27A)$_{eq.}$	1.884(10)
W(3A)-O(21A)$_{eq.}$	1.976(9)	W(6A)-O(29A)$_{eq.}$	1.976(9)	W(9A)-O(32A)$_{eq.}$	1.984(10)
W(3A)-O(12A)$_{eq.}$	1.878(10)	W(6A)-O(26A)$_{eq.}$	1.875(9)	W(9A)-O(21A)$_{eq.}$	1.891(9)
W(10A)-O(9A)$_{ter.}$	1.741(10)	Cu(1A)-O(27B)$_{ap.}$	2.5525(1)	Bi(1A)-O(18A)	2.134(8)
W(10A)-O(34A)$_{ter.}$	1.762(8)	Cu(1A)-O(28A)$_{ap.}$	2.302(9)	Bi(1A)-O(4A)	2.137(8)
W(10A)-O(11A)$_{eq.}$	2.122(9)	Cu(1A)-O(36A)	1.984(10)	Bi(1A)-O(6A)	2.129(9)
W(10A)-O(19A)$_{eq.}$	2.119(8)	Cu(1A)-O(37A)	1.966(12)		
W(10A)-O(25A)$_{eq.}$	1.995(8)	Cu(1A)-O(7A)	1.976(10)		
W(10A)-O(35A)$_{eq.}$	1.949(9)	Cu(1A)-O(20A)	1.939(8)		

Cu-2B

Bond	d / Å	Bond	d / Å	Bond	d / Å
W(1B)-O(13B)$_{ax.}$	2.197(8)	W(4B)-O(12B)$_{ax.}$	2.243(8)	W(7B)-O(1B)$_{ax.}$	2.257(8)
W(1B)-O(25B)$_{ter.}$	1.746(8)	W(4B)-O(21B)$_{ter.}$	2.337(8)	W(7B)-O(27B)$_{ter.}$	1.715(9)
W(1B)-O(6B)$_{eq.}$	2.040(9)	W(4B)-O(15B)$_{eq.}$	1.881(9)	W(7B)-O(2B)$_{eq.}$	1.967(8)
W(1B)-O(8B)$_{eq.}$	2.081(8)	W(4B)-O(20B)$_{eq.}$	1.937(9)	W(7B)-O(5B)$_{eq.}$	1.990(9)
W(1B)-O(32B)$_{eq.}$	1.809(8)	W(4B)-O(23B)$_{eq.}$	1.998(8)	W(7B)-O(16B)$_{eq.}$	1.967(8)
W(1B)-O(33B)$_{eq.}$	1.815(9)	W(4B)-O(31B)$_{eq.}$	1.904(9)	W(7B)-O(19B)$_{eq.}$	1.814(9)
W(2B)-O(13B)$_{ax.}$	2.300(8)	W(5B)-O(12B$_{ax.}$	2.218(8)	W(8B)-O(1B)$_{ax.}$	2.243(8)
W(2B)-O(26B)$_{ter.}$	1.709(9)	W(5B)-O(17B)$_{ter.}$	1.729(8)	W(8B)-O(35B)$_{ter.}$	1.716(9)
W(2B)-O(23B)$_{eq.}$	1.842(8)	W(5B)-O(11B)$_{eq.}$	1.998(9)	W(8B)-O(2B)$_{eq.}$	1.918(8)
W(2B)-O(6B)$_{eq.}$	1.870(8)	W(5B)-O(15B)$_{eq.}$	2.038(8)	W(8B)-O(3B)$_{eq.}$	1.925(8)
W(2B)-O(10B)$_{eq.}$	1.955(8)	W(5B)-O(16B)$_{eq.}$	1.876(9)	W(8B)-O(4B)$_{eq.}$	1.922(9)
W(2B)-O(24B)$_{eq.}$	1.983(9)	W(5B)-O(18B)$_{eq.}$	1.822(9)	W(8B)-O(7B)$_{eq.}$	1.924(8)
W(3B)-O(13B)$_{ax.}$	2.337(8)	W(6B)-O(12B)$_{ax.}$	2.276(9)	W(9B)-O(1B)$_{ax.}$	2.251(8)
W(3B)-O(22B)$_{ter.}$	1.730(8)	W(6B)-O(34B)$_{ter.}$	1.731(10)	W(9B)-O(29B)$_{ter.}$	1.727(9)
W(3B)-O(3B)$_{eq.}$	1.901(9)	W(6B)-O(9B)$_{eq.}$	1.900(9)	W(9B)-O(4B)$_{eq.}$	1.992(8)
W(3B)-O(8B)$_{eq.}$	1.859(9)	W(6B)-O(11B)$_{eq.}$	1.908(9)	W(9B)-O(5B)$_{eq.}$	1.923(8)
W(3B)-O(10B)$_{eq.}$	1.931(9)	W(6B)-O(20B)$_{eq.}$	1.973(9)	W(9B)-O(9B)$_{eq.}$	1.901(8)
W(3B)-O(14B)$_{eq.}$	1.993(8)	W(6B)-O(24B)$_{eq.}$	1.874(9)	W(9B)-O(14B)$_{eq.}$	1.861(9)
W(10B)-O(30B)$_{ter.}$	1.752(9)	CU(1B)-O(17A)$_{ap.}$	2.846(11)	BI(1B)-O(1B)	2.128(8)
W(10B)-O(28B)$_{ter.}$	1.737(9)	CU(1B)-O(25B)$_{ap.}$	2.191(8)	BI(1B)-O(12B)	2.141(9)
W(10B)-O(7B)	1.971(8)	CU(1B)-O(18B)	1.934(9)	BI(1B)-O(13B)	2.117(8)
W(10B)-O(31B)	1.971(8)	CU(1B)-O(19B)	1.931(8)		
W(10B)-O(32B)	2.131(8)	CU(1B)-O(36B)	1.991(9)		
W(10B)-O(33B)	2.108(9)	CU(1B)-O(37B)	2.001(9)		

Table S3.5. List of selected bond lengths for **Cu-3** (ax. = axial, ter. = terminal, eq. = equatorial).

Cu-3A

Bond	d / Å	Bond	d / Å	Bond	d / Å
W(1A)-O(28A)$_{ax.}$	2.229(11)	W(4A)-O(18A)$_{ax.}$	2.231(11)	W(7A)-O(37A)$_{ax.}$	2.217(11)
W(1A)-O(10A)$_{ter.}$	1.749(12)	W(4A)-O(34A)$_{ter.}$	1.725(11)	W(7A)-O(17A)$_{ter.}$	1.748(11)
W(1A)-O(1A)$_{eq.}$	1.807(11)	W(4A)-O(2A)$_{eq.}$	1.917(11)	W(7A)-O(5A)$_{eq.}$	1.958(11)
W(1A)-O(21A)$_{eq.}$	1.807(11)	W(4A)-O(9A)$_{eq.}$	1.902(12)	W(7A)-O(6A)$_{eq.}$	1.936(11)
W(1A)-O(14A)$_{eq.}$	2.064(11)	W(4A)-O(25A)$_{eq.}$	1.895(11)	W(7A)-O(7A)$_{eq.}$	1.936(11)
W(1A)-O(19A)$_{eq.}$	2.040(12)	W(4A)-O(22A)$_{eq.}$	1.992(12)	W(7A)-O(13A)$_{eq.}$	1.794(11)
W(2A)-O(28A)$_{ax.}$	2.271(11)	W(5A)-O(18A)$_{ax.}$	2.222(12)	W(8A)-O(37A)$_{ax.}$	2.218(10)
W(2A)-O(35A)$_{ter.}$	1.765(13)	W(5A)-O(33A)$_{ter.}$	1.729(12)	W(8A)-O(29A)$_{ter.}$	1.711(11)
W(2A)-O(15A)$_{eq.}$	1.925(12)	W(5A)-O(4A)$_{eq.}$	1.790(11)	W(8A)-O(3A)$_{eq.}$	1.922(12)
W(2A)-O(16A)$_{eq.}$	1.978(12)	W(5A)-O(6A)$_{eq.}$	1.942(11)	W(8A)-O(5A)$_{eq.}$	1.952(12)
W(2A)-O(14A)$_{eq.}$	1.868(12)	W(5A)-O(11A)$_{eq.}$	2.014(12)	W(8A)-O(8A)$_{eq.}$	1.937(12)
W(2A)-O(22A)$_{eq.}$	1.850(12)	W(5A)-O(9A)$_{eq.}$	1.968(11)	W(8A)-O(20A)$_{eq.}$	1.899(11)
W(3A)-O(28A)$_{ax.}$	2.299(11)	W(6A)-O(18A)$_{ax.}$	2.260(12)	W(9A)-O(37A)$_{ax.}$	2.284(11)
W(3A)-O(26A)$_{ter.}$	1.746(12)	W(6A)-O(32A)$_{ter.}$	1.695(13)	W(9A)-O(36A)$_{ter.}$	1.736(12)
W(3A)-O(3A)$_{eq.}$	1.920(11)	W(6A)-O(11A)$_{eq.}$	1.890(12)	W(9A)-O(7A)$_{eq.}$	1.868(12)
W(3A)-O(15A)$_{eq.}$	1.922(12)	W(6A)-O(16A)$_{eq.}$	1.888(12)	W(9A)-O(8A)$_{eq.}$	1.941(11)
W(3A)-O(19A)$_{eq.}$	1.884(12)	W(6A)-O(25A)$_{eq.}$	1.969(11)	W(9A)-O(23A)$_{eq.}$	1.900(12)
W(3A)-O(23A)$_{eq.}$	1.942(12)	W(6A)-O(27A)$_{eq.}$	1.887(12)	W(9A)-O(27A)$_{eq.}$	1.902(11)
W(10A)-O(30A)$_{ter.}$	1.731(13)	CU(1A)-O(24B)$_{ap.}$	2.461(13)	BI(1A)-(O18A)	2.121(11)
W(10A)-O(31A)$_{ter.}$	1.735(13)	CU(1A)-O(10A)$_{ap.}$	2.231(12)	BI(1A)-(O28A)	2.131(11)
W(10A)-O(1A)	2.124(11)	CU(1A)-O(13A)	1.972(11)	BI(1A)-O(37A)	2.160(10)
W(10A)-O(20A)	1.998(12)	CU(1A)-O(4A)	1.942(12)		
W(10A)-O(21A)	2.134(11)	CU(1A)-O(12A)	1.986(12)		
W(10A)-O(2A)	1.983(12)	CU(1A)-O(24A)	1.971(11)		

Cu-3B

Bond	d / Å	Bond	d / Å	Bond	d / Å
W(1B)-O(37B)$_{ax.}$	2.181(11)	W(4B)-O(9B)$_{ax.}$	2.241(10)	W(7B)-O(3B)$_{ax.}$	2.249(11)
W(1B)-O(6B)$_{ter.}$	1.719(11)	W(4B)-O(18B)$_{ter.}$	1.745(10)	W(7B)-O(24B)$_{ter.}$	1.730(11)
W(1B)-O(1B)$_{eq.}$	1.826(11)	W(4B)-O(7B)$_{eq.}$	1.894(11)	W(7B)-O(10B)$_{eq.}$	1.948(10)
W(1B)-O(2B)$_{eq.}$	1.787(11)	W(4B)-O(19B)$_{eq.}$	1.955(11)	W(7B)-O(11B)$_{eq.}$	1.994(11)
W(1B)-O(33B)$_{eq.}$	2.000(11)	W(4B)-O(25B)$_{eq.}$	1.897(11)	W(7B)-O(12B)$_{eq.}$	1.966(10)
W(1B)-O(34B)$_{eq.}$	2.106(11)	W(4B)-O(27B)$_{eq.}$	1.903(11)	W(7B)-O(23B)$_{eq.}$	1.800(11)
W(2B)-O(37B)$_{ax.}$	2.283(10)	W(5B)-O(9B)$_{ax.}$	2.225(11)	W(8B)-O(3B)$_{ax.}$	2.258(10)
W(2B)-O(26B)$_{ter.}$	1.703(12)	W(5B)-O(28B)$_{ter.}$	1.738(11)	W(8B)-O(31B)$_{ter.}$	1.719(10)
W(2B)-O(13B)$_{eq.}$	1.948(10)	W(5B)-O(10B)$_{eq.}$	1.900(10)	W(8B)-O(4B)$_{eq.}$	1.918(11)
W(2B)-O(19B)$_{eq.}$	1.877(11)	W(5B)-O(21B)$_{eq.}$	1.804(11)	W(8B)-O(12B)$_{eq.}$	1.932(11)
W(2B)-O(20B)$_{eq.}$	1.960(11)	W(5B)-O(25B)$_{eq.}$	2.003(10)	W(8B)-O(14B)$_{eq.}$	1.926(11)
W(2B)-O(33B)$_{eq.}$	1.878(11)	W(5B)-O(15B)$_{eq.}$	2.003(11)	W(8B)-O(30B)$_{eq.}$	1.942(11)
W(3B)-O(37B)$_{ax.}$	2.316(10)	W(6B)-O(9B)$_{ax.}$	2.267(11)	W(9B)-O(3B)$_{ax.}$	2.233(10)
W(3B)-O(29B)$_{ter.}$	1.735(11)	W(6B)-O(32B)$_{ter.}$	1.736(11)	W(9B)-O(16B)$_{ter.}$	1.717(11)
W(3B)-O(13B)$_{eq.}$	1.922(11)	W(6B)-O(15B)$_{eq.}$	1.908(11)	W(9B)-O(4B)$_{eq.}$	1.975(10)
W(3B)-O(14B)$_{eq.}$	1.884(11)	W(6B)-O(17B)$_{eq.}$	1.934(11)	W(9B)-O(11B)$_{eq.}$	1.922(11)
W(3B)-O(34B)$_{eq.}$	1.838(11)	W(6B)-O(20B)$_{eq.}$	1.867(11)	W(9B)-O(17B)$_{eq.}$	1.897(10)
W(3B)-O(22B)$_{eq.}$	2.028(11)	W(6B)-O(27B)$_{eq.}$	1.954(11)	W(9B)-O(22B)$_{eq.}$	1.841(11)
W(10B)-O(5B)$_{ter.}$	1.715(11)	CU(1B)-O(17A)$_{ap.}$	2.648(13)	BI(1B)-O(3B)	2.132(10)
W(10B)-O(8B)$_{ter.}$	1.763(12)	CU(1B)-O(6B)$_{ap.}$	2.202(11)	BI(1B)-O(9B)	2.144(10)
W(10B)-O(1B)	2.047(11)	CU(1B)-O(36B)	1.979(12)	BI(1B)-O(37B)	2.133(11)
W(10B)-O(2B)	2.198(11)	CU(1B)-O(35B)	2.012(12)		
W(10B)-O(7B)	1.970(11)	CU(1B)-O(21B)	1.953(11)		
W(10B)-O(30B)	1.962(11)	CU(1B)-O(23B)	1.937(11)		

Table S3.6. BVS values for the transition metal centers of **Cu-1**, **Cu-2**, and **Cu-3.**

Cu-1							
Atom	BVS-Value	Atom	BVS-Value	Atom	BVS-Value	Atom	BVS-Value
Bi1A	3.2237	W5A	5.8989	Bi1B	3.2093	W5B	6.0019
Cu1A	2.0848	W6A	6.0164	Cu1B	2.0261	W6B	5.9893
W1A	6.0207	W7A	5.9626	W1B	6.0439	W7B	5.9726
W2A	5.9993	W8A	5.9488	W2B	6.0151	W8B	5.9693
W3A	5.9868	W9A	6.0197	W3B	5.9700	W9B	5.9289
W4A	5.9632	W10A	5.9618	W4B	6.0305	W10B	5.9143
Cu-2							
Atom	BVS-Value	Atom	BVS-Value	Atom	BVS-Value	Atom	BVS-Value
Bi1A:	3.1824	W5A	6.0483	Bi1B	3.2099	W5B	5.9139
Cu1A:	1.9099	W6A	5.8529	Cu1B	1.9768	W6B	5.9641
W1A	5.9611	W7A	5.8400	W1B	5.9471	W7Bv	5.8783
W2A	6.0447	W8A	5.9944	W2B	6.0712	W8B	5.9760
W3A	6.0040	W9A	6.0923	W3B	5.8620	W9B	5.9739
W4A	6.0379	W10A	5.8905	W4B	5.9172	W10B	5.8848
Cu-3							
Atom	BVS-Value	Atom	BVS-Value	Atom	BVS-Value	Atom	BVS-Value
Bi1A	3.1953	W5A	5.9571	Bi1B	3.1872	W5B	5.9215
Cu1A	1.9381	W6A	6.1850	Cu1B	1.9426v	W6B	5.9367
W1A	5.9577	W7A	5.8286	W1B	6.1474v	W7B	5.9117
W2A	5.9520	W8A	5.9810	W2B	6.0669	W8B	5.8887
W3A	5.8540	W9A	6.0381	W3B	5.9293	W9B	6.1306
W4A	5.9347	W10A	5.9226	W4B	5.9761	W10B	6.0228

Table S3.7. List of selected bond lengths for **Cu-4** (left) and **Cu-5** (right) (ax. = axial, ter. = terminal, eq. = equatorial).

Cu-4

Bond	d / Å	Bond	d / Å	Bond	d / Å
W(1)-O(8)$_{ax.}$	2.255(14)	W(4)-O(11)$_{ax.}$	2.233(14)	W(7)-O(13)$_{ax.}$	2.258(15)
W(1)-O(22)$_{ter.}$	1.724(14)	W(4)-O(31)$_{ter.}$	1.729(17)	W(7)-O(29)$_{ter.}$	1.728(16)
W(1)-O(9)$_{eq.}$	1.879(13)	W(4)-O(6)$_{eq.}$	1.853(13)	W(7)-O(10)$_{eq.}$	1.835(13)
W(1)-O(1)$_{eq.}$	1.849(13)	W(4)-O(17)$_{eq.}$	1.989(14)	W(7)-O(12)$_{eq.}$	1.893(15)
W(1)-O(5)$_{eq.}$	1.948(12)	W(4)-O(38)$_{eq.}$	1.993(14)	W(7)-O(18)$_{eq.}$	1.965(12)
W(1)-O(4)$_{eq.}$	1.985(12	W(4)-O(36)$_{eq.}$	1.924(6)	W(7)-O(19)$_{eq.}$	1.985(13)
W(2)-O(11)$_{ax.}$	2.230(13)	W(5)-O(11)$_{ax.}$	2.274(12)	W(8)-O(13)$_{ax.}$	2.278(18)
W(2)-O(21)$_{ter.}$	1.717(13)	W(5)-O(34)$_{ter.}$	1.722(13)	W(8)-O(32)$_{ter.}$	1.73(2)
W(2)-O(2)$_{eq.}$	1.824(12)	W(5)-O(3)$_{eq.}$	1.913(13)	W(8)-O(19)$_{eq.}$	1.900(16)
W(2)-O(3)$_{eq.}$	1.989(12)	W(5)-O(16)$_{eq.}$	1.929(16)	W(8)-O(23)$_{eq.}$	1.907(17)
W(2)-O(17)$_{eq.}$	1.912(16)	W(5)-O(27)$_{eq.}$	1.901(5)	W(9)-O(35)$_{ax.}$	2.243(16)
W(2)-O(9)$_{eq.}$	1.978(15)	W(5)-O(38)$_{eq.}$	1.890(18)	W(9)-O(33)$_{ter.}$	1.694(19)
W(3)-O(8)$_{ax.}$	2.269(17)	W(6)-O(35)$_{ax.}$	2.257(13)	W(9)-O(14)$_{eq.}$	1.842(13)
W(3)-O(26)$_{ter.}$	1.693(18)	W(6)-O(30)$_{ter.}$	1.727(14)	W(9)-O(15)$_{eq.}$	1.910(6)
W(3)-O(16)$_{eq.}$	1.915(15)	W(6)-O(7)$_{eq.}$	1.827(12)	W(9)-O(24)$_{eq.}$	1.981(14)
W(3)-O(4)$_{eq.}$	1.930(14)	W(6)-O(12)$_{eq.}$	1.954(16)	W(9)-O(25)$_{eq.}$	1.946(15)
Cu(1)-O(39)	2.22(3)	W(6)-O(28)$_{eq.}$	1.960(14)	Cu(1)-Cu(2)	4.8831(42)
Cu(1)-O(14)	1.932(14)	W(6)-O(25)$_{eq.}$	1.965(18)	Cu(2)-Cu(2)	4.8333(27)
Cu(1)-O(6)	1.936(13)	Bi(1)-O(11)	2.111(12)		
Cu(2)-O(40)	2.170(15)	Bi(1)-O(8)	2.092(19)		
Cu(2)-O(1)	1.930(13)	Bi(2)-O(13)	2.82(2)		
Cu(2)-O(2)	1.952(14)	Bi(2)-O(35)	2.099(13)		
Cu(2)-O(10)	1.928(13)				

Cu-5

Bond	d / Å	Bond	d / Å	Bond	d / Å
W(1)-O(4)$_{ax.}$	2.259(8)	W(2)-O(3)$_{ax.}$	2.260(8)	W(3)-O(3)$_{ax.}$	2.227(9)
W(1)-O(10)$_{ter.}$	1.730(10)	W(2)-O(13)$_{ter.}$	1.726(10)	W(3)-O(15)$_{ter.}$	1.728(10)
W(1)-O(16)$_{eq.}$	1.824(9)	W(2)-O(2)$_{eq.}$	1.845(10)	W(3)-O(12)$_{eq.}$	1.955(10)
W(1)-O(19)$_{eq.}$	1.966(7)	W(2)-O(14)$_{eq.}$	1.918(4)	W(3)-O(5)$_{eq.}$	1.932(9)
W(1)-O(7)$_{eq.}$	2.005(9)	W(2)-O(12)$_{eq.}$	1.966(11)	W(3)-O(1)$_{eq.}$	2.013(9)
W(1)-O(5)$_{eq.}$	1.912(9)	W(2)-O(9)$_{eq.}$	1.974(10)	W(3)-O(6)$_{eq.}$	1.828(9)
W(4)-O(3)$_{ax.}$	2.269(9)	W(5)-O(4)$_{ax.}$	2.296(13)	Cu(1)-O(8)$_{ap.}$	2.234(14)
W(4)-O(17)$_{ter.}$	1.727(10)	W(5)-O(8)$_{ter.}$	1.720(13)	Cu(1)-O(6)$_{eq.}$	1.951(10)
W(4)-O(9)$_{eq.}$	1.944(10)	W(5)-O(7)$_{eq.}$	1.889(9)	Cu(1)-O(16)$_{eq.}$	1.959(10)
W(4)-O(1)$_{eq.}$	1.904(10)	W(5)-O(11)$_{eq.}$	1.911(9)	Cu(1)-Cu(4)	2.76(2)
W(4)-O(18)$_{eq.}$	1.908(3)	Bi(1)-O(3)	2.114(8)	Cu(1)-Cu(3)	2.871(12)
W(4)-O(11)$_{eq.}$	1.917(9)	Bi(1)-O(4)	2.080(12)	Cu(4)-O(16)$_{eq.}$	2.058(11)
Cu(2)-O(2)$_{eq.}$	1.935(10)	Cu(3)-O(2)$_{eq.}$	1.970(14)	Cu(4)-Cu(1)	2.76(2)
Cu(2)-Cl	2.557(13)	Cu(3)-O(6)	2.121(14)		
		Cu(2)-Cu(3)	2.755(13)		

Table S3.8. BVS values for **Cu-4** and **Cu-5**.

Cu-4

Atom	BVS-	Atom	BVS-	Atom	BVS-
Bi1	3.3133	W3	6.0345	W9	6.0987
Bi2	3.3683	W4	5.7934	W10	5.9270
Cu1	2.0968	W5	6.0465		
Cu2	2.1038	W6	5.8981		
W1	6.0325	W7	5.9672		
W2	5.9913	W8	6.0710		

Cu-5

Atom	BVS-	Atom	BVS-
Bi1	3.2899	W4	5.9701
Cu1	2.0147	W5	6.1400
Cu2	2.1030		
W1	5.9084		
W2	5.9256		
W3	5.8974		

Table S3.9. List of selected bond lengths (left) and bond valence sum (BVS) values (right) for **Cu-6** (ax. = axial, ter. = terminal, eq. = equatorial).

Cu-6

Bond	d / Å	Bond	d / Å	Bond	d / Å
W(1)-O(15)$_{ax.}$	2.238(4)	W(4)-O(13)$_{ter.}$	1.723(5)	Cu(1)-O(12)	2.4727(0)
W(1)-O(10)$_{ter.}$	1.736(5)	W(4)-O(9)$_{ter.}$	1.777(4)	Cu(1)-O(9)	1.907(5)
W(1)-O(3)$_{eq.}$	1.878(4)	W(4)-O(3)	2.329(4)	Cu(1)-OW$_1$	1.962(5)
W(1)-O(4)$_{eq.}$	1.959(4)	W(4)-O(2)	2.078(4)		
W(1)-O(6)$_{eq.}$	2.105(4)	W(4)-O(7)	1.948(4)		
W(1)-O(8)$_{eq.}$	1.789(4)	W(4)-O(9)	1.777(4)		
W(2)-O(15)$_{ax.}$	2.264(4)	W(5)-O(21)$_{ter.}$	1.747(4)		
W(2)-O(20)$_{ter.}$	1.717(4)	W(5)-O(11)$_{ter.}$	1.745(5)		
W(2)-O(2)$_{eq.}$	1.830(4)	W(5)-O(5)	2.213(4)		
W(2)-O(5)$_{eq.}$	1.898(4)	W(5)-O(8)	2.198(4)		
W(2)-O(4)$_{eq.}$	1.933(4)	W(5)-O(16)	1.959(4)		
W(2)-O(17)$_{eq.}$	2.043(4)	W(5)-O(18)	1.887(4)		
W(3)-O(15)$_{ax.}$	2.243(4)	W(6)-O(12)$_{ter.}$	1.749(4)		
W(3)-O(19)$_{ter.}$	1.716(4)	W(6)-O(14)$_{ter.}$	1.747(4)		
W(3)-O(1)$_{eq.}$	1.949(4)	W(6)-O(7)	1.891(5)		
W(3)-O(6)$_{eq.}$	1.877(5)	W(6)-O(3)	2.236(4)		
W(3)-O(17)$_{eq.}$	1.875(4)	W(6)-O(16)	1.912(4)		
W(3)-O(18)$_{eq.}$	1.967(4)	W(6)-O(5)	2.265(4)		

Cu-6

Atom	BVS-Value	Atom	BVS-Value	Atom	BVS-Value
Bi1A	3.2237	W5A	5.8989	Bi1B	3.2093
Cu1A	2.0848	W6A	6.0164	Cu1B	2.0261
W1A	6.0207	W7A	5.9626	W1B	6.0439
W2A	5.9993	W8A	5.9488	W2B	6.0151
W3A	5.9868	W9A	6.0197	W3B	5.9700
W4A	5.9632	W10A	5.9618	W4B	6.0305
W5B	6.0019				
W6B	5.9893				
W7B	5.9726				
W8B	5.9693				
W9B	5.9289				
W10B	5.9143				

3.3.3 POMs Based on a {B-β-$BiW_{10}O_{37}$} Subunit

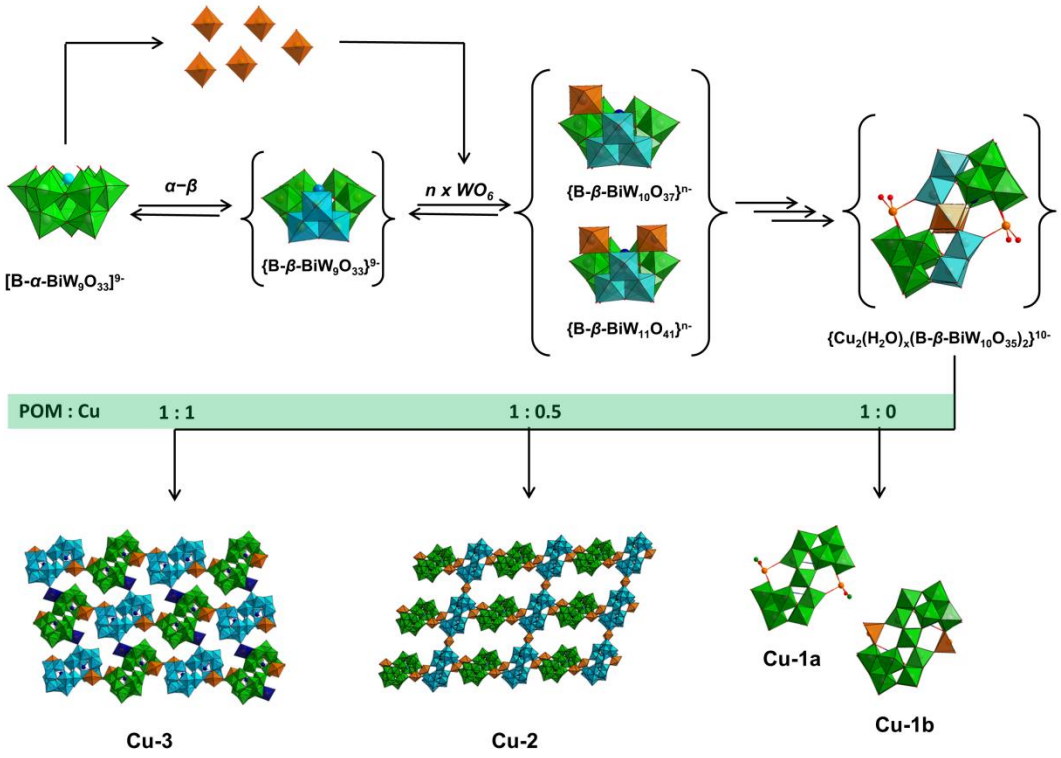

Figure S3.1. Schematic formation of Cu substituted Krebs-type POMs.

In all of the Krebs-type structures **Cu-1**, **Cu-2**, and **Cu-3**, the first coordination sphere of the Bi heteroatom is located in a pyramidal coordination environment with Bi–O bond lengths in the range between 2.117(8) Å and 2.160(10) Å and angles between (84.2-88.7°) for the the Bi–O_{ax} bonds. The same labeling scheme was used for tungsten atoms in the structures **Cu-1** – **Cu-3**. The tungsten atoms W(1)-W(9) represent the hypothetical {BiW_9O_{37}} unit where they are in a distorted octahedral coordination environment with W–O bond lengths between 1.695(13) Å and 1.765(13) Å (terminal oxygen atoms), between 1.783(10) Å and 2.198(11) Å (equatorial O atoms) and between 1.735(10) Å and 2.337(8) Å for the axial oxygen atoms. The tungsten atom W(10) as a part of the transition metal core, displays a slightly different coordination environment with W–O bonds ranging from 1.715(11) Å to 2.198(11) Å. Intermetallic W···W distances are in the range of 3.2425(1) Å to 3.5010(1) Å between edge sharing WO_6 octahedra and between 3.6368(1) Å and 3.7137(1) Å for corner sharing WO_6 octahedra. The W···W

distance to the ligand bridging WO_6 octahedron of W(10) is slightly longer (3.5479(1) Å – 3.9417(1) Å). The oxidation state of the metal cations of the polyanion was checked by BVS analysis[59] and an oxidation state of +II for Cu, +VI for W and +III for Bi was confirmed (Table S3.3-Table S3.5 and Table S3.6).

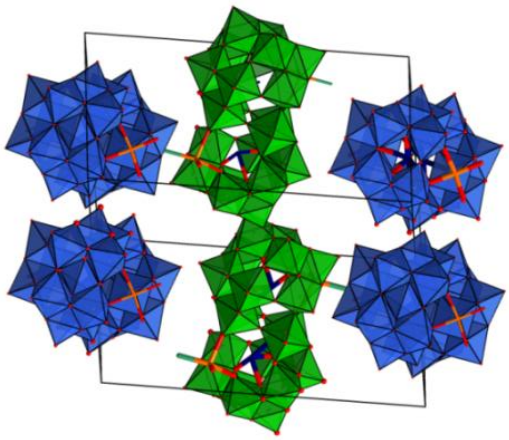

Figure S3.2. Arrangement of the polyanions **Cu-1a** (green) and **Cu-1b** (blue) in the unit cell; crystal water molecules and counter-cations have been omitted for clarity.

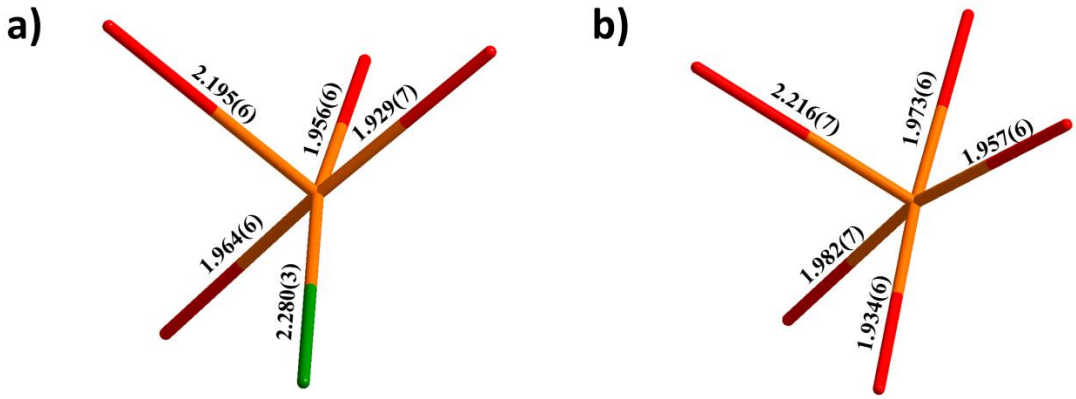

Figure S3.3. Coordination geometry of Cu(II) cations in the transition metal belt of **Cu-1a** (a) and **Cu-1b** (b).

The Cu center of **Cu-1b** is found in an almost square pyramidal coordination environment. It is coordinated by two water ligands with Cu–O bond lengths of 1.982(7) Å and 1.973(6) Å as well

as by two oxygen atoms of the [B-β-BiW_9O_{33}]$^{9-}$ subunit with slightly shorter Cu–O bond lengths (1.957(6) Å and 1.934(6) Å). A fifth oxygen atom is located in the apical position with a Cu–O bond length of 2.216(7) Å. In the coordination sphere of **Cu-1a**, one of the crystal water molecules is substituted by a chloride ligand which leads to a distortion of the square pyramidal coordination geometry. The Cl^- ion is found at a distance of 2.280(3) Å from the Cu (II) center, coplanar with the coordinating water ligand (1.964(6) Å) and the two terminal oxygen atoms of the {β-B-BiW_9O_{33}} subunit at 1.956(6) Å and 1.929(7) Å, respectively. The apical position of the distorted pyramid is occupied by another oxygen atom of the subunit at 2.195(6) Å (Figure S3.3). The presence of the Cl^- ligand leads to slightly shorter Cu–O bonds. A total of 11 Na^+ counter-cations and 83 crystal water molecules have been refined between the two isolated polyanions **Cu-1a** and **Cu-2b** which are not connected by additional Cu(II) cations. Each Na^+ site was found to be fully occupied.

The two POM monomers in the 1D-chains of **Cu-2** and **Cu-3** are bridged via the Cu(II) ion of the transition metal belt to a terminal oxygen atom of the adjacent monomer (Figure S3.1). The two CuO_6 octahedra of the monomers are shown in orange. The resulting 1D-chains are connected into a 2D layer by additional chain-bridging Cu(II) cations (orange octahedra). Figure 3.2 gives an overview of the connectivity in the layers of **Cu-2** and **Cu-3**.

The bridging Cu atom in **Cu-2** is located on the $\bar{1}$ symmetry site, and its octahedral coordination environment contains four crystal water molecules in the equatorial plane with an average Cu–O bond length of 1.966 Å. The axial positions of the CuO_6 octahedron are occupied by the terminal oxygen atoms of the tungsten atom at a distance of 2.3294(1) Å. Bridging in **Cu-3** occurs via 2 Cu atoms and through terminal oxygen atoms of different tungsten centers of the repeating unit compared to the arrangement in **Cu-2**, thus resulting in a different 2D network from **Cu-2**. The Cu···Cu distances between the copper atoms of the polyanions **Cu-1**, **Cu-2**, and **Cu-3** are generally in the same range between 10.0269(1) Å and 10.276(3) Å.

3.3.4 POMs Based on the [B-α-BiW_9O_{33}]$^{9-}$ Building Block

3.3.4.1 Detailed Structural Analysis of Cu-4 and Cu-5

Cu-4 and **Cu-5** crystallize in the monoclinic space group $P2_1/m$ and in the tetragonal space group $P\bar{4}2_1m$, respectively. Crystal structure refinement reveals the presence of a tungstobismuthate of the type $[Cu_3(H_2O)M(Q)_3(A\text{-}\alpha\text{-}BiW_9O_{33})_2]^{n-}$ (M = Rb, K or Cu; Q = H_2O or Cl; n = 12). While M and Q can be defined clearly in **Cu-4**, disorder in the transition metal belt of **Cu-5** indicates that it is composed of polyanions with different belt compositions (§3.3.4.2). **Cu-5** consists of single polyanions linked into a 3D-network, while the polyanions in **Cu-4** crystallize without Cu–O–W bridging.

The polyanions constituting **Cu-4** and **Cu-5** are isostructural. The Bi heteroatom coordinates to 3 oxygen atoms with Bi–O bond lengths between 2.080(12) Å and 2.114(8) Å and Bi–O bond angles between 86.1(3) and 88.3(7)°. All tungsten atoms exhibit distorted octahedral coordinations with bond lengths between 1.693(18) Å and 1.730(10) Å, for the terminal oxygen atoms, 1.824(9) Å and 2.013(9) Å for equatorial O atoms and between 2.227(9) Å and 2.296(13) Å for the axial oxygen atoms. Intermetallic W···W distances between edge sharing WO_6 octahedra are in the range of 3.3163(8) Å to 3.3431(7) Å and range from 3.6910(8) Å to 3.7153(11) Å for corner sharing WO_6 octahedra.

The fully occupied Cu(II) positions Cu(1) and Cu(2) in **Cu-4** and **Cu-5** form a triangle with Cu–Cu–Cu angles between 59.326(43)° and 60.337(38)° and interatomic Cu···Cu distances between 4.8831(42) Å and 4.935(24) Å. Interatomic distances in **Cu-5** between the fully occupied Cu(II) positions and the disordered Cu(II) sites Cu(3) and Cu(4) are between 2.755(13) Å and 2.871(12) Å.

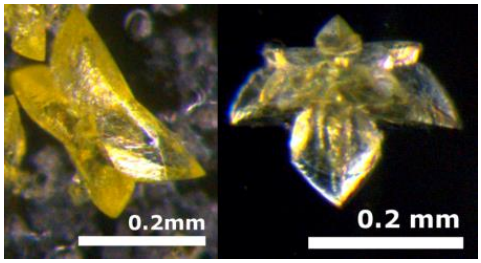

Figure S3.4. Representative image of **Cu-5** crystals recorded on a stereomicroscope.

3.3.4.2 Detailed Description of the Cu/K Disorder in Cu-5

While **Cu-4** does not display disorder, the transition metal belt of 3D-$K_{6.89}Cu_{0.43}H_{0.93}[(Cu_3(H_2O)_2Cl)(K_{2.68}Cu_{0.32}(H_2O)_3(B\text{-}\alpha\text{-}BiW_9O_{33})_2]\cdot 13H_2O$ (**Cu-5**) shows a high degree of disorder. This renders the unambiguous assignment of counter-cations difficult.

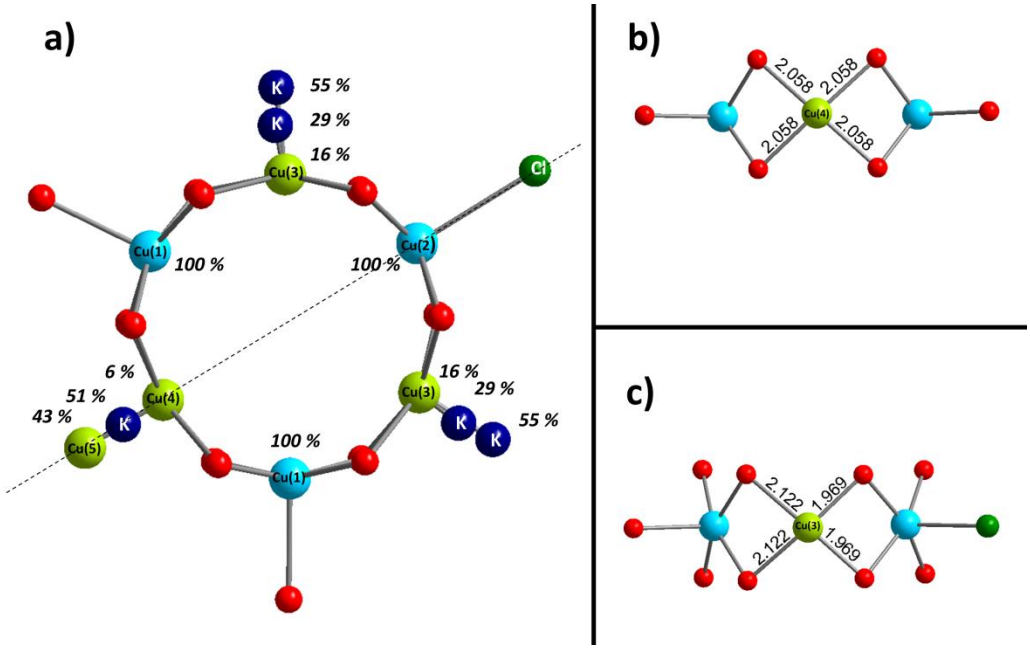

Figure S3.5. (a) Ball and stick representation of the transition metal core of **Cu-5**. **(b)** Coordination environment of Cu(4). **(c)** Coordination environment of Cu(5). Color code: O = red = O, Cl = dark green, K = dark blue, Cu (disordered) = green, Cu (100 %) = blue.

Compared to **Cu-4** where cavities between Cu atoms are fully occupied by Rb^+ cations, the cavities in **Cu-5** are occupied with K^+, Cu(II) cations and coordinating water ligands which are found on disordered positions. The water ligands of the disordered Cu(II) cations have not been included in the model. This disorder is indicated by residual electron density maxima in the cavities between Cu(1) and Cu(2) and between Cu(1) and Cu(1), respectively,which are less than 1.0 Å apart. Given the position of the electron density maxima in the cavities between Cu(1) and Cu(1') with distances to O atoms between 1.970(14) and 2.121(14) Å and the square planar coordination geometry, the peak was refined as Cu atom Cu(3). The electron density maximum between Cu(2) and Cu(1) was found in a similar coordination environment with Q–O bond lengths of 2.058(11) Å and it was therefore refined as Cu(4). The occupancies of the only

partially occupied Cu(3) and Cu(4) sites were refined to 0.160(04) for Cu(3) and 0.065(04) for Cu(4) which indeed is very small. In the cavity where Cu(4) is located, another electron density maximum without a specific coordination environment or characteristic bond distances was found. In line with the overall Cu content determined by elemental analysis this electron density was refined as Cu(5) with occupancy 0.425(04) This assignment is supported by the atomic displacement parameters which are in agreement with this atom type.

The cavities between Cu(2)/Cu(1) and Cu(1)/Cu(1) are alternatively filled with K^+ and Cu(II) cations. They were summed up to 1 using the linear restraints (SUMP instruction).

3.3.5 Analytical Characterization of Cu-5

3.3.5.1 Magnetic Susceptibility of Cu-5

Fitting the data using the Curie-Weiss law (eq. 3.1) did not lead to satisfactory results at low temperature. Using a model which was previously reported and used to fit the data for the 3D network structure $Na_9[Cu_3Na_3(H_2O)_9(B\text{-}\alpha\text{-}AsW_9O_{33})_2]$ led to better results (eq. 3.2).[36]

$$\chi_m = \frac{C}{T-\Theta} \qquad \text{(eq. 3.1)}$$

χ_m = molar magnetic susceptibility, C = Curie constant, T = Temperature, Θ = Curie temperature

$$\chi_m = \frac{Ng^2\beta^2}{4k(T-\Theta)}\left[\frac{1+5\exp\left(\frac{3J}{kT}\right)}{1+\exp\left(\frac{3J}{kT}\right)}\right] \qquad \text{(eq. 3.2)}$$

The best least squares fit is achieved with the spin-exchange factor J = -1.19228264 cm^{-1}, a Curie temperature θ = 0.17577707 K which is consistent with g = 2.67.

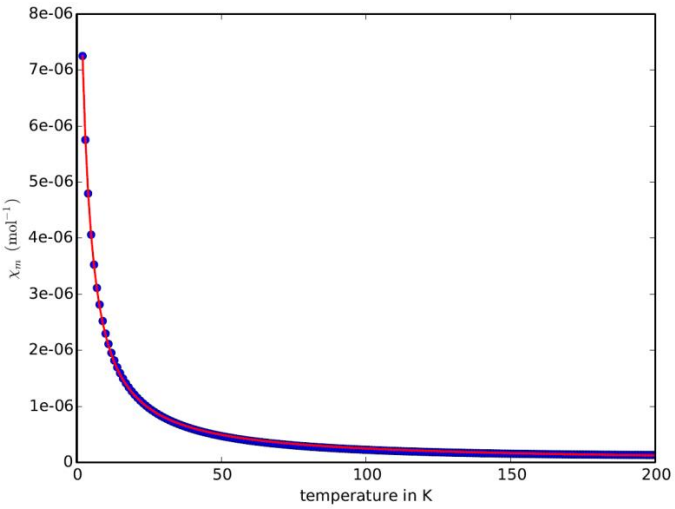

Figure S3.6. Temperature dependence of χ_m of **Cu-5** between 2 and 200 K, at 500 Oe.

3.3.5.2 FT-IR Spectrum of Cu-5

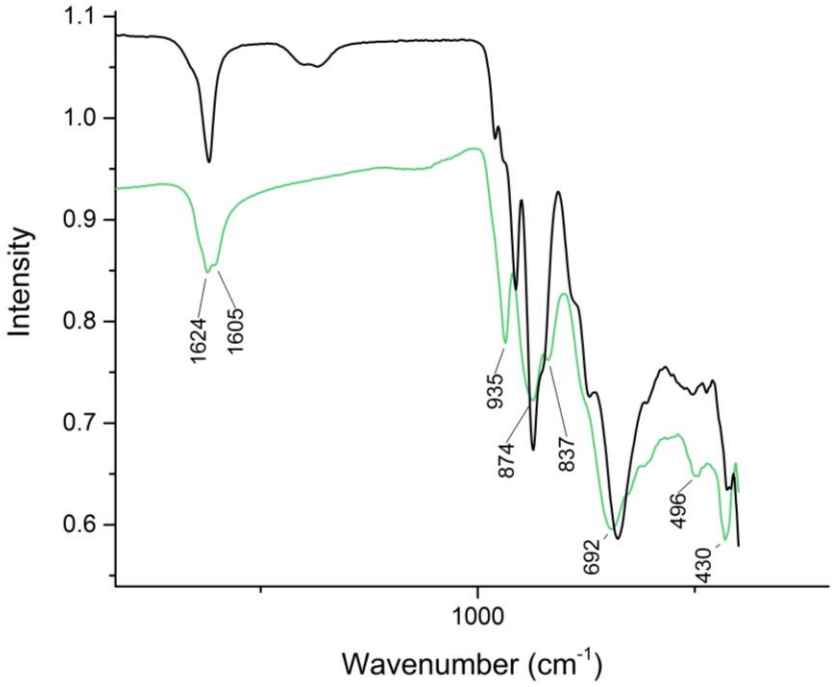

Figure S3.7. FT-IR spectrum of **Cu-5** (green) vs. the BiW_9 precursor (black).

3.3.6 Powder X-ray Diffractogram of Cu-5

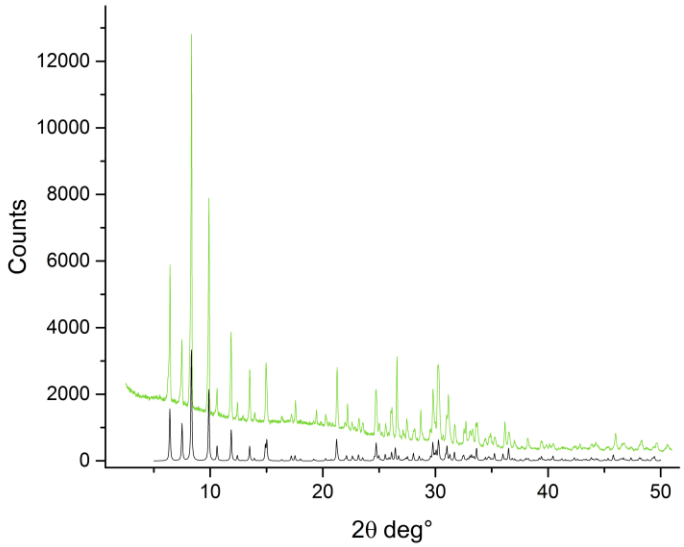

Figure S3.8. PXRD pattern of **Cu-5** (Cu $K_{\alpha 1}$): calculated (black), measured (green).

3.3.7 High Resolution Mass Spectrometry of Cu-5

The average structural information obtained from single crystal X-ray structure determination leaves the question open as to whether the polyanions $\{Cu_5(H_2O)_4Cl(BiW_9O_{33})_2\}$ and $\{Cu_6(H_2O)_5Cl(BiW_9O_{33})_2\}$ truly exist. The distinction between polyanions with different cores should in principle be possible by high resolution mass spectrometry through their specific masses giving rise to distinct signals. The distribution of polyanions was calculated from their refined site occupancies in the transition metal belt, assuming that the substitution of an additional Cu(II) cation does not alter the probability for the incorporation of a subsequent one (stochastically independent events). The plausibility of this assumption is subject of further studies. Calculated results show low probabilities for the formation of polyanions with Cu_5 and Cu_6 cores (Table S3.10). The HR-ESI-MS peak with z = 5- was analyzed in detail. The polyanion $[Cu_3(H_2O)_3(BiW_9O_{33})_2]^{12-}$ contains cavities which are filled alternately with K^+ or Cu^{2+} cations. Whether these cations should be considered as part of the structure is unresolved from structural data, but important for the assignment of specific peaks to polyanion structures. A large number of different $[Cu_3(H_2O)_xCl_{3-x}Cu_yK_{3-y}(BiW_9O_{33})_2]$ - a·K b·H$\}^{5-}$ (x = 0-3, y = 0-3) polyanions may be detected and potassium adducts may form with the polyanions, i.e. the values of a and b need to be adjusted to an overall polyanion charge of 5-. Due to the formation of K^+ adducts and an unknown number of water ligands or Cl^- coordinating to the transition metal core, a variety of species may be detected. This leads to an overlap of the signals from the different species and does not allow the unambiguous identification of a specific polyanion.

Table S3.10. List of possible species to be observed in the HR-ESI MS of **Cu-5.**

Fragment	**Mass**	**Probability[a]**
$\{Cu_3(H_2O)_2Cl(BiW_9O_{33})_2\}^{12-}$	5044.52	81.29 %
$\{Cu_4(H_2O)_3Cl(BiW_9O_{33})_2\}^{10-}$	5126.46	16.00 %
$\{Cu_5(H_2O)_4Cl(BiW_9O_{33})_2\}^{8-}$	5208.40	2.56 %
$\{Cu_6(H_2O)_5Cl(BiW_9O_{33})_2\}^{6-}$	5272.44	0.15 %

[a] Assuming a stochastically independent distribution of Cu(II) cations.

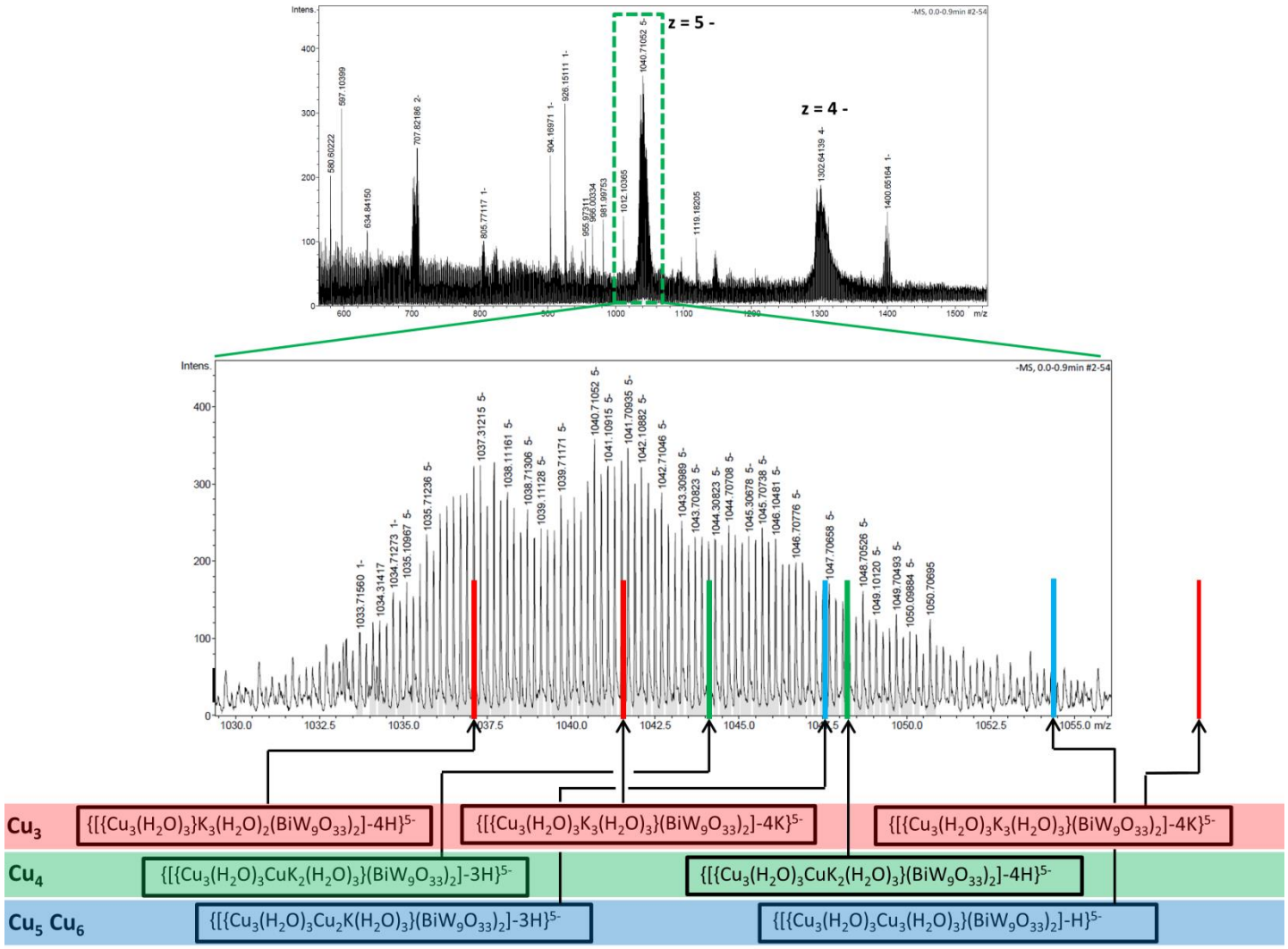

Figure S3.9. HR-ESI-MS of **Cu-5** with positions of different possible heteropolyanions with their possible K/H adducts; blue = Cu_5, Cu_6 cores, green = Cu_4 cores, red = Cu_3 cores.

3.3.8 Photocatalytic Properties of Cu-5

All catalytic tests were performed in 10 mL headspace vials, sealed with a natural rubber septum (VWR) and a crimp cap (Supelco). Catalytic test solutions were irradiated under stirring with a blue LED (460 nm 4650 Lux). O_2 evolution was monitored with a Clark sensor (OX-N) from Unisense and quantified by GC (Agilent Technologies 7820A gas chromatograph, with helium 6.0 purity). H_2 evolution was monitored with a Clark-type H_2 sensitive sensor (H2-NP) from Unisense and quantified by GC (Varian CP 3800 Gas Chromatograph). The sensors were calibrated prior to each experiment with a two point calibration using a sample with known concentrations of O_2/H_2. In order to quantify the amount of hydrogen produced during catalysis, gas samples from the headspace were analyzed by gas chromatography.

3.3.8.1 Photocatalytic O_2 Evolution

$[Ru(bpy)_3]Cl_2$ was used as photosensitizer (PS) and $Na_2S_2O_8$ as sacrificial electron acceptor. The catalytic activity was tested in three different buffer solutions (acetate pH = 4.75; NaPi pH = 7.0; borate pH = 8.0 at 100 µM buffer concentration). This covers a pH range in which O_2 evolution has been reported previously for similar polyoxometalate-based water oxidation catalysts. The formation of a solid precipitate (POM-PS complex) was observed in all photocatalytic tests. Previous studies have investigated such POM-PS complex formation through electrostatic interactions of the negatively charged polyanion and the positively charged photosensitizer cation $[Ru(bpy)_3]^{2+}$ in more detail.[60–66] The observed characteristic FT-IR bands of the POM-PS complex can be assigned to the polyanion and to the ruthenium sensitizer, respectively. The elemental composition was analyzed by an EDX mapping which indicates the presence of larger tungsten containing domains, probably due to residual undissolved **Cu-5** (Figure S3.10).

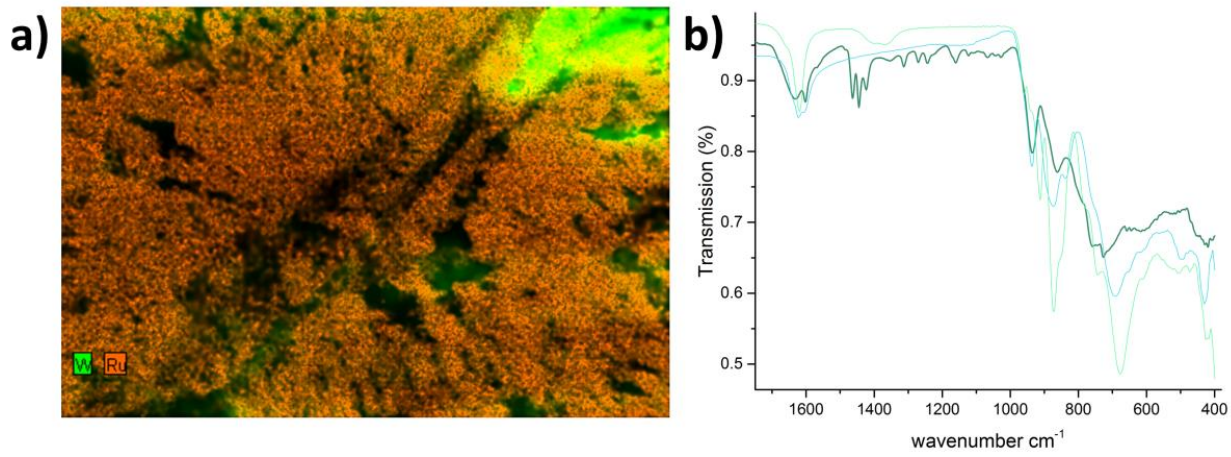

Figure S3.10. (**a**) EDX mapping of the PS-complex (magnification 230x) showing the distribution of W and Ru. (**b**) IR spectrum of the PS complex of **Cu-5** (black) vs. pristine **Cu-5** (blue) $Na_9[BiW_9O_{33}]\cdot 19.5\ H_2O$ (blue).

3.3.8.2 Photocatalytic H_2 Evolution

An ascorbate buffer system at pH 4 was prepared in demineralized water (8.0 mL), and ascorbic acid (88.0 mg, 0.499 mmol) and sodium ascorbate (98.0 mg, 0.494 mmol) were added for a total buffer concentration of 0.12 M. $[Ru(bpy)_3]Cl_2\cdot 6H_2O$ (1 mM) was used as photosensitizer according to previous standard protocols.[67,62] The catalyst was dissolved in 1.0 mL of the prepared buffer solution and added dropwise, affording turbid solutions in the presence of the photosensitizer due to POM-PS complex formation (see Figure S3.10). This phenomenon was observed in catalytic tests with **Cu-5** as well as in catalytic tests with $[BiW_9O_{33}]^{9-}$. All catalytic tests were prepared under exclusion of light and purged with Ar gas for 15 min prior to irradiation with a blue LED (λ = 470 nm, 4650 LUX).

Table S3.11. Results of photocatalytic tests with **Cu-5**, BiW_9, and blank measurements.

Compound	Concentration (µM)	H_2 (µL)	TON[a]
Cu-5	10.7	65.2	16.4
Cu-5	23.0	55.9	1.6
Cu-5	48.6	46.4	5.5
Cu-5	104.0	40.1	0.5
Blank$_{(max)}$	---	39.1	---
Blank$_{(min)}$	---	29.9	---
BiW_9	12.3	114.1	34.4
BiW_9	23.8	41.0	8.8
BiW_9	25.8	41.1	8.1
BiW_9	55.1	152.8	11.3
BiW_9	73.3	131.7	7.0
BiW_9	108.9	128.6	4.6
BiW_9	122.8	112.1	3.4
BiW_9	148.7	99.5	2.4
$CuSO_4$	25.0	21.9	0
$CuSO_4$	100.0	7.03	0
$CuSO_4$	150.0	12.2	0

[a] TONs were calculated after subtraction of the background contribution to the total amount of H_2.

For **Cu-5** concentrations in the range of 12.5 – 100 µM, formation of 41 to 65 µL H_2 was observed, i.e. values slightly above the background in the absence of catalyst (Table S3.11). The highest TON was obtained for 10.7 µM **Cu-5** (TON = 31.2). Reference experiments with the lacunary precursor $[B\text{-}\alpha\text{-}BiW_9O_{33}]^{9-}$ afforded an approximately three-fold higher catalytic activity at a catalyst concentration of 50.0 µM with respect to molar H_2 formation and an approx. double TON compared to **Cu-5**. Catalytic tests with lower **BiW_9** concentrations (≤ 50 µM) show a high variance due to difficulties in sample preparation for the particularly low amounts of catalyst (approximately 0.2-0.5 mg). The lower evolved H_2 quantities and TONs for **Cu-5** compared to **BiW_9** shows that Cu-functionalization is not a straightforward strategy to improve tungstobismuthate based H_2 evolution catalysts. The POM-PS complex (cf. above) of **Cu-5** and $[Ru(bpy)_3]^{2+}$ photosensitizer can be considered as potential active species according to previous studies.[66,60,61] Therefore, it was collected by centrifugation, air dried and characterized by FT-IR spectroscopy and EDX analysis (Figure S3.10). Catalyst recycling experiments were then performed in a fresh solution of ascorbate buffer with $[Ru(bpy)_3]Cl_2$, where the POM-PS complex (497 µg) was added instead of the pristine catalyst and dispersed by sonication for 30 min.

Subtraction of the background H_2 formation by $[Ru(bpy)_3]^{2+}$ demonstrated that no additional H_2 amounts are formed in the presence of the recycled catalyst.

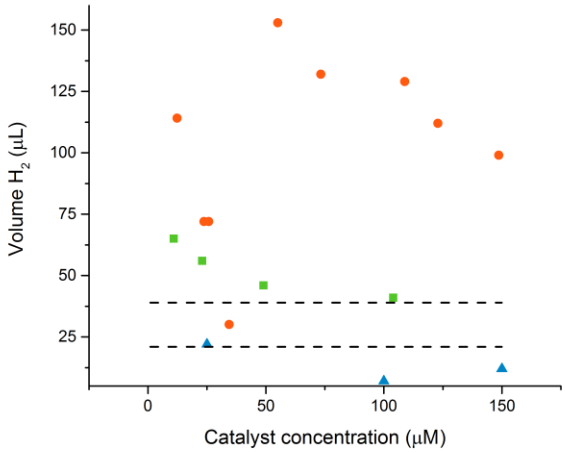

Figure S3.11. H_2 yields quantified by GC analysis of **Cu-5** (green), $CuSO_4 \cdot 5H_2O$ (blue), and BiW_9 (red); the dotted line shows the maximal/minimal amount of H_2 formed in absence of catalyst. Conditions: ascorbate buffer (1.2 M, pH = 4.0), $[Ru(bpy)_3]Cl_2$ (1 mM), irradiation by LED (460 nm 4650 LUX).

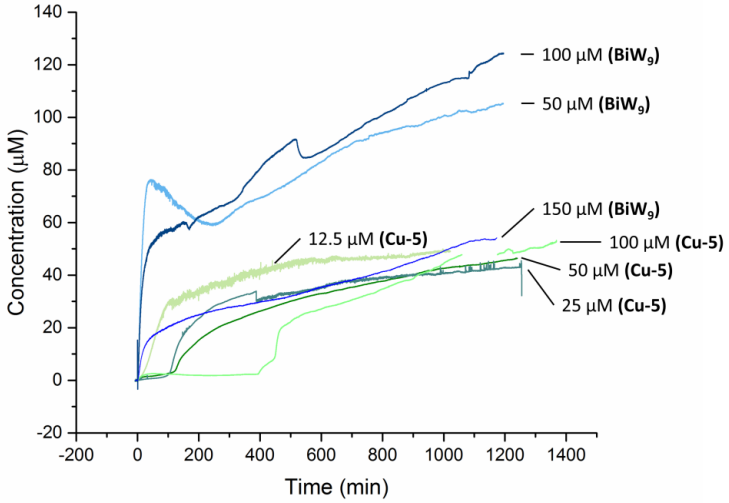

Figure S3.12. Time dependent H_2 evolution measured with a H_2 sensitive Clark-type sensor: 50-150 µM $[BiW_9O_{33}]^{9-}$ (blue), 12.5-100 µM **Cu-5** (green).

3.3.9 The Structure of Cu(II) Bridged Paratungstate B (Cu-6)

The paratungstate B structure is composed of two different subunit types, namely the cap-type $\{HW_3O_{13}\}$ in which three WO_6 octahedra share a common O atom (W–O bond lengths, terminal: 1.716(4)-1.736(5) Å; axial 2.238(4)-2.264(4) Å; equatorial: 1.789(4)-2.105(4) Å) and a $\{W_3O_{14}\}$ unit of three edge sharing WO_6 octahedron without any shared oxygen atom (Figure S3.13; W–O bond lengths, terminal: 1.723(5)-1.777(4) Å; equatorial: 1.777(4)-2.329(4) Å). Bridging of monomeric $[H_2W_{12}O_{40}]^{10-}$ units occurs via coordination to a Cu(II) ion with Jahn-Teller distorted octahedral coordination geometry.

A total of 4 sodium and 4 potassium counter-cations were refined according to their coordination geometry. Charge balance is achieved by taking into account two hydrogen atoms coordinating to the oxygen atoms O(15) inside of the polyanion. The presence of hydrogen atoms was established earlier by neutron diffraction studies.[39]

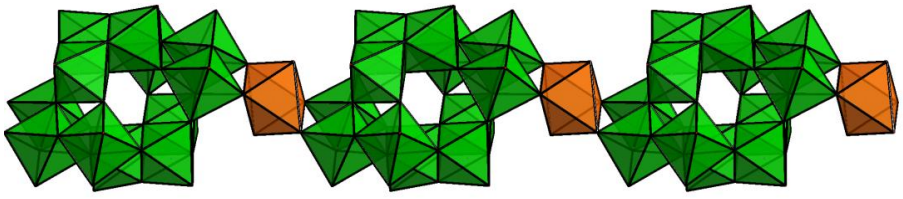

Figure S3.13. Polyhedral ball-and stick representation of **Cu-6**.

3.3.10 Experimental

3.3.10.1 Preparation of Single Crystals

All chemicals were obtained commercially and used without further purification. The lacunary precursor $Na_9[BiW_9O_{34}]\cdot 19.5H_2O$ was prepared according to published procedures and characterized by FT-IR spectroscopy.[68] Repeated syntheses of this precursor showed that these commonly used protocols may also result in the formation of $[W_{12}O_{42}]^{12-}$ or $[Bi_2W_{22}O_{76}]^{12-}$. Furthermore this precursor may contain a small amount of an insoluble impurity which cannot be detected by IR or PXRD. It can be removed from the reaction mixture prior to the addition of the counter cation by filtration over celite. Regarding the low stability of this precursor and the likelihood that it undergoes partial decomposition or α-β isomerization, $Na_9[BiW_9O_{34}]\cdot 19.5H_2O$ cannot be purified by recrystallization.

All reported procedures in the following resulted in the formation of at least one high quality single crystal for structure analysis. Formation of phase pure bulk material could **only** be confirmed for **Cu-5** by PXRD analysis.

3.3.10.2 Source of $Na_{12}[Cu_2(H_2O)_4Cl_2(B\text{-}\beta\text{-}BiW_{10}O_{35})_2]\cdot 36.5H_2O$ / $Na_{10}[Cu_2(H_2O)_6(B\text{-}\beta\text{-}BiW_{10}O_{35})_2]$ $36.5H_2O$ (Cu-1)

A solution of $Na_9[BiW_9O_{34}]\cdot 19.5H_2O$ (4.00 g, 1.65 mmol) was prepared in demineralized H_2O (40 mL). The starting material $Na_9[BiW_9O_{34}]\cdot 19.5H_2O$ may contain minor amounts of an insoluble impurity which was removed by filtration over celite. A solution of $CuSO_4\cdot 5H_2O$ (20 mL, 2.4 mM) was added dropwise under vigorous stirring, the colorless solution thereby becomes green. During the addition of the copper sulfate solution, a solid precipitated which was removed by centrifugation. A solution of saturated KCl was added dropwise to the stirred reaction mixture until a solid precipitated which re-dissolved after a few seconds. The green solution was left for crystallization, which led to the formation of crystals of **Cu-1**.

3.3.10.3 Source of 2D-$Na_7K_3Cu_{0.5}Cl[Cu_2(H_2O)_4(B\text{-}\beta\text{-}BiW_{10}O_{35})_2]\cdot 29.5H_2O$ (Cu-2), 2D-$Na_{5.5}K_{2.5}Cu[Cu_2(H_2O)_4(B\text{-}\beta\text{-}BiW_{10}O_{35})_2]\cdot 17.5H_2O$ (Cu-3) and $Na_6Rb_6[Cu_3(H_2O)_3(B\text{-}\beta\text{-}BiW_9O_{33})_2]\cdot 21H_2O$ (Cu-4) crystals

Crystals of **Cu-2**, **Cu-3** and **Cu-4** were obtained from the same reaction mixture by adding different counter-cations.

A solution of of $Na_9[BiW_9O_{34}]\cdot 19.5H_2O$ (1.00 g, 0.41 mmol) was prepared in demineralized H_2O (10 mL). The starting material $Na_9[BiW_9O_{34}]$ $19.5H_2O$ may contain a small amount of an insoluble impurity which was removed by filtration over celite. A solution of $CuSO_4\cdot 5H_2O$ (10 mL, 1.2 mM) was added dropwise to the stirred reaction mixture. During the addition, the color changed to green. The pH after the addition was 5.3. The reaction mixture was divided into 2 parts of 10 mL.

Cu-2 and Cu-3: A saturated solution of KCl was added to the stirred reaction mixture until a solid precipitated which was removed by filtration over celite. The reaction mixture was left for crystallization. Crystals of **Cu-2** and **Cu-3** form simultaneously with an unidentified green slurry. The crystals were removed carefully from this slurry and stored in a saturated solution of KCl.

Cu-4: A solution of RbCl (1.0 M) was added dropwise to the stirred reaction mixture until a solid formed which was removed by filtration. The green solution was left for crystallization which led to the formation of crystals of **Cu-4**.

3.3.10.4 Source of 3D-$K_{6.89}Cu_{0.43}H_{0.93}[(Cu_3(H_2O)_2Cl)(K_{2.68}Cu_{0.32}(H_2O)_3(B\text{-}\alpha\text{-}BiW_9O_{33})_2]\cdot 13H_2O$ (Cu-5).

A solution of $CuSO_4\cdot 5H_2O$ (0.40 g, 1.60 mmol, 4.0 eq.) was prepared in demineralized H_2O (5 mL), the pH of this solution was 3.9. The precursor $Na_9[BiW_9O_{33}]\cdot 19.5H_2O$ (1.00 g, 0.41 mmol, 1.0 eq.) was added as a solid in small portions. The volume of the reaction mixture was increased to 10 mL by adding H_2O. The reaction mixture was stirred for 2 h, and a solid precipitate was removed by filtration through celite. The pH of the reaction mixture after stirring was 5.0. A saturated solution of KCl (2 mL) was added and the reaction mixture was left for crystallization. Yellow crystals and a fine white precipitate formed overnight. The crystals were removed carefully from the reaction mixture (41.7 mg, 3.49 %). Elemental analysis: calc. for

$Bi_2ClCu_{3.82}H_{15.93}K_{9.19}O_{82}W_{18}$ (found): Bi 7.34 (7.68), Cl 0.62 (0.42), Cu 4.26 (4.29), W 58.13 (55.4), K 6.31 (6.12). (ATR FT-IR cm^{-1}): 1624, 1605, 935, 874, 837, 692, 496, 430.

3.3.10.5 Source of 1D-$Na_4K_4Cu[H_2W_{12}O_{42}]\cdot 24H_2O$ (Cu-6).

A solution of $Na_9[BiW_9O_{33}]\cdot 19.5H_2O$ (3.00 g, 1.24 mmol, 1.0 eq.) was prepared in demineralized H_2O (30 mL); all undissolved solids were removed by filtration. A solution of $CuSO_4\cdot 5H_2O$ (10 mL, 0.12 M) was added dropwise and the color of the reaction mixture changed to green. A solid which precipitated during the addition was removed by filtration over celite. A saturated solution of KCl (0.75 mL) was added and the reaction mixture was left for crystallization. Colorless block-like crystals were observed in the reaction mixture after a few days.

3.3.11 Instrumentation

For a list of instruments and procedures used for the characterization of **Ga-1** and **Ga-2** see §1.17.2.

3.4 References

[1] F. Hussain, F. Conrad, G. R. Patzke, *Angew. Chem. Int. Ed.* **2009**, *48*, 9088–9091.

[2] P.-E. Car, B. Spingler, S. Weyeneth, J. Patscheider, G. R. Patzke, *Polyhedron* **2013**, *52*, 151–158.

[3] H. Jin, Y. Qi, E.-B. Wang, Y. Li, X. Wang, C. Qin, S. Chang, *Cryst. Growth. Des.* **2006**, *6*, 2693–2698.

[4] H. Fu, W. Chen, E.-B. Wang, J. Liu, S. Chang, *Inorg. Chim. Acta.* **2009**, *362*, 1412–1420.

[5] G. Rousseau, L. M. Rodriguez-Albelo, W. Salomon, P. Mialane, J. Marrot, F. Doungmene, I.-M. Mbomekallé, P. De Oliveira, A. Dolbecq, *Cryst. Growth. Des.* **2015**, *15*, 449–456.

[6] B.-W. Chen, W.-L. Chen, Y.-G. Li, E.-B. Wang, *J. Clust. Sci.* **2011**, *22*, 73–85.

[7] C. Tourne, A. Revel, G. Tourne, M. Vendrell, *C. R. Acad. Sci. Paris* **1973**, *281 C*, 933.

[8] M. Bösing, I. Loose, H. Pohlmann, B. Krebs, *Chem. Eur. J.* **1997**, *3*, 1232–1237.

[9] Y.-Q. Jiao, C. Qin, X.-L. Wang, C.-G. Wang, C.-Y. Sun, H.-N. Wang, K.-Z. Shao, Z.-M. Su, *Chem. Asian J.* **2014**, *9*, 470–478.

[10] C.-Y. Sun, S.-X. Liu, C.-L. Wang, L.-H. Xie, C.-D. Zhang, B. Gao, E.-B. Wang, *J. Coord. Chem.* **2007**, *60*, 567–579.

[11] F. Evangelisti, P.-E. Car, O. Blacque, G. R. Patzke, *Catal. Sci. Technol.* **2013**, *3*, 3117–3129.

[12] C. Roşu, T. J. R. Weakley, *Acta Crystallogr. C.* **1999**, *55*.

[13] I. Loose, E. Droste, M. Bösing, P. Heinrich, Michael, H., Dickman, C. Roşu, M. T. Pope, B. Krebs, *Inorg. Chem.* **1999**, *38*, 2688–2694.

[14] M. Bösing, A. Nöh, I. Loose, B. Krebs, *J. Am. Chem. Soc.* **1998**, *120*, 7252–7259.

[15] X.-J. Su, M. Gao, L. Jiao, R.-Z. Liao, P. E. M. Siegbahn, J.-P. Cheng, M.-T. Zhang, *Angew. Chem. Int. Ed.* **2015**, *54*, 4909–4914.

[16] S. M. Barnett, K. I. Goldberg, J. M. Mayer, *Nat. Chem.* **2012**, *4*, 498–502.

[17] R. Al-Oweini, A. Sartorel, B. S. Bassil, M. Natali, S. Berardi, F. Scandola, U. Kortz, M. Bonchio, *Angew. Chem. Int. Ed.* **2014**, *53*, 11182–11185.

[18] A. Sartorel, M. Carraro, G. Scorrano, R. De Zorzi, S. Geremia, N. D. McDaniel, S. Bernhard, M. Bonchio, *J. Am. Chem. Soc.* **2008**, *130*, 5006–5007.

[19] Y. V. Geletii, B. Botar, P. Kögerler, D. A. Hillesheim, D. G. Musaev, C. L. Hill, *Angew. Chem. Int. Ed.* **2008**, *47*, 3896–3899.

[20] H. Lv, J. Song, Yurii V. Geletii, J. W. Vickers, Jordan M. Sumliner, D. G. Musaev, Paul Kögerler, P. F. Zhuk, John Bacsa, G. Zhu, C. L. Hill, *J. Am. Chem. Soc.* **2014**, *136*, 9268–9271.

[21] Q. Yin, J. M. Tan, C. Besson, Y. V. Geletii, D. G. Musaev, A. E. Kuznetsov, Z. Luo, K. I. Hardcastle, C. L. Hill, *Science* **2010**, *328*, 342–345.

[22] R. Al-Oweini, B. S. Bassil, J. Friedl, V. Kottisch, M. Ibrahim, M. Asano, B. Keita, G. Novitchi, Y. Lan, A. Powell, U. Stimming, U. Kortz, *Inorg. Chem.* **2014**, *53*, 5663–5673.

[23] *Molecular Water Oxidation Catalysis*, John Wiley & Sons, Ltd, **2014**.

[24] S. M. Barnett, C. R. Waidmann, M. L. Scheuermann, J. C. Nesvet, K. Goldberg, J. M. Mayer in *Molecular Water Oxidation Catalysis*, John Wiley & Sons, Ltd, **2014**.

[25] J. Wu, C.-X. Wang, Z.-H. Su, K. Yu, Y.-L. Xu, B.-B. Zhou, *Chin. J. Struct. Chem.*, *31*, 271–279.

[26] L. Wang, K. Yu, B.-B. Zhou, Z.-H. Su, S. Gao, L.-L. Chu, J.-R. Liu, *Dalton Trans.* **2014**, *43*, 6070–6078.

[27] I. Lindqvist, *Acta Crystallogr.* **1952**, *5*, 667–670.

[28] H. T. Evans, O. W. Rollins, *Acta Crystallogr. B.* **1976**, *32*, 1565–1567.

[29] K. D. von Allmen, P.-E. Car, O. Blacque, T. Fox, R. Müller, G. R. Patzke, *Z. anorg. allg. Chem.* **2014**, *640*, 781–789.

[30] M. A. Halcrow, *Chem. Soc. Rev.* **2013**, *42*, 1784–1795.

[31] C. X. Weichenberger, P. V. Afonine, K. Kantardjieff, B. Rupp, *Acta Crystallogr. D.* **2015**, *71*, 1023–1038.

[32] P. I. Molina, H. N. Miras, D.-L. Long, L. Cronin, *Dalton Trans.* **2014**, *43*, 5190–5199.

[33] P. Mialane, J. Marrot, E. Rivière, J. Nebout, G. Hervé, *Inorg. Chem.* **2001**, *40*, 44–48.

[34] U. Kortz, N. K. Al-Kassem, M. G. Savelieff, N. A. Al Kadi, M. Sadakane, *Inorg. Chem.* **2001**, *40*, 4742–4749.

[35] J.-P. Wang, P.-T. Ma, J. Li, H.-Y. Niu, J.-Y. Niu, *Chem. Asian J.* **2008**, *3*, 822–833.

[36] U. Kortz, S. Nellutla, A. C. Stowe, N. S. Dalal, J. van Tol, B. S. Bassil, *Inorg. Chem.* **2004**, *43*, 144–154.

[37] X. Xu, F. Luo, W. Luo, J. Chen, *Z. Naturforsch. B.* **2009**, *64*, 269–273.

[38] Q.-J. Kong, C.-J. Zhang, Y.-G. Chen, *J. Mol. Struct.* **2010**, *964*, 82–87.

[39] H. T. J. Evans, E. Prince, *J. Am. Chem. Soc.* **1983**, *105*, 4838–4839.

[40] C. Rocchiccioli-Deltcheff, R. Thouvenot, R. Franck, *Spectrochimica Acta Part A: Molecular Spectroscopy* **1976**, *32*, 587–597.

[41] R. Thouvenot, M. Fournier, R. Franck, C. Rocchiccioli-Deltcheff, *Inorg. Chem.* **1984**, *23*, 598–605.

[42] C. Rocchiccioli-Deltcheff, M. Fournier, R. Franck, R. Thouvenot, *Inorg. Chem.* **1983**, *22*, 207–216.

[43] A. C. Stowe, S. Nellutla, N. S. Dalal, U. Kortz, *Eur. J. Inorg. Chem.* **2004**, *2004*, 3792–3797.

[44] D. Rusu, A. R. Tomasa, G. L. Turdean, I. Cojocaru, B. Oana, M. Rusu, *Rev. Roum. Chim.* **2012**, *57*, 327–336.

[45] X. Xu, L. Zhang, Y. Zhang, B. Qi, L. Fang, *Z. Naturforsch. B.* **2009**, *64*, 821–825.

[46] C. Roşu, D. Rasu, T. J. R. Weakley, *J. Chem. Crystallogr.* **2003**, *33*, 751–755.

[47] D. Rusu, C. Roşu, C. Crăciun, L. David, M. Rusu, G. Marcu, *J. Mol. Struct.* **2001**, *563–564*, 427–433.

[48] G.-L. Xue, H.-L. Wang, Z.-H. Xie, Q.-Z. Shi, J.-W. Wang, D.-Q. Wang, *Chinese J. Chem.* **2004**, *22*, 159–161.

[49] C. Roşu, M. Rusu, N. Casañ-Pastor, C. J. Gómez-Garciac, *Syn. React. Inorg. Met.* **2000**, *30*, 369–377.
[50] Y.-W. Li, Y.-H. Wang, Y.-G. Li, E.-B. Wang, W.-L. Chen, Q. Wu, Q. Shi, *Inorg. Chim. Acta.* **2009**, *362*, 1078–1082.
[51] Z. Zhang, *J. Chem. Crystallogr.* **2012**, *42*, 333–337.
[52] B. Li, L. Bi, W. Li, L. Wu, *J. Solid State Chem.* **2008**, *181*, 3337–3343.
[53] C.-J. Zhang, Y.-G. Chen, D.-m. Shi, H.-j. Pang, *Z. Naturforsch. B.* **2014**, *63b*, 187–192.
[54] S. V. Radio, N. A. Melnik, E. S. Ivantsova, V. N. Baumer, *J. Struct. Chem.* **2014**, *55*, 879–886.
[55] B. Wang, G.-F. Hou, R.-Q. Meng, L.-H. Bi, B. Li, L.-X. Wu, *CrystEngComm* **2011**, *13*, 1360–1365.
[56] Delina Barats-Damatov, L. J. W. Shimon, Y. Feldman, Tatyana Bendikov, R. Neumann, *Inorg. Chem.* **2015**, *54*, 628–634.
[57] R. S. Winter, L. De-Liang, L. Cronin, *Inorg. Chem.* **2015**, *54*, 4151–4155.
[58] K.-Y. Wang, Z. Lin, B. S. Bassil, X. Xing, A. Haider, B. Keita, G. Zhang, C. Silvestru, U. Kortz, *Inorg. Chem.* **2015**, *54*, 10530–10532.
[59] I. D. Brown, D. Altermatt, *Acta Crystallogr. B.* **1985**, *41*, 244–247.
[60] P.-E. Car, M. Guttentag, K. K. Baldridge, R. Alberto, G. R. Patzke, *Green. Chem.* **2012**, *14*, 1680–1688.
[61] J. J. Stracke, R. G. Finke, *ACS Catal.* **2014**, *4*, 909–933.
[62] K. D. von Allmen, R. Moré, R. Müller, J. Soriano-López, A. Linden, G. R. Patzke, *ChemPlusChem* **2015**, *80*, 1389–1398.
[63] N. Fay, V. M. Hultgren, A. G. Wedd, T. E. Keyes, R. J. Forster, D. Leane, A. M. Bond, *Dalton Trans.* **2006**, 4218–4227.
[64] M. K. Seery, L. Guerin, R. J. Forster, E. Gicquel, V. Hultgren, A. M. Bond, A. G. Wedd, T. E. Keyes, *J. Phys. Chem. A* **2004**, *108*, 7399–7405.
[65] T. E. Keyes, E. Gicquel, L. Guerin, R. J. Forster, V. M. Hultgren, A. M. Bond, A. G. Wedd, *Inorg. Chem.* **2003**, *42*, 7897–7905.
[66] J. Gao, S. Cao, Q. Tay, Y. Liu, L. Yu, K. Ye, P. C. S. Mun, Y. Li, G. Rakesh, S. C. J. Loo, Z. Chen, Y. Zhao, C. Xue, Q. Zhang, *Sci. Rep.* **2013**, *3*, 1853–1858.
[67] C. Bachmann, B. Probst, M. Guttentag, R. Alberto, *Chem. Commun.* **2014**, *50*, 6737–6739.
[68] B. Botar, T. Yamase, E. Ishikawa, *Inorg. Chem. Commun.* **2000**, *3*, 579–584.

Chapter 4

Nickel-Containing Keggin-type Polyoxometalates as Hydrogen Evolution Catalysts: Photochemical Structure Activity Relationships

4 Nickel Containing Keggin-type POMs for H_2 Evolution

All results presented in chapter 3 have been published:
Kim von Allmen†, René Moré†, Rafael Müller, Joaquín Soriano-López, Anthony Linden and Greta R. Patzke* ChemPlusChem, **2015**, 80 (9), 1389-1398. DOI: 10.1002/cplu.201500074
† = Equal contribution

4.1 Introduction

Fossil fuels have been the cornerstone of modern technology and their limited reserves have launched a worldwide search for sustainable energy alternatives. Artificial photosynthesis is an elegant strategy for converting light energy into storable chemical fuels in a single process.[1–3] Currently, overall water splitting setups are frequently based on separate water oxidation and reduction catalysts (WOCs and WRCs).[4–7] However, structure-activity relationships (SAR) and underlying mechanisms pose a challenge in WOC/WRC design and are under intense investigation, especially for larger molecular or nanostructured catalysts.[8–10]

Polyoxometalates (POMs) keep attracting research attention due to their exceptional compositional and size diversity that extends from molecular to nanoscale dimensions. These versatile metal-oxo clusters are preferably formed from tungsten, molybdenum and vanadium in their highest oxidation states,[11–20] and they can host a wide range of transition metals.[10,21–24] POMs furthermore display a rich redox chemistry that can be fine-tuned through their manifold structural modifications.[25–28] Their unique structural flexibility renders POMs ideal model compounds for catalytic structure-activity studies in artificial photosynthesis research. Since the breakthrough discovery of the first POM based water oxidation catalyst $[Ru_4(\mu\text{-}O)_4(\mu\text{-}OH)_2(H_2O)_4(SiW_{10}O_{36})]^{10-}$,[29–31] numerous POM-WOCs with different metal cores have been reported.[32–35] Predictive design of high performance POM-WOCs with abundant metal cores still remains a challenge and the detailed mechanistic steps of the respective O_2 evolution cycles have not been fully elucidated for most catalysts. In contrast, considerably less is known about the application of POMs as photochemical water reduction catalysts. Their activity as electrocatalysts for electrochemical H_2 evolution,

however, has been studied in more detail.[36,37,25,38,39] Earlier work in organic photocatalysis demonstrated that POMs can reduce protons in aerobic media to molecular hydrogen.[23,40]

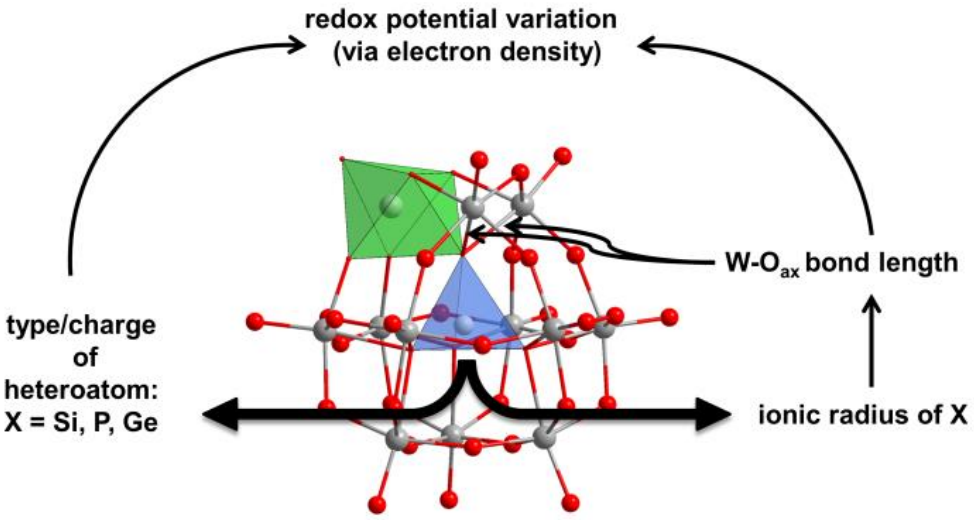

Figure 4.1. Ball and stick representation of polyanions **P-1**, **Ge-2**, and **Si-3** (blue tetrahedron: heteroatom, green polyhedron: {NiO_6}).

Nonetheless, only a limited number of polyoxometalates have been tested to date as water reduction catalysts (WRC) for visible light driven H_2 evolution (Table 4.1). These examples vary widely with respect to structural features, with Keggin-type compounds emerging as key targets.[40–44] The influence of transition metal substitution on the H_2 evolution activity was recently investigated for two series of Keggin-type POMs, namely $[M(H_2O)TiW_{11}O_{39}]^{n-}$ (M = Fe, Co, Zn)[42] and $[M(H_2O)SiW_{11}O_{39}]^{6-}$ (M = Cu, Ni, Co, Zn).[44] Another study on transition metal free Keggin-type catalysts $[XW_{12}O_{40}]^{n-}$ (X = P, Si, Fe, H) reported H_2 evolution for all members of the series with P-substituted representatives displaying the most positive reduction potential.[40] The effect of the heteroatom in Keggin-type structures was reviewed by Weinstock et al. for catalytic O_2 reduction.[45] Heteroatom-based efficiency tuning has also been applied to POM-WOCs, such as the Co substituted WOC $[\{Co_4(OH)_3(PO_4)\}_4(XW_9O_{34})_4]^{n-}$ (X = Si, Ge, As; n = 32 for Si, Ge; n = 28 for As and P). Light driven water oxidation performance depended on the heteroatom as follows: Si ≤ P < As < Ge.[24] This notable influence of redox-inert sites on the overall reaction mechanism is an interesting analogy to the intensely investigated role of the Ca^{2+} center in photosystem II.[46–49]

Most recently, Hill et al. reported a breakthrough in terms of turnover number (TON) for the sandwich-type WRC $[Ni_4(H_2O)_2(PW_9O_{34})_2]^{10-}$ which catalyzes light driven H_2 evolution with a TON of 6500 in long-term catalytic tests over 7d.[50]

However, the previously reported POM-WRCs have been tested under very different catalytic conditions (Table 4.1), often in the presence of co-catalysts, such as Pt containing compounds, additional photosensitizers or specifically in organic solvents.[51] As reported earlier for POM WOCs,[52] catalyst stability is also a critical issue in H_2 evolution catalysis.[53] This renders the systematic derivation of structure-activity relationships from the present studies difficult.

Herein we report on the nickel substituted Keggin-type POMs $[Ni(H_2O)PW_{11}O_{39}]^{5-}$ (**P-1**), $[Ni(H_2O)GeW_{11}O_{39}]^{6-}$ (**Ge-2**), and $[Ni(H_2O)SiW_{11}O_{39}]^{6-}$ **(Si-3)**. The title compounds were investigated for WRC activity with $[Ru(bpy)_3]^{2+}$ as photosensitizer in aqueous media without additional co-catalysts. The choice of nickel was inspired by its key function as the active site in natural hydrogenase enzymes,[54] along with its high activity in solid-state and molecular WRCs and versatile structural chemistry.[55–61] Hydrogen production among the Ni-based Keggin-POM series clearly depends on the respective heteroatom (Figure 4.1). The observed catalytic trends were correlated with electrochemical characterizations and with electronic structures of the Ni-containing POMs emerging from DFT calculations.

4.2 Results and Discussion

4.2.1 Single Crystal X-ray Structure Determination

The packing motifs and molecular structures of the title compound series $K_5[Ni(H_2O)PW_{11}O_{39}]\cdot 14H_2O$ **(P-1)**, $K_6[Ni(H_2O)GeW_{11}O_{39}]\cdot 14H_2O$ **(Ge-2)** and $K_6[Ni(H_2O)SiW_{11}O_{39}]\cdot 14H_2O$ **(Si-3)** were determined by single crystal X-ray diffraction (Figure 4.2). All three Ni-monosubstituted Keggin-type polyoxotungstates **P-1**, **Ge-2**, and **Si-3** are essentially isostructural and crystallize in the tetragonal space group $P\bar{4}n2$ (Z = 2). Although two other space groups display the same systematic absences, only structure solution in $P\bar{4}n2$ leads to geometrically and chemically consistent structural models with the central heteroatoms located on a $\bar{4}$ symmetry site. The same space group has furthermore been found for related Keggin-type structures.[62–65] The oxocluster structure of $[Ni(H_2O)PW_{11}O_{39}]^{5-}$ **(P-1)** has previously been reported in a different space group ($P4_2/ncm$)

with Cs^+ as a counter-cation.[66] All three crystal structures reported here show Ni/W disorder at one W site which was refined with a Ni/W site occupancy ratio of 0.25:0.75 in line with elemental analyses. This value leads to reasonable atomic displacement parameters for the Ni/W(1) disordered sites. Bond valence sum (BVS) values for non-disordered tungsten atoms are in the range of 6.02-6.17 in agreement with the +VI oxidation state. For all oxygen atoms, BVS values are close to 2 (1.89-1.99 for terminal oxygen atoms, 1.75-2.50 for equatorial oxygen atoms), thus indicating the presence of oxo groups.

Table 4.1. Overview of studies on POM WRCs (PS = photosensitizer, ED = electron donor, Co-cat = Co-catalyst).<

POM	PS/ED	Co-cat	Medium	TON/TOF[a]	Time (h)	Ref.
$[XW_{12}O_{40}]^{n-}$ (X = P, Si, Fe, H)	---/isopropyl alcohol	Pt	0.1 M $HClO_4$	8.2/---	24	[40]
α-$[Al(H_2O)SiW_{11}O_{39}]^{5-}$	EosinY/TEOA	Pt	1.0 M HCl	12.5/7 s^{-1}	20	[41]
$[M(H_2O)TiW_{11}O_{39}]^{n-}$ (M = Fe, Co, Zn)	---/polyvinyl alcohol (PVA)	---	PVA/H_2O (pH = 1.0)	3.2/--- (M = Co)	3	[42]
$[Co^{III}(H_2O)Co^{II}W_{11}O_{39}]^{7-}$	EosinY/TEOA	Pt	H_2O	100/7·10^{-6} s^{-1}	2.3	[43]
$[M(H_2O)SiW_{11}O_{39}]^{n-}$ (M = Ni, Cu, Co, Zn)	---/Zn powder	Pt	H_2O	1.5/--- (M = Cu)	6	[44]
$[Ni_4(H_2O)(PW_9O_{34})_2]^{10-}$	$[Ir(ppy)_2(dtbbpy)]^+$/TEOA	---	CH_3CN/DMF	290/---	2.5	[50]
$[Mn_4(H_2O)_2(VW_9O_{34})_2]^{10-}$	$[Ru(bpy)_3]^{2+}$/TEOA	---	DMF/H_2O	42/---	5.5	[51]
$[Sn_4(SiW_9O_{34})_2]^{12-}$	---/MeOH	Pt	MeOH (20 vol. %)	1.4/7·10^{-6} s^{-1}	56	[67]
$[Fe_6Se_6W_{34}O_{124}(OH)_{16}]^{18-}$	---/MeOH	---	MeOH (20 vol. %)	181/1.4 10^{-3} s^{-1}	12	[68]
$[Fe_{10}Se_8W_{62}O_{222}(OH)_{18}(H_2O)_4]^{28-}$	---/MeOH	---	MeOH (20 vol. %)	193/4.5 10^{-3} s^{-1}	12	[68]
$[Nb_4O_6(SiW_9Nb_3O_{40})_4]^{20-}$	---/MeOH	Pt	MeOH (10 vol. %)	220/15·10^{-3} s^{-1}	12	[69]
$[H_2MNb_9O_{28}]^{n-}$ (M = Ni, Co, Mn, Fe, Cr)	---/MeOH	---	MeOH (20 vol. %)	7.5/--- (M = Ni)	8	[53]
$[H_2TeNb_5O_{19}]^{5-}$	---/MeOH	Te	MeOH (20 vol. %)	11/0.4 10^{-3} s^{-1}	---	[70]
$[Cu(en)_2]_{11}K_6Na_2[Nb_{24}O_{72}H_9]_2$	POM[b]/TEA	Co[c]	H_2O	116/---	50	[71]
$[\{Ce(H_2O)\}_2\{Ce(CH_3CN)\}_2(\mu_4\text{-}O)(\gamma\text{-}SiW_{10}O_{36})_2]^{6-}$	---/4-methoxybenzyl-alcohol	Pt	DMAC	249/---	10	[72]
$[P_2W_{17}O_{61}\text{-}\{O(SiC_{36}H_{23}N_3O_2Ir)_2\}]^{6-}$	---/NEt_3	---	DMF/HOAc	41/69.4·10^{-6} s^{-1}	n·24	[73]
WO_3 on SiO_2	---/---	---	MeOH (20 vol. %)	---/---	---	[74]
$[Ni(H_2O)GeW_{11}O_{39}]^{6-}$	$[Ru(bpy)_3]^{2+}$/ascorbic acid	---	ascorbate buffer	36.8/9·10^{-3} s^{-1}	15	This study

[a] TOF values were standardized whenever possible; [b] POM is used both as sensitizer and WOC; [c] as cobaloxime $[Co^{III}(dmgH)_2\text{-}pyCl]$; [d] this work.

BVS analysis of the oxygen atoms coordinated to the disordered Ni/W centres afforded unreasonable values. The W-O bond lengths for terminal oxygen atoms are in the range of 1.675(15) - 1.702(16) Å and between 1.702(16) and 2.045(11) Å for equatorial oxygen atoms (Table S4.1-Table S4.5). This is in agreement with literature values for Keggin-type polyanions.[75,76]

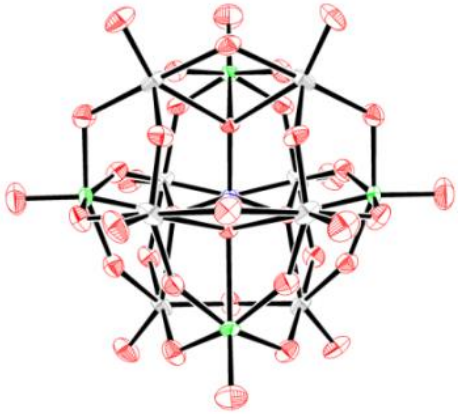

Figure 4.2. ORTEP representation of **Ge-2** at 50% ellipsoid probability (Ni/W disordered site: green; O: red; W: grey; Ge: blue.

The influence of the central heteroatom X on the X-O_{ax} bond lengths is a key tuning parameter in the present study, because the electron density on the tungsten atoms depends on the W-O_{ax} bond lengths and influences the redox behavior of the polyanion.[75,76] Shortening of X-O_{ax} bonds consequently leads to elongation of the W/Ni-O_{ax} bonds. Bond distances between the heteroatom and the axial oxygen atom increase in the order P-O 1.554(12) Å < Si-O 1.627(9) Å < Ge-O 1.738(9) Å. The corresponding bond length between the axial oxygen atom and the disordered Ni/W center decreases in the following order 2.438(10) Å P > 2.372(10) Å Si > 2.335(9) Å Ge. An analogous decrease is observed for the average W-Oax bond length involving the ordered tungsten atom sites W(2) and W(3), i.e. 2.466(11) Å P > 2.399(9) Å Si > 2.344(9) Å Ge. All structural models were completed by refining potassium cations and crystal water molecules, both found on disordered positions in the crystal structures. The number of refined crystal water molecules is in good agreement with thermogravimetric analysis (TGA) results (Figure S4.4-Figure S4.5). The phase purity of all Ni-substituted compounds was verified by comparing experimental powder X-ray diffraction data (PXRD, Figure 4.4 and Figure S4.1-Figure S4.2) and HR-ESI Mass spectra (Figure S4.13-Figure S4.16) to patterns calculated from the single crystal data. As a reference, the crystal structure of $K_8[GeW_{11}O_{39}]\cdot 13H_2O$ (**Ge-4**) was determined (space group: $P\bar{4}3m$).

Earlier reports found the $K_{2.5}Ca_2H_{1.5}$ salt to crystallize in a different space group (*C*2/*c*), thereby illustrating the major structure-directing effect of the counter-cations.[77] While PXRD analysis of bulk samples indicates phase purity of the material (Figure 4.3 and Figure S4.1-Figure S4.2), HR-ESI MS and elemental analysis data suggest the presence of a small impurity amount (< 5 %), most likely $[GeW_{12}O_{40}]^{4-}$, which falls below the detection limit of PXRD techniques.

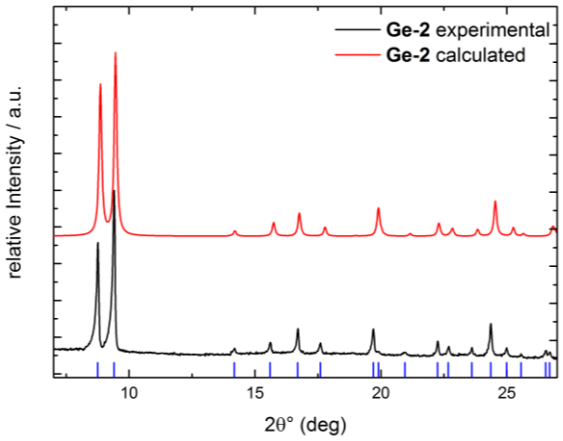

Figure 4.3. PXRD pattern of **Ge-2** after background correction (black line) vs. calculated pattern (red line); the blue lines represent calculated peak positions after indexing with ReXcell.

The PXRD patterns of the four reported POMs were compared with calculated patterns at 1.5406 Å based on their single crystal structures utilizing the Platon program package. Experimental PXRD patterns were baseline corrected and indexed by the ReXcell[78] software applying the dichotomy method.[79] Indexing procedures resulted in tetragonal symmetry for **P-1**, **Ge-2**, and **Si-3** and cubic symmetry for **Ge-4**. The experimental PXRD patterns closely resemble the calculated ones and slight peak shifts are caused by thermal expansion.

Table 4.2. Unit cell parameters and crystal symmetry of all structures derived from PXRD data by ReXcell (error ranges are not given by the software).

Compound	**Symmetry**	**a / Å**	**b / Å**	**c / Å**	**α / °**	**β / °**	**γ / °**	**V / Å^3**
P-1	tetragonal	14.19487	14.19487	12.45659	90	90	90	2509.9
Ge-2	tetragonal	14.21714	14.21714	12.45654	90	90	90	2517.8
Si-3	tetragonal	14.20499	14.20499	12.45837	90	90	90	2513.9
Ge-4	cubic	10.67105	10.67105	10.67105	90	90	90	1215.1

Table 4.3. Crystallographic and structural refinement data for (**P-1**, **Ge-2**, **Si-3** and **Ge-4**).

	P-1	**Ge-2**	**Si-3**	**Ge-4**
Empirical formula	$K_5PNiW_{11}O_{54}H_{30}$	$K_6GeNiW_{11}O_{54}H_{30}$	$K_6SiNiW_{11}O_{54}H_{30}$	$GeH_{26}K_8O_{52}W_{11}$
Formula weight ($g \cdot mol^{-1}$)	3201.62	3282.38	3237.83	3265.86
Temperature (K)	183.00(10)	183.00(4)	183.00(10)	183.05(10)
Wavelength (Å)	Mo $K\alpha_1$ (0.71073)	Mo $K\alpha_1$ (0.71073)	Mo $K\alpha_1$ (0.71073)	Mo $K\alpha_1$ (0.71073)
Crystal system	Tetragonal	Tetragonal	Tetragonal	Cubic
Space group	$P\bar{4}n2$ (118)	$P\bar{4}n2$ (118)	$P\bar{4}n2$ (118)	$P\bar{4}3m$ (215)
a (Å)	14.1537(4)	14.1045(3)	14.0862(2)	10.63880(10)
c (Å)	12.5319(5)	12.4698(4)	12.4573(3)	10.63880(10)
V ($Å^3$)	2510.48(17)	2480.70(13)	2471.79(9)	1204.14(3)
Z	2	2	2	1
ρ_{calc} (g/cm^{-3})	4.196	4.354	4.310	4.468
Crystal size (mm)	0.23 x 0.11 x 0.05	0.66 x 0.10 x 0.08	0.50 x 0.28 x 0.20	0.28 x 0.26 x 0.11
Reflections collected/unique	31012/4448	12664/4391	12336/4391	9387/883
Unique observed reflections	3447	3802	3745	850
θ range (°)	2.17-32.87	2.63-32.57	2.56-32.60	2.70-32.445
F(000)	2828	2900	2864	1440
Reflections/restraints/parameters	4448/355/184	4391/367/185	4391/493/185	883/44/88
Goodness-of-fit	1.031	1.111	1.105	1.244
R_1[a] [$I>2\sigma(I)$]	0.0433	0.0368	0.0402	0.0309
wR_2[b] (all data)	0.1343	0.1034	0.1110	0.0654

[a] $R_1 = \sum (F_o - F_c)/\sum F_o$; $I > 2\sigma(I)$ [b] $wR_2 = \{\sum w(F_o^2 - F_c^2)^2/\sum w(F_o^2)^2\}^{1/2}$

4.2.2 Spectroscopic Characterization

The title compounds were characterized by ATR FT-IR and Raman spectroscopy (§4.8.2). All three Ni-substituted Keggin-POMs display related characteristic internal W-O vibrations over the FT-IR range between 1200 and 400 cm^{-1}.[76,75] The terminal oxygen vibrations are shifted towards slightly lower wavelengths compared to the expected 960-1000 cm^{-1} range for transition metal-free POMs. The strong vibration of **P-1** at 1057 cm^{-1} is assigned to the asymmetric P-O stretching motion (Figure S4.6; reference value for $[\alpha\text{-}PW_{12}O_{40}]^{3-}$: 1080 cm^{-1}).[75,76] Likewise, Ge-O and Si-O vibrations are observed at 867 cm^{-1} (**Ge-2**) and 920 cm^{-1} (**Si-3**), respectively. Mixing of different vibrational modes in POMs has been reported by Thouvenot et al. for isostructural compounds, and the observed Raman bands correspond well with reference data (Figure S4.10-Figure S4.12).[75,76] Bands around 980 cm^{-1} (**P-1**), 920 cm^{-1} (**Ge-2**), 550 cm^{-1} (**Si-3**) and between 100 - 300 cm^{-1} can be assigned to different W-O motions.

UV-vis spectroscopic investigations of the nickel-substituted polyoxotungstates in the range of 800-200 nm in acetate buffer solution (pH 4) show the typical transitions of Ni(II) in an octahedral coordination environment[80–82] (ν_2: $^3T_{1g}(F) \leftarrow {}^3A_{2g}(F)$ and ν_3: $^3T_{1g}(P) \leftarrow {}^3A_{2g}(F)$) and strong LMCT transitions in the near UV region (Figure 4.4).

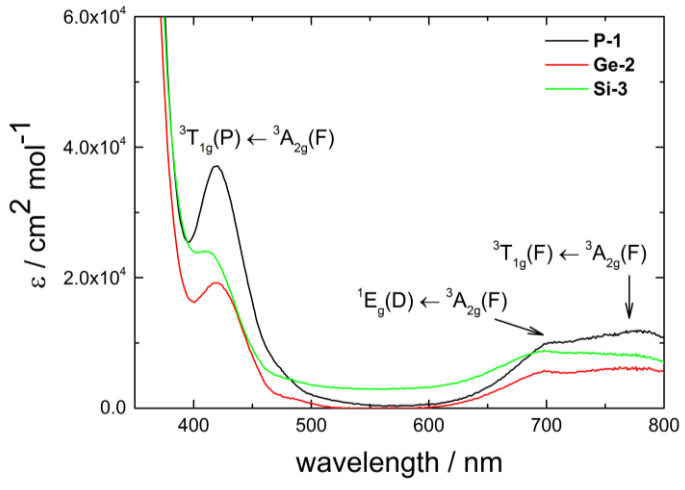

Figure 4.4. UV-vis spectra of **P-1**, **Ge-2** and **Si-3** (5 mM) in acetate buffer (50 mM, pH 4) showing the respective d-d transitions.

A shoulder in the absorption band of the $^3T_{1g}(F) \leftarrow {}^3A_{2g}(F)$ transition is assigned to the spin forbidden $^1E_g(D) \leftarrow {}^3A_{2g}(F)$ transition which becomes visible due to strong spin orbital coupling effects. The $^3T_{2g}(F) \leftarrow {}^3A_{2g}(F)$ transition could not be monitored due to limitations

of the present spectrometer setup (cf. experimental part). However, one has to keep in mind that an application of Tanabe-Sugano diagrams for a deeper analysis of UV-vis spectra requires nearly perfect octahedral symmetry. As the octahedral building blocks of the title POMs are highly distorted, further quantification of ligand field spitting (10 Dq) and Racah parameter (B) would be rather speculative. Nonetheless the UV-vis spectra confirm a nearly octahedral environment of the nickel in the POM.

X-ray absorption near-edge spectroscopy (XANES) at the Ni K-edge and W L_3-edge was performed in order to study the electronic structure of all nickel-substituted POMs. Comparison with XANES data for reference Ni(II) and W(VI) compounds clearly showed Ni valence states of +2 and W valence states of +6 for all POMs (Figure 4.5). The W L_3-edge spectra show a strong white line caused by 5d ← 2p transitions.[83,84] This white line peak could be fitted by linear combination of an arctangent as a stepfunction and two Lorentzians (Figure 4.6 and Figure S4.1). **P-1**, **Ge-2**, and **Si-3** all display peak intensity ratios of 1.5 in agreement with the octahedral symmetry of the tungsten center. Peak fitting allows the calculation of the ligand field splitting 10 Dq for the octahedral {WO_6} units to 3.0 eV **(P-1)** < 3.9 eV **(Si-3)** < 4.1 eV **(Ge-2)**. Likewise, XAFS measurements on the W-L_3 edge show maximum electron density on the W centers among the series for **Ge-2**.

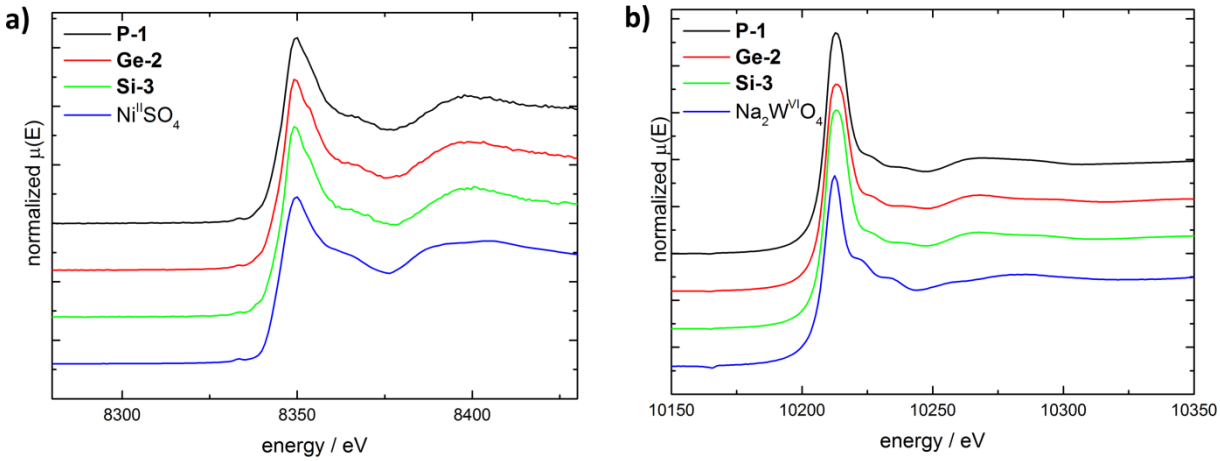

Figure 4.5. (a) Ni K-edge XANES spectra of **P-1**, **Ge-2**, and **Si-3** vs. Ni^{II}SO$_4$ as reference compound. **(b)** W L_3-edge XANES spectra of **P-1**, **Ge-2**, and **Si-3** vs. $Na_2W^{VI}O_4$ as reference compound.

X-ray absorption spectra were collected at the Swiss Norwegian BeamLine BM01b (ESRF Grenoble). All spectra were measured on solid samples dispersed in cellulose pellets. The Ni

K-edge XANES spectra of **P-1**, **Ge-2** and **Si-3** were recorded in fluorescence mode due to the strong resonant absorption of tungsten. All other spectra were recorded in transmission mode. Metal foil (nickel or tungsten) was used as energy calibration standard for all experiments. $Ni^{II}SO_4$ and $Na_2W^{VI}O_4$ were used as reference compounds for validation of the valence states +2 and +6 of the nickel and the tungsten centers, respectively. Energy calibration, background removal and Fourier transformation of XAS spectra were performed with the Athena software and EXAFS fits were performed with the Artemis software.[85]

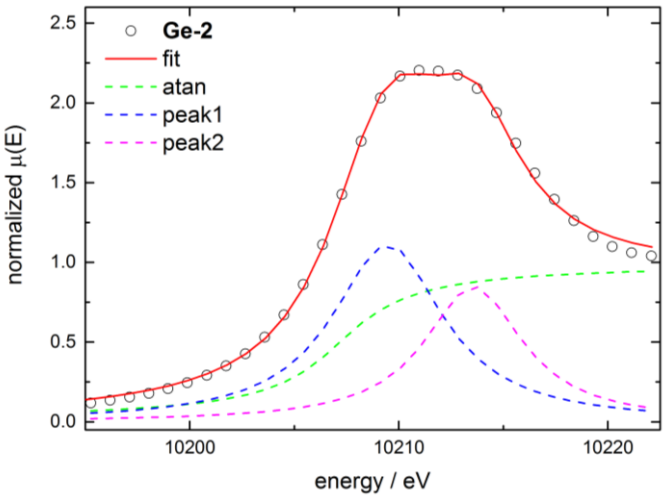

Figure 4.6. W L_3-edge XANES spectrum of **Ge-2** with fit base arctangent function and Lorentzian peaks.

4.3 Photocatalytic Hydrogen Evolution

Photocatalytic tests with a standard ascorbic acid/$[Ru(bpy)_3]^{2+}$ assay were run to completion over 15 h and the results are summarized in Table 4.4. Turnover frequencies (TOF) have been calculated from the slope of the Clark electrode signal during the first 120 seconds of the catalytic reaction and were normalized to the amount of H_2 quantified by GC measurements. Turnover numbers have been calculated according to the standard definition (TON = $n(H_2)/n(cat)$). Both parameters are compared separately for the title catalysts.

Baseline activity of a system containing only the photosensitizer $[Ru(bpy)_3]Cl_2$ in ascorbate buffer was carefully determined, as well as the activity of a reference system containing $[Ru(bpy)_3]Cl_2$ and $Ni(NO_3)_2$ without POM catalyst. Blank experiments in the absence of any nickel species showed an average formation of 3.00 µmol H_2 over 3 d.

Table 4.4. Summary of photocatalytic tests.

Compound	WRC (µM)	H_2 (µM)	TON	TOF[a] (10^{-3} s^{-1})
P-1	58	4.4	10.8	9.7
Ge-2[b]	51	21	52	8.7
Si-3	51	3.0 [c]	inactive	---
Ge-4	49	5.7	14	4.1
$[PW_{12}O_{40}]^{3-}$	50	5.1	12.8	3
$[SiW_{12}O_{40}]^{-4}$	52	2.3[c]	inactive	---
$Ni(NO_3)_2$	100/200	3.6/3.0	4.6/1.9	7.7/0.98
GeO_2	90	2.1[c]	inactive	---
Blank	---	3	---	---

[a] Determined from the initial 60 s slope of Clark electrode traces. [b] Average values. [b] Catalyst shows no H_2 evolution activity above the blank level (last entry). Conditions: high power LED 470 nm, 1 mM $[Ru(bpy)_3]^{2+}$, 0.12 M ascorbate buffer, pH 4.

The activity of nickel nitrate was investigated at 100 µM. We conclude from the low observed performance that possible Ni^{2+} ion leaching from the POM-WRCs does not result in the formation of an active secondary catalyst. Visible-light-driven H_2 evolution with **P-1** and **Ge-2** is above the blank level (Table 4.4). The total amount of H_2 generated from **Ge-2** clearly exceeds the amount formed by **P-1** (Figure 4.7). **Si-3** shows no significant catalytic activity in

terms of TON and TOF, i.e. the total amount of H_2 is not above the background, nor does the catalyst exert an accelerating effect on the initial 120 seconds of the reaction.

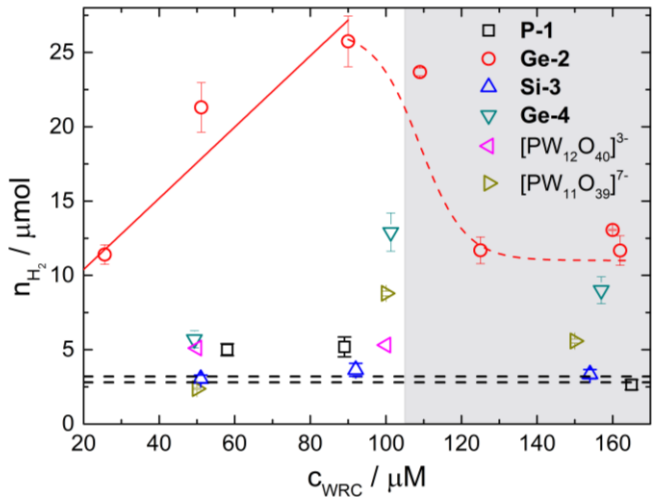

Figure 4.7. Comparison of the amount of H_2 formed in photocatalytic tests for **P-1**, **Ge-2** and **Si-3** (25-150 µM) vs. the selected reference compounds $[PW_{12}O_{40}]^{3-}$, $[PW_{11}O_{39}]^{7-}$ and **Ge-4** (high power LED 470 nm, 1 mM $[Ru(bpy)_3]^{2+}$, 0.12 M ascorbate buffer, pH 4; black dashed lines: amount of H_2 formed in the absence of WRC, grey area: concentration range where H_2 evolution decreases again with increasing catalyst concentration.

The influence of Ni substitution on the catalytic activity was determined with nickel-free structural analogues. As attempts to synthesize the isostructural $[GeW_{12}O_{40}]^{4-}$ were not fruitful, the related polyanion $[GeW_{11}O_{39}]^{8-}$ was tested. This lacunary compound represents the primary decomposition product which would emerge from hypothetical Ni leaching in solution. Neither silicotungstic acid $[SiW_{12}O_{40}]^{4-}$ nor **Si-3** showed significant activity under the given conditions. H_2 production with the other two nickel-free Keggin POMs $[GeW_{11}O_{39}]^{8-}$ **(Ge-4)** and phosphotungstic acid $[PW_{12}O_{40}]^{3-}$ is above the background in terms of TON. Whereas Ni-substitution is crucial for the WRC activity of **Ge-2**, no substantial activity difference was found for **P-1**, $[PW_{12}O_{40}]^{3-}$ and $[PW_{11}O_{39}]^{7-}$ considering the amount of H_2 formed. At catalyst concentrations above 100 µM the total amount of H_2 formed decreases and the TON drops. The precise reason for this TON decrease is unknown to date. One hypothesis is that a two-electron reduction of a given POM molecule is less likely at higher POM/PS ratios, while another explanation might be linked to the decreasing effective photosensitizer concentration through formation of the POM-PS complex (see §4.3.3).

However, these hypotheses remain to be verified by quenching and transient absorption measurements, which are scheduled for a more detailed mechanistic follow-up study.

The structurally similar, nickel-free compounds **Ge-4** and $[PW_{12}O_{40}]^{3-}$ reach TONs up to 16±2 and 13±2, respectively. The maximum TON for P-1 (11±1) is observed at catalyst concentrations of 58 µM, i.e. Ni-substitution does not exert a significant effect on the catalytic activity. In contrast, turnover numbers for **Ge-2** remain almost constant at 37.1±0.4 for the optimal working concentration range (<100 µM) (cf. Table 4.4).

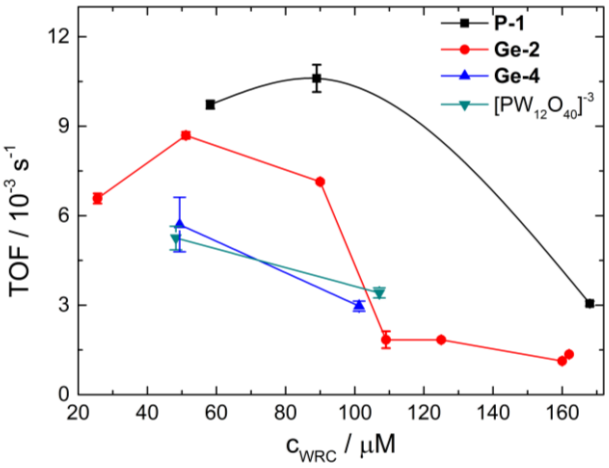

Figure 4.8. Comparison of TOF values obtained from initial rates for the nickel containing POMs **P-1** and **Ge-2** vs. their nickel-free analogues **Ge-4** and $[PW_{12}O_{40}]^{3-}$ (experimental conditions: high power LED 470 nm, 1 mM $[Ru(bpy)_3]^{2+}$, 0.12 M ascorbate buffer, pH 4; data points are connected for clarity).

TOF values for the active POMs **P-1** and **Ge-2** and their nickel-free counterparts **Ge-4** and $[PW_{12}O_{40}]^{3-}$ are displayed in Figure 4.8. **P-1** shows the highest TOF values.

Nevertheless, the overall amount of H_2 evolved by **P-1** is lower than for **Ge-2** despite its higher initial TOF. This indicates a rapid deactivation of the phosphorus containing catalyst (Figure 4.9). As spectroscopic investigations point to structural integrity of **P-1** in solution, the activity decrease is most likely not due to degradation. A higher extent of back electron transfer from the reduced P-1 species to dehydroascorbate than for the reduced **Ge-2** species is a more plausible explanation. Related effects were previously reported for a molecular Co-based WRC and prevented by introducing the additional electron donor tris(2-carboxyethyl)phosphine which is capable of reducing the dehydroascorbate to prevent back

electron transfer.[86] Herein we did not block back electron transfer in the first place, because such information may be crucial for interpreting the observed H_2 evolution trends. Attempts have been made to keep the assay system as straightforward as possible to avoid an overlay of SAR and additional factors.

All in all, **Ge-1** emerges as the most efficient WRC among the series in terms of its highest TON value, because **P-1** is deactivated after ca. 60 s despite its high TOF value.

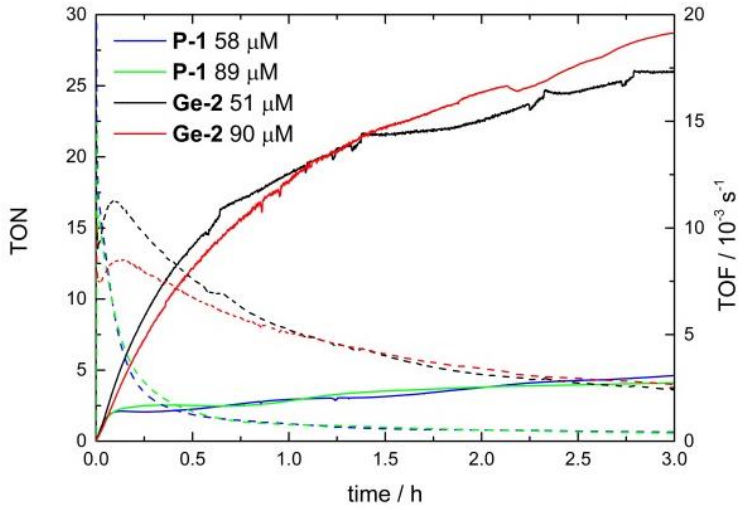

Figure 4.9. Comparison of TON (solid) and TOF (dashed) values for the initial 3 h of the photocatalytic H_2 evolution for different concentrations of **P-1** and **Ge-2** (high power LED 470 nm, 1 mM $[Ru(bpy)_3]^{2+}$, 0.12 M ascorbate buffer, pH 4).

4.3.1 Catalyst Recycling Experiments

POMs have been reported previously to form colloidal adducts with $[Ru(bpy)_3]^{2+/3+}$ through strong electrostatic attraction. However, the precise composition and structure of these amorphous precipitates frequently remains unknown.[33,87–91,68,92] The POM-PS complex of **Ge-2** was collected from the reaction mixture by centrifugation. The solid phase obtained after air-drying was recycled as catalyst and added to fresh ascorbate buffer solution containing $[Ru(bpy)_3]Cl_2$. The total amount of H_2 per recycling run is significantly lower than from a pristine solution of catalyst (107.2 µL recovered, 629.8 µL fresh), but still above the background (78.0 µL). H_2 evolution activity could be increased by sonication of the POM-PS complex suspension for 2 h (240.13 µM). This indicates a lower reactivity of aged POM-PS aggregates compared to molecular species and in situ formed colloids. We compare absolute H_2 amounts here, because a full structural POM-PS characterization turned out rather challenging.

4.3.2 Solution Stability

High resolution mass spectra of the three Ni-containing Keggin POMs were recorded in order to verify their integrity and solution stability. The mass spectrum of $[Ni(H_2O)GeW_{11}O_{39}]^{6-}$ **(Ge-2)** shows the polyanion at different protonation states. The peaks are assigned as follows: m/z = 694.8079 $[NiGeW_{11}O_{39}\text{-}2H]^{4-}$, 926.7480 $[NiGeW_{11}O_{39}\text{-}3H]^{3-}$ and 1390.6244 $[NiGeW_{11}O_{39}\text{-}4H]^{2-}$. Each charge state is accompanied by different Na/K adducts. The observed masses for **P-1**, **Ge-2** and **Si-3** are about 18 u below the calculated values, which indicates the removal of the aqua ligand attached to the Ni site. All in all, the observed mass peaks confirm the purity of the title compounds in line with their PXRD patterns (Figure 4.3, Figure S4.1 and Figure S4.2). Their stability in aqueous solution was further confirmed by UV-vis spectroscopy (Figure S4.17-Figure S4.18). Slight changes in the UV-vis spectra exclusively set in for **Ge-4** over a time period of 9.5 h (Figure S4.18, b), which is most likely due to a transformation of the minor impurities in $[GeW_{11}O_{39}]^{8-}$ (cf. above). Leaching of Ge or Ni species into the solution is less plausible, because GeO_2 and $Ni(NO_3)_2$ as representative side products remained inactive in reference experiments (Table 4.4). Furthermore, the absence of a significant time lag strongly points to **Ge-2** as the active water reduction catalyst.

4.3.3 Characterization of POM-PS Complexes

Post-catalytic POM-PS precipitates of the title compounds were isolated and characterized by FT-IR and Raman spectroscopy. FT-IR and Raman spectra of all POM-PS complexes can best be described as a superposition of the spectra of the respective pristine WRCs and $[Ru(bpy)_3]^{2+}$ (Figure 4.10, Figure S4.27 and Figure S4.28).

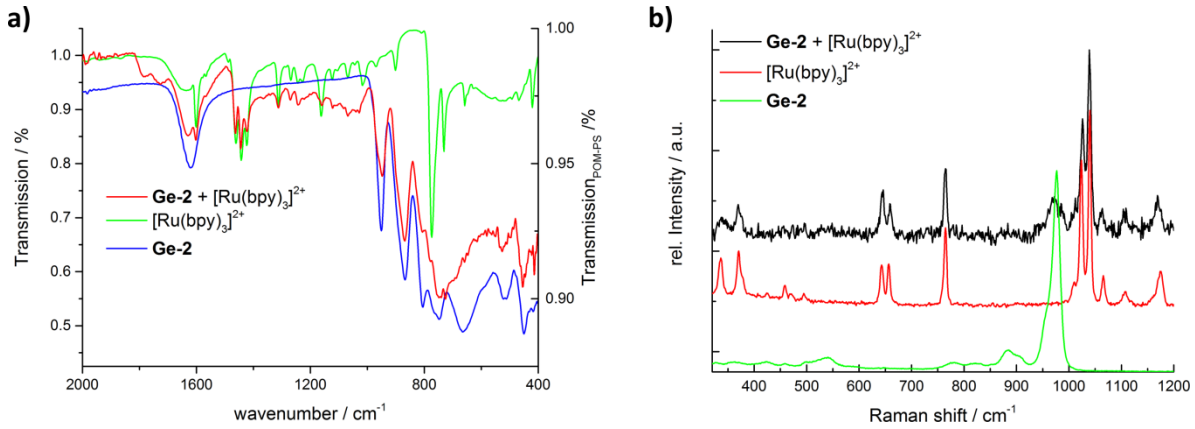

Figure 4.10. (a) FT-IR spectrum and **(b)** Raman spectrum of the post-catalytic precipitate of **Ge-2** in comparison with reference spectra of **Ge-2** and $[Ru(bpy)_3]Cl_2$.

All observed bands can be attributed either to the photosensitizer or the POM without additional peaks, i.e. no new chemical species are formed. The presence of all characteristic absorption bands of the respective POMs in the FT-IR spectra provides further strong evidence for their structural integrity in their POM-PS complexes. Whereas broadened signals in the Raman spectra are most probably arising from the low crystallinity of the POM-PS complexes, all characteristic bands of the ruthenium photosensitizer are visible. Presence of the weak Ru-N stretching vibrations at 337 cm^{-1} and 372 cm^{-1} clearly indicates structural stability of the $[Ru(bpy)_3]^{2+}$ cation in the POM-PS complexes.[93] The Ru/W ratio was determined to 21:67 by EDX analyses. This corresponds approximately to 3 $[Ru(bpy)_3]^{2+}$ molecules per polyanion and is in agreement with the expected number of $[Ru(bpy)_3]^{2+}$ molecules to compensate the -6 charge of the $[Ni(H_2O)GeW_{11}O_{39}]^{6-}$ polyanion. In short, POM-PS complex formation retains part of the catalytic activity and does not involve significant degradation or transformation of the individual constituents.

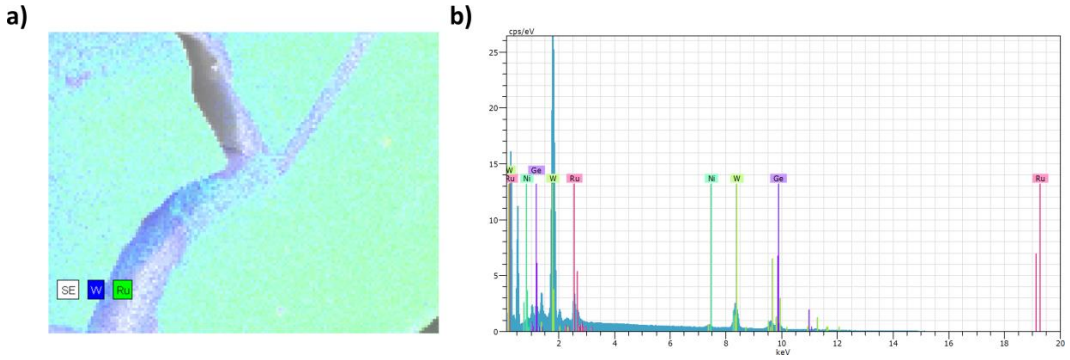

Figure 4.11. Post catalytic sample of **Ge-2**, **(a)** EDX-mapping, **(b)** EDX spectrum.

The Ru/W ratio was determined to 21:67 which corresponds to approx. 3 $Ru(bpy)_3]^{2+}$ molecules per polyanion which agrees well with the expected number of $[Ru(bpy)_3]^{2+}$ molecules to compensate the -6 charge of $[Ni(H_2O)GeW_{11}O_{39}]^{6-}$. EDX analyses were performed on the dried POM-PS complex of post-catalytic **Ge-2**. In order to improve the EDX mapping statistics, measurements were performed on a larger surface which was not smooth (see crack in Figure 4.11).

Table 4.5. Results of the EDX elemental analysis of the post-catalytic sample of **Ge-2**.

El	AN	Series	Atom. C [at. %]	Error[wt.%]
Ni	28	K-series	6,90	0,1
Ge	32	K-series	4,88	0,1
Ru	44	L-series	21,28	0,3
W	74	L-series	66,94	1,4

4.4 Electrochemical Characterization

Voltammetric electrochemical characterizations within potential ranges confined to reversible electron transfer reactions were performed to characterize the redox behavior of the molecular catalysts. Investigation of the electrocatalytic properties at lower potentials (under turnover conditions) is a rather complex task due to two overlapping processes, namely irreversible reduction of the catalyst and the formation of layers on the working electrode. Trace crossing observed at scans towards lower potentials is attributed to electrode activation and follow-up reactions. A more precise kinetic description is thus beyond the scope of the present study.

Cyclic voltammetry (CV) and differential pulse voltammetry (DPV) measurements of **P-1, Ge-2** and **Si-3** between 0.90 V and -0.95 V (all potentials given vs. Ag/AgCl) show two

reversible waves (**I** and **II**, cf. Figure 4.12). These two electron waves, as suggested by the peak differences ΔE between 65 mV and 114 mV, can be assigned to the reduction of W(VI) to W(V). The respective potentials of these tungsten reductions depend on the heteroatom, and they are pH dependent due to coupled proton transfers. The linear potential shifts suggest the involvement of 2-3 protons (Figure S4.30).

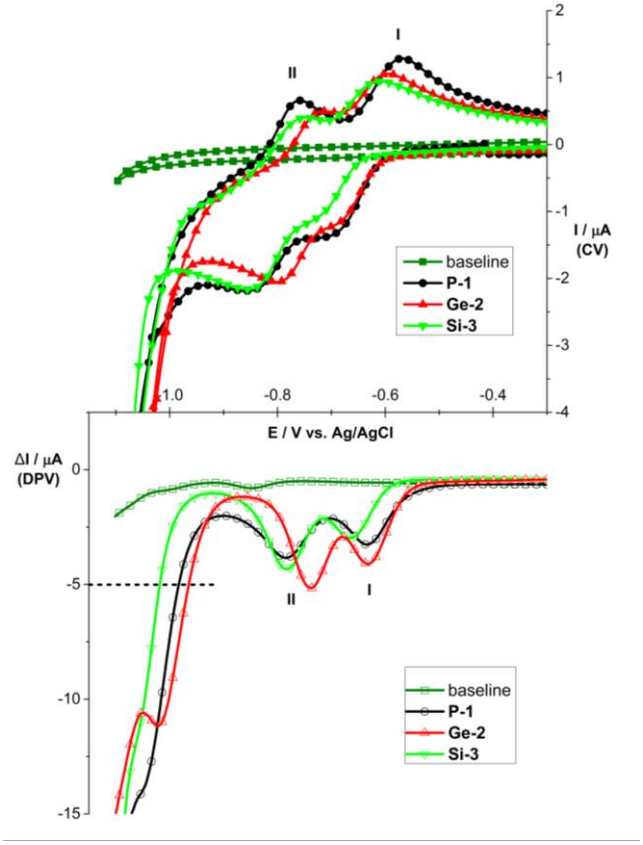

Figure 4.12. Reversible CV and DPV measurements of **P-1**, **Ge-2** and **Si-3** at a concentration of 5 mM in acetate buffer (50 mM) pH 4, sweep rate (10 mV/s) (dashed line: definition of the onset potential as the potential where a current difference of -5 µA is reached).

The first reduction **I** for **P-1** and **Ge-2** was observed at closely related half-wave potentials ($E_{1/2}(I_{P\text{-}1})$ = -635 mV and $E_{1/2}(I_{Ge\text{-}2})$ = -643 mV) compared to a lower potential for **Si-3** ($E_{1/2}(I_{Si\text{-}3})$ = -668 mV). The second reduction **II** occurs for **Ge-2** at a potential of $E_{1/2}(II_{Ge\text{-}2})$ = -763 mV and for **P-1** and **Si-3** at virtually identical lower potentials $E_{1/2}(II_{P\text{-}1})$ = -810 mV and $E_{1/2}(II_{Si\text{-}3})$ = -815 mV. The difference between the two half-wave potentials ($\Delta E_{1/2}$ = $E_{1/2}(I)$ - $E_{1/2}(II)$) decreases with increasing bond valence of the W-O_{ax} bonds (Figure S4.29). This behavior is in line with previous results for transition metal-free Keggin POMs.[94–96] Earlier studies on the influence of the heteroatom on the electrochemistry and acidity of Keggin-type $[XW_{12}O_{40}]^{n-}$ POMs demonstrated that the first one electron reduction wave in

non-protic solvents depends on the charge of the POM and the ionic radius, whereas the reduction process in protic solvents is almost exclusively influenced by the ionic radius of the heteroatom.[97,98]Multi-electron reduction of the title POMs was observed as shoulder or peak overlapping with the onset current of electrocatalytic hydrogen formation at lower potentials (-1.0 V to -1.1 V). The onset potential for this superposition of electrochemical processes is most positive for **Ge-2** and most negative for **Si-3**, which is in line with the catalytic activity trends for photochemical hydrogen evolution.

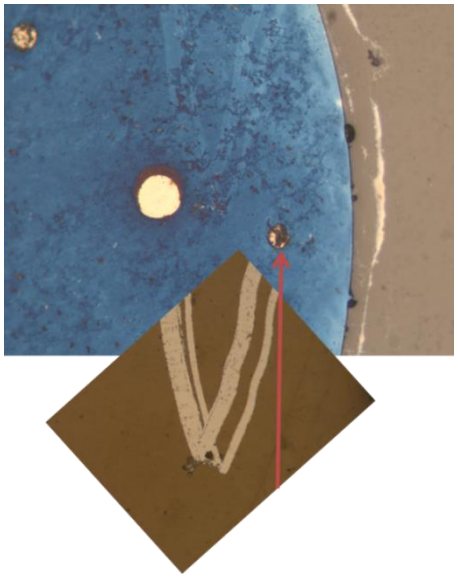

Figure 4.13. Formation of blue surface layer (top, after 3 CVs (-1.0 to -0.2 V, 5 mV/s) and 3 CVs (-1.2 to -0.2 V, 5 mV/s) using the brown layer covered and scratched GC electrode (bottom, same as in Figure S4.29). Analytic conditions: $K_6[Ni(H_2O)SiW_{11}O_{39}]\cdot$(**Si-3**) in ascorbate buffer, pH 4.

The corresponding reduction potential is sufficiently positive to permit oxidative quenching of the $[Ru(bpy)_3]^{*2+}$ excited state.[99] Electrodeposition of thin films of reduced metal oxides on the glassy carbon working electrode is observed in the same potential window Figure S4.29). The formation of similar films has been reported earlier by Nadjo et al.[100,101] Consecutive cycling to -1.2 V shows the disappearance of the reversible redox features and a current decrease at the lower potential limit. This indicates that these newly formed layers are electro-inactive. Hydrogen formation in blank measurements with glassy carbon electrodes sets in at -1.1 V and reaches significant currents at -1.2 V. Simultaneously with the observed electrochemical deactivation of the electrode by layer formation, the effective resulting current drops to similar levels than for blank measurements. The superposition of POM multi-electron reduction and electrocatalytic H_2 production in combination with layer formation on

the electrode renders finding a correlation between electro- and photochemical behaviour difficult. Generally, both processes frequently follow different mechanistic pathways so that activity trends should be extrapolated from one method to another with caution.[102]

4.5 DFT Calculations

The electronic structures of the three different POMs presented in this study were compared with DFT calculations in search of differences associated with the respective heteroatoms that could account for the observed trends in photochemical hydrogen evolution. Calculated electronic and structural data are summarized in Table 4.6. The results agree well with the experimentally determined structural data and afford triplets in the ground state, with the spin density of the two unpaired electrons localized on the Ni atom. All three title compounds display closely related HOMO-LUMO energy gaps, namely 4.32, 4.35, and 4.37 eV for **P-1**, **Ge-2**, and **Si-3**, respectively. H_2 evolution catalyzed by nickel-substituted POMs implies a 2-electron reduction of the catalyst, followed by reduction of two protons and H_2 evolution upon catalyst recovery.

Table 4.6. Electronic and structural data for **P-1**, **Ge-2** and **Si-3** (all compounds exhibit d8 configuration and a spin of 1).

POM	q	$d_{(Ni\text{-}Ot)}$ [a]	$d_{(Ni/W\text{-}Oax)}$ [b]	$d_{(X\text{-}Oax)}$ [c]	□(Ni)
P-1	-5	2.103	2.366	1.575	1.71
Ge-2	-6	2.125	2.248	1.726	1.69
Si-3	-6	2.139	2.285	1.639	1.69

[a] Ni-terminal oxygen bond lengths. [b] Disordered Ni/W-axial oxygen bond lengths. [c] Heteroatom-axial oxygen bond lengths.

The LUMOs display a major contribution to the W(VI) atoms with weights above 73 % for all three POMs. In line with electrochemical characterizations, initial electron transfer to the POM reduces one W(VI) center to W(V). The contribution of the heteroatoms to the LUMO is below 0.1% for the title compounds so that these influences do not cause the observed catalytic activity differences in photochemical H_2 evolution.

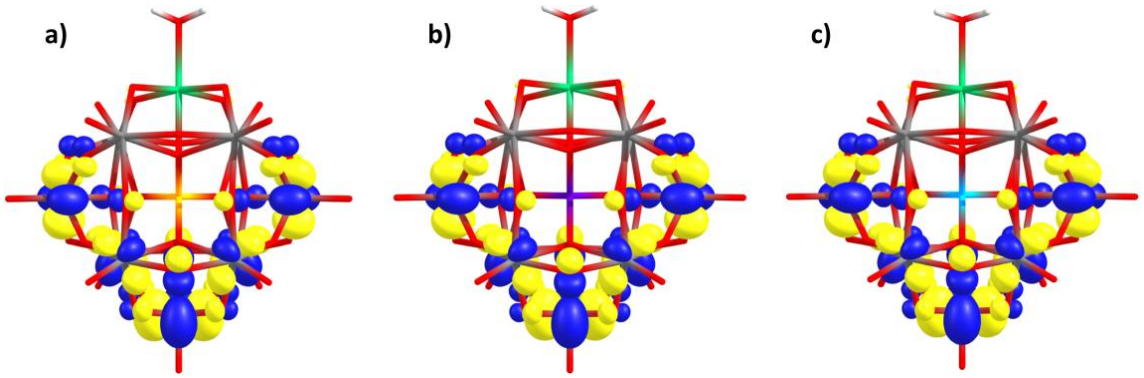

Figure 4.14. LUMO representations for POMs **P-1** (a), **Ge-2** (b), and **Si-3** (c).

4.6 Conclusions

Three nickel substituted Keggin-type POMs $[Ni(H_2O)PW_{11}O_{39}]^{5-}$ (**P-1**), $[Ni(H_2O)GeW_{11}O_{39}]^{6-}$ (**Ge-2**) and $[Ni(H_2O)SiW_{11}O_{39}]^{6-}$ (**Si-3**) along with Ni-free reference POMs were synthesized, structurally characterized and further analyzed by a wide range of spectroscopic and electrochemical methods. The heteroatom (X = P, Ge, Si) exerts a strong influence on the catalytic activity of the Ni-POM series in visible-light-driven photochemical hydrogen evolution with standard assays ($[Ru(bpy)_3]^{2+}$ photosensitizer, ascorbate buffer, aqueous media). **Ge-2** displayed the highest TON among the title POMs. In contrast, the introduction of Ni centres did not improve the catalytic activity of P-containing Keggin POMs, and the Si-based compounds did not show significant hydrogen evolution at all. **Ge-2** was found to be stable under operational conditions, whereas **P-1** undergoes rapid deactivation on a minute scale after high initial TOF values. At first glance, the electrochemical hydrogen evolution onset potentials for **Ge-2** and **P-1** are in line with the photochemical activity trends. However, both processes proceed along quite different pathways, as indicated by irreversible electrodeposition of thin films of reduced metal oxides. DFT calculations showed that the heteroatom-related contribution to the respective LUMO (< 0.1 % for **Ge-2**, **P-1** and **Si-3**) was not sufficient to account for its observed significant influence on the catalytic activity. Further mechanistic and spectroscopic studies, including time resolved luminescence spectroscopy, are now under way to correlate the empirically observed structure-activity relationships with key steps of the catalytic cycle. All in all, the present study illustrates the challenges associated with rational design guidelines for POM catalysts in photochemical water splitting processes.

4.7 Experimental Section

4.7.1 Synthesis of $K_5[Ni(H_2O)PW_{11}O_{39}]\cdot 12H_2O$ **(P-1)**

The synthesis of **P-1** is based on a procedure reported by Weakley and Malik.[103] $Na_2WO_4\cdot 2H_2O$ (12.50 g, 37.90 mmol) and Na_2HPO_4 (1.60 g, 11.30 mmol) were dissolved in water (75 mL) and heated to 100 °C. Concentrated HCl (10 mL, 32 %) was added dropwise to the stirred reaction mixture. After the complete addition, the reaction mixture was cooled to room temperature and poured into a separation funnel. Diethylether (10 mL) was added and the mixture was shaken. The organic layer was removed, water (25 mL) was added to the combined organic fraction and the mixture was heated to 95 °C. A solution of $Ni(NO_3)_2\cdot 6H_2O$ (1.00 g, 3.40 mmol) in acetate buffer was added to the hot reaction mixture, which has been prepared as follows: dissolution of $Ni(NO_3)_2\cdot 6H_2O$ in a minimum amount of hot water, followed by the addition of potassium acetate buffer (10 mL, pH 7, pH adjusted with glacial acetic acid). The reaction mixture was stirred for 2 min at 95 °C and then cooled to 60 °C. Methanol was added (25 mL) and the reaction mixture was kept overnight at 8 °C. The green precipitate was filtered and washed with water and methanol. Yield: 5.73 g, 1.79 mmol, 51.90 % based on $Na_2WO_4\cdot 2H_2O$.

FT-IR (ATR): $\tilde{\nu}$ = 1615, 1403, 1057, 955, 883, 789, 760, 688, 590, 502, 485 cm^{-1}; UV-vis (NaOAc/HOAc pH 4): $\lambda_{max}(\varepsilon)$ = 419 nm (33.6 $dm^3\,mol^{-1}\,cm^{-1}$); elemental analysis calcd. (%) for $K_5NiPW_{11}O_{54}H_{30}$ (3201.62): K 6.11, W 63.16, Ni 1.99, P 1.05; found: K 6.09, W 63.5, Ni 1.68, P 0.93.

4.7.2 Synthesis of $K_6[Ni(H_2O)GeW_{11}O_{39}]\cdot 14H_2O$ **(Ge-2)**

Ge-2 was synthesized according to a procedure reported by Weakley and Malik.[7] GeO_2 (0.50 g, 4.80 mmol) was dissolved in NaOH solution (10 mL, 5 %). A solution of $Na_2WO_4\cdot 2H_2O$ (17.00 g, 51.60 mmol) in water (30 mL) was added, and the reaction mixture was heated to 95 °C. HCl (10 mL, 32 %) was added dropwise to the stirred reaction mixture. After complete addition, the reaction mixture was cooled to room temperature and $H_4[GeW_{12}O_{40}]$ was extracted with diethylether. Water was added to the combined organic fractions (40 mL) and the mixture heated to 70 °C. A solution of $Ni(NO_3)_2\cdot 6H_2O$ (1.25 g, 4.25 mmol) in hot water was (5 mL) was added. A buffer solution prepared from CH_3COOK (21.0 g) and glacial acetic acid (2 mL) in hot water (25 mL) was added to the Ni containing reaction mixture. A green solid was collected by filtration and recrystallized from water at 60 °C. Yield: 7.40 g, 2.30

mmol, 50.2 %. FT-IR (ATR): $\tilde{\nu}$ = 1621, 951, 867, 805, 747, 665, 552, 450, 418 cm^{-1}; UV-vis (NaOAc/HOAc pH 4): $\lambda_{max}(\varepsilon)$ = 419 nm (19.2 $dm^3 mol^{-1} cm^{-1}$); elemental analysis calcd. (%) for $K_6NiGeW_{11}O_{54}H_{30}$ (3282.4): K 7.15, W 61.6, Ni 1.79, Ge 2.21; found: K 7.34, W 61.9, Ni 1.71, Ge 2.27.

4.7.3 Synthesis of $K_6[Ni(H_2O)SiW_{11}O_{39}]\cdot 14H_2O$ **(Si-3)**

Si-3 was synthesized according to a procedure reported by Weakley and Malik.[7] $H_4[SiW_{12}O_{40}]\cdot 7H_2O$ (14.0 g , 4.70 mmol) was dissolved in water (95 °C). $NiSO_4\cdot 7H_2O$ (1.60 g, 6.10 mmol) in hot water (10 mL) was added dropwise, followed by addition of a solution of CH_3COOK (15 g) in hot water (15 mL). The pH of this solution was adjusted to 7 with glacial acetic acid. The reaction mixture was kept at 95 °C for 1 min. Slow diffusion of MeOH into the reaction mixture leads to the formation of green crystals. Yield: 10.6 g, 3.3 mmol, 67.7 % based on $H_4[SiW_{12}O_{40}]$

FT-IR (ATR): $\tilde{\nu}$ = 1619, 1562, 1407, 1341, 998, 955, 780, 759, 678, 509, 481 cm^{-1}; UV-vis (NaOAc/HOAc pH 4): $\lambda_{max}(\varepsilon)$ = 410 nm (26.7 $dm^3 mol^{-1} cm^{-1}$); elemental analysis calcd. (%) for $K_6NiSiW_{11}O_{54}H_{30}$ (3237.8): K 7.25, W 62.5, Ni 1.81, Si 0.87 found: K 7.48, W 62.3, Ni 1.79; Si 0.89.

4.7.4 Synthesis of $K_8[GeW_{11}O_{39}]\cdot 13\ H_2O$ **(Ge-4)**

Ge-4 was synthesized by the following procedure: GeO_2 (0.10 g, 0.97 mmol) was dissolved in NaOH (2 mL 10 %) solution. An aqueous solution of $Na_2WO_4\cdot 2H_2O$ (3.40 g, 10.30 mmol) in H_2O (6 mL) was added. HCl (2 mL conc.) was added dropwise to the stirred reaction mixture at 95 °C. The reaction mixture was cooled to room temperature and the $H_4[GeW_{12}O_{40}]$ acid was extracted with diethylether. Water was added to the organic fraction (8 mL) and the mixture was heated to 70 °C. Potassium acetate (3.4 g, 34.6 mmol) in H_2O (5 mL) was added. A white precipitate was obtained by adding methanol. Yield: 1.50 g, 0.48 mmol, 55.9 %.

FT-IR (ATR): $\tilde{\nu}$ = 1618, 953, 874, 845, 781, 690, 513, 461, 438, 417 cm^{-1}; elemental analysis calcd. (%) for $K_8GeW_{11}O_{52}H_{26}$ (3265.9): K 9.58, W 61.92, Ge 2.22; found: K 8.95, W 62.1, Ge 2.06. 2nd analysis for K (9.27)

4.7.5 X-ray Diffraction Experiments / Structure Refinement

Crystal structure analysis was done by standard procedures, for a list of programs and instruments used see §1.16. Further details on the crystal structure investigations may be obtained from the Fachinformationszentrum Karlsruhe, D-76344 Eggenstein-Leopoldshafen, Germany (Fax: +49 7247 808 666; email crysdata@fiz-karlsruhe.de), by citing the depository numbers CSD-429186 (**P-1**), CSD-429187 (**Ge-2**), CSD-429188 (**Si-3**) and CSD-429189 (**Ge-4**).

4.7.6 Instruments

For a complete list of instruments and procedures used for the characterization of **P-1, Ge-2, Si-3** and **Ge-4** see §1.17.2.

4.7.7 Electrochemistry

Electroanalytical experiments were performed at an analyte concentration of 0.5 mM in sodium acetate buffer (50 mM, pH 4). A glassy carbon disc working electrode was used (2 mm diameter) with a Pt-rod as the counter electrode and Ag/AgCl (3 M KCl, 210 mV vs. SHE) as the reference electrode. Measurements were conducted in a rotating disc electrode setup (Metrohm, VA Computrace 797) in combination with a potentiostat (Metrohm, Autolab, Nova 1.10). Representative cyclic voltammograms were measured at a sweep rate of 10 mV/s starting from the respective open cell potential after the electrolyte had been purged with N_2 gas for 30 min. Differential pulse voltammograms were measured towards negative potentials after 10 s equilibration time at 0.2 V. Working electrodes were polished with aluminium oxide powder (grain size 0.3 µm) using a Metrohm polishing kit prior to the measurements except for experiments which aimed to observe the effect of layer deposition on the electrodes.

4.7.8 Photocatalytic H_2 Evolution Tests

All catalytic tests were performed in 10 mL headspace vials, sealed with a natural rubber septum (VWR) and a crimp cap (Supelco). An ascorbate buffer system at pH 4 was prepared from ascorbic acid (88.0 mg, 0.499 mmol) and sodium ascorbate (98.0 mg, 0.494 mmol) in demineralized water (8.0 mL) resulting in a total buffer concentration of 0.12 M. $[Ru(bpy)_3]Cl_2 \cdot 6H_2O$ (1 mM) was used as photosensitizer. The catalyst was dissolved in 1.0 mL buffer solution and added dropwise. Addition of the POM catalyst to the test solution

containing the photosensitizer affords turbid solutions. All catalytic tests were prepared under the exclusion of light.

Catalytic test solutions were irradiated under stirring with a blue LED (460 nm 4650 Lux). Hydrogen evolution was monitored with a Clark-type hydrogen sensor (H2-NP) from Unisense. The sensor was calibrated prior to each experiment with a two point calibration using a sample with a known concentration of H_2. In order to quantify the amount of hydrogen produced during catalysis, gas samples from the headspace were analyzed by gas chromatography (Varian CP 3800 Gas Chromatograph).

4.7.9 Computational Methods

Calculations were performed with the Gaussian09 program package.[104] All geometries were fully optimized at DFT level by means of the hybrid exchange-correlation B3LYP functional. The LANL2DZ pseudopotential was used for Ni, W, Ge, P and Si atoms. The 6-31g(d,p) basis set was used for O atoms directly bound to Ni and the 6-31g basis set for the remaining atoms. All structures were optimized in water using the IEF-PCM approach to model the solvent effects (ε = 78.36 and UFF radii). Open shells were computed at an unrestricted DFT level. Theoretical magnetic analysis of the anion is beyond the scope of the present study. The nature of all stationary points was verified by analytical computation of vibrational frequencies, which were also used for calculation of free energy contributions.

4.8 Appendix

4.8.1 X-ray Analysis and Thermogravimetry

Table S4.1. Selected bond distances for $K_5[Ni(H_2O)PW_{11}O_{39}]\cdot 14\ H_2O$ (**P-1**).

Bond	Distance / Å	Bond	Distance / Å
$W(1)/Ni(1)\text{-}O(3)_{ax.}$	2.438(10)	$W(3)\text{-}O(3)_{ax.}$	2.449(11)
$W(1)/Ni(1)\text{-}O(2)_{ter.}$	1.728(11)	$W(3)\text{-}O(1)_{ter.}$	1.675(15)
$W(1)/Ni(1)\text{-}O(5)_{eq.}$	1.853(17)	$W(3)\text{-}O(4)_{eq.}$	1.945(14)
$W(1)/Ni(1)\text{-}O(7)_{eq.}$	2.002(15)	$W(3)\text{-}O(6)_{eq.}$	1.876(16)
$W(1)/Ni(1)\text{-}O(8)_{eq.}$	1.858(14)	$W(3)\text{-}O(8)_{eq.}$	1.848(13)
$W(1)/Ni(1)\text{-}O(9)_{eq.}$	1.965(15)	$W(3)\text{-}O(9)_{eq.}$	1.967(15)
$W(2)\text{-}O(3)_{ax.}$	2.482(11)	P(1)-O(3)	1.554(12)
$W(2)\text{-}O(10)_{ter.}$	1.69(2)		
$W(2)\text{-}O(4)_{eq.}$	1.953(14)		
$W(2)\text{-}O(5)_{eq.}$	1.835(15)		
$W(2)\text{-}O(6)_{eq.}$	1.838(15)		
$W(2)\text{-}O(7)_{eq.}$	1.979(15)		

Table S4.2. Selected bond distances for $K_6[Ni(H_2O)GeW_{11}O_{39}]\cdot 14\ H_2O$ (**Ge-2**).

Bond	Distance / Å	Bond	Distance / Å
$W(1)/Ni(1)\text{-}O(3)_{ax.}$	2.335(9)	$W(3)\text{-}O(3)_{ax.}$	2.328(9)
$W(1)/Ni(1)\text{-}O(2)_{ter.}$	1.711(10)	$W(3)\text{-}O(1)_{ter.}$	1.691(15)
$W(1)/Ni(1)\text{-}O(5)_{eq.}$	1.860(12)	$W(3)\text{-}O(4)_{eq.}$	2.026(12)
$W(1)/Ni(1)\text{-}O(7)_{eq.}$	2.055(12)	$W(3)\text{-}O(6)_{eq.}$	1.850(10)
$W(1)/Ni(1)\text{-}O(8)_{eq.}$	1.830(11)	$W(3)\text{-}O(8)_{eq.}$	1.833(11)
$W(1)/Ni(1)\text{-}O(9)_{eq.}$	2.036(12)	$W(3)\text{-}O(9)_{eq.}$	2.007(12)
$W(2)\text{-}O(3)_{ax.}$	2.360(9)	Ge(1)-O(3)	1.738(9)
$W(2)\text{-}O(10)_{ter.}$	1.691(15)		
$W(2)\text{-}O(4)_{eq.}$	2.045(11)		
$W(2)\text{-}O(5)_{eq.}$	1.826(12)		
$W(2)\text{-}O(6)_{eq.}$	1.815(10)		
$W(2)\text{-}O(7)_{eq.}$	1.997(12)		

Table S4.3. Selected bond distances for $K_6[Ni(H_2O)SiW_{11}O_{39}]\cdot 14\ H_2O$ (**Si-3**).

Bond	Distance / Å	Bond	Distance / Å
$W(1)/Ni(1)\text{-}O(3)_{ax.}$	2.372(10)	$W(3)\text{-}O(3)_{ax.}$	2.380(9)
$W(1)/Ni(1)\text{-}O(2)_{ter.}$	1.708(11)	$W(3)\text{-}O(1)_{ter.}$	1.682(15)
$W(1)/Ni(1)\text{-}O(5)_{eq.}$	1.852(12)	$W(3)\text{-}O(4)_{eq.}$	1.997(12)
$W(1)/Ni(1)\text{-}O(7)_{eq.}$	2.032(12)	$W(3)\text{-}O(6)_{eq.}$	1.840(12)
$W(1)/Ni(1)\text{-}O(8)_{eq.}$	1.838(12)	$W(3)\text{-}O(8)_{eq.}$	1.837(12)
$W(1)/Ni(1)\text{-}O(9)_{eq.}$	2.028(13)	$W(3)\text{-}O(9)_{eq.}$	1.985(13)
$W(2)\text{-}O(3)_{ax.}$	2.418(9)	Si(1)-O(3)	1.627(9)
$W(2)\text{-}O(10)_{ter.}$	1.702(16)		
$W(2)\text{-}O(4)_{eq.}$	2.026(11)		
$W(2)\text{-}O(5)_{eq.}$	1.832(12)		
$W(2)\text{-}O(6)_{eq.}$	1.815(12)		
$W(2)\text{-}O(7)_{eq.}$	1.987(12)		

Table S4.4. Selected bond distances for $K_8[GeW_{11}O_{39}]\cdot 13H_2O$ (**Ge-4**).

Bond	Distance / Å	Bond	Distance / Å
$W(1)\text{-}O(1)_{ter.}$	1.687(11)	Ge(1)-O(3)	1.731(17)
$W(1)\text{-}O(3)_{ax.}$	2.356(9)		
$W(1)\text{-}O(2)_{eq.}$	2.040(7)		
$W(1)\text{-}O(4)_{eq.}$	1.850(3)		

Table S4.5. Bond valence calculations for **P-1**, **Ge-2**, **Si-3** and **Ge-4**.

$[Ni(H_2O)\{PW_{11}O_{39}\}]^{5-}$ **(P-1)**		$[Ni(H_2O)\{GeW_{11}O_{39}\}]^{6-}$ **(Ge-2)**		$[Ni(H_2O)\{SiW_{11}O_{39}\}]^{6-}$ **(Si-3)**	
W(2)	6.17	W(2)	6.12	W(2)	6.07
W(3)	6.14	W(3)	6.02	W(3)	6.14
P(1)	4.93	Ge(1)	4.26	Si(1)	4.08
O(1)	1.99	O(1)	1.96	O(1)	1.99
O(2)	1.37[a]	O(2)*	1.44[a]	O(2)	1.45[a]
O(3)	1.94	O(3)	2.02	O(3)	1.87
O(4)	1.83	O(4)	1.48[b]	O(4)	1.57[b]
O(5)	2.33	O(5)	2.36	O(5)	2.37
O(6)	2.32	O(6)	1.48[b]	O(6)	2.50
O(7)	1.66[a]	O(7)	1.60[a]	O(7)	1.64[a]
O(8)	2.29	O(8)	2.41	O(8)*	2.39
O(9)*	1.75	O(9)	1.55[a]	O(9)	1.60[a]
O(10)	1.93	O(10)	1.93	O(10)	1.89
$[GeW_{11}O_{39}]^{8-}$ **(Ge-4)**					
W(1)[b]	5.88				
Ge(1)	4.32				
O(1)	1.99				
O(2)	1.60				
O(3)	2.06				
O(4)	2.50				

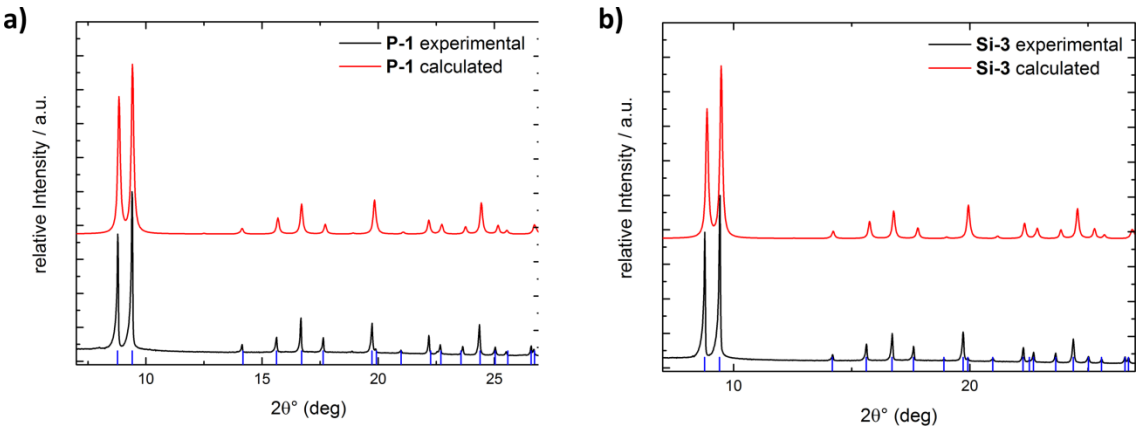

Figure S4.1. PXRD pattern of after background correction (black line) vs. calculated pattern (red line); the blue lines represent calculated peak positions after indexing with ReXcell. (a) **P-1**, (b) **Si-3**.

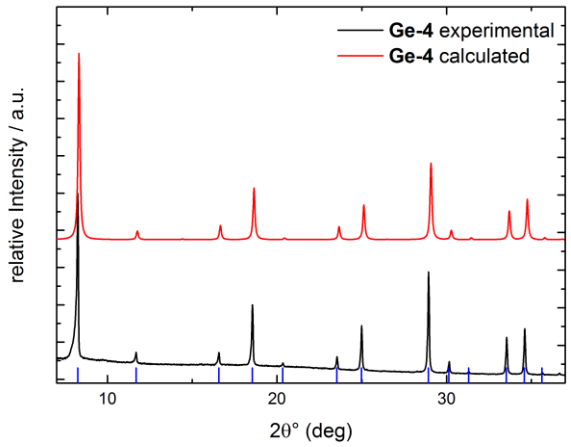

Figure S4.2. PXRD pattern of **Ge-4** after background correction (black line) vs. calculated pattern (red line); the blue lines represent calculated peak positions after indexing with ReXcell.

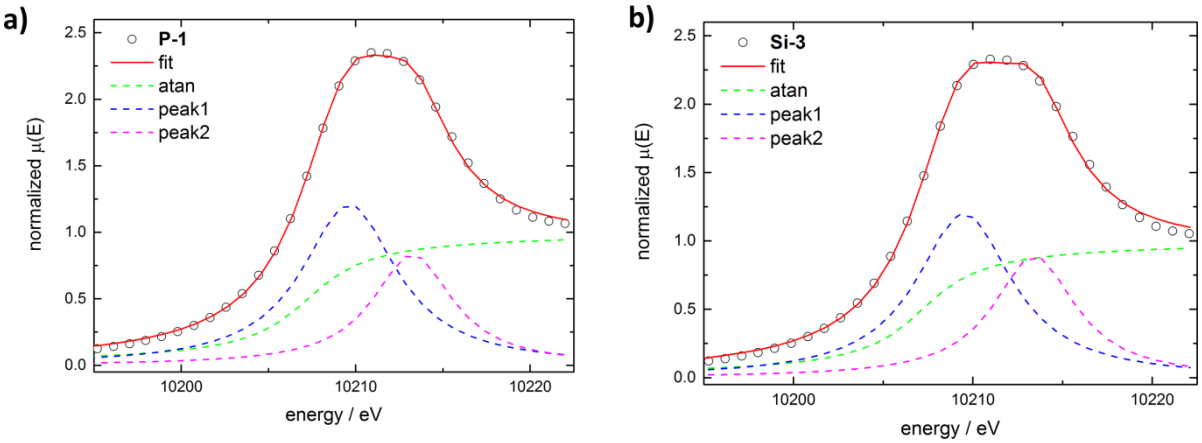

Figure S4.3. W L3-edge XANES spectrum of with fit base arctangent function and Lorentzian peaks (a) **P-1**, (b) **Si-3**.

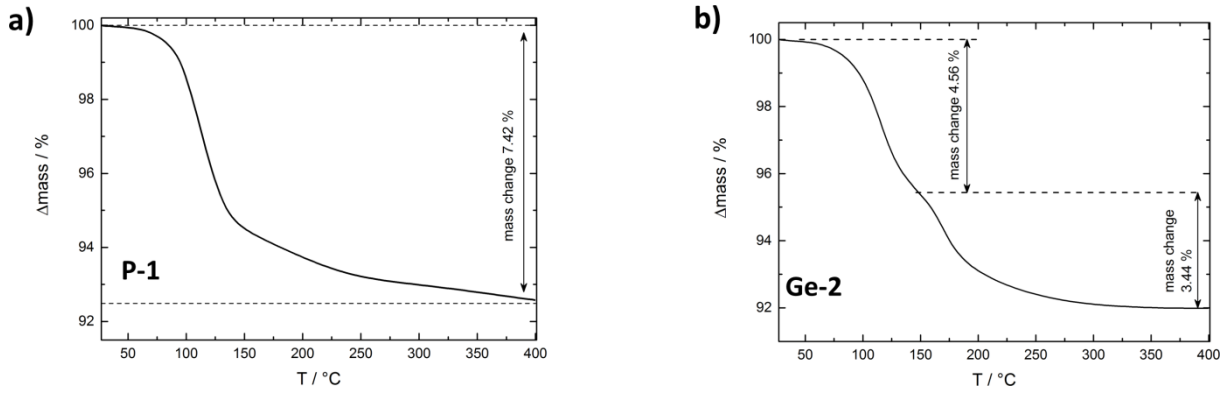

Figure S4.4. Thermogravimmetric analysis of (a) **P-1**, (b) **Ge-2**.

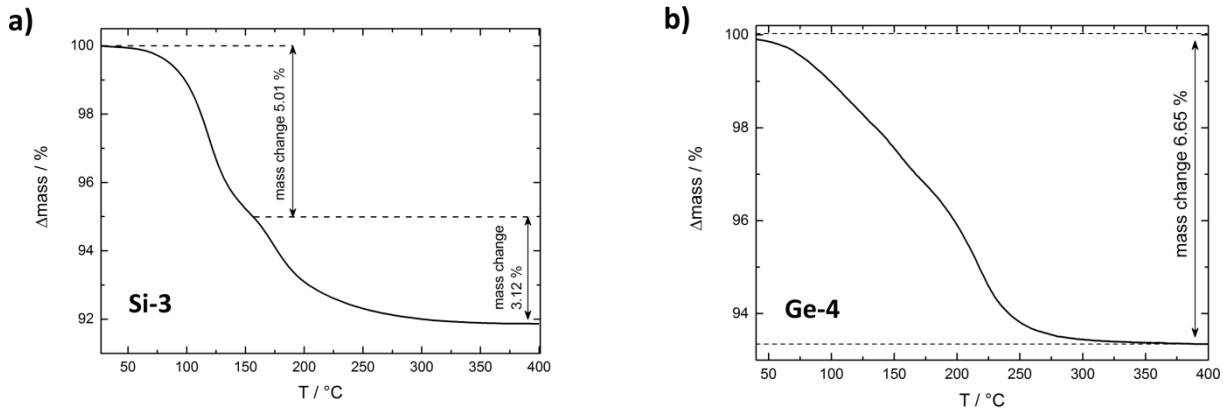

Figure S4.5. Thermogravimmetric analysis of (a) **Si-3**, (b) **Ge-4**.

4.8.2 Spectroscopic Characterization

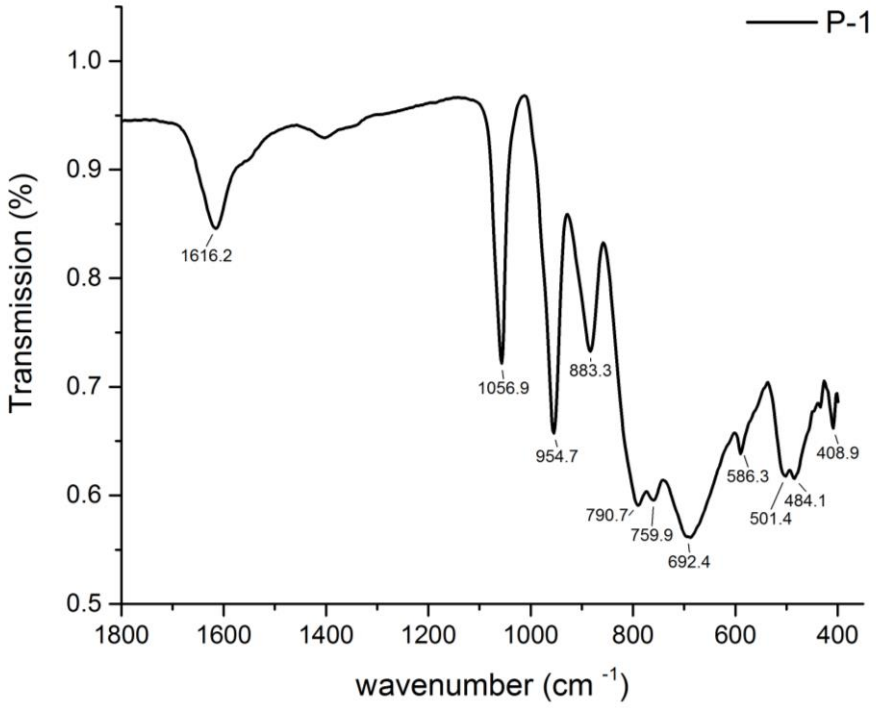

Figure S4.6. ATR FT-IR spectrum of **P-1**.

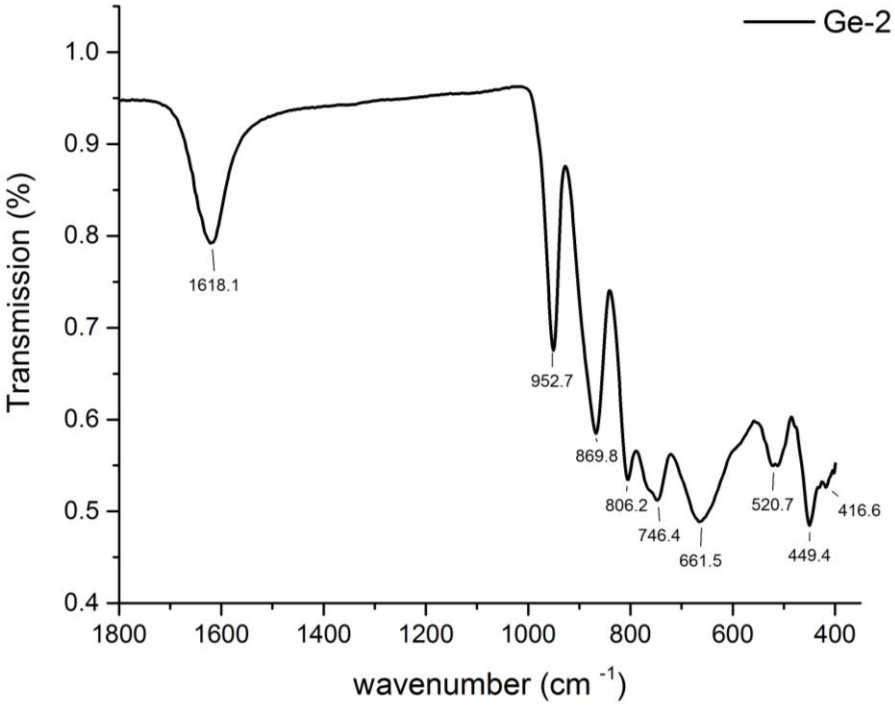

Figure S4.7. ATR FT-IR spectrum of **Ge-2.**

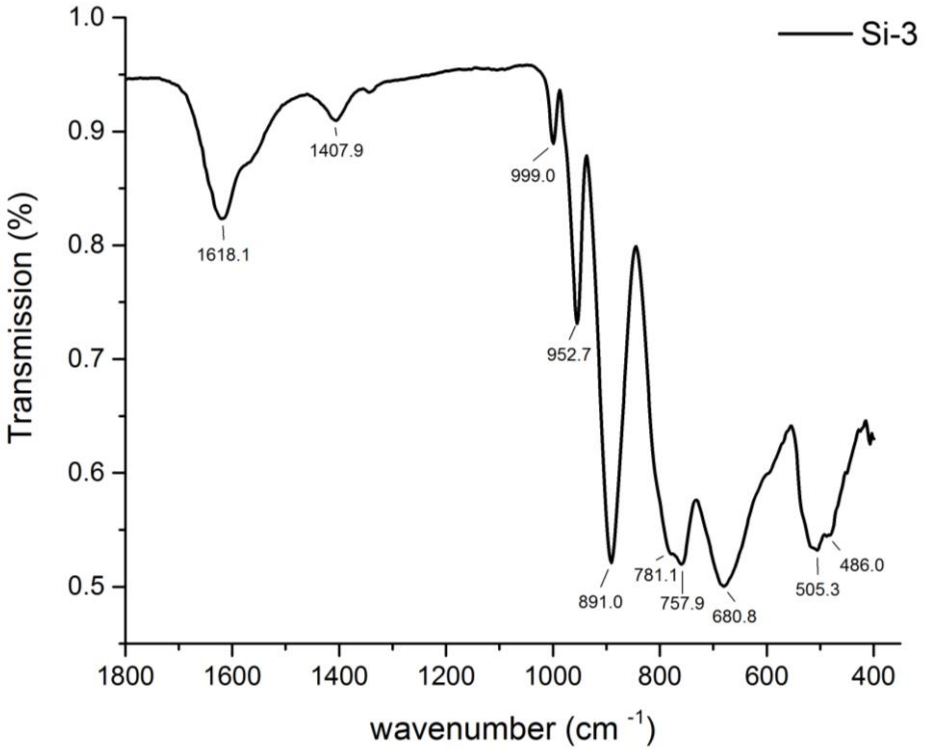

Figure S4.8. ATR FT-IR spectrum of **Si-3**.

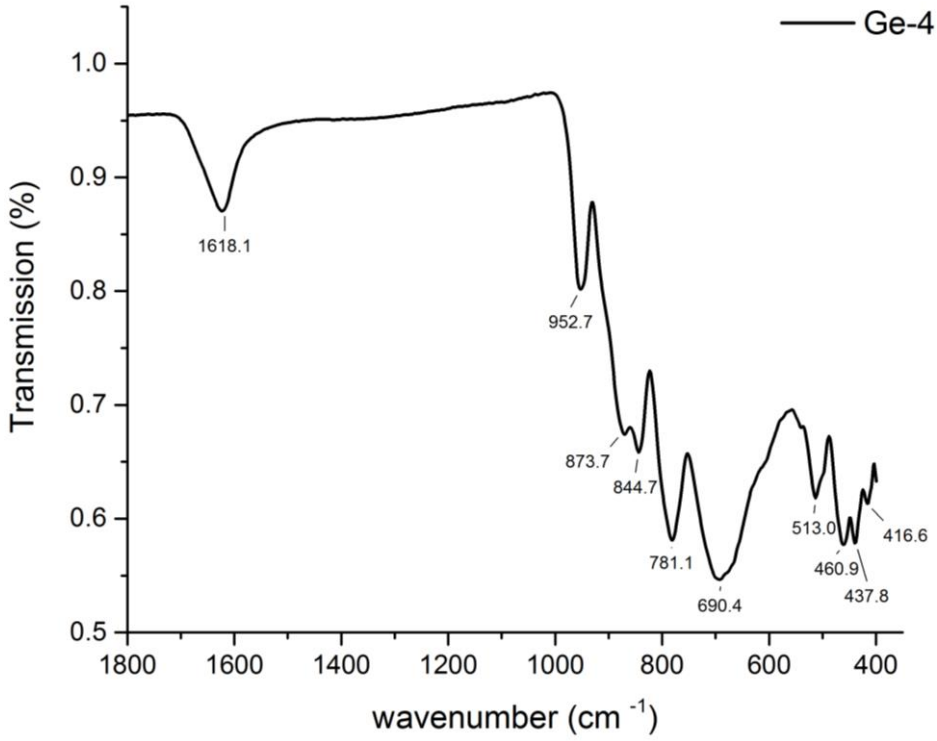

Figure S4.9. ATR FT-IR spectrum of **Ge-4**.

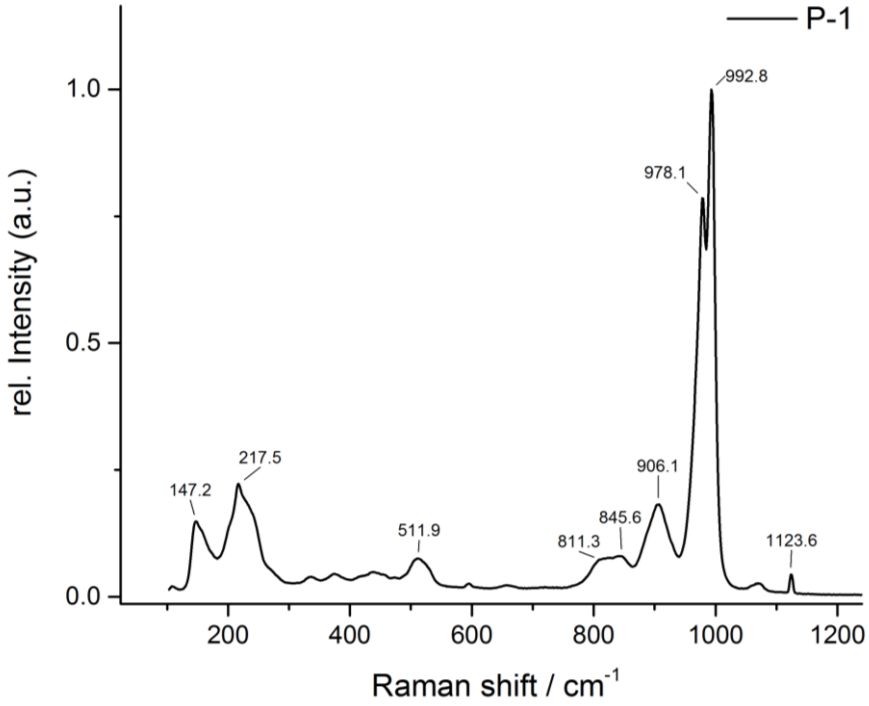

Figure S4.10. Raman spectrum of **P-1**.

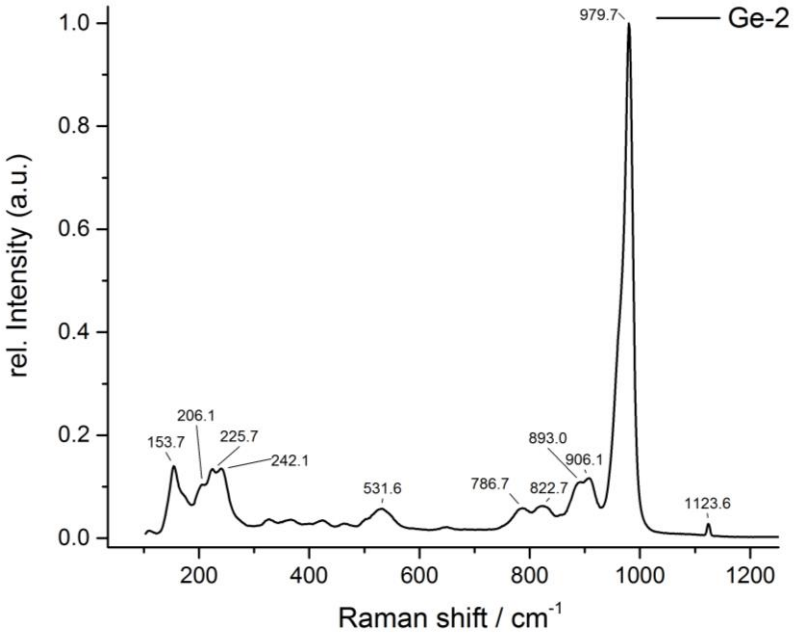

Figure S4.11. Raman spectrum of **Ge-2.**

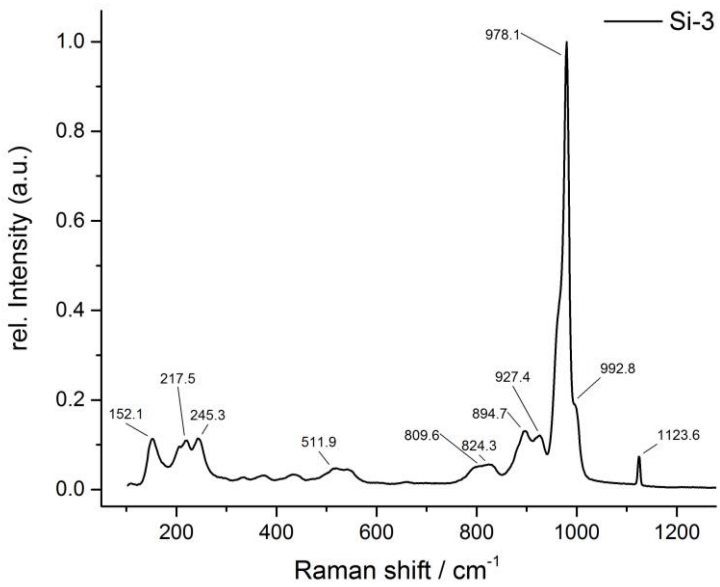

Figure S4.12. Raman spectrum of **Si-3**.

4.8.3 Stability Tests: HR-ESI MS and UV/vis Spectroscopy

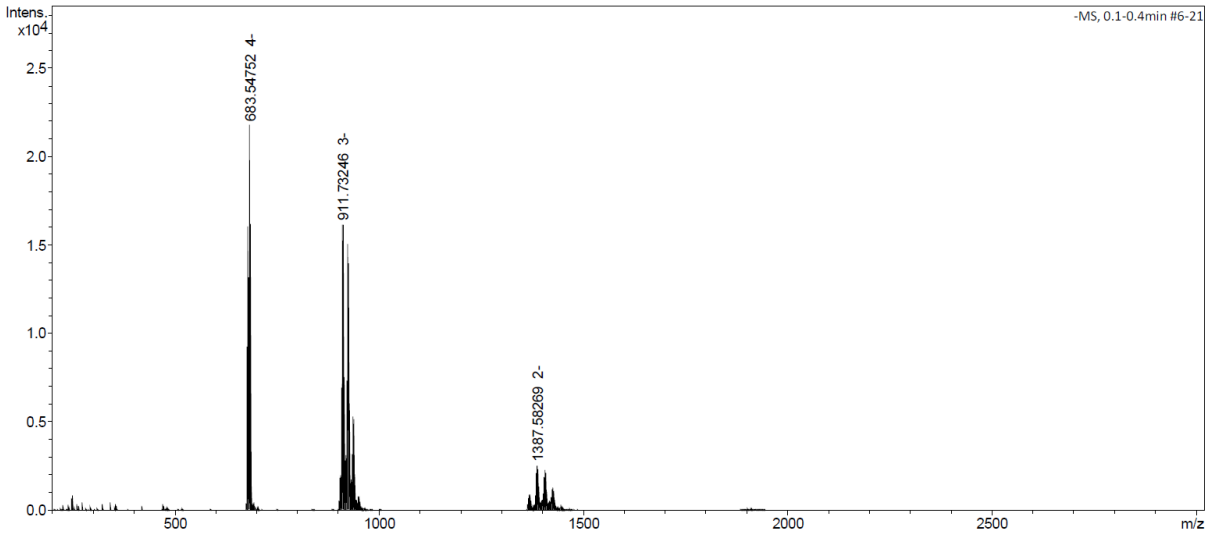

Figure S4.13. HR ESI MS spectrum of **P-1** in water

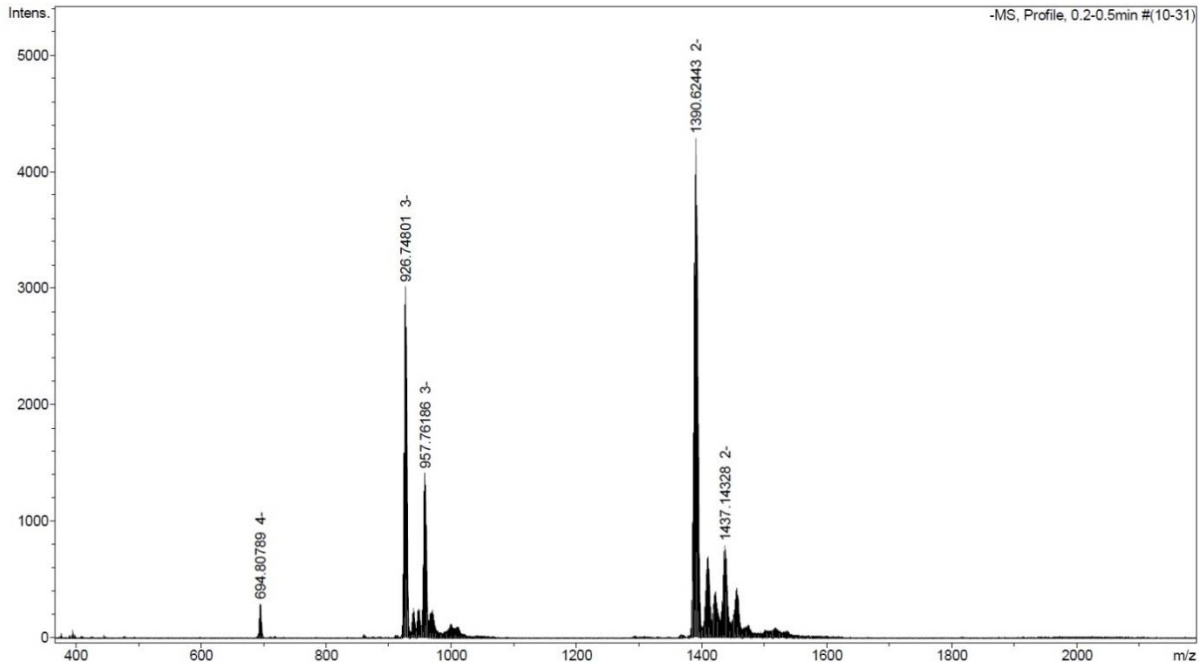

Figure S4.14. HR ESI MS spectrum of **Ge-2** in water.

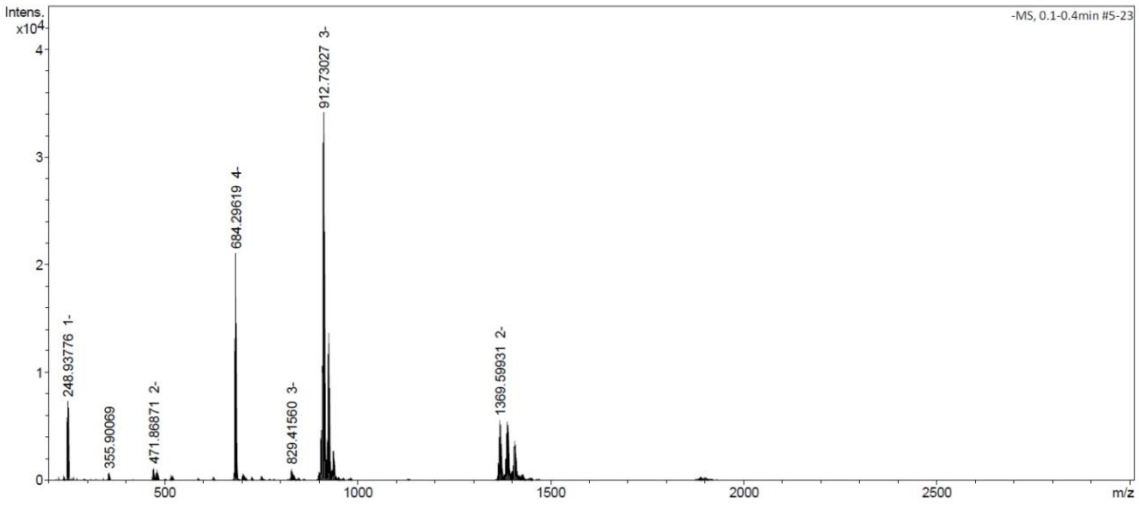

Figure S4.15. HR ESI MS spectrum of **Si-3** in water.

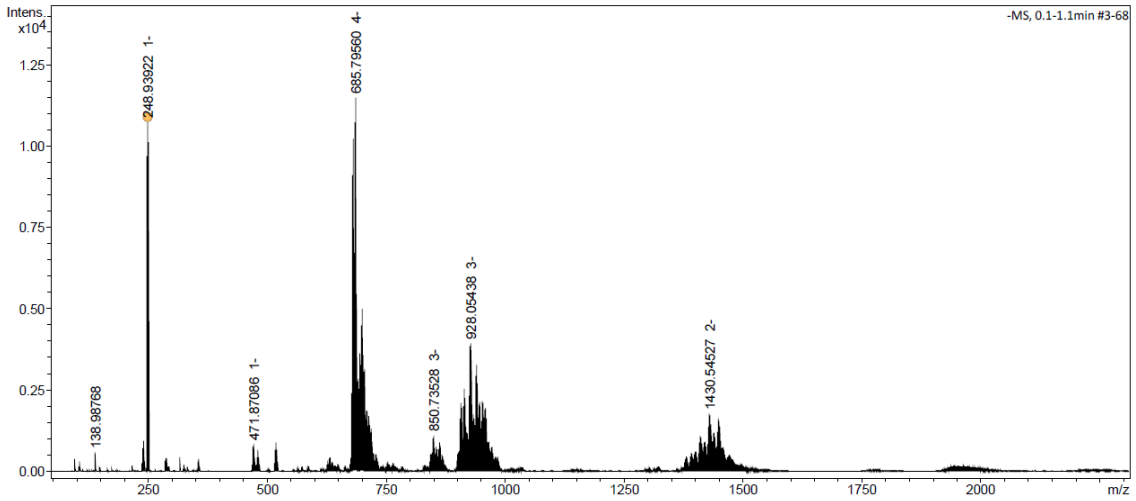

Figure S4.16. HR ESI MS spectrum of **Ge-4** in water.

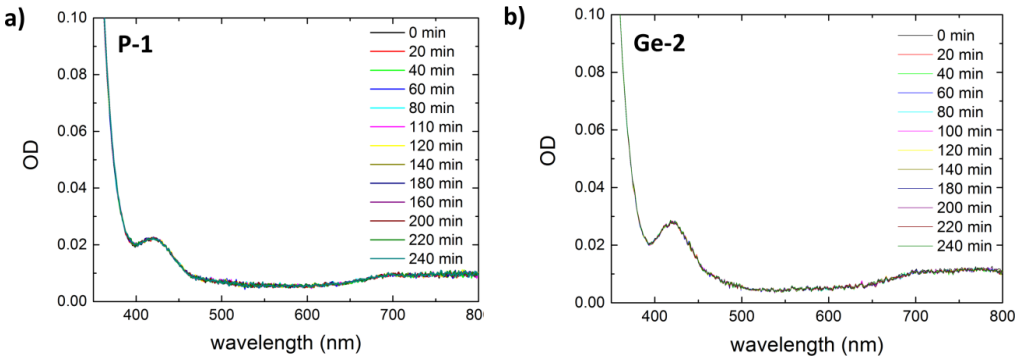

Figure S4.17. Time-dependent UV-vis spectra of (a) **P-1** and (b) **Ge-2** in acetate buffer (50 mM, pH 4).

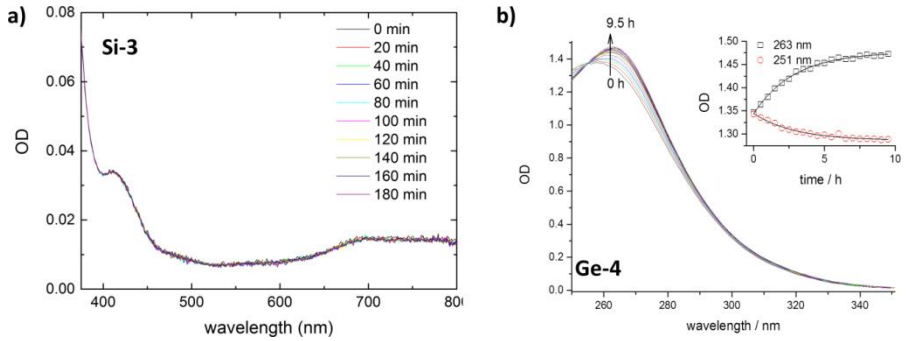

Figure S4.18. (a) Time dependent UV-vis spectra of **Si-3** in acetate buffer (50 mM, pH 4), **(b)** Time-dependent UV-vis spectra in of **Ge-4** in acetate buffer (50 mM, pH 4, inset: time traces at 251 nm (red circles) and 263 nm (black squares)).

4.8.4 Photocatalytic H_2 Evolution Experiments

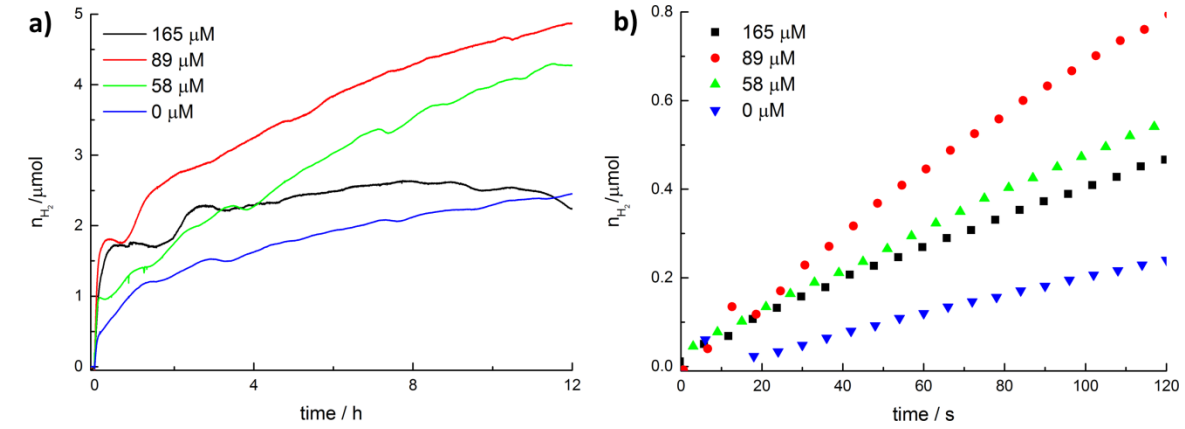

Figure S4.19. Clark electrode data for different concentrations of **P-1**: **(a)** long time kinetics, **(b)** initial phase of hydrogen evolution (experimental conditions: high power LED 470 nm, 1 mM $[Ru(bpy)_3]^{2+}$, 0.12 M ascorbate buffer, pH 4).

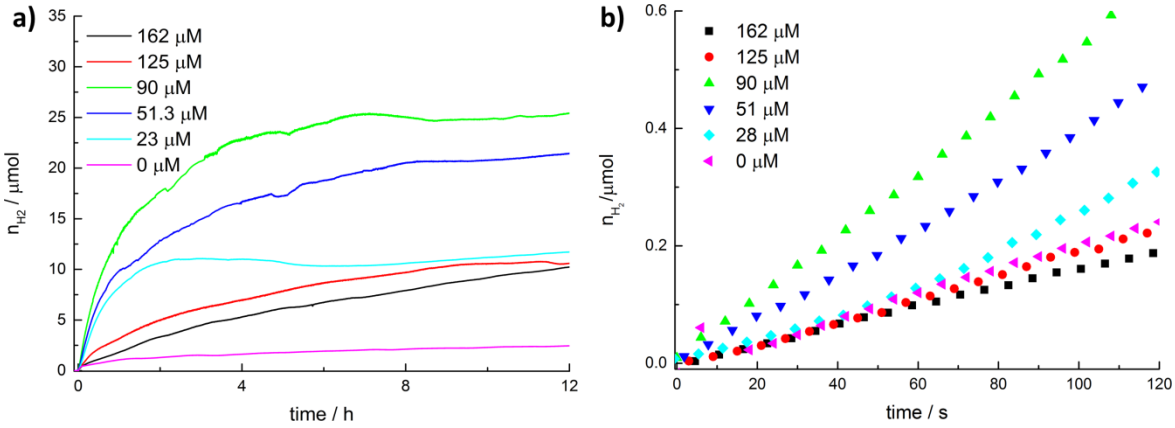

Figure S4.20. Clark electrode data for different concentrations of **Ge-2**: **(a)** long time kinetics, **(b)** initial phase of hydrogen evolution (experimental conditions: high power LED 470 nm, 1 mM $[Ru(bpy)_3]^{2+}$, 0.12 M ascorbate buffer, pH 4)

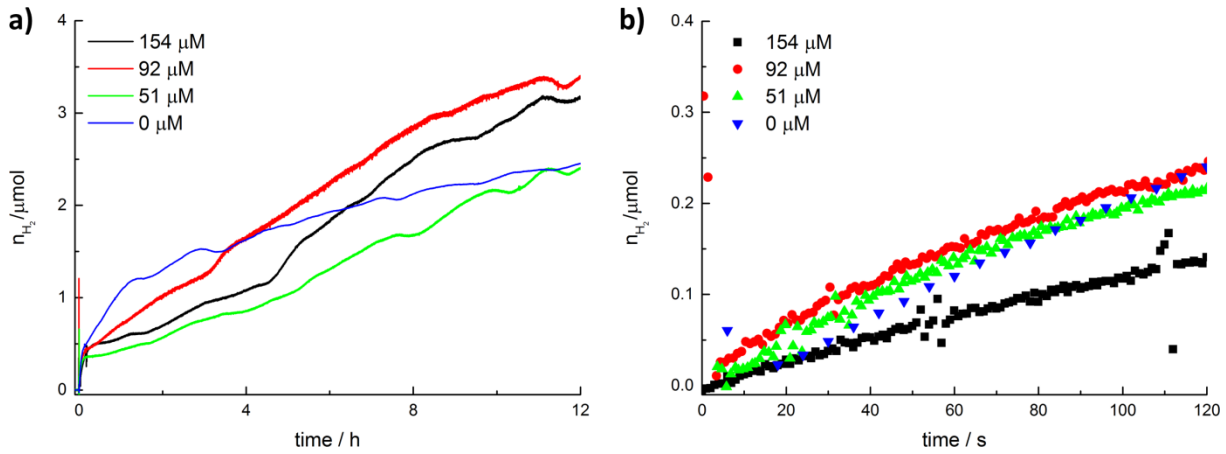

Figure S4.21. Clark electrode data for different concentrations of **Si-3**: **(a)** long time kinetics, **(b)** initial phase of hydrogen evolution (experimental conditions: high power LED 470 nm, 1 mM $[Ru(bpy)_3]^{2+}$, 0.12 M ascorbate buffer, pH 4).

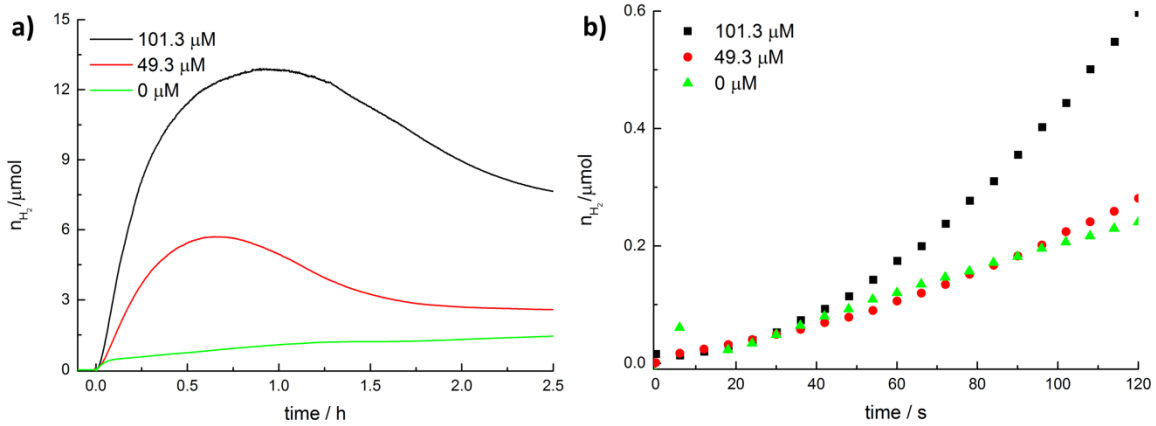

Figure S4.22. Clark electrode data for different concentrations of **Ge-4**: **(a)** long time kinetics, **(b)** initial phase of hydrogen evolution (experimental conditions: high power LED 470 nm, 1 mM $[Ru(bpy)_3]^{2+}$, 0.12 M ascorbate buffer, pH 4).

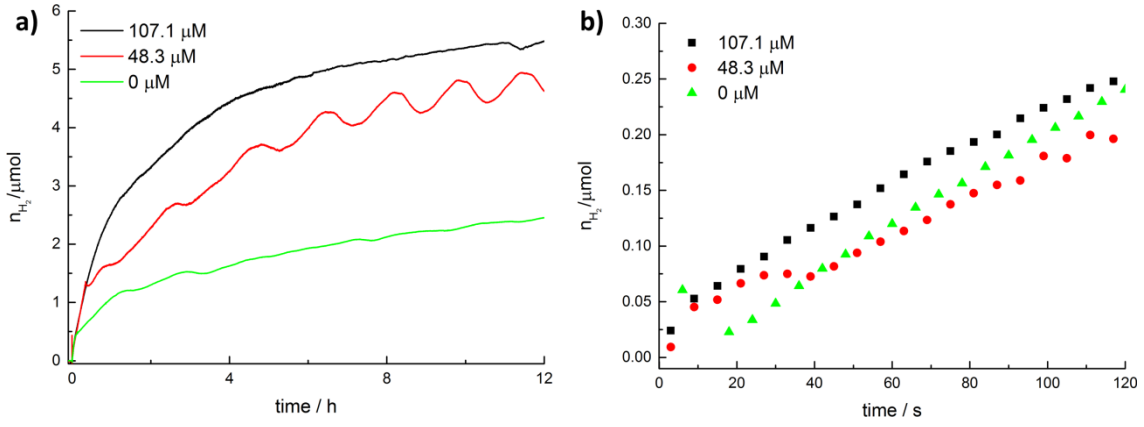

Figure S4.23. Clark electrode data for different concentrations of $[PW_{12}O_{40}]^{3-}$: **(a)** long time kinetics, **(b)** initial phase of hydrogen evolution (experimental conditions: high power LED 470 nm, 1 mM $[Ru(bpy)_3]^{2+}$, 0.12 M ascorbate buffer, pH 4). (The oscillation is caused by vibrations of the climate control system in the lab during the overnight experiment.)

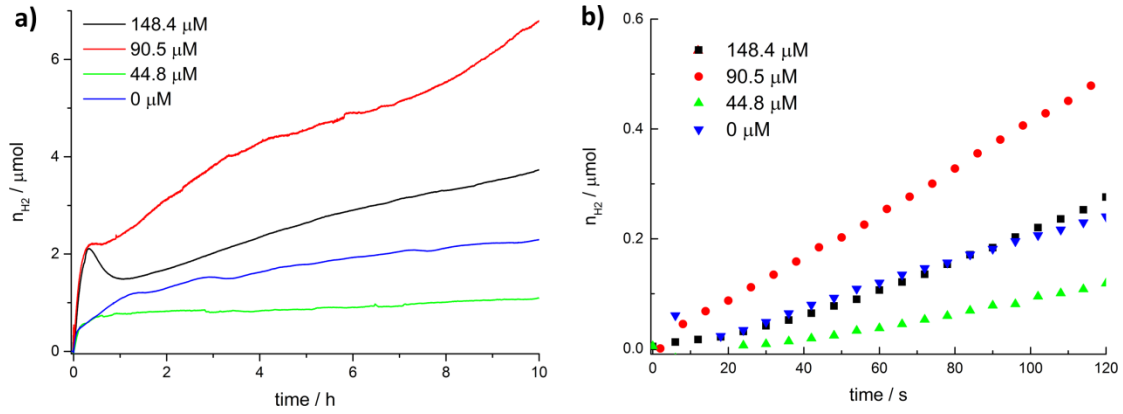

Figure S4.24. Clark electrode data for different concentrations of $[PW_{11}O_{39}]^{7-}$. **(a)** long time kinetics, **(b)** initial phase of hydrogen evolution (experimental conditions: high power LED 470 nm, 1 mM $[Ru(bpy)_3]^{2+}$, 0.12 M ascorbate buffer, pH 4).

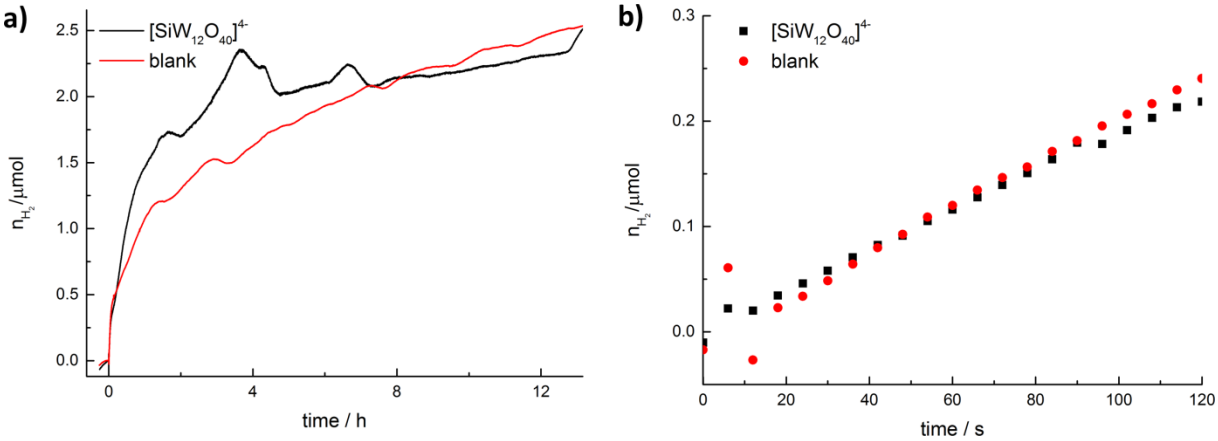

Figure S4.25. Clark electrode data for different concentrations of 100 µM $[SiW_{12}O_{40}]^{4-}$ vs. blank experiment: **(a)** long time kinetics, **(b)** initial phase of hydrogen evolution (experimental conditions: high power LED 470 nm, 1 mM $[Ru(bpy)_3]^{2+}$, 0.12 M ascorbate buffer, pH 4).

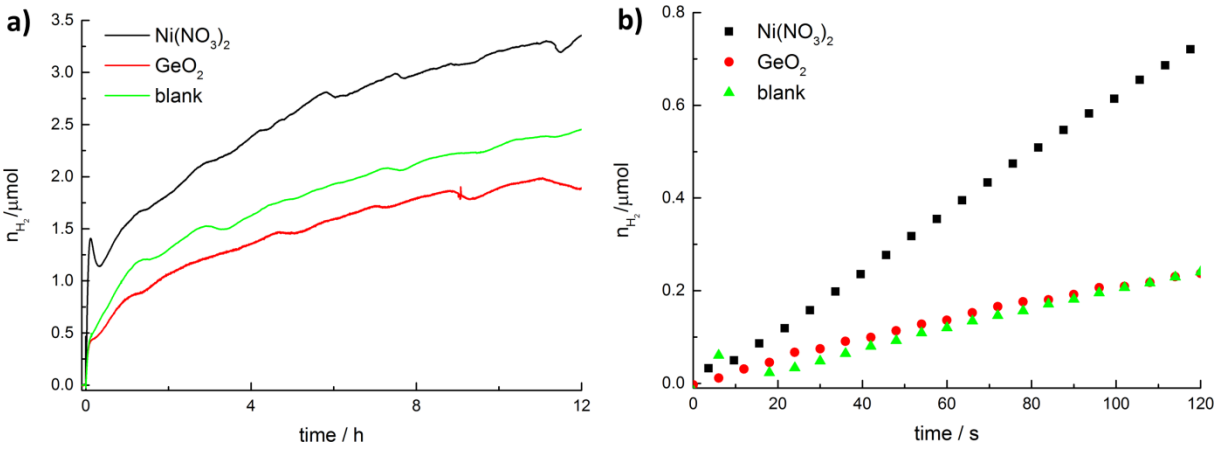

Figure S4.26. Clark electrode data for reference experiments with $Ni(NO_3)_2$ and GeO_2 vs. blank experiments: **(a)** long time kinetics, **(b)** initial phase of hydrogen evolution (experimental conditions: high power LED 470 nm, 1 mM $[Ru(bpy)_3]^{2+}$, 0.12 M ascorbate buffer, pH 4).

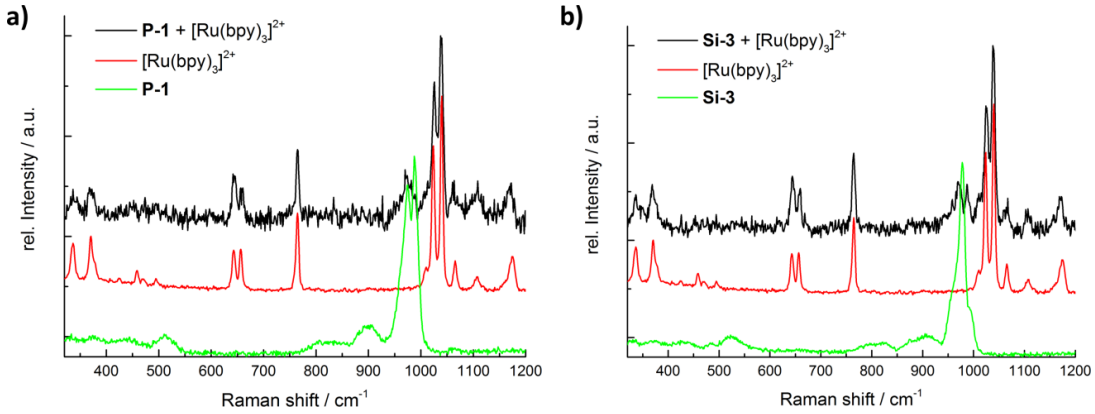

Figure S4.27. Raman spectra of post-catalytic precipitates of (a) **P-1**, (b) **Si-3** in comparison with reference spectra of **P-1** or **Si-3** and $[Ru(bpy)_3]Cl_2$.

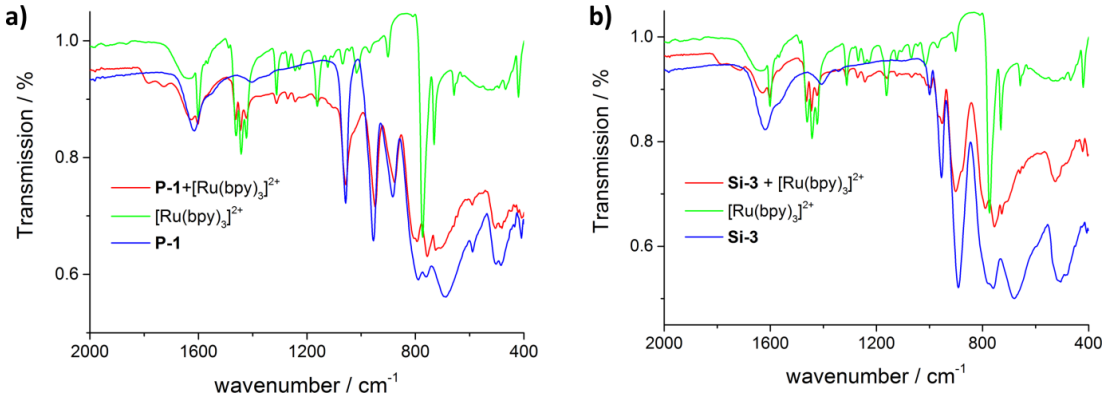

Figure S4.28. FT-IR spectra of post-catalytic precipitate of (a) **P-1**, (b) **Si-3** in comparison with reference spectra of **P-1** or **Si-3** and $[Ru(bpy)_3]Cl_2$.

4.8.5 Electrochemistry of $K_m[Ni(OH_2)XW_{11}O_{39}]$ (X= P, Ge or Si; m= 5 or 6)

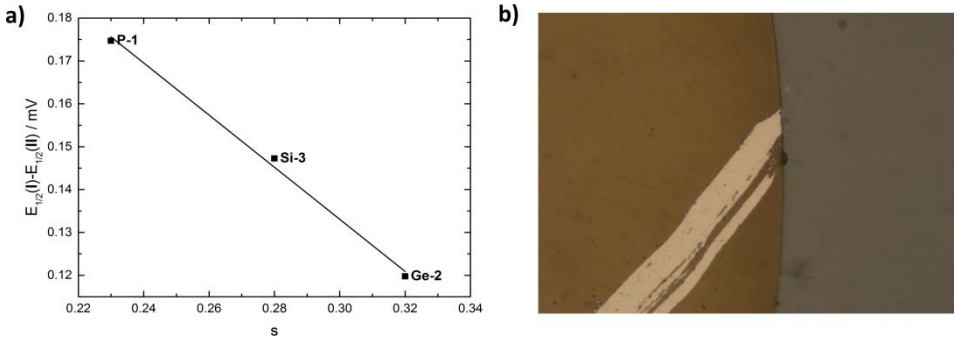

Figure S4.29. (a) Differences of reduction potentials I and II as function of the bond valence of the W-O_{Ax} bond, **(b)** Microscopic image of the brown layer electrodeposited from **Si-3** after 50 cycles to -1.2 V vs Ag/AgCl (partially scratched layer to show the contrast to bare glassy carbon) .

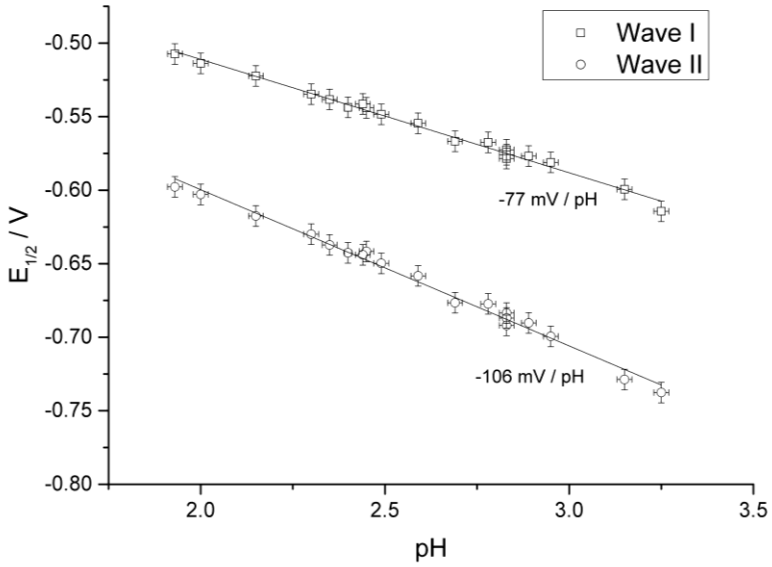

Figure S4.30. pH dependent shift of the redox potential for the reversible waves of **Ge-2**.

Table S4.6. Photocatalytic activity of the Ni-POMs **P-1**, **Ge-2** and **Si-3** vs. selected reference systems.

	[WRC] / µM	n(H_2) / µmol	TON	rate / 10^{-3} µmol s^{-1}	TOF / 10^{-3} s^{-1}
P-1	50.7	4.40±0.30	10.80±0.70	0.66±0.01	1.63±0.02 [a]
P-1	58.0	5.00±0.40	10.90±0.90	4.53±0.06	9.7±0.1
P-1	89.0	5.20±0.70	7.30±0.90	7.55±0.03	10.60±0.40 [a]
P-1	95.7	5.40±0.40	7.10±0.50	0.45±0.03	0.58±0.04
P-1	146.3	4.40±0.20	3.80±0.20	0.33±0.05	0.28±0.02 [a]
P-1	165.0	2.60±0.30	2.00±0.30	4.10±0.01	3.05±0.08
Ge-2	23.4	13.6±1.00	73.00±1.00	1.20±0.10	6.50±0.5
Ge-2	25.4	18.9±1.00	84.00±2.00	0.80±0.10	4.10±0.2
Ge-2	28.0	8.00±1.00	33.0±5.00	2.07±0.06	9.2±0.3
Ge-2	51.0	14.00±3.00	35.0±8.00	3.66±0.05	9.0±0.2
Ge-2	51.3	24.00±2.00	59.00±4.00	2.90±0.10	7.00±0.03
Ge-2	90.0	26.00±2.00	36.00±2.00	5.14±0.04	7.14±0.05
Ge-2	109.04	23.70±0.30	27.70±0.30	1.60±0.20	1.80±0.30
Ge-2	125.0	12.00±1.00	11.70±0.90	1.84±0.05	1.84±0.05
Ge-2	162.0	12.00±1.00	9.00±0.80	1.75±0.04	1.35±0.02
Si-3	51.0	3.00±0.30	7.50±0.60	2.35±0.07	5.70±0.2
Si-3	92.0	3.60±0.40	5.0±0.60	2.50±0.10	3.40±0.1
Si-3	154.0	3.40±0.40	2.70±0.30	1.33±0.05	1.10±0.04
Ge-4	49.3	5.70±0.50	14.00±1.00	1.61±0.06	4.10±0.2
Ge-4	101.3	13.00±1.00	16.00±1.00	2.40±0.20	3.00±0.2
$[PW_{12}O_{40}]^{3}$	48.2	5.10±0.50	13.00±1.00	2.00±0.20	5.30± 0.4
$[PW_{12}O_{40}]^{3-}$	107.1	5.30±0.50	6.4±0.60	2.90±0.10	3.40±0.1
$[PW_{11}O_{39}]^{7-}$	44.8	2.38±0.06	6.2±0.20	0.60±0.40	2.00±1.00
$[PW_{11}O_{39}]^{7-}$	90.5	8.80±0.20	12.2±0.30	4.15±0.06	5.73± 0.09
$[PW_{11}O_{39}]^{7-}$	148.4	5.60±0.20	4.7±0.20	1.60±0.05	1.35±0.04
$[SiW_{12}O_{40}]^{4-}$	100.0	2.70±0.30	3.30±0.30	2.00±0.10	2.50±0.10
$Ni(NO_3)_2$	100.0	3.60±0.40	4.60±0.50	6.20±0.10	7.70±0.20
$Ni(NO_3)_2$	200.0	3.00±0.20	1.90±0.10	1.56±0.07	0.98±0.04
GeO_2	50.0	2.10±0.20	5.30±0.50	2.40±0.80	6.00±2.00
Blank	---	3.10±0.30	---	2.10±0.40	---
Blank	---	2.90±0.20	---		---

[a] Measurements have been done with a new H_2 sensor with a different response time.

4.9 References

[1] V. Balzani, A. Credi, M. Venturi, *ChemSusChem* **2008**, *1*, 26–58.

[2] Y. Tachibana, L. Vayssieres, J. R. Durrant, *Nat. Photonics* **2012**, *6*, 511–518.

[3] K. S. Joya, Y. F. Joya, K. Ocakoglu, R. van de Krol, *Angew. Chem. Int. Ed.* **2013**, *52*, 10426–10437.

[4] S. Berardi, S. Drouet, L. Francas, C. Gimbert-Surinach, M. Guttentag, C. Richmond, T. Stoll, A. Llobet, *Chem. Soc. Rev.* **2014**, *43*, 7501–7519.

[5] Z. Han, R. Eisenberg, *Accounts Chem. Res.* **2014**, *47*, 2537–2544.

[6] M. D. Kärkäs, O. Verho, E. V. Johnston, B. Åkermark, *Chem. Rev.* **2014**, *114*, 11863–12001.

[7] A. Singh, L. Spiccia, *Coord. Chem. Rev.* **2013**, *257*, 2607–2622.

[8] C. G. Morales-Guio, L.-A. Stern, X. Hu, *Chem. Soc. Rev.* **2014**, *43*, 6555–6569.

[9] K. Maeda, *ACS Catal.* **2013**, *3*, 1486–1503.

[10] J. M. Sumliner, H. Lv, J. Fielden, Y. V. Geletii, C. L. Hill, *Eur. J. Inorg. Chem.* **2014**, *2014*, 635–644.

[11] M. T. Pope, A. Müller, *Angew. Chem. Int. Ed.* **1991**, *30*, 34–48.

[12] M. T. Pope in *Comprehensive Coordination Chemistry 5II6* (Ed.: J. A. Meyer), Pergamon, Oxford, **2003**.

[13] C. L. Hill in *Comprehensive Coordination Chemistry 5II6* (Eds.: J. A. Meyer, T. J. McCleverty), Pergamon, Oxford, **2003**.

[14] M. T. Pope in *Handbook on the Physics and Chemistry of Rare Earths* (Eds.: K. A. Gschneidner, V. K. Pecharsky), Elsevier, **2008**.

[15] J.-F. Lemonnier, S. Duval, S. Floquet, E. Cadot, *Isr. J. Chem.* **2011**, *51*, 290–302.

[16] A. Müller, P. Gouzerh, *Chem. Soc. Rev.* **2012**, *41*, 7431–7463.

[17] Y. Wang, I. A. Weinstock, *Chem. Soc. Rev.* **2012**, *41*, 7479–7496.

[18] M.-P. Santoni, G. S. Hanan, B. Hasenknopf, *Coord. Chem. Rev.* **2014**, *281*, 64–85.

[19] U. Kortz, A. Müller, J. van Slageren, J. Schnack, N. S. Dalal, M. Dressel, *Coord. Chem. Rev.* **2009**, *253*, 2315–2327.

[20] E. Cadot, M. N. Sokolov, V. P. Fedin, C. Simonnet-Jegat, S. Floquet, F. Sécheresse, *Chem. Soc. Rev.* **2012**, *41*, 7335–7353.

[21] H. Lv, Y. V. Geletii, C. Zhao, J. W. Vickers, G. Zhu, Z. Luo, J. Song, T. Lian, D. G. Musaev, C. L. Hill, *Chem. Soc. Rev.* **2012**, *41*, 7572–7589.

[22] Z. Huang, Y. V. Geletii, D. G. Musaev, C. L. Hill, T. Lian, *Ind. Eng. Chem. Res.* **2012**, *51*, 11850–11859.

[23] C. Streb, *Dalton Trans.* **2012**, *41*, 1651–1659.

[24] O. Oms, A. Dolbecq, P. Mialane, *Chem. Soc. Rev.* **2012**, *41*, 7497–7536.

[25] M. Sadakane, E. Steckhan, *Chem. Rev.* **1998**, *98*, 219–238.

[26] I.-M. Mbomekallé, X. López, J. M. Poblet, F. Sécheresse, B. Keita, L. Nadjo, *Inorg. Chem.* **2010**, *49*, 7001–7006.

[27] H. El Moll, G. Rousseau, A. Dolbecq, O. Oms, J. Marrot, M. Haouas, F. Taulelle, E. Rivière, W. Wernsdorfer, D. Lachkar, E. Lacôte, B. Keita, P. Mialane, *Chem-Eur. J.* **2013**, *19*, 6753–6765.

[28] D. M. Fernandes, J. G. Vos, C. Freire, *J. Collloid Interf. Sci.* **2014**, *420*, 127–135.

[29] Y. V. Geletii, B. Botar, P. Kögerler, D. A. Hillesheim, D. G. Musaev, C. L. Hill, *Angew. Chem. Int. Ed.* **2008**, *47*, 3896–3899.

[30] Y. V. Geletii, B. Botar, P. Kögerler, D. A. Hillesheim, D. G. Musaev, C. L. Hill, *Angew. Chem.-Ger. Edit.* **2008**, *120*, 3960–3963.

[31] A. Sartorel, M. Carraro, G. Scorrano, R. De Zorzi, S. Geremia, N. D. McDaniel, S. Bernhard, M. Bonchio, *J. Am. Chem. Soc.* **2008**, *130*, 5006–5007.

[32] Q. Yin, J. M. Tan, C. Besson, Y. V. Geletii, D. G. Musaev, A. E. Kuznetsov, Z. Luo, K. I. Hardcastle, C. L. Hill, *Science* **2010**, *328*, 342–345.

[33] F. Puntoriero, G. La Ganga, A. Sartorel, M. Carraro, G. Scorrano, M. Bonchio, S. Campagna, *Chem. Commun.* **2010**, *46*, 4725–4727.

[34] X.-B. Han, Z.-M. Zhang, T. Zhang, Y.-G. Li, W. Lin, W. You, Z.-M. Su, E.-B. Wang, *J. Am. Chem. Soc.* **2014**, *136*, 5359–5366.

[35] J. J. Stracke, R. G. Finke, *ACS Catal.* **2014**, *4*, 909–933.

[36] G. A. Olah, *Angew. Chem. Int. Ed.* **2013**, *52*, 104–107.

[37] J. A. Turner, *Science* **2004**, *305*, 972–974.

[38] B. Rausch, M. D. Symes, G. Chisholm, L. Cronin, *Science* **2014**, *345*, 1326–1330.

[39] B. Nohra, H. El Moll, L. M. Rodriguez-Albelo, P. Mialane, J. Marrot, C. Mellot-Draznieks, M. O'Keeffe, R. N. Biboum, J. Lemaire, B. Keita, L. Nadjo, A. Dolbecq, *J. Am. Chem. Soc.* **2011**, *133*, 13363–13374.

[40] A. Ioannidis, E. Papaconstantinou, *Inorg. Chem.* **1985**, *24*, 439–441.

[41] X. Liu, Y. Li, S. Peng, G. Lu, S. Li, *Int. J. of Hydrogen Energ.* **2012**, *37*, 12150–12157.

[42] X. Shang, R. Liu, G. Zhang, S. Zhang, H. Cao, Z. Gu, *New J. Chem.* **2014**, *38*, 1315–1320.

[43] J. Zhao, Yong Ding, J. Wei, X. Du, Y. Yu, R. Han, *Int. J. of Hydrogen Energ.* **2014**, *39*, 18908–18918.

[44] Z. Wang, Y. Lu, Y.-G. Li, S. Wang, E.-B. Wang, *Chinese Science Bulletin* **2012**, *57*, 2265–2268.

[45] O. Snir, Y. Wang, M. E. Tuckerman, Y. V. Geletii, I. A. Weinstock, *J. Am. Chem. Soc.* **2010**, *132*, 11678–11691.

[46] V. J. DeRose, I. Mukerji, M. J. Latimer, V. K. Yachandra, K. Sauer, M. P. Klein, *J. Am. Chem. Soc.* **1994**, *116*, 5239–5249.

[47] K. Yamaguchi, S. Yamanaka, H. Isobe, T. Saito, K. Kanda, Y. Umena, K. Kawakami, J.-R. Shen, N. Kamiya, M. Okumura, H. Nakamura, M. Shoji, Y. Yoshioka, *Int. J. Quantum Chem.* **2013**, *113*, 453–473.

[48] P.-H. Lin, M. K. Takase, T. Agapie, *Inorg. Chem.* **2015**, *54*, 59–64.

[49] J. S. Kanady, P.-H. Lin, K. M. Carsch, R. J. Nielsen, M. K. Takase, W. A. Goddard, T. Agapie, *J. Am. Chem. Soc.* **2014**, *136*, 14373–14376.

[50] H. Lv, W. Guo, K. Wu, Z. Chen, J. Bacsa, D. G. Musaev, Y. V. Geletii, S. M. Lauinger, T. Lian, C. L. Hill, *J. Am. Chem. Soc.* **2014**, *136*, 14015–14018.

[51] H. Lv, J. Song, Z. Haiming, Y. V. Geletii, J. Bacsa, Z. Chongchao, T. Lian, D. G. Musaev, C. L. Hill, *J. Catal.* **2013**, *307*, 48–54.

[52] J. J. Stracke, R. G. Finke, *J. Am. Chem. Soc.* **2011**, *133*, 14872–14875.

[53] J.-H. Son, J. Wang, W. H. Casey, *Dalton Trans.* **2014**, *43*, 17928–17933.

[54] J. M. Poblet, X. López, C. Bo, *Chem. Soc. Rev.* **2003**, *32*, 297–308.

[55] F. E. Osterloh, *Chem. Mater.* **2008**, *20*, 35–54.

[56] T. Peng, X. Zhang, H. Lv, L. Zan, *Catal. Commun.* **2012**, *28*, 116–119.

[57] Z. Han, F. Qiu, R. Eisenberg, P. L. Holland, T. D. Krauss, *Science* **2012**, *338*, 1321–1324.

[58] A. K. Agegnehu, C.-J. Pan, J. Rick, J.-F. Lee, W.-N. Su, B.-J. Hwang, *J. Mater. Chem.* **2012**, *22*, 13849–13854.

[59] W. Grochala, *Phys. Chem. Chem. Phys.* **2006**, *8*, 1340–1345.

[60] M. L. Helm, M. P. Stewart, R. M. Bullock, R. M. DuBois, D. L. DuBois, *Science* **2011**, *333*, 863–866.

[61] P. Hermosilla-Ibanez, P.-E. Car, A. Vega, J. Costamagna, F. Caruso, J.-Y. Pivan, E. Le Fur, E. Spodine, D. Venegas-Yazigi, *CrystEngComm* **2012**, *14*, 5604–5612.

[62] H. Weiner, H.-J. Lunk, J. Fuchs, B. Ziemer, R. Stösser, C. Pietzsch, P. Reich, *Z. anorg. allg. Chem.* **1991**, *594*, 191–201.

[63] X.-P. Yang, C.-Z. Chen, X.-P. Lin, Z.-C. Yang, Z.-B. Chen, J. Lin, *Jiegou Huaxue* **1997**, *16*, 488–491.

[64] S.-B. Shao, X.-P. Yang, C.-Z. Chen, Z.-B. Huang, D.-S. Gao, *Jiegou Huaxue* **1997**, *16*, 68–71.

[65] X. Lin, *J. Fujian Teach. Univ. Nat. Sci. Ed.* **2005**, *21*, 70–74.

[66] T. J. R. Weakley, *J. Cryst. Spectrosc.* **1987**, *17*, 383–391.

[67] Z. Zhang, Q. Lin, S.-T. Zheng, X. Bu, P. Feng, *Chem. Commun.* **2011**, *47*, 3918–3920.

[68] W.-C. Chen, C. Qin, X.-L. Wang, Y.-G. Li, H.-Y. Zang, Y.-Q. Jiao, P. Huang, K.-Z. Shao, Z.-M. Su, E.-B. Wang, *Chem. Commun.* **2014**, *50*, 13265–13267.

[69] Z.-X. Yang, P. Huang, L. Zhao, M. Zhang, Y.-T. Zhang, Z.-M. Su, *Inorg. Chem. Commun.* **2014**, *44*, 195–197.

[70] J.-H. Son, J. Wang, F. E. Osterloh, P. Yu, W. H. Casey, *Chem. Commun.* **2014**, *50*, 836–838.

[71] Z. Wang, H.-Q. Tan, W.-L. Chen, Y.-G. Li, E.-B. Wang, *Dalton Trans.* **2012**, *41*, 9882–9884.

[72] K. Suzuki, F. Tang, Y. Kikukawa, K. Yamaguchi, N. Mizuno, *Chem. Lett.* **2014**, *43*, 1429–1431.

[73] B. Matt, J. Fize, J. Moussa, H. Amouri, A. Pereira, V. Artero, G. Izzet, A. Proust, *Energ. Environ. Sci.* **2013**, *6*, 1504–1508.

[74] G. Liu, X. Wang, X. Wang, H. Han, C. Li, *J. Catal.* **2012**, *293*, 61–66.

[75] C. Rocchiccioli-Deltcheff, M. Fournier, R. Franck, R. Thouvenot, *Inorg. Chem.* **1983**, *22*, 207–216.

[76] R. Thouvenot, M. Fournier, R. Franck, C. Rocchiccioli-Deltcheff, *Inorg. Chem.* **1984**, *23*, 598–605.

[77] Q.-X. Han, J.-P. Wang, L.-H. Song, *Acta Crystallogr. E.* **2006**, *62*, i201-i203.

[78] M. Bortolotti, I. Lonardelli, *J. Appl. Cryst.* **2013**, *46*, 259–261.

[79] A. Boultif, D. Louër, *J. Appl. Cryst.* **2004**, *37*, 724–731.

[80] D. Nicholls, *Complexes and First-Row Transition Elements*,, Macmillan Press, London, **1971**.

[81] C. J. Ballhause, *Molecular Electronic Structure of Transition Metal Complexes*, McGraw-Hill, New York, **1980**.

[82] Y. Tanabe, S. Sugano, *J. Phys. Soc. JPN.* **1954**, *9*, 766–779.

[83] Y. Tanabe, S. Sugano, *J. Phys. Soc. JPN.* **1956**, *11*, 864–877.

[84] Y. Tanabe, S. Sugano, *J. Phys. Soc. JPN.* **1954**, *9*, 753–766.

[85] B. Ravel, M. Newville, *J. Synchrotron Radiat.* **2005**, *12*, 537–541.

[86] C. Bachmann, B. Probst, M. Guttentag, R. Alberto, *Chem. Commun.* **2014**, *50*, 6737–6739.

[87] P.-E. Car, M. Guttentag, K. K. Baldridge, R. Alberto, G. R. Patzke, *Green. Chem.* **2012**, *14*, 1680–1688.

[88] J. Gao, S. Cao, Q. Tay, Y. Liu, L. Yu, K. Ye, P. C. S. Mun, Y. Li, G. Rakesh, S. C. J. Loo, Z. Chen, Y. Zhao, C. Xue, Q. Zhang, *Sci. Rep.* **2013**, *3*, 1853–1858.

[89] F. Evangelisti, P.-E. Car, O. Blacque, G. R. Patzke, *Catal. Sci. Technol.* **2013**, *3*, 3117–3129.

[90] T. E. Keyes, E. Gicquel, L. Guerin, R. J. Forster, V. M. Hultgren, A. M. Bond, A. G. Wedd, *Inorg. Chem.* **2003**, *42*, 7897–7905.

[91] M. K. Seery, L. Guerin, R. J. Forster, E. Gicquel, V. Hultgren, A. M. Bond, A. G. Wedd, T. E. Keyes, *J. Phys. Chem. A* **2004**, *108*, 7399–7405.

[92] N. Fay, V. M. Hultgren, A. G. Wedd, T. E. Keyes, R. J. Forster, D. Leane, A. M. Bond, *Dalton Trans.* **2006**, 4218–4227.

[93] O. Poizat, C. Sourisseau, *J. Phys. Chem.* **1984**, *88*, 3007–3014.

[94] S. Yamazoe, Y. Hitomi, T. Shishido, T. Tanaka, *J. Phys. Chem. C.* **2008**, *112*, 6869–6879.

[95] D.-Y. Cho, J. Park, J. Yu, J.-G. Park, *J. Phys-Condens. Mat.* **2012**, *24*, 55503.

[96] U. Jayarathne, P. Chandrasekaran, A. F. Greene, J. T. Mague, S. DeBeer, K. M. Lancaster, S. Sproules, J. P. Donahue, *Inorg. Chem.* **2014**, *53*, 8230–8241.

[97] S. Himeno, M. Takamoto, *J. Electroanal. Chem.* **2002**, *528*, 170–174.

[98] K. Nakajima, K. Eda, S. Himeno, *Inorg. Chem.* **2010**, *49*, 5212–5215.

[99] C. R. Bock, J. A. Connor, A. R. Gutierrez, Thomas J. Meyer, D. G. Whitten, B. P. Sullivan, J. K. Nagle, *J. Am. Chem. Soc.* **1979**, *101*, 4815–4824.

[100] B. Keita, U. Kortz, L. R. B. Holzle, S. Brown, L. Nadjo, *Langmuir* **2007**, *23*, 9531–9534.

[101] M. Ammam, B. Keita, L. Nadjo, I.-M. Mbomekallé, J. Fransaer, *J. Electroanal. Chem.* **2010**, *645*, 65–73.

[102] J. M. Thomsen, S. W. Sheehan, S. M. Hashmi, J. Campos, U. Hintermair, R. H. Crabtree, G. W. Brudvig, *J. Am. Chem. Soc.* **2014**, *136*, 13826–13834.

[103] T. J. R. Weakley, S. A. Malik, *J. Inorg. Nucl. Chem.* **1967**, *29*, 2935–2944.

[104] Frisch, G. W. Trucks, H. B. Schlegel, G. E. Scuseria, M. A. Robb, J. R. Cheeseman, G. Scalmani, V. Barone, B. Mennucci, G. A. Petersson, H. Nakatsuji, M. Caricato, X. Li, H. P. Hratchian, A. F. Izmaylov, J. Bloino, G. Zheng, J. L. Sonnenberg, M. Hada, M. Ehara, K. Toyota, R. Fukuda, J. Hasegawa, M. Ishida, T. Nakajima, Y. Honda, O. Kitao, H. Nakai, T. Vreven, J. A. Montgomery Jr., J. E. Peralta, F. Ogliaro, M. Bearpark, J. J. Heyd, E. Brothers, K. N. Kudin, V. N. Staroverov, R. Kobayashi, J. Normand, K. Raghavachari, A. Rendell, J. C. Burant, S. S. Iyengar, J. Tomasi, M. Cossi, N. Rega, J. M. Millam, M. Klene, J. E. Knox, J. B. Cross, V. Bakken, C. Adamo, J. Jaramillo, R. Gomperts, R. E. Stratmann, O. Yazyev, A. J. Austin, R. Cammi, C. Pomelli, J. W. Ochterski, R. L. Martin, K. Morokuma, V. G. Zakrzewski, G. A. Voth, P. Salvador, J. J. Dannenberg, S. Dapprich, A. D. Daniels, O. Farkas, J. B. Foresman, J. V. Ortiz, J. Cioslowski, D. J. Fox, *Gaussian 09, Revision A.02*.

Chapter 5

New Gallium Containing Polyoxotungstates

5 New Gallium Containing Polyoxotungstates

All results in chapter 4 have been published:

Kim von Allmen, Pierre-Emmanuel Car, Olivier Blacque, Thomas Fox, Rafael Müller, Greta R. Patzke. Zeitschrift für Anorganische und Allgemeine Chemie, **2014**, 640 (5), 781. DOI: 10.1002/zaac.201300669

5.1 Introduction

Targeted development of POM-based materials[1] requires their rapid screening for desired properties through structure-activity relationships, so that libraries of well characterized POMs are essential for their efficient selection.[2,3] Among the multitude of POM clusters and structural architectures, gallium-based representatives remain synthetically and structurally challenging targets. Therefore we present a step-wise solution access to the new gallium-containing silicotungstates $[Ga_6(H_2O)_x\{A\text{-}\alpha\text{-}SiW_9O_{34}(OH)_y\}_2]^{n-}$ (**Ga-1**) and $[Ga_4(H_2O)_2\{A\text{-}\alpha\text{-}SiW_{10}O_{38}\}_2]^{12-}$ (**Ga-2**) starting from the lacunary Keggin-type precursor $[A\text{-}\alpha\text{-}SiW_9O_{34}]^{10-}$.[4]

Gallium-based POMs[5–13] primarily attracted research interest due to their promising application perspectives in radiopharmaceuticals through incorporation of the radioactive isotopes ^{67}Ga and ^{68}Ga which are established for labeling techniques in anticancer therapy and positron emission tomography (PET).[14–17] This diagnostic technique permits in vivo observation of the distribution patterns of radioactive Ga-containing imaging agents via 3D monitoring of body parts. Whereas transition metal complexes are most frequently applied for this purpose, bio-active POMs remain to be explored as interesting multi-functional compounds for new theragnostic approaches.[18] Antiviral properties of POMs have been widely investigated by international research groups[19–21] and Yamamoto et al. first studied the Ga-containing Keggin-type POM $[BGa(H_2O)W_{11}O_{39}]^{6-}$ which was found to inhibit both HIV-1 and simian immunodeficiency virus at rather low concentrations.[7]

To date, only a limited number of Ga-POM has been fully structurally characterized, and in these known examples, gallium is most frequently present as a tetrahedral $\{GaO_4\}$ center of Keggin-type anions. Alternatively, gallium can substitute up to three octahedrally coordinated tungsten centers of the basic Keggin-POM framework.

Tungstogallate acid $H_5GaW_{12}O_{40}$ was first reported and characterized by ^{71}Ga and ^{183}W NMR spectroscopy by Fedotov et al. in 1987,[6] followed by further detailed investigations of Niu et al.[12] The lacunary precursor $Na_9[\alpha\text{-}GaW_9O_{34}H_2]\cdot 14H_2O$ was prepared by Liu et al.,[10] and it was subsequently used for the synthesis of the vanadium substituted monomer $[\alpha\text{-}GaW_9V_3O_{40}]^{8-}$ which was spectroscopically characterized with ^{183}W and ^{51}V NMR techniques.[10]

The lacunary $[\beta\text{-}GaW_9O_{34}]^{11-}$ Keggin building block was used by Liuha et al. in 1994 for the reaction with a series of transition metal cations, including Co(II), Mn(II), Ni(II), Fe(III) and V(V).[9] The sandwich type POMs $[M_4(H_2O)_2(GaW_9O_{34})_2]^{14-}$ (M = Cu, Zn) based on the lacunary $[\alpha\text{-B-}GaW_9O_{34}]^{11-}$ precursor were structurally characterized by Drews et al.[13]

Replacement of tungsten centers by gallium is expected to be facilitated through the similar ionic radii of octahedrally coordinated W(VI) and Ga(III) (0.74 Å and 0.76 Å, resprectively).[22] However, for reasons that are probably associated with crystal growth issues, detailed structural characterization of the emerging POMs with partially substituted Ga/W-frameworks remains difficult, and to the best of our knowledge, few crystallographic data have been reported for this polyoxotungstate type to date. Nevertheless, synthesis and NMR spectroscopic characterization of the $\alpha/\beta\text{-}[SiW_9O_{37}\{Ga(H_2O)\}_3]^{7-}$ monomers were reported by Pope et al.[8] The monomeric germanotungstate $[\beta\text{-}GeW_9Ga_3O_{37}(H_2O)_3]^{7-}$ and the dimer $[\alpha\text{-}Ge_2W_{18}Ga_6(H_2O)_3O_{74}]^{14-}$ were synthesized and characterized with ^{183}W NMR IR and FAB mass spectrometry by Meng et al., and the connection of the two $\{GeW_9Ga_3\}$ fragments by three water molecules was proposed.[11] Gallium substituted Keggin and Wells-Dawson anions with the general formula $[\alpha\text{-}XGa(OH_2)W_{11}O_{39}]^{n-}$ and $[X_2Ga(OH_2)W_{17}O_{61}]^{n-}$ (X = Si, P, B) have been reported by Zonnevijlle et al.,[5] however, none of the above compounds was characterized with single crystal X-ray diffraction. Such data is only available for the transformation of a Ga-containing polyoxomolybdate, i.e. the reversible hydrolysis of the Anderson-type POM $[Ga(OH)_6Mo_6O_{18}]^{3-}$ into $[\alpha\text{-}(GaO_4)Mo_{12}O_{35}(OH)]^{4-}$.[23]

Consequently, gallium containing POMs have attracted computational interest. Poblet et al. found the relative energy of the α- and β-isomers, respectively, among the $[XW_{12}O_{40}]$ (X = Al, Si, P, Ga, Ge, As) series to depend on the degree of reduction of the Keggin framework.[24] The equilibrium of the α- and β-isomers of tungstogallate acid has later been investigated in more detail by means of ^{183}W and ^{71}Ga NMR spectroscopy by Hill et al.,[25] and conversion of the pure α-isomer into an $\alpha\text{-}/\beta$-mixture was observed at 200 °C within 24 h.

5.2 Structure and Properties of New Gallium-containing Polyoxotungstates

In the following, we illustrate how the selective reaction of the trilacunary [A-α-SiW_9O_{34}]$^{10-}$ precursor with gallium nitrate in aqueous solution provides access to two new similar sandwich-type POMs $K_{10}[Ga_6(H_2O)_3\{A\text{-}\alpha\text{-}SiW_9O_{35}(OH)_2\}_2]\cdot 35.5H_2O$ (**Ga-1a**) and $K_m[Ga_6(H_2O)_x\{A\text{-}\alpha\text{-}SiW_9O_{34}(OH)_y\}_2]\cdot nH_2O$ (**Ga-1b**) along with a route to the novel dimeric Ga-POM $K_{12}[Ga_4(H_2O)_2\{A\text{-}\alpha\text{-}SiW_{10}O_{38}\}_2]\cdot 30H_2O$ (**Ga-2**). The structural features of both POM types are analyzed and compared and their application-oriented properties are evaluated with a wide range of methods.

5.3 Results and Discussion

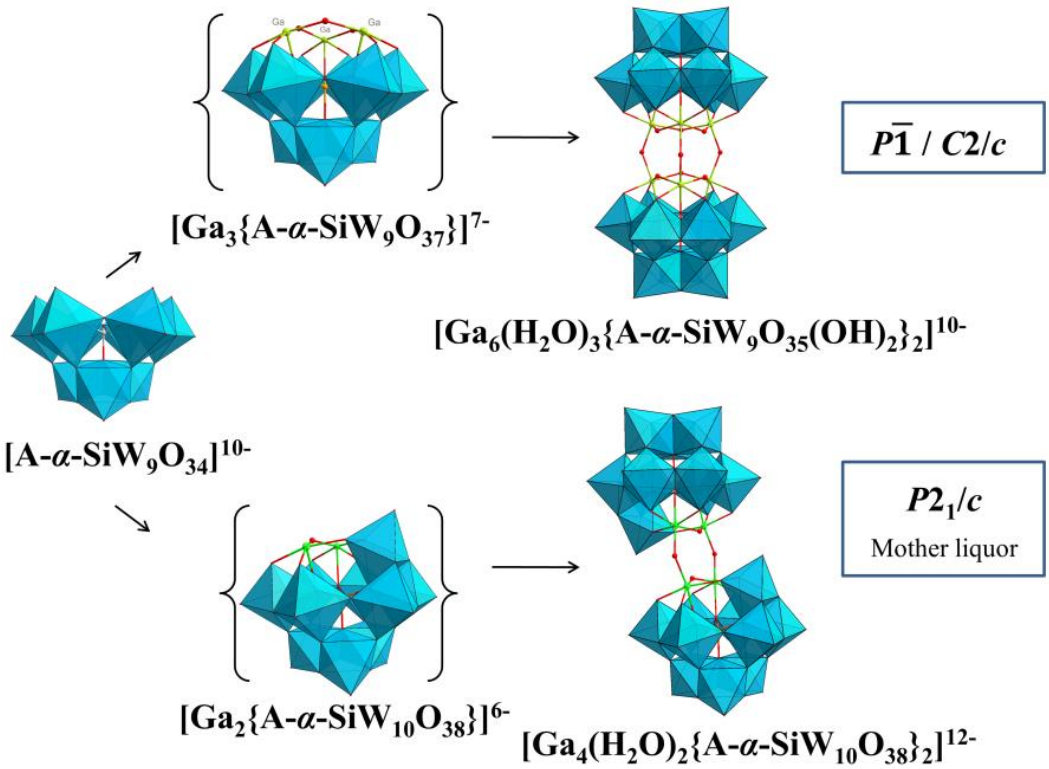

Figure 5.1. Proposed formation of **Ga-1a** and **Ga-2** (Ga: green, O: red, WO_6 octahedra: blue).

5.3.1 Crystal Growth and Selection

The dimeric Ga-POM $[Ga_6(H_2O)_x\{A\text{-}\alpha\text{-}SiW_9O_{34}(OH)_y\}_2]^{n-}$ (**Ga-1**) was obtained from an aqueous solution of $Na_{10}[A\text{-}\alpha\text{-}SiW_9O_{34}]\cdot 15H_2O$ and $Ga(NO_3)_3\cdot nH_2O$ at 80 °C and pH 4.75, followed by the addition of solid KCl to form a white precipitate. The new Ga-POM **Ga-1**

crystallizes in two similar structures, namely in the monoclinic form **Ga-1a** (S.G. *C*2/*c*) and in the triclinic form **Ga-1b** (S.G. $P\bar{1}$) (Figure S5.2). A mixture of single crystals of **Ga-1a/Ga-1b** was obtained overnight by recrystallization of the white precipitate in hot water.

Compound **Ga-2** in phase pure and single crystalline form was obtained after removal of **Ga-1a** and **Ga-1b** through slow evaporation of the mother liquor. Careful single crystal selection of **Ga-1a/Ga-1b** revealed the formation of crystals of a third Ga-POM with different unit cell parameters (a = 18.1491(5) Å, b = 20.2374(5) Å, c = 24.1789(6) Å, α = 90.00°, β = 111.730(3)°, γ = 90.00°). Crystal structure refinement identified this side product as a Ga-POM **Ga-3** with the general formula $[Ga_4(H_xO)_6(Si_2W_{18}O_{66})]^{n-}$ (x = 0-2) (Figure S5.2). The embedment of four gallium atoms into an open Wells-Dawson silicotungstate ligand is related to the structural motif of previously reported lanthanide containing silicotungstates.[26,27] Unfortunately, numerous attempts to isolate it in pure form failed. All characterizations of compound 1a were performed on individually selected single crystalline samples, except for electrochemical characterizations, catalytic tests and UV/vis absorption measurements. Phase pure batches for analytical investigations were prepared from selected crystals which were cut into smaller fragments, followed by unit cell determination on a single crystal X-ray diffractometer. Crystallographic data are summarized in Table 5.1 and Table S5.1-Table S5.3.

Table 5.1. Crystallographic data and structural refinement for compounds (**Ga-1a**), (**Ga-1b**), (**Ga-2**).

	(Ga-1a)	**(Ga-1b)[a]**	**(Ga-2)**
Empirical formula	$K_{10}Si_2Ga_6W_{18}O_{112.5}H_{81}$	-	$K_{12}Si_2Ga_4W_{20}O_{108}H_{64}$
Formula weight ($g \cdot mol^{-1}$)	6056.15	-	6273.45
Temperature	183 K	183 K	183 K
Wavelength (λ/Å)	0.71073	0.71069	0.71069
Crystal system	monoclinic	triclinic	monoclinic
Space group	*C*2/*c*	$P\bar{1}$	$P2_1/c$
a (Å)	22.7077(6)	13.1610(4)	32.064(5)
b (Å)	12.8766(2)	18.9038(6)	15.2749(7)
c (Å)	37.8222(15)	20.2462(8)	17.821(3)
α (°)	90.00	115.420(3)	90.00
β (°)	103.815(3)	101.558(3)	144.92(4)
γ (°)	90.00	89.997(2)	90.00
V ($Å^3$)	10739.2(6)	4436.1(3)	5016.8(11)
Z	2	2	3
ρ_{calc} (g/cm^{-3})	3.746	4.207	4.111
Crystal size	0.03 x 0.07 x 0.18	0.04 x 0.09 x 0.22	0.09 x 0.14 x 0.27
Reflections collected/unique	50615/13334	52064/16223	50485/23627
Unique observed reflections	10217	11950	19174
θ range (°)	2.25-28.28	3.00-25.35	2.89-37.7
F(000)	10868	4914	8364
Data/restraints/parameters	13334/0/626	21273/0/1106	23627/0/668
Goodness-of-fit	1.101	1.104	1.057
R_1[a] [I>2σ(I)]	0.0664	0.0609	0.0389
wR_2[b]	0.1361	0.1345	0.0882
R_1[a] [I>2σ(I)] (all data)	0.0889	0.0888	0.0530
wR_2[b] (all data)	0.1503	0.1479	0.0882

5.4 Crystal Structure of $K_{10}[Ga_6(H_2O)_3\{A\text{-}\alpha\text{-}SiW_9O_{35}(OH)_2\}_2]\cdot 35.5H_2O$ (Ga-1a)

Single crystal X-ray data refinements of both compounds **Ga-1a** and **Ga-1b** revealed their similar structural architectures based on two identical $[Ga_3\{A\text{-}\alpha\text{-}SiW_9O_{34}(OH)_y\}]^{n-}$ Keggin type fragments which are interconnected by three oxygen atoms. Polyanions of **Ga-1a** and **Ga-1b** are isostructural with the transition metal-substituted POMs $[M_6(OH_q)(XW_9O_{34})_2]^{n-}$ (M = Ti, Nb; X = P, Ge; q = 0-2).[28–30] A related motif has been assigned to $[Ge_2W_{18}Ga_6(H_2O)_3O_{74}]^{14-}$ on the basis of spectroscopic data.[11] Despite recrystallization and careful selection of various single crystals, full anisotropic refinement of the triclinic polyoxometalate **Ga-1b** including all oxygen atoms remained impossible. Therefore, a representative detailed structural description of the monoclinic form **Ga-1a** is given here. (Table S5.2, Table S5.1, Table S5.3 and Figure 5.2). Complete single crystal X-ray data refinement of **Ga-1a** revealed that the polyanion is formed by two identical and

crystallographically equivalent $[Ga_3\{A\text{-}\alpha\text{-}SiW_9O_{35}(OH)_2\}]^{5-}$ Keggin-type fragments interconnected via three water molecules. The $[Ga_3\{A\text{-}\alpha\text{-}SiW_9O_{35}(OH)_2\}]^{5-}$ fragment contains one $\{W_3O_{13}\}$ triad and three $\{GaW_2O_{13}\}$ edge sharing subunits surrounding a central tetrahedral SiO_4. All gallium atoms display an octahedral coordination geometry with Ga···O bond distance ranges of 1.920(5)-2.138(9) Å, 1.923(10)-2.152(9) Å and 1.929(9)-2.139(9) Å for Ga(1), Ga(2) and Ga(3), respectively (Figure 5.2). The nine crystallographically independent tungsten atoms are octahedrally coordinated with bond distances in the range from 2.3338(8) to 2.383(8) Å for the longer internal W···O bonds and from 1.711(10) to 1.730(9) Å for the shortest external W···O bonds, whereas the equatorial W···O bond distances range between 1.825(10) and 1.990(9) Å. Intermetallic W···W distances between 3.3663(6) and 3.3735(6) Å were observed for the edge-sharing WO_6 octahedra and from 3.7129(10) to 3.7403(7) Å for the corner-sharing WO_6 octahedra, respectively. The Ga···Ga interatomic distances range from 3.539(2) to 3.6513(19) Å, while the interatomic Ga···W distances between GaO_6 and WO_6 octahedra are shorter (3.1963(16) to 3.2236(15) Å). The central silicon atom exhibits a tetrahedral coordination geometry with Si···O bond distances in the range from 1.614(9) to 1.634(10) Å. **Ga-1a** is surrounded by crystal water molecules, by two fully occupied (K(1), K(2)) and by three disordered potassium ions (K(3), K(4) and K(5)). The latter ions are disordered over two or three crystallographic positions, with partial occupancies of 70|30, 50|25|25 and 55|45%, respectively, for K(3A)|K(3B), K(4A)|K(4B)|K(4C) and K(5A)|K(5B). The coordination numbers of the potassium counter-cations increase from 5 (K(5B)) over 6 (K(4B), K(4C)), 7 (K(3A)), 8 (K(1), K(2), K(3B), K(5A)) to 9 (K(3B), K(4A)) with K···O bond distances between 2.63(2) and 3.29(4) Å. Bond valence sum (BVS) calculations confirm an oxidation state of +6 for all tungsten atoms (BVS range of 5.8-6.1) and the +4 oxidation state of the silicon heteroatom (BVS 4.06). The BVS values of 3.03, 3.01 and 3.01, respectively, for Ga(1), Ga(2) and Ga(3) agree very well with the expected oxidation state of +3. All oxygen atoms exhibit BVS values between 1.63 and 2.01, thus indicating an oxidation state of -2, except for O(31), O(34), O(37), O(38) and O(39). The two values of 0.6 for O(37) and O(39) suggest the presence of water molecules, while the three values of 1.17, 1.10 and 1.04, respectively, for O(31), O(34) and O(38) are in the range for hydroxo groups. Nevertheless, comparison of the rather short distances between O(31) and the neighboring Ga(1) and Ga(3) centers with other Ga···O bond distances excludes the presence of a hydroxo group between the two Ga atoms.

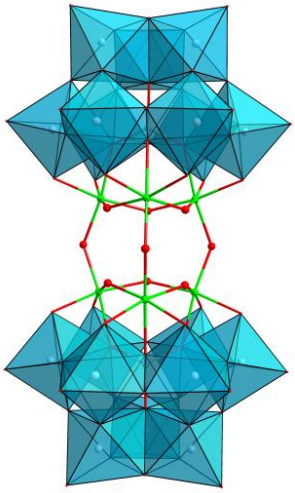

Figure 5.2. Combined polyhedral/ball-and-stick representation of $[Ga_6(H_2O)_x\{A\text{-}\alpha\text{-}SiW_9O_{34}(OH)_y\}_2]^{n-}$ (**Ga-1**) (Ga: green, O: red, WO_6 octahedra: blue).

The formula of compound 1a was derived from the combination of well-established analytical techniques for polyoxometalate characterization. Potassium content and overall polyanion charge were obtained from crystal structure determinations in line with elemental analysis and BVS calculations, and the crystal water molecule contents were determined from thermogravimetric analyses.

5.5 Crystal Structure of $K_{12}[Ga_4(H_2O)_2\{A\text{-}\alpha\text{-}SiW_{10}O_{38}\}_2]\cdot 30H_2O$ (Ga-2)

The new POM **Ga-2** crystallizes in the monoclinic space group $P2_1/c$. Whereas the structural architecture of **Ga-2** is related to a previously reported phosphotungstate with a tetranuclear iron core $[(CH_3)_4N]_{10}[Fe_4(OH)_4(PW_{10}O_{37})_2]\cdot 15H_2O$,[31] its individual features are slightly different, e.g. with respect to the bridging water molecules between the two constituting symmetry equivalent $[Ga_2\{A\text{-}\alpha\text{-}SiW_{10}O_{38}\}]^{6-}$ Keggin fragments (Table S5.1 and Table S5.2). The Keggin-type building blocks consist of two corner-sharing $\{W_3O_{13}\}$ and $\{GaW_2O_{13}\}$ subunits, respectively, surrounding the central SiO_4 tetrahedron, which exhibits Si···O bond distances between 1.625(4) to 1.638(4) Å. The two gallium atoms display octahedral coordination environments with Ga···O bond distances ranging from 1.903(4) to 2.214(4) Å for Ga(1) and from 1.899(4) to 2.223(4) Å for Ga(2) (Figure S5.1). All tungsten atoms are octahedrally coordinated with bond distances in the range between 1.795(4) and 2.038(4) Å for equatorial W···O bonds, and between 2.316(4) to 2.356(4) Å for the elongated internal W···O bonds, whereas the characteristically short external W···O bond distances range from

1.698(4) to 1.732(5) Å. Intermetallic distances were determined between 3.202(2) and 3.236(3) Å and between 3.5295(14) and 3.5315(14) Å, for edge sharing and corner sharing Ga···W octahedra, respectively. The Ga···Ga distance was found to be 3.5023(14) Å, whereas the W···W distances range from 3.3338(9) to 3.400(3) Å and from 3.692(3) to 3.749(3) Å for edge-sharing and corner-sharing WO_6 octahedra, respectively. The polyanion **Ga-2** is surrounded by crystal water molecules and six fully occupied potassium ion sites, with coordination numbers increasing from 7 (K(5)) over 8 (K(1), K(2), K(4)) to 9 (K(3), K(6)) and according K···O bond distances ranging from 2.614(9) to 3.26(2) Å. BVS values of 3.04 and 3.05 for Ga(1) and Ga(2) clearly confirm the oxidation state of +3 for Ga. The central Si atom is present in the +4 oxidation state (BVS value of 4.04). All tungsten atoms exhibit BVS values between 5.94 and 6.08, which agree well with the expected tungsten oxidation state of +6. BVS values of all oxygen atoms (1.6 to 2.1) indicate an oxidation state of -2, except for O(38) and O(39). The BVS value of 1.2 for O(38) suggests the presence of a hydroxy group. However, as outlined for compound 1a above, the shortest bond length between Ga(2) and O(39) compared to other Ga···O bond distances excludes the presence of an aqua group, despite the lower BVS 0.6 observed for O(39). As described for **Ga-1a**, an analogous combination of crystal structure, BVS and TGA analyses was applied to determine the formula of **Ga-2**.

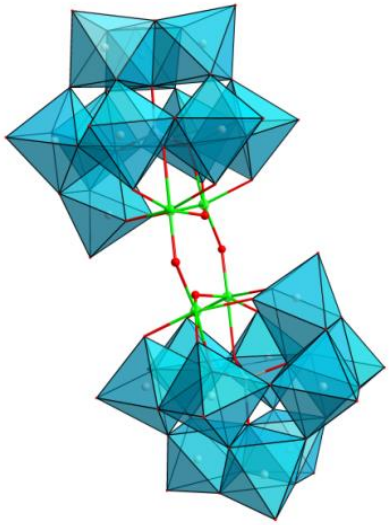

Figure 5.3. Combined polyhedral/ball-and-stick representation of $[Ga_4(H_2O)_2\{A\text{-}\alpha\text{-}SiW_{10}O_{38}\}_2]^{12-}$ (**Ga-2**) (Ga: green, O: red, WO_6 octahedra: blue).

Both POM types were furthermore characterized with PXRD measurements in the solid state. PXRD patterns of the bulk material obtained from the crystallization of **Ga-1** show a mixture of monoclinic and triclinic compounds (Figure S5.3). Attempts to record a PXRD pattern on a sample prepared from selected crystals of **Ga-1a** (Figure 5.4) which were stored for ca. 2 weeks after isolation from the reaction mixture indicated that they had undergone a transformation into amorphous materials. This is probably due to loss of crystal water, so that single crystal measurements were performed on crystals coated with Paratone oil to avoid contact with air. Phase purity of **Ga-2** is evident from good agreement of calculated and recorded PXRD patterns (Figure S5.4).

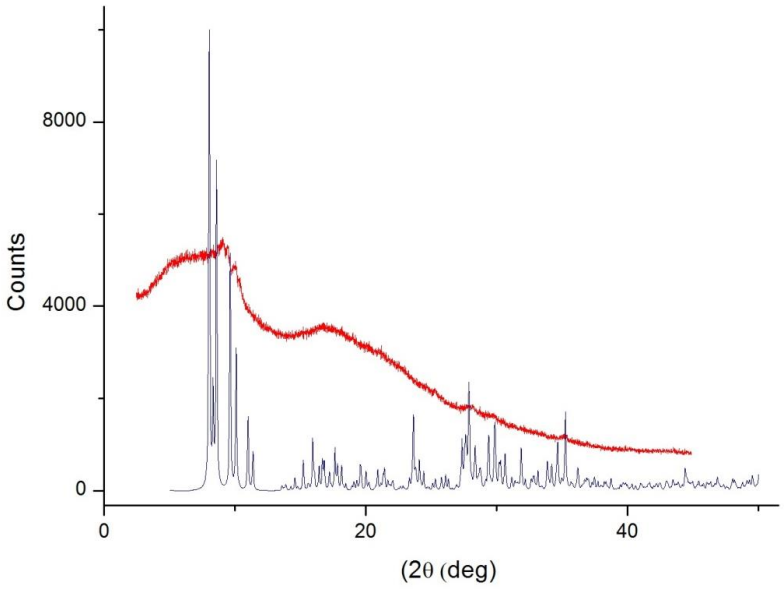

Figure 5.4. PXRD pattern recorded on a single crystalline sample of **Ga-1a** (**red**) vs. calculated pattern (**blue**).

The ATR-FTIR spectra of compounds **Ga-1a** and **Ga-2** both show bands around 993(w), 949(m), 896(s), 772(sh), 732(s), 654(s), 516(s), 493(s) which are assigned to terminal, corner-sharing and edge-sharing asymmetric ν_{as}(W-O) vibrations, respectively (Figure 5.5). Comparison of the characteristic bands at 949 cm^{-1} $\nu(W{=}O_d)$, 896 cm^{-1} $\nu_{as}(W\text{-}O_b)$, and 772 cm^{-1} $\nu_{as}(W\text{-}O_c)$ with the lacunary precursor $[A\text{-}\alpha\text{-}SiW_9O_{34}]^{10-}$ shows a significant shift which is indicative of the formation of a new compound.[32]

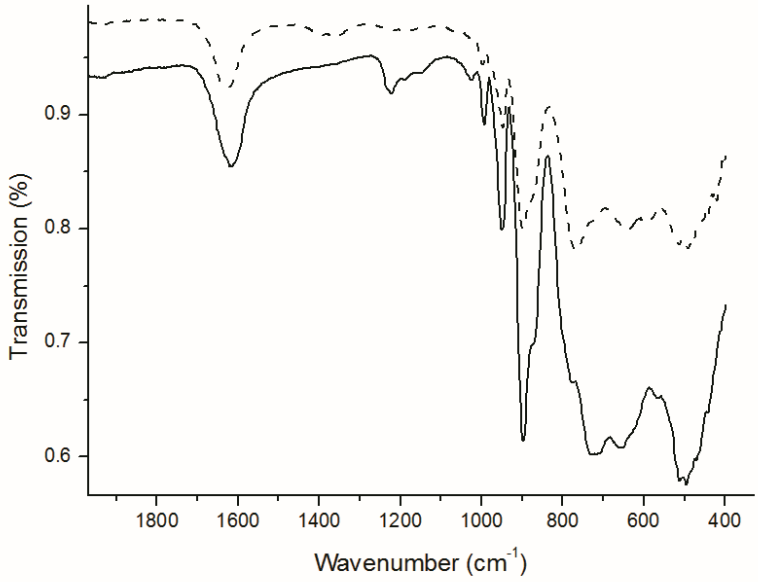

Figure 5.5. ATR-FTIR spectra of **Ga-1a** (black) and **Ga-2** (dashed).

Raman spectra of both compounds (Figure S5.8, left) display the characteristic symmetric and asymmetric W-O_b vibrations of tungstosilicic acid[32] at 974 and 947 cm^{-1}, respectively. The set of three lines assigned to the W-O_b-W vibrations is shifted towards lower wavenumbers and the W-O_a vibration appears at 247.3 cm^{-1}. The assignment of these bands was done by comparing UV/vis spectra of compounds **Ga-1a** and **Ga-2** (Figure S5.9). Both exclusively show an absorption maximum in the UV range around 260 nm and no further peaks in the visible range. Time dependent stability of compound **Ga-1a** was monitored in the UV range in different media at pH 1 (HCl) and pH 8 (borate buffer), respectively, over a period of 120 min. No significant decrease in absorption was observed (Figure S5.10), thus pointing to the stability of **Ga-1a** under electrochemical measurement conditions (see below).

ESI-MS currently attracts increasing research interest as a versatile method to study the formation and stability of polyoxometalates in solution,[33] especially in light of current investigations into the homogeneous nature of polyoxometalate-based water oxidation catalysts.[34,35] Samples of **Ga-1a** and **Ga-2** were thus investigated with high resolution electrospray ionization mass spectrometry (HR-ESI) in order to obtain more detailed information about their structural stability (Figure 5.6).

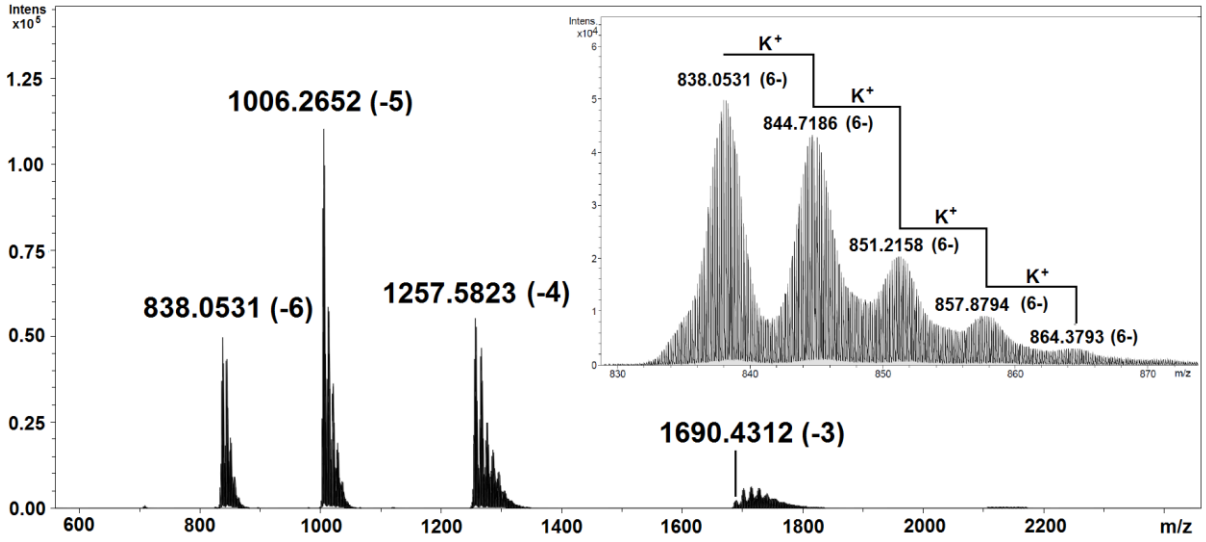

Figure 5.6. HR-ESI of **Ga-1a** with detailed view of the peaks at m/z = 838.0531 (inset).

The ESI-MS spectrum of **Ga-1a** (Figure 5.6) shows four groups of peaks at m/z 838.0531 (-6); 1006.2652 (-5) and 1257.5823 (-4). The corresponding masses of the first three peaks (5028.3186, 5031.3260 and 5030.3292) can be attributed to the protonated polyanion **Ga-1a** $\{[Ga_6(H_2O)_3\{\alpha\text{-}SiW_9O_{35}(OH)_2\}_2]+nH\}^{(10-n)-}$ (n = 4-6). The absence of peaks arising from the monomer of **Ga-1a** and of any fragments resulting from loss of gallium indicates that the sandwich-type structure remains intact under the given conditions. A survey of assigned peaks together with a simulation of the peak at m/z = 838.0531 is shown in the supporting information (Table S5.4, Figure S5.15). In contrast, the HR-ESI mass spectrum of **Ga-2** (Table S5.5, Figure S5.13-Figure S5.15) shows peaks at m/z = 871.4172 (-3) and 654.3110 (-4) which are assigned to the fragments $\{[Ga_2SiW_{10}O_{38}]+3H\}^{3-}$ and $\{[Ga_2SiW_{10}O_{38}]+2H\}^{4-}$. This indicates an equilibrium between the dimeric POM and its monomers:

$$[Ga_4(H_2O)_2\{A\text{-}\alpha\text{-}SiW_{10}O_{38}\}_2]^{12-} \rightarrow 2\ [Ga_2\{A\text{-}\alpha\text{-}SiW_{10}O_{38}\}]^{6-} + 2\ H_2O \qquad \text{(eq. 5.1)}$$

The remaining three groups of peaks at m/z = 878.4229 (-6), 1053.7107 (-5) and 1337.1175 (-4) arise from different protonation states of the dimer $\{[Ga_4(H_2O)_2\{A\text{-}\alpha\text{-}SiW_{10}O_{38}\}_2]+nH\}^{(12-n)-}$. Overlapping peaks of the monomer and the dimer lead to a shift in the observed intensities for the single species so that the calculated and observed isotopic pattern do not precisely match.

The solution structure of **Ga-1a** and **Ga-2** was further investigated by ^{183}W NMR spectroscopy in D_2O/H_2O (1:1). Due to symmetry reasons, differentiation between the

presence of a monomeric and a dimeric solution species is not possible in either case. The NMR spectrum of **Ga-1a** (Figure S5.11) showed two peaks at -81.3 and -160.6 ppm (vs. Na_2WO_4 reference). Although complete integration was not possible, due to the low signal to noise ratio even after 18074 scans at a sample concentration of 14.2 mM, the signal at -81.3 was found to be more intense.

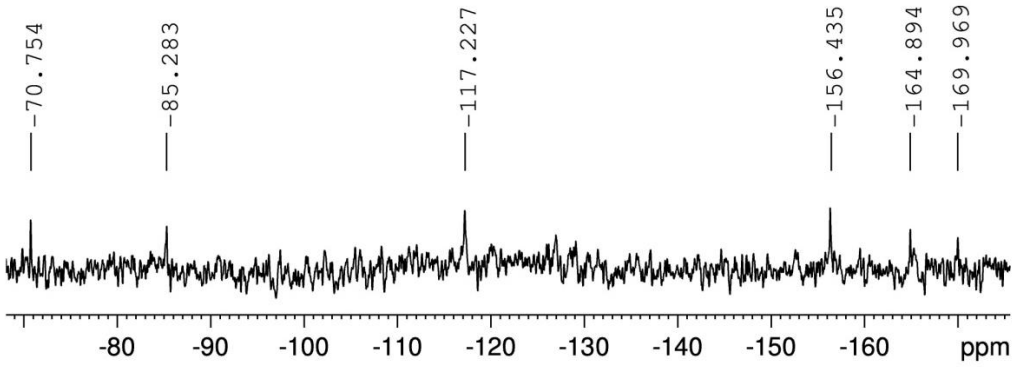

Figure 5.7. ^{183}W NMR spectrum of $K_{12}[Ga_4(H_2O)_2\{A\text{-}\alpha\text{-}SiW_{10}O_{38}\}_2]\cdot 30H_2O$ **(Ga-2)** in D_2O/H_2O (1:1).

The presence of two peaks in the spectrum is coherent with the D_{3h} symmetry of **Ga-1a** and indicates that the protons associated with the bridging oxygen atoms between the gallium centers are either present as H_3O^+ counter-cations or undergo a rapid proton exchange which is faster than the NMR timescale. Moreover, leaching of Ga(III) during the measurement is unlikely, because it would lead to significant changes in the ^{183}W NMR spectrum as previously reported by Finke et al. for the cleavage of dimeric $[A\text{-}\alpha\text{-}Si_2W_{18}Nb_6O_{77}]^{8-}$ into $[SiW_9Nb_3O_{40}]^{7-}$ fragments.[28] A survey of chemical shifts reported for POMs which are structurally related to **Ga-1a** is given in Table 5.2. The observed ^{183}W-NMR spectrum of **Ga-2** (Figure 5.7) clearly indicates the presence of a single species. The absence of additional resonances indicates that no significant leaching of gallium occurs during the measurement time of 60 h.

Table 5.2. ^{183}W NMR shifts of **Ga-1a** vs. related compounds.

Anion	δ_w (ppm)	δ_w (ppm)	ref.
$[Ga_6(H_2O)_3\{\alpha\text{-}SiW_9O_{35}(OH)_2\}_2]^{10-}$	-81.3	-160.6	this work
$[\alpha\text{-}SiW_9O_{37}\{Ga(H_2O)\}_3]^{7-}$	-80.4 (2)	-159.7 (1)	[8]
$[\alpha\text{-}Ge_2W_{18}Ga_6O_{74}(H_2O)_3]^{14-}$	-127.0(1)	-141.0(2)	[11]
$[\alpha,\alpha\text{-}P_2W_{18}Ti_6O_{77}]^{12-}$	-109.7	-131.5	[30]
$[\alpha,\alpha\text{-}Si_2W_{18}Nb_6O_{77}]^{12-}$ [a]	-114.3	-142.6	[28]
$[Ge_2Ti_6W_{18}O_{77}]^{14-}$	-107.45	-127.76	[29]

[a] in DMF/CD_3CN

Attempts to measure ^{71}Ga NMR spectra have been made, but the rapid T_1-relaxation of the gallium core results in broad lines which do not afford detailed structural information. **Ga-1** was further investigated with ATR-FTIR spectroscopy. No significant changes were observed over a period of 420 min in acetate buffer (pH 4.75; Figure S5.8, right) so that **Ga-1** is considered stable under the given conditions.

The electrochemical properties of compounds **Ga-1** and **Ga-2** were characterized through cyclic voltammetry at different pH values in various media. No significant electrochemical waves could be observed in borate and NaPi buffer (pH = 8 or 7, respectively). In acetate buffer, a half wave at -0.97 V was attributed to the reduction of the W(VI) centers of the Keggin-type ligand (Figure S5.16, left). Reference cyclic voltammograms of $Ga(NO_3)_3$ and the precursor material $[A\text{-}\alpha\text{-}SiW_9O_{34}]^{10-}$ in acetate buffer (pH 4.75) display no distinct redox waves. This indicates that the observed waves arise from the reduction of the tungsten centers of **Ga-1**, and neither from the starting material nor from any decomposition products. In a more acidic environment two almost reversible waves at -0.84 V and -0.72 V are observed. The peak separation of the wave (I-I') is 0.108 V, and for the (II-II') wave a value of 0.084 V is found. Compared with literature data, these values suggest a two electron transfer for wave (I-I') and a one electron transfer for wave (II-II'), and the results correspond to earlier reports on the metatungstate anion $[H_2W_{12}O_{40}]^{6-}$ by Launay.[36–38] Both waves are well separated at pH 1 (HCl medium) with half-wave potentials of -0.51 V and -0.67 V, respectively (Figure 5.8). The pH dependent separation of the redox waves I-I' (0.084V pH=1.0) and II-II' (Figure S5.16, right) is a characteristic feature of polyoxometalates.[37,39] The intense, almost irreversible peak (III) observed in the cyclic voltammogram of **Ga-1** in 0.1 M HCl at the potential of -0.79 V (Figure 5.8) could in principle be indicative of catalytic hydrogen evolution.[40,41] However, considering the mechanism proposed by Launay, this peak is rather

attributed to an approx. 10e$^-$ reduction. A broad, non-reversible wave (IV) is observed at a potential of +0.28 V for scans performed beyond potentials of -0.80 V (Figure S5.17, left).

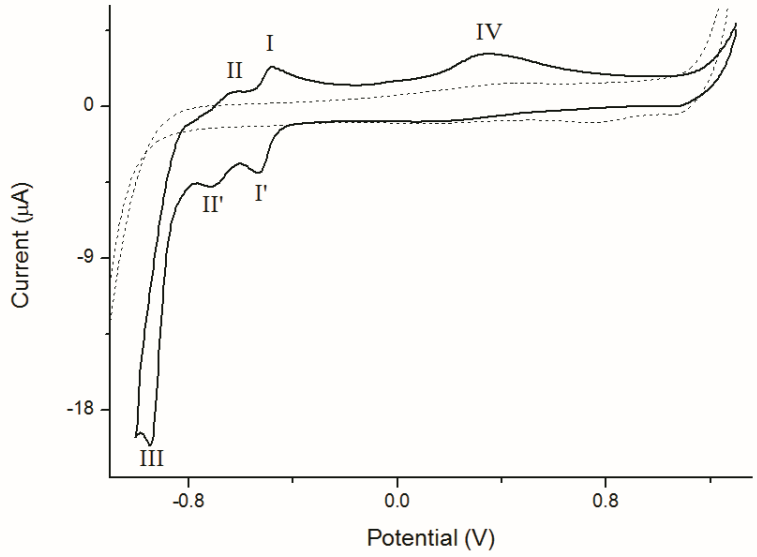

Figure 5.8. CV of **Ga-1** in HCl (0.1 M, pH 1), 50 mV/s vs. Ag/AgCl (red) vs. pure solvent (black, dashed).

As compound **Ga-1** shows a similar protonation behavior upon reduction as reported for $[H_2W_{12}O_{40}]^{6-}$, this peak might be assigned to the oxidation of reaction products from preceding, coupled electrochemical and protonation reactions.[42]

The cyclic voltammogram of compound **Ga-2** (Figure S5.17, right) at pH 1.0 in 0.1 M HCl shows two distinct reduction waves for the tungsten centers at -0.44 V (I-I') and at -0.62 V (II-II'), respectively.

5.6 Catalytic activity of $[Ga_6(H_2O)_x\{A\text{-}\alpha\text{-}SiW_9O_{34}(OH)_y\}_2]^{n-}$ (Ga-1)

5.6.1 Photocatalytic Activity

Activity in visible light driven hydrogen evolution was observed for various POMs.[43–45] Therefore **Ga-1** (mixture of **Ga-1a**/**Ga-1b**) was subjected to preliminary catalytic tests for visible-light-driven photochemical water reduction in the presence of $[Ru(bpy)_3]^{2+}$ as a photosensitizer (details cf. Experimental). The observed absence of hydrogen evolution under

these conditions does not generally exclude catalytic activity of **Ga-1**, given that CV measurements were performed at pH 1 compared to pH 4 of the photocatalytic buffer medium. Further pH-dependent activity tests are thus worthwhile.

5.6.2 Alcohol Oxidation Activity Tests

Polyoxometalates have been identified as promising catalysts for key organic transformations, such as alcohol oxidation or olefin epoxidation.[46] Therefore, catalytic activity of **Ga-1** was tested for a representative series of alcohols in higher catalyst concentrations than reported in our previous work.[47] Unexpectedly, **Ga-1** remained inactive for the oxidation of cyclopentanol, 2-hexanol, benzyl alcohol, and octanol as substrates, and the reasons for this catalytic inactivity are currently investigated.

5.7 Conclusion

The reaction of the lacunary fragment [A-α-SiW_9O_{34}]$^{10-}$ with gallium nitrate in aqueous media at 80 °C leads to the formation of two new gallium-containing polyoxometalates $K_{10}[Ga_6(H_2O)_3\{A\text{-}\alpha\text{-}SiW_9O_{35}(OH)_2\}_2]\cdot 35.5H_2O$ (**Ga-1a**) and $K_{12}[Ga_4(H_2O)_2\{A\text{-}\alpha\text{-}SiW_{10}O_{38}\}_2]\cdot 30H_2O$ (**Ga-2**). Crystallization of the novel Ga-polyanion **Ga-1** affords a mixture of monoclinic (**Ga-1a**) and triclinic (**Ga-1b**) compounds. Solid state samples of POMs (preferably **Ga-1a**) and **Ga-2** were structurally fully characterized with single crystal X-ray and powder diffraction techniques, and both compounds were spectroscopically analyzed with ATR-FTIR, Raman and UV/vis techniques. Solution stability of both Ga-POM types was investigated with HR-ESI mass spectrometry and ^{183}W NMR spectroscopy. Whereas HR-ESI spectra display the complete dimeric polyanion of **Ga-1a**, HR-ESI peaks of **Ga-2** point to an equilibrium of sandwich-type POM with the monomeric building block. Most importantly, ^{183}W NMR spectroscopy in solution did not give any indication of gallium leaching from the novel polyanions. Generally, crystalline Ga-POMs remain a synthetically elusive target so that our further attempts to structurally characterize gallium containing sandwich-type Keggin POMs with the general formula $[Ga_6(OH_q)_3\{A\text{-}\alpha\text{-}XW_9O_{37}\}_2]^{n-}$ (X = P, As, Ge, V, q = 0-2) remained unsuccessful. Reaction of gallium nitrate with the $\{W_6O_{24}\}$ precursor and the lacunary Wells-Dawson anion $[P_2W_{15}O_{56}]^{12-}$ did not afford crystals of gallium substituted products either.[48,49] Instead of the desired formation of sandwich-type structures, gallium is easily exchanged with the central heteroatom X. Electrochemical investigations of both compounds displayed the characteristic redox behavior of tungsten centers of the POM

framework. Interestingly, CV data for **Ga-1** in acidic media indicated its possible catalytic activity in water reduction. As first tests for photocatalytic hydrogen evolution did not show activity of 1, more detailed parameter screening experiments are required, which also applies for catalytic alcohol oxidation tests.

All in all, this study paved the way to two new sandwich-type Ga-POMs which can be selectively accessed through fractional crystallization. Their structural characterization amplified this rather elusive polyoxometalate family, and the stable embedment of gallium centers between the lacunary units renders them interesting POM building blocks for materials construction.

5.8 Synthesis

5.8.1 Preparation of $[Ga_6(H_2O)_x\{A\text{-}\alpha\text{-}SiW_9O_{34}(OH)_y\}_2]^{n-}$ (Ga-1)

A solution of $Ga(NO_3)_3{\cdot}nH_2O$ (1.08 g, 4.22 mmol, 2.6 eq.) was prepared in water (10 mL). $Na_{10}[A\text{-}\alpha\text{-}SiW_9O_{34}]{\cdot}15H_2O$ (3.90 g, 1.59 mmol, 1.0 eq.) was added in small portions. Next, the reaction mixture was sonicated in an ultrasonic bath until complete dissolution of all solids was achieved. The stirred solution was heated to 80 °C for 40 min, followed by adjustment of the pH to 4.75 with HCl (0.5 M). Addition of solid KCl (0.80 g) led to the formation of a white solid which was collected by centrifugation. Recrystallization from hot water afforded a mixture of small crystals with different morphologies (yield: 207 mg, 0.0342 mmol, 8.0 % based on tungsten starting material). Larger crystals of **Ga-1a** were obtained through slow evaporation of the reaction mixture, followed by separation from the crystal mixture of **Ga-1a** and **Ga-1b**.

Characterization of **Ga-1a** ($K_{10}[Ga_6(H_2O)_3\{A\text{-}\alpha\text{-}SiW_9O_{35}(OH)_2\}_2]{\cdot}35.5H_2O$). IR (ATR-FTIR cm^{-1}): 1615 (m), 1221(w), 993(w), 949(m), 896(s), 772(sh), 732(s), 654(s), 516(s), 493(s). Raman (Ar 514.7 nm, cm^{-1}): 973.6, 950.3 (sh), 881.6, 823.6, 561.1, 514.0, 248.5, 222.2, 155.4. Elemental analysis (%), calc for $K_{10}Si_2Ga_6W_{18}O_{112.5}H_{81}$ (found): Si, 0.93 (1.00); Ga, 6.91 (7.22); W, 54.64 (57.45); K, 6.46 (6.825); Na, 0.00 (0.30). ^{183}W NMR (500 MHz, D_2O/H_2O, 25°C): 81.3, -160.6.

Elemental analysis indicates the presence of approximately 0.8 of a sodium atom. However, during the crystal structure refinement an additional sodium atom could not be located. A possible exchange of a crystal water molecule with sodium did not result in reasonable coordination geometries for sodium or led to very high anisotropic displacement parameters. Therefore we suggest that the representative structural model does not contain sodium as a countercation and that the observed amount is probably due to sample preparation issues.

Thermal analysis of **Ga-1a** shows a weight loss of 6.48 % between 30 and 500 °C which corresponds to the loss of 22 H_2O molecules (Figure S5.5, left). The water molecule content was determined by crystal structure determination and by elemental analysis. Thermogravimetric analysis was performed after a period of several days following the crystallographic data collection, and comparison of the results further confirms the instability of **Ga-1a** under atmospheric conditions.

5.8.2 Preparation of $K_{12}[Ga_4(H_2O)_2\{A\text{-}\alpha\text{-}SiW_{10}O_{38}\}_2]\cdot 30\ H_2O$ (Ga-2)

Compound **Ga-2** was obtained as transparent and irregular plates from the mother liquor of **Ga-1** at pH 3.8. The solid product was collected by filtration, dissolved in a minimum amount of water and subjected to recrystallization at 5 °C. The formation of **Ga-2** is very sensitive to the reaction conditions and it requires a substantial reduction of the volume of the mother liquor (yield: 150 mg, 0.023 mmol, 1.5 % based on tungsten starting material). IR (ATR-FTIR cm^{-1}): 1645 (m), 1630 (sh), 1059 (w), 999 (w), 980 (w), 958 (w), 947 (m), 901 (s), 885 (sh), 771 (s). Raman (Ar 514.7 nm, cm^{-1}): 971.9, 955.0 (sh), 880.5, 824.8, 243.2, 213.8, 158.2. Elemental analysis (%), calc for $K_{12}Si_2Ga_4W_{20}O_{108}H_{64}$ (found): Si, 0.90 (0.925); Ga 4.45 (4.335); W, 58.61 (57.9); K, 7.48 (8.44); Na, 0.00 (0.10). ^{183}W NMR (500 MHz, D_2O/H_2O, 25°C): -70.8, -85.3, -117.3, -156.4, -164.9, -170.0.

As the crystal structure refinement does not indicate the presence of sodium, the low sodium content derived from elemental analysis (below 20% of a fully occupied position) is probably due to random substitution or slight impurities during sample preparation.

A weight loss of 7.2 % is observed for compound **Ga-2** in the range between 30 and 200 °C which corresponds to 25 H_2O molecules (Figure S5.5, right). Related differences in thermogravimetrically and crystallographically determined water molecule contents have been frequently reported in polyoxometalate chemistry.[50]

5.8.3 X-ray Diffraction Experiments

Crystal structure analysis was done by standard procedures, for a list of programs and instruments used see §1.16. Further details on the crystal structure investigations may be obtained from the Fachinformationszentrum Karlsruhe, D-76344 Eggenstein-Leopoldshafen, Germany (Fax: +49 7247 808 666; email crysdata@fiz-karlsruhe.de), by citing the depository numbers CSD-427153 (**Ga-1a**) and CSD-427154 (**Ga-2**).

5.8.4 Visible-Light-Driven Water Reduction

Activity was investigated in ascorbate buffer (0.10 M, pH 4.0) and $[Ru(bpy)_3]Cl_2$ was used as photosensitizer (0.90 mM). The stirred catalytic mixture was irradiated in a headspace vial with a blue LED (470 nm, 465 LUX) and hydrogen evolution was monitored with a hydrogen sensitive sensor.

5.8.5 Catalytic Alcohol Oxidation Tests

Catalytic water oxidation tests were performed as follows: A solution of **Ga-1** (10 µM, 74 µM) and substrate (2.5 mmol), was prepared in water (8 mL) and placed in a headspace vial. Hydrogen peroxide (12.5 mmol) was added and the stirred reaction mixture was heated to 80 °C for 3.5 h. This was followed by the extraction with diethyl ether (3 x 10 mL) and removal of the solvent by rotary evaporation. The conversion of the alcohol to the corresponding ketone/aldehyde was monitored by ^{1}H-NMR spectroscopy.

5.9 Appendix

5.9.1 X-ray Diffraction Structural Analysis

Table S5.1. BVS calculations of the metal ions in **Ga-1a** and **Ga-2**.

BVS values of **Ga-1a**					BVS values of **Ga-2**			
$K_{10}[Ga_6(H_2O)_3\{\alpha\text{-}SiW_9O_{35}(OH)_2\}_2]$					$K_{12}[Ga_4(H_2O)_2\{\alpha\text{-}SiW_{10}O_{38}\}_2]$			
W(1)	6.0226	O(29)	1.6780		W(1)	5.9415	O(28)	2.0520
W(2)	5.9994	O(30)	1.7759		W(2)	5.9800	O(29)	1.7756
W(3)	6.0894	O(31)	1.1717		W(3)	5.9871	O(30)	1.9275
W(4)	5.8763	O(32)	1.7125		W(4)	5.9988	O(31)	1.8977
W(5)	5.9380	O(33)	1.7428		W(5)	6.0810	O(32)	1.9049
W(6)	5.9258	O(34)	1.1047		W(6)	6.0486	O(33)	1.9780
W(7)	5.8598	O(35)	1.6612		W(7)	6.0852	O(34)	1.8462
W(8)	5.9230	O(37)	1.7278		W(8)	6.0067	O(35)	2.0386
W(9)	5.8495	O(38)	1.0468		W(9)	6.0638	O(37)	2.0342
		O(39)	0.5861		W(10)	5.9648	O(38)	1.1666
Ga(1)	3.0321						O(39)	0.6186
Ga(2)	3.0112				Ga(1)	3.0391		
Ga(3)	3.1151				Ga(2)	3.1549		
Si(1)	4.0651				Si(1)	4.0450		

Bond valence sums were calculated with the online bond valence calculator softbv 0.96 (http://www.softbv.net).

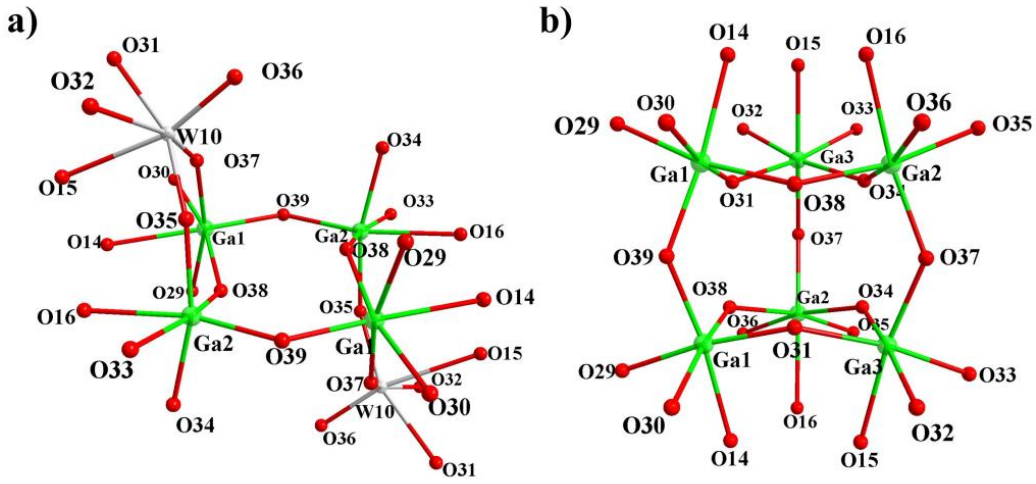

Figure S5.1. Ball-and-stick representations of: **(a)** the $\{Ga_6\}$ core of $K_{10}[Ga_6(H_2O)_3\{A\text{-}\alpha\text{-}SiW_9O_{35}(OH)_2\}_2]\cdot 35.5H_2O$ (**Ga-1a**) and **(b)** of the $\{Ga_4\}$ core in $K_{12}[Ga_4(H_2O)_2\{A\text{-}\alpha\text{-}SiW_{10}O_{38}\}_2]\cdot 30H_2O$ (**Ga-2**) (Ga: green, W: grey, O: red).

Table S5.2. Selected bond distances (**left**) $K_{10}[Ga_6(H_2O)_3\{A\text{-}\alpha\text{-}SiW_9O_{35}(OH)_2\}_2]$ (**Ga-1a**), (**right**) $K_{12}[Ga_4(H_2O)_2\{A\text{-}\alpha\text{-}SiW_{10}O_{38}\}_2]$ (**Ga-2**)

Bond	d / Å	Bond	d / Å	Bond	d / Å
W(1)-O(13)$_{ax.}$	2.349(9)	W(5)-O(15)$_{ax.}$	2.362(8)	W(9)-O(14)$_{ax.}$	2.383(8)
W(1)-O(4)$_{ter.}$	1.722(10)	W(5)-O(19)$_{ter.}$	1.730(9)	W(9)-O(27)$_{ter.}$	1.720(10)
W(1)-O(8)$_{eq.}$	1.863(9)	W(5)-O(18)$_{eq.}$	1.900(10)	W(9)-O(29)$_{eq.}$	1.836(9)
W(1)-O(3)$_{eq.}$	1.949(9)	W(5)-O(32)$_{eq.}$	1.845(10)	W(9)-O(28)$_{eq.}$	1.933(9)
W(1)-O(7)$_{eq.}$	1.863(9)	W(5)-O(20)$_{eq.}$	1.932(10)	W(9)-O(12)$_{eq.}$	1.976(9)
W(1)-O(1)$_{eq.}$	1.924(9)	W(5)-O(8)$_{eq.}$	1.981(10)	W(9)-O(26)$_{eq.}$	1.914(9)
W(2)-O(13)$_{ax.}$	2.338(8)	W(6)-O(15)$_{ax.}$	2.370(8)	Ga(1)-O(14)$_{ax.}$	2.138(9)
W(2)-O(5)$_{ter.}$	1.721(10)	W(6)-O(21)$_{ter.}$	1.714(9)	Ga(1)-O(39)$_{aq.}$	1.920(5)
W(2)-O(9)$_{eq.}$	1.875(9)	W(6)-O(20)$_{eq.}$	1.944(10)	Ga(1)-O(38)$_{eq.}$	1.972(8)
W(2)-O(1)$_{eq.}$	1.943(10)	W(6)-O(9)$_{eq.}$	1.977(10)	Ga(1)-O(29)$_{eq.}$	1.977(9)
W(2)-O(2)$_{eq.}$	1.940(9)	W(6)-O(22)$_{eq.}$	1.913(9)	Ga(1)-O(31)$_{eq.}$	1.921(8)
W(2)-O(10)$_{eq.}$	1.872(10)	W(6)-O(33)$_{eq.}$	1.832(11)	Ga(1)-O(30)$_{eq.}$	1.958(9)
W(3)-O(13)$_{ax.}$	2.353(9)	W(7)-O(16)$_{ax.}$	2.355(8)	Ga(2)-O(16)$_{ax.}$	2.152(9)
W(3)-O(6)$_{ter.}$	1.711(10)	W(7)-O(23)$_{ter.}$	1.723(9)	Ga(2)-O(37)$_{aq.}$	1.923(10)
W(3)-O(2)$_{eq.}$	1.931(9)	W(7)-O(24)$_{eq.}$	1.922(10)	Ga(2)-O(35)$_{eq.}$	1.959(9)
W(3)-O(12)$_{eq.}$	1.867(9)	W(7)-O(35)$_{eq.}$	1.850(10)	Ga(2)-O(38)$_{eq.}$	1.967(8)
W(3)-O(11)$_{eq.}$	1.870(9)	W(7)-O(10)$_{eq.}$	1.968(10)	Ga(2)-O(36)$_{eq.}$	1.962(8)
W(3)-O(3)$_{eq.}$	1.944(9)	W(7)-O(22)$_{eq.}$	1.910(9)	Ga(2)-O(34)$_{eq.}$	1.937(8)
W(4)-O(14)$_{ax.}$	2.359(8)	W(8)-O(16)$_{ax.}$	2.374(8)	Ga(3)-O(15)$_{ax.}$	2.139(9)
W(4)-O(17)$_{ter.}$	1.715(10)	W(8)-O(25)$_{ter.}$	1.721(9)	Ga(3)-O(37)$_{aq.}$	1.929(9)
W(4)-O(1)$_{eq.}$	1.930(9)	W(8)-O(26)$_{eq.}$	1.910(10)	Ga(3)-O(32)$_{eq.}$	1.948(9)
W(4)-O(7)$_{eq.}$	1.990(9)	W(8)-O(11)$_{eq.}$	1.963(10)	Ga(3)-O(33)$_{eq.}$	1.975(5)
W(4)-O(30)$_{eq.}$	1.825(10)	W(8)-O(24)$_{eq.}$	1.951(9)	Ga(3)-O(34)$_{eq.}$	1.966(8)
W(4)-O(28)$_{eq.}$	1.956(9)	W(8)-O(36)$_{eq.}$	1.843(9)	Ga(3)-O(31)$_{eq.}$	1.931(8)
Si1-O(13)	1.634(10)	Si1-O(14)	1.614(9)	Si1-O(15)	1.626(8)
Si1-O(16)	1.633(8)				

Bond	d / Å	Bond	d / Å	Bond	d / Å
W(1)-O(13)$_{ax.}$	2.355(4)	W(5)-O(14)$_{ax.}$	2.328(4)	W(9)-O(16)$_{ax.}$	2.334(4)
W(1)-O(4)$_{ter.}$	1.717(4)	W(5)-O(19)$_{ter.}$	1.702(4)	W(9)-O(27)$_{ter.}$	1.714(4).
W(1)-O(3)$_{eq.}$	1.940(4)	W(5)-O(18)$_{eq.}$	1.935(4)	W(9)-O(34)$_{eq.}$	1.805(4)
W(1)-O(12)$_{eq.}$	1.874(4)	W(5)-O(20)$_{eq.}$	1.919(4)	W(9)-O(12)$_{eq.}$	1.995(4)
W(1)-O(1)$_{eq.}$	1.964(4)	W(5)-O(8)$_{eq.}$	1.806(4)	W(9)-O(28)$_{eq.}$	1.893(4)
W(1)-O(7)$_{eq.}$	1.866(4)	W(5)-O(30)$_{eq.}$	1.806(4)	W(9)-O(26)$_{eq.}$	1.948(4)
W(2)-O(13)$_{ax.}$	2.316(4)	W(6)-O(15)$_{ax.}$	2.356(4)	W(10)-O(15)$_{ax.}$	2.328(4)
W(2)-O(5)$_{ter.}$	1.704(4).	W(6)-O(21)$_{ter.}$	1.705(4)	W(10)-O(36)$_{ter.}$	1.732(5)
W(2)-O(8)$_{eq.}$	1.871(4)	W(6)-O(9)$_{eq.}$	1.932(4)	W(10)-O(37)$_{eq.}$	1.795(4)
W(2)-O(9)$_{eq.}$	1.905(4)	W(6)-O(31)$_{eq.}$	1.869(4)	W(10)-O(32)$_{eq.}$	2.034(4)
W(2)-O(2)$_{eq.}$	1.953(4)	W(6)-O(22)$_{eq.}$	1.941(4)	W(10)-O(31)$_{eq.}$	2.038(4)
W(2)-O(1)$_{eq.}$	1.939(4)	W(6)-O(20)$_{eq.}$	1.901(4)	W(10)-O(35)$_{eq.}$	1.821(4)
W(3)-O(13)$_{ax.}$	2.339(4)	W(7)-O(15)$_{ax.}$	2.337(4)	Ga(1)-O(14)$_{ax.}$	2.214(4)
W(3)-O(6)$_{ter.}$	1.719(4)	W(7)-O(23)$_{ter.}$	1.698(4)	Ga(1)-O(39)$_{aq.}$	1.903(4)
W(3)-O(3)$_{eq.}$	1.947(4)	W(7)-O(22)$_{eq.}$	1.911(4)	Ga(1)-O(38)$_{eq.}$	1.935(4)
W(3)-O(11)$_{eq.}$	1.947(4)	W(7)-O(24)$_{eq.}$	1.910(4)	Ga(1)-O(30)$_{eq.}$	1.973(4)
W(3)-O(10)$_{eq.}$	1.938(4)	W(7)-O(32)$_{eq.}$	1.874(4)	Ga(1)-O(29)$_{eq.}$	1.972(4)
W(3)-O(2)$_{eq.}$	1.935(4)	W(7)-O(10)$_{eq.}$	1.938(4)	Ga(1)-O(37)$_{eq.}$	1.927(4)
W(4)-O(14)$_{ax..}$	2.340(4)	W(8)-O(16)$_{ax.}$	2.317(4)	Ga(2)-O(16)$_{ax.}$	2.223(4)
W(4)-O(17)$_{ter.}$	1.718(4)	W(8)-O(25)$_{ter.}$	1.724(4).	Ga(2)-O(39)$_{aq.}$	1.906(4)
W(4)-O(29)$_{eq.}$	1.821(4)	W(8)-O(24)$_{eq.}$	1.926(4)	Ga(2)-O(33)$_{eq.}$	1.965(4)
W(4)-O(7)$_{eq.}$	1.984(4)	W(8)-O(26)$_{eq.}$	1.936(4)	Ga(2)-O(38)$_{eq.}$	1.932(4)
W(4)-O(18)$_{eq.}$	1.926(4)	W(8)-O(33)$_{eq.}$	1.800(4)	Ga(2)-O(34)$_{eq.}$	1.961(4)
W(4)-O(28)$_{eq.}$	1.920(4)	W(8)-O(11)$_{eq.}$	1.999(4)	Ga(2)-O(35)$_{eq.}$	1.899(4)
Si(1)-O(13)	1.631(4)	Si(1)-O(14)	1.625(4)	Si(1)-O(15)	1.635(4)
Si(1)-O(16)	1.638(4)				

Table S5.3. Selected bond distances for $K_m[Ga_6(H_2O)_x\{A\text{-}\alpha\text{-}SiW_9O_{34}(OH)_y\}_2]\cdot nH_2O$ (**Ga-1b**)

Bond	d / Å	Bond	d / Å	Bond	d / Å	Bond	d / Å	Bond	d / Å	Bond	d / Å
W(1)-O(13)$_{ax.}$	2.347(14)	W(5)-O(14)$_{ax.}$	2.358(13)	W(9)-O(16)$_{ax.}$	2.359(15)	W(13)-O(63)$_{ax.}$	2.322(14)	W(17)-O(65)$_{ax.}$	2.344(13)	Ga(3)-O(15)$_{ax.}$	2.108(13)
W(1)-O(4)$_{ter.}$	1.689(13	W(5)-O(20)$_{ter.}$	1.700(14)	W(9)-O(32)$_{ter.}$	1.721(16)	W(13)-O(54)$_{ter.}$	1.733(17)	W(17)-O(73)$_{ter.}$	1.708(14)	Ga(3)-O(40)$_{aq.}$	1.934(14)
W(1)-O(3)$_{eq.}$	1.910(15)	W(5)-O(21)$_{eq.}$	1.930(15)	W(9)-O(31)$_{eq.}$	1.956(13)	W(13)-O(55)$_{eq.}$	1.964(14)	W(17)-O(72)$_{eq.}$	1.807(15)	Ga(3)-O(35)$_{eq.}$	1.969(13)
W(1)-O(7)$_{eq.}$	1.813(13)	W(5)-O(19)$_{eq.}$	1.876(14)	W(9)-O(33)$_{eq.}$	1.850(14)	W(13)-O(66)$_{eq.}$	1.903(13)	W(17)-O(74)$_{eq.}$	1.938(14)	Ga(3)-O(26)$_{eq.}$	1.952(14)
W(1)-O(8)$_{eq.}$	1.954(14)	W(5)-O(9)$_{eq.}$	1.896(13)	W(9)-O(36)$_{eq.}$	1.942(13)	W(13)-O(53)$_{eq.}$	1.842(13)	W(17)-O(67)$_{eq.}$	2.002(13)	Ga(3)-O(12)$_{eq.}$	1.973(13)
W(1)-O(1)$_{eq.}$	1.963(14)	W(5)-O(30)$_{eq.}$	1.900(13)	W(9)-O(29)$_{eq.}$	1.946(14)	W(13)-O(47)$_{eq.}$	1.931(14)	W(17)-O(66)$_{eq.}$	1.942(14)	Ga(3)-O(25)$_{eq.}$	1.952(14)
W(2)-O(14)$_{ax}$	2.339(12)	W(6)-O(14)$_{ax}$	2.328(14)	W(10)-O(63)$_{ax.}$	2.397(13)	W(14)-O(64)$_{ax.}$	2.353(14)	W(18)-O(65)$_{ax.}$	2.304(13)	Ga(4)-O(65)$_{ax.}$	2.249(13)
W(2)-O(5)$_{ter.}$	1.704(13)	W(6)-O(22)$_{ter.}$	1.744(15)	W(10)-O(44)$_{ter.}$	1.722(15)	W(14)-O(56)$_{ter.}$	1.724(14)	W(18)-O(75)$_{ter.}$	1.715(15)	Ga(4)-O(38)$_{aq.}$	1.920(14)
W(2)-O(9)$_{eq.}$	1.948(14)	W(6)-O(21)$_{eq.}$	1.911(14)	W(10)-O(41)$_{eq.}$	1.920(14)	W(14)-O(55)$_{eq.}$	1.874(14)	W(18)-O(74)$_{eq.}$	1.918(14)	Ga(4)-O(71)$_{eq.}$	1.914(14)
W(2)-O(1)$_{eq.}$	1.892(14)	W(6)-O(23)$_{eq.}$	1.861(13)	W(10)-O(43)$_{eq.}$	1.956(14)	W(14)-O(52)$_{eq.}$	1.964(13)	W(18)-O(76)$_{eq.}$	1.807(14)	Ga(4)-O(72)$_{eq.}$	1.984(15)
W(2)-O(2)$_{eq.}$	1.948(14)	W(6)-O(31)$_{eq.}$	1.889(13)	W(10)-O(48)$_{eq.}$	1.822(14)	W(14)-O(57)$_{eq.}$	1.903(14)	W(18)-O(68)$_{eq.}$	1.955(13)	Ga(4)-O(70)$_{eq.}$	1.971(12)
W(2)-O(10)$_{eq.}$	1.950(14)	W(6)-O(10)$_{eq.}$	1.930(12)	W(10)-O(47)$_{eq.}$	1.947(14)	W(14)-O(67)$_{eq.}$	1.866(13)	W(18)-O(69)$_{eq.}$	1.927(14)	Ga(4)-O(76)$_{eq.}$	1.951(14)
W(3)-O(15)$_{ax.}$	2.391(12)	W(7)-O(15)$_{ax}$	2.351(14)	W(11)-O(62)$_{ax.}$	2.386(13)	W(15)-O(64)$_{ax.}$	2.339(14)	Ga(1)-O(16)$_{ax.}$	2.180(14)	Ga(5)-O(62)$_{ax.}$	2.177(14)
W(3)-O(6)$_{ter.}$	1.728(13)	W(7)-O(24)$_{ter.}$	1.723(15)	W(11)-O(45)$_{ter.}$	1.714(14)	W(15)-O(58)$_{ter.}$	1.755(13)	Ga(1)-O(38)$_{aq.}$	1.939(13)	Ga(5)-O(40)$_{aq.}$	1.920(14)
W(3)-O(12)$_{eq.}$	1.806(14)	W(7)-O(23)$_{eq.}$	1.999(13)	W(11)-O(50)$_{eq.}$	1.926(14)	W(15)-O(51)$_{eq.}$	1.955(14)	Ga(1)-O(35)$_{eq.}$	1.922(13)	Ga(5)-O(61)$_{eq.}$	1.943(15)
W(3)-O(3)$_{eq.}$	1.922(15)	W(7)-O(36)$_{eq.}$	1.907(13)	W(11)-O(49)$_{eq.}$	1.823(14)	W(15)-O(57)$_{eq.}$	1.958(14)	Ga(1)-O(33)$_{eq.}$	1.979(15)	Ga(5)-O(49)$_{eq.}$	1.961(13)
W(3)-O(11)$_{eq.}$	1.949(14)	W(7)-O(25)$_{eq.}$	1.821(13)	W(11)-O(42)$_{eq.}$	1.952(13)	W(15)-O(68)$_{eq.}$	1.887(13)	Ga(1)-O(34)$_{eq.}$	1.950(14)	Ga(5)-O(77)$_{eq.}$	1.946(15)
W(3)-O(2)$_{eq.}$	1.999(14)	W(7)-O(11)$_{eq.}$	1.931(13)	W(11)-O(41)$_{eq.}$	1.916(14)	W(15)-O(59)$_{eq.}$	1.878(13)	Ga(1)-O(27)$_{eq.}$	1.959(14)	Ga(5)-O(70)$_{eq.}$	1.956(12)
W(4)-O(13)$_{ax.}$	2.377(14)	W(8)-O(16)$_{ax}$	2.332(14)	W(12)-O(64)$_{ax.}$	2.334(14)	W(16)-O(62)$_{ax.}$	2.323(14)	Ga(2)-O(13)$_{ax.}$	2.098(14)	Ga(6)-O(63)$_{ax.}$	2.123(13)
W(4)-O(18)$_{ter.}$	1.672(15)	W(8)-O(28)$_{ter.}$	1.707(14)	W(12)-O(46)$_{ter.}$	1.723(15)	W(16)-O(60)$_{ter.}$	1.715(15)	Ga(2)-O(39)$_{aq.}$	1.920(15)	Ga(6)-O(39)$_{aq.}$	1.941(14)
W(4)-O(17)$_{eq.}$	1.840(14)	W(8)-O(27)$_{eq.}$	1.848(14)	W(12)-O(43)$_{eq.}$	1.872(14)	W(16)-O(50)$_{eq.}$	1.952(14)	Ga(2)-O(26)$_{eq.}$	1.945(13)	Ga(6)-O(71)$_{eq.}$	1.901(14)
W(4)-O(37)$_{eq.}$	1.884(13)	W(8)-O(30)$_{eq.}$	1.970(13)	W(12)-O(52)$_{eq.}$	1.926(13)	W(16)-O(61)$_{eq.}$	1.804(14)	Ga(2)-O(34)$_{eq.}$	1.945(13)	Ga(6)-O(77)$_{eq.}$	1.969(15)
W(4)-O(19)$_{eq.}$	1.956(14)	W(8)-O(29)$_{eq.}$	1.899(15)	W(12)-O(51)$_{eq.}$	1.929(13)	W(16)-O(59)$_{eq.}$	1.970(14)	Ga(2)-O(7)$_{eq.}$	1.966(13)	Ga(6)-O(53)$_{eq.}$	1.964(14)
W(4)-O(8)$_{eq.}$	1.943(13)	W(8)-O(37)$_{eq.}$	1.927(13)	W(12)-O(42)$_{eq.}$	1.893(14)	W(16)-O(69)$_{eq.}$	1.905(14)	Ga(2)-O(17)$_{eq.}$	1.963(14)	Ga(6)-O(48)$_{eq.}$	1.970(14)
Si(1)-O(13)	1.652(16)	Si(1)-O(16)	1.638(14)	Si(1)-O(15)	1.629(14)	Si(2)-O(62)	1.624(14)	Si(2)-O(65)	1.624(14)	Si(2)-O(63)	1.633(14)
Si(1)-O(14)	1.642(13)					Si(2)-O(64)	1.633(15)				

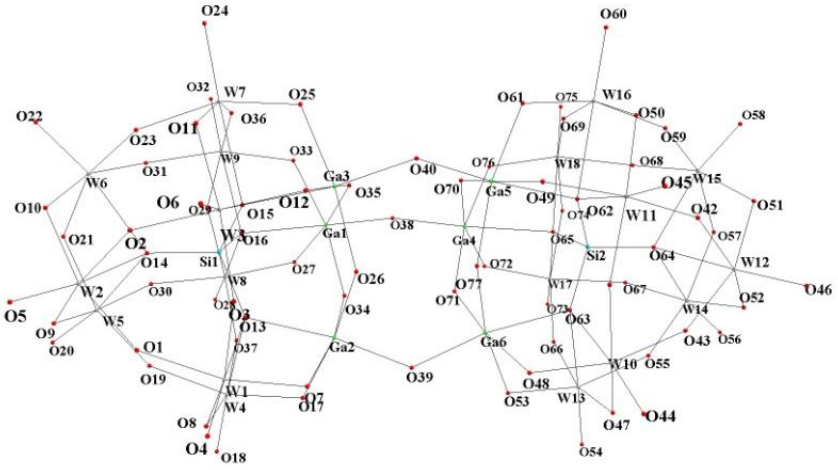

Figure S5.2. Ball-and-stick representation of $K_m[Ga_6(H_2O)_x\{\alpha\text{-}SiW_9O_{34}(OH)_y\}_2]\cdot nH_2O$ (**Ga-1b**).

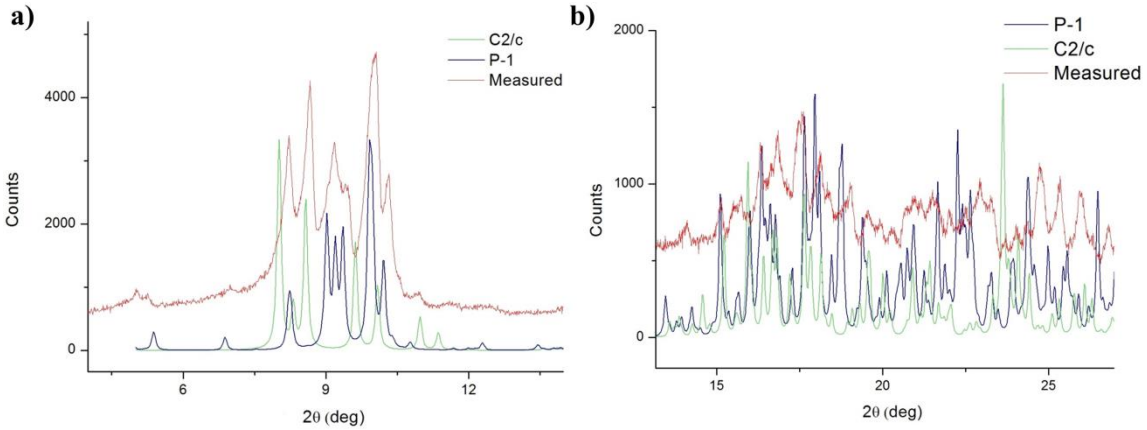

Figure S5.3. PXRD pattern of the solid product, isolated from the reaction mixture. Measured pattern of **Ga-1** (red), calculated data for monoclinic Ga-1a (green, *C*2/*c*) and triclinic **Ga-1b** (blue, $P\bar{1}$). **(a)** 2θ range = 5-13°, **(b)** 2θ range = 13-30°. Cu radiation (1.54056 Å), transmission mode.

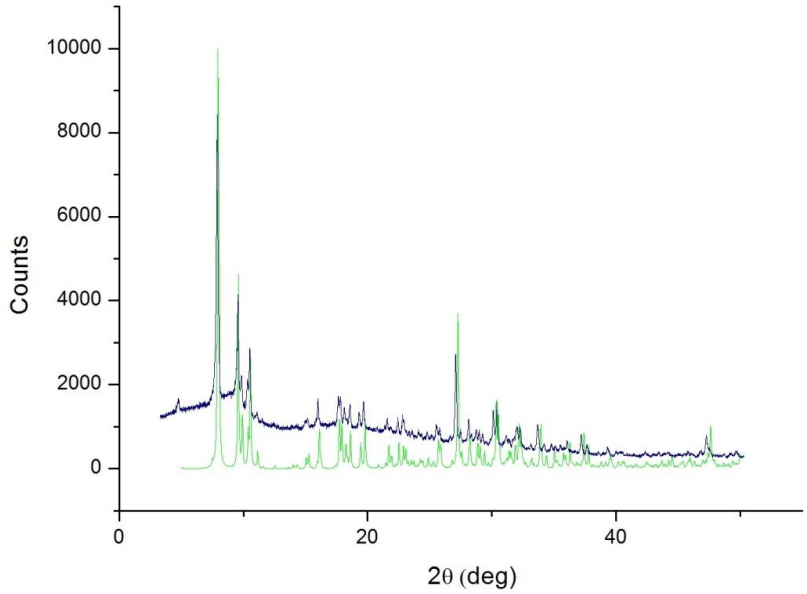

Figure S5.4. PXRD pattern of $K_{12}[Ga_4(H_2O)_2\{A\text{-}\alpha\text{-}SiW_{10}O_{38}\}_2]\cdot 30H_2O$ (**Ga-2**) (blue) vs. calculated pattern (green).

5.9.2 Thermogravimetric analyses (TGA)

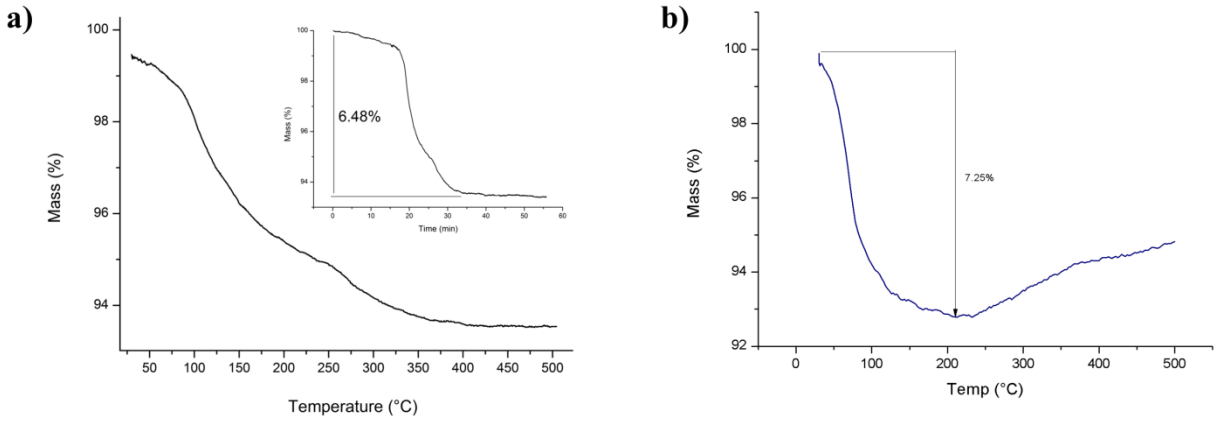

Figure S5.5. (a) Thermogravimetric analysis of $K_{10}[Ga_6(H_2O)_3\{A\text{-}\alpha\text{-}SiW_9O_{35}(OH)_2\}_2]\cdot 35.5H_2O$ (**Ga-1a**), the recorded weigh loss of 5.90 % corresponds to 20 water molecules. **(b)** Thermogravimetric analysis of $K_{12}[Ga_4(H_2O)_2\{A\text{-}\alpha\text{-}SiW_{10}O_{38}\}_2]\cdot 30H_2O$ (**Ga-2**). The recorded weight loss of 7.25 % corresponds to 25 water molecules.

5.9.3 Spectroscopic Characterization

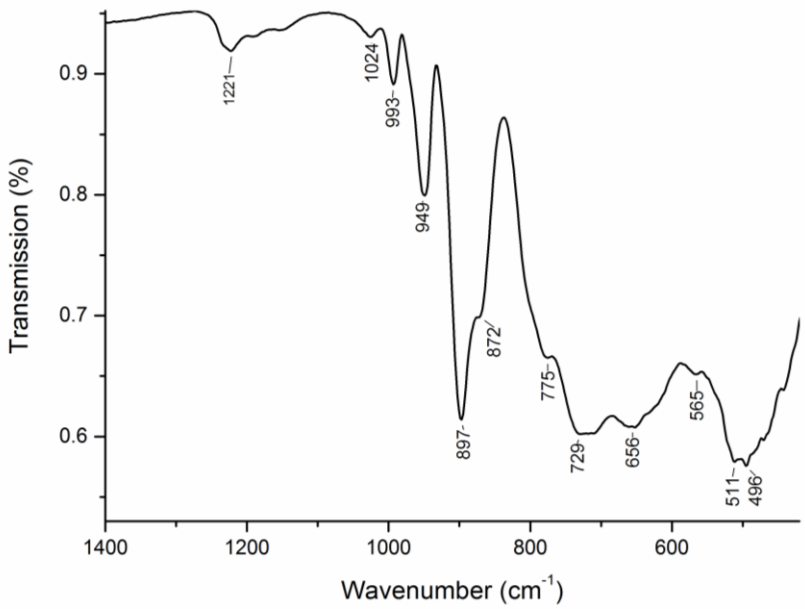

Figure S5.6. ATR FT-IR spectrum of $K_{10}[Ga_6(H_2O)_3\{A\text{-}\alpha\text{-}SiW_9O_{35}(OH)_2\}_2]\cdot 35.5H_2O$ (**Ga-1a**).

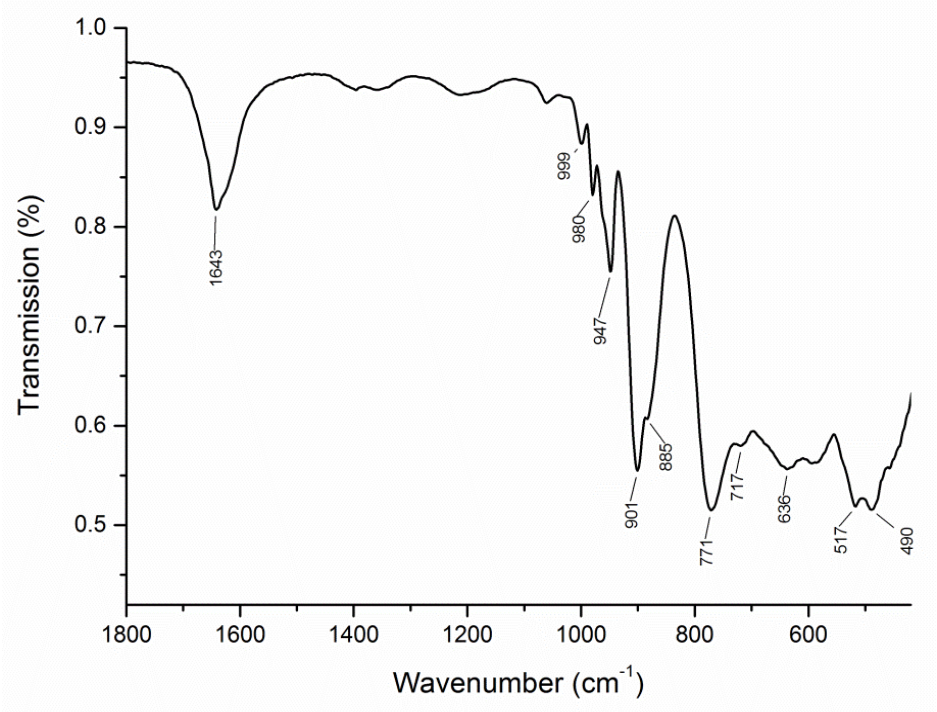

Figure S5.7. ATR FT-IR spectrum of $K_{12}[Ga_4(H_2O)_2\{A\text{-}\alpha\text{-}SiW_{10}O_{38}\}_2]\cdot 30H_2O$ (**Ga-2**).

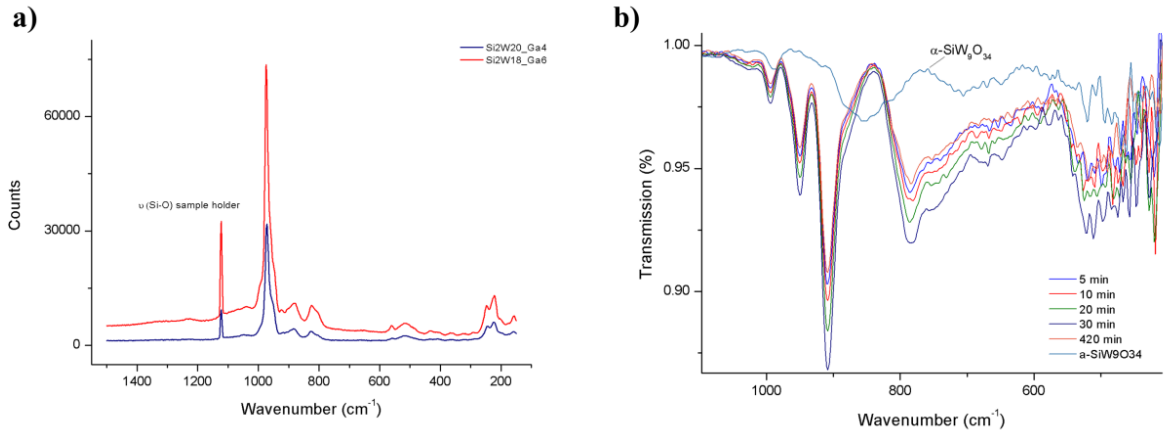

Figure S5.8. (a) Raman spectra of $K_{10}[Ga_6(H_2O)_3\{A\text{-}\alpha\text{-}SiW_9O_{35}(OH)_2\}_2]$ (**Ga-1a**) (red) and $K_{12}[Ga_4(H_2O)_2\{A\text{-}\alpha\text{-}SiW_{10}O_{38}\}_2]\cdot 30H_2O$ (**Ga-2**) (blue), laser: Ar-Ion, 514.5 nm. **(b)** ATR FT-IR spectra of a saturated solution of $[Ga_6(H_2O)_x\{A\text{-}\alpha\text{-}SiW_9O_{34}(OH)_y\}_2]^{n-}$ (**Ga-1a/b**) in acetate buffer solution (pH 4.75) recorded over 420 min.

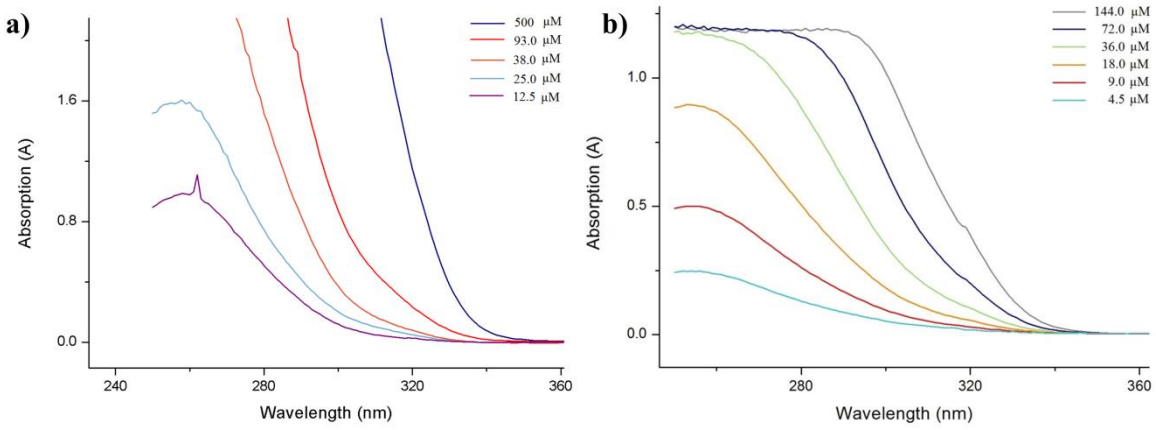

Figure S5.9. (a) Concentration-dependent UV/vis spectra of $[Ga_6(H_2O)x\{A\text{-}\alpha\text{-}SiW_9O_{34}(OH)_y\}_2]^{n-}$ **(Ga-1)** in H_2O. **(b)** Concentration-dependent UV/vis spectra of $K_{12}[Ga_4(H_2O)_2\{A\text{-}\alpha\text{-}SiW_{10}O_{38}\}_2]\cdot 30H_2O$ **(Ga-2)** in H_2O.

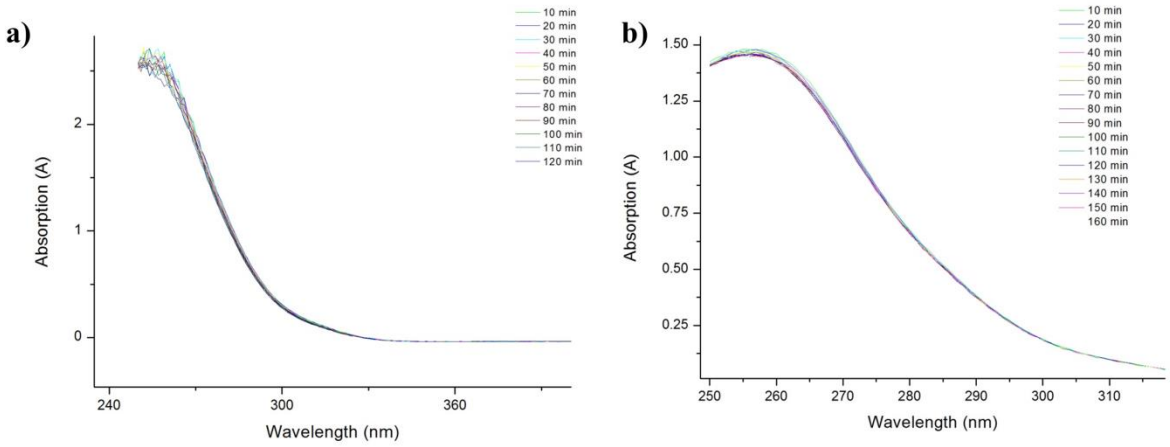

Figure S5.10. Time dependent UV/vis spectra of **Ga-1** in 0.1 M HCl (pH 1.0) **(a)**. Time dependent UV/vis spectra of **Ga-1** in 0.05 M borate buffer (pH 8.0) **(b)**.

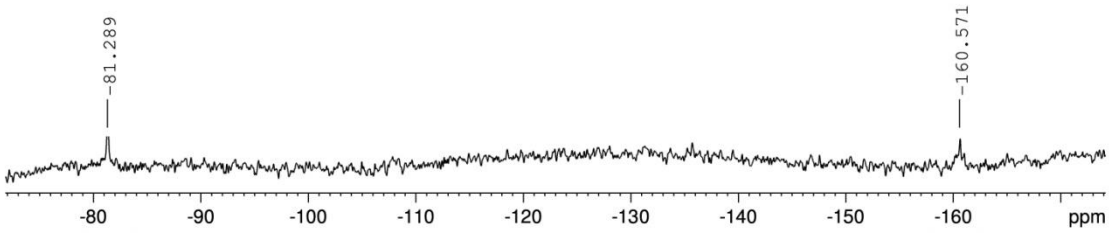

Figure S5.11. ^{183}W NMR spectrum of $K_{10}[Ga_6(H_2O)_3\{\alpha\text{-}SiW_9O_{35}(OH)_2\}_2]\cdot 35.5H_2O$ (**Ga-1a**) in D_2O/H_2O (1:1).

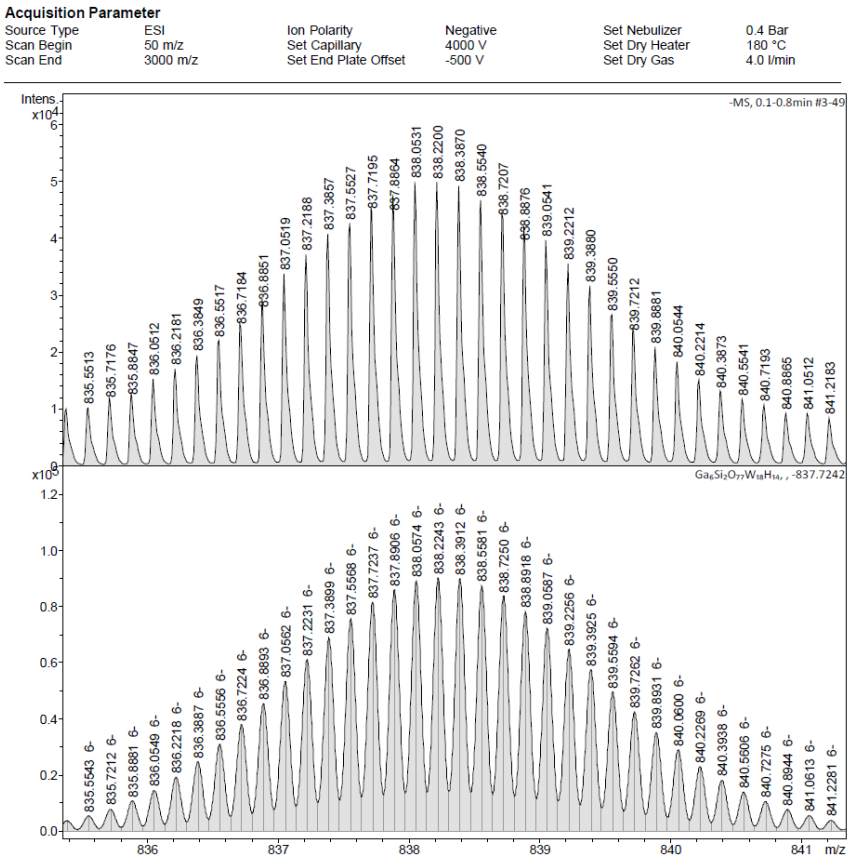

Figure S5.12. (**top**) ESI-MS spectrum for (**Ga-1a**) (FWHM = 20'000). (**bottom**) simulated ESI-MS spectrum of **Ga-1a** $\{[Ga_6(H_2O)_3\{A\text{-}\alpha\text{-}SiW_9O_{35}(OH)_2\}_2]+4H\}^{6-}$.

Table S5.4. Assignment of HR-ESI mass peaks of **(Ga-1a)** $\{[Ga_6(H_2O)_3\{A\text{-}\alpha\text{-}SiW_9O_{35}(OH)_2\}_2]+nH\}^{(10-n)-}$.

Peak	z	$Mass_{exp.}$	Fragment	Mwt
838.0531	-6	5028.3186	$\{[Ga_6(H_2O)_3\{\alpha\text{-}SiW_9O_{35}(OH)_2\}_2]+4H\}^{6-}$	5029.7267
1006.2652	-5	5031.3260	$\{[Ga_6(H_2O)_3\{\alpha\text{-}SiW_9O_{35}(OH)_2\}_2]+5H\}^{5-}$	5030.7347
1257.5823	-4	5030.3292	$\{[Ga_6(H_2O)_3\{\alpha\text{-}SiW_9O_{35}(OH)_2\}_2]+6H\}^{4-}$	5031.7426
1690.4312	-3	5071.2936	$\{[Ga_6(H_2O)_3\{\alpha\text{-}SiW_9O_{35}(OH)_2\}_2]+6H+K\}^{3-}$	5070.8409

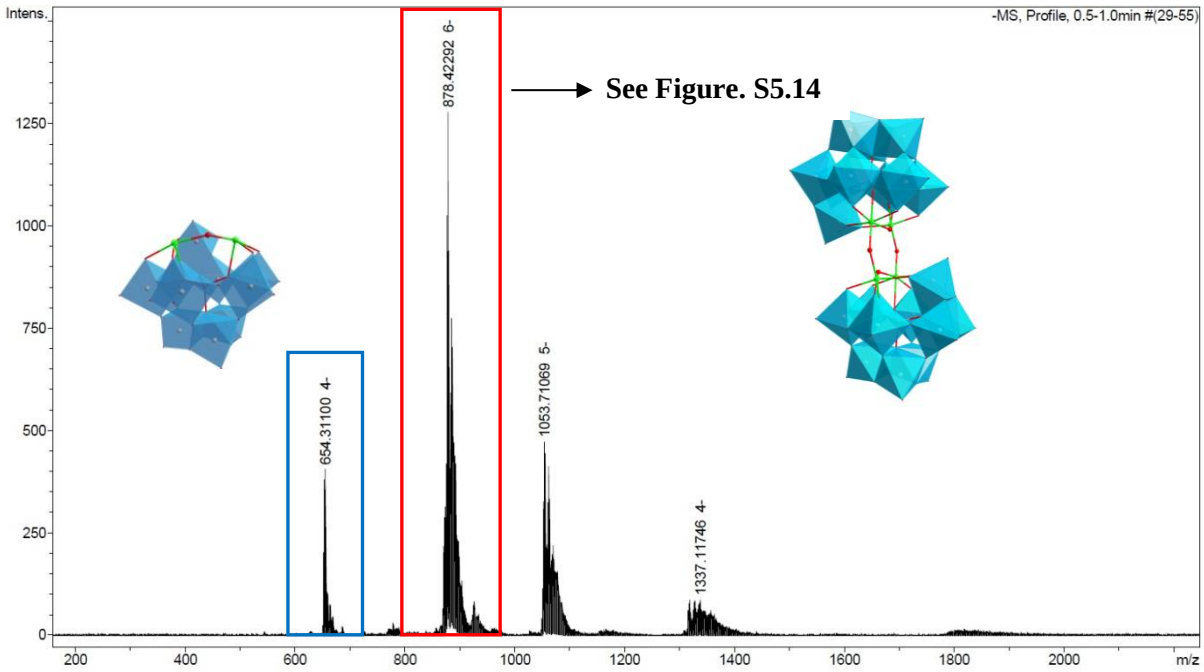

Figure S5.13. HR-ESI spectrum of $K_{12}[Ga_4(H_2O)_2\{A\text{-}\alpha\text{-}SiW_{10}O_{38}\}_2]\cdot 30H_2O$ (**Ga-2**) in H_2O; blue frame: peaks assigned to the fragment $[(SiGa_2W_{10}O_{38})\text{-}2H]^{4-}$; red frame: peaks assigned to the fragment $[Ga_4(H_2O)_2\{A\text{-}\alpha\text{-}SiW_{10}O_{38}\}_2]+6H]^{6-}$.

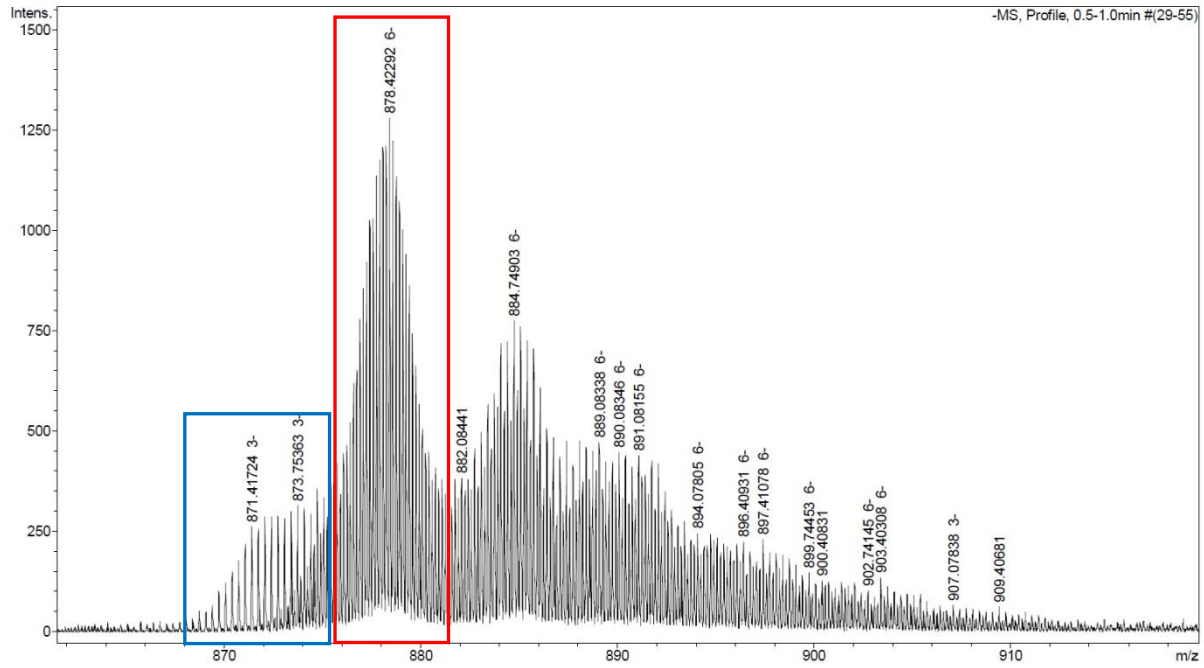

Figure S5.14. Enlarged view of HR-ESI spectrum of (**Ga-2**) in H_2O; blue frame: peaks assigned to the fragment $\{[SiGa_2W_9O_{38}]\text{-}3H\}^{3-}$; red frame: peaks assigned to the fragment $\{[Si_2Ga_4W_{20}O_{78}]+6H\}^{6-}$.

Table S5.5. Assignment of HR-ESI mass peaks of (**Ga-2**) $[Ga_4(H_2O)_2\{A\text{-}\alpha\text{-}SiW_{10}O_{38}\}_2]+nH]^{(12-n)-}$.

Peak[a]	z	$Mass_{exp.}$	Fragment	Mwt
871.4172	-3	2614.2516	$\{[Ga_2SiW_{10}O_{38}]+3H\}^{3-}$	2616.9506
654.3110	-4	2617.2440	$\{[Ga_2SiW_{10}O_{38}]+2H\}^{4-}$	2615.9427
878.4229	-6	5270.5374	$\{[Ga_4(H_2O)_2\{\alpha\text{-}SiW_{10}O_{38}\}_2]+6H\}^{6-}$	5267.9159
1053.7107	-5	5268.5535	$\{[Ga_4(H_2O)_2\{\alpha\text{-}SiW_{10}O_{38}\}_2]+7H\}^{5-}$	5268.9239
1337.1176	-4	5348.4704	$\{[Ga_4(H_2O)_2\{\alpha\text{-}SiW_{10}O_{38}\}_2]+6H+2K\}^{4-}$	5344.0967

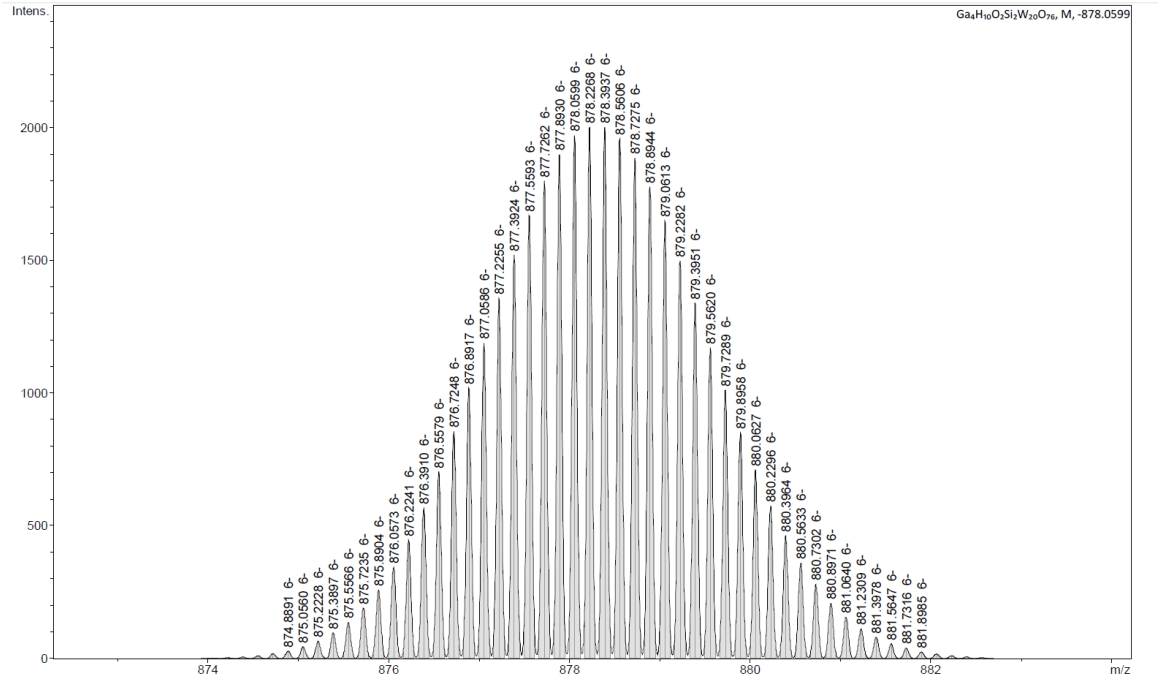

Figure S5.15. Simulated ESI-MS spectrum for polyanion (**Ga-2**) $\{[Ga_4(H_2O)_2\{A\text{-}\alpha\text{-}SiW_{10}O_{38}\}_2]+6H\}^{6-}$.

5.9.4 Electrochemical Characterization

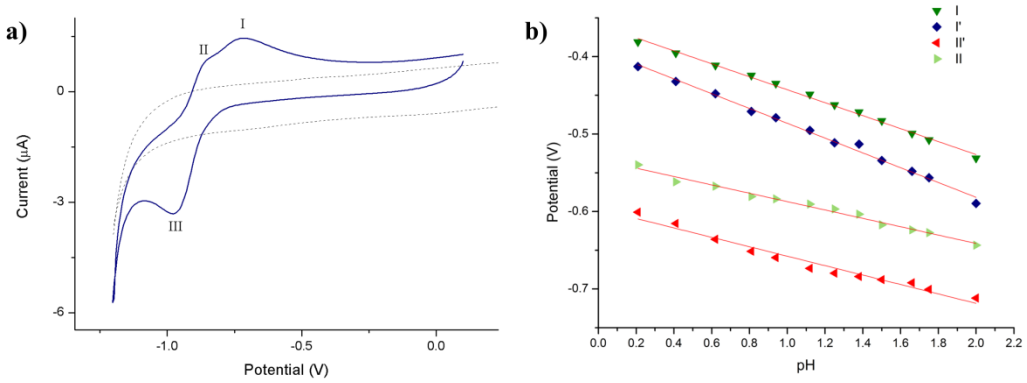

Figure S5.16. (a) Cyclic voltammogram of $[Ga_6(H_2O)_x\{A\text{-}\alpha\text{-}SiW_9O_{34}(OH)_y\}_2]^{n-}$ **(Ga-1)** (0.1 M acetate buffer, pH 4.75, ref = Ag/AgCl; WE = glassy carbon disc; CE = platinum, c = 160 µM; scan rate = 50 mV/s; solvent: dashed line). **(b)** pH dependence of the redox peaks I-I' and II-II' of **(Ga-1)** in 0.1M HCl; pH range 0.2-2.

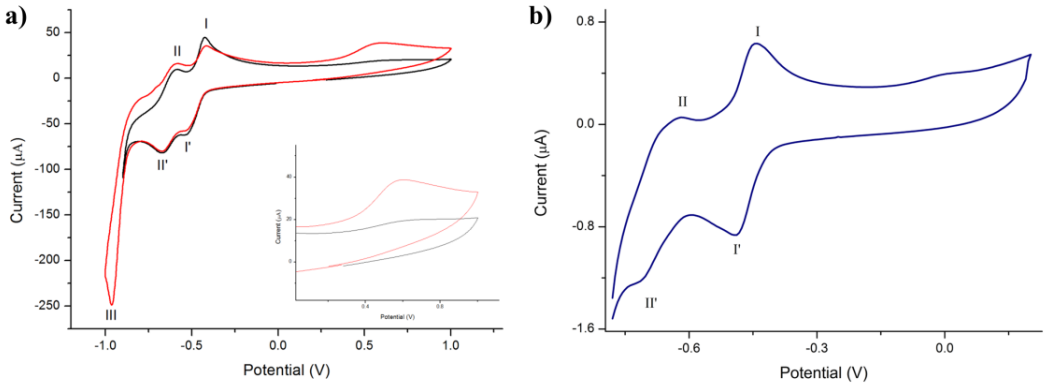

Figure S5.17. (a) Cyclic voltammogram of $[Ga_6(H_2O)_x\{\alpha\text{-}SiW_9O_{34}(OH)_y\}_2]^{n-}$ **(Ga-1)** at 0.74mM. **(b)** Cyclic voltammogram of $[Ga_4(H_2O)_2\{\alpha\text{-}SiW_{10}O_{38}\}_2]^{12-}$ **(Ga-2)** at 50µM. Conditions: 0.1 M HCl, pH 1.0; ref = Ag/AgCl; WE = glassy carbon disc; CE = platinum, scan rate = 50 mV/s.

Table S5.6. Summarized slopes for pH dependent peak potentials.

Equation	**y = a + bx**	**Adj. R-Square**	**0.99342**
		Value V/[pH]	**Standard Deviation**
I	Slope	-0.08371	0.00168
I'	Slope	-0.09559	0.00234
II	Slope	-0.05401	0.00199
II'	Slope	-0.06090	0.00340

5.10 References

[1] A. Proust, R. Thouvenot, P. Gouzerh, *Chem. Commun.* **2008**, 1837–1852.

[2] C. L. Hill, M. S. Weeks, R. F. Schinazi, *J. Med. Chem.* **1990**, *33*, 2767–2772.

[3] H. El Moll, W. Zhu, E. Oldfield, L. M. Rodriguez-Albelo, P. Mialane, J. Marrot, N. Vila, I.-M. Mbomekallé, E. Rivière, C. Duboc, A. Dolbecq, *Inorg. Chem.* **2012**, *51*, 7921–7931.

[4] A. Tézé, G. Hervé, R. G. Finke, D. K. Lyon (Eds.) *α-, β-, and γ-Dodecatungstosilicic Acids: Isomers and Related Lacunary Compounds*.

[5] F. Zonnevijlle, C. M. Tourné, G. F. Tourne, *Inorg. Chem.* **1982**, *21*, 2742–2750.

[6] M. A. Fedotov, L. P. Kazanskii, *B. Acad. Sci. USSR CH+* **1988**, *37*, 1789–1792.

[7] N. Yamamoto, D. Schols, E. de Clercq, Z. Debyser, R. Pauwels, J. Balzarini, H. Nakashima, M. Baba, M. Hosoya, R. Snoeck, *Mol. Pharmacol.* **1992**, *42*, 1109–1117.

[8] J. Liu, F. Ortega, P. Sethuraman, D. E. Katsoulis, C. E. Costello, M. T. Pope, *J. Chem. Soc. Dalton* **1992**, 1901–1906.

[9] B. Lihua, J. Peng, Y.-G. Chen, J. Lu, L. Qu, *Polyhedron* **1994**, *13*, 2421–2424.

[10] J. Liu, X. Zhan, Y.-G. Chen, G. Li, J.-P. Wang, *Transition Met. Chem.* **1995**, *20*, 327–329.

[11] L. Meng, J. F. Liu, *Chinese J. Chem.* **1995**, *13*, 334–339.

[12] J.-Y. Niu, M.-X. Li, J.-P. Wang, Y. Bo, *J. Chem. Crystallogr.* **2003**, *33*, 799–803.

[13] D. Drewes, E. M. Limanski, B. Krebs, *Eur. J. Inorg. Chem.* **2005**, *2005*, 1542–1546.

[14] M. A. Green, M. J. Welch, *Int. J. Rad. Appl. Instrum. B.* **1989**, *16*, 435–448.

[15] Z. Li, P. S. Conti, *Adv. Drug Deliver. Rev.* **2010**, *62*, 1031–1051.

[16] M. Vorster, A. Maes, C. van de Wiele, M. Sathekge, *Nucl. Med. Commun.* **2013**, *34*, 834–854.

[17] A. Sanchez-Crespo, *Appl. Radiat. Isotopes* **2013**, *76*, 55–62.

[18] S. R. Banerjee, M. G. Pomper, *Appl. Radiat. Isotopes* **2013**, *76*, 2–13.

[19] J. Liu, W.-J. Mei, A.-W. Xu, C.-P. Tan, S. Shi, L.-N. Ji, *Antivir. Res.* **2004**, *62*, 65–71.

[20] B. Hasenknopf, *Front. Biosci.* **2005**, *10*, 275–287.

[21] A. Flütsch, T. Schroeder, M. G. Grütter, G. R. Patzke, *Bioorg. Med. Chem. Lett.* **2011**, *21*, 1162–1166.

[22] R. D. Shannon, *Acta Crystallogr. A.* **1976**, *32*, 751–767.

[23] S. Himeno, S. Murata, K. Eda, *Dalton Trans.* **2009**, 6114–6119.

[24] X. López, J. M. Maestre, C. Bo, J. M. Poblet, *J. Am. Chem. Soc.* **2001**, *123*, 9571–9576.

[25] K. M. Sundaram, W. A. Neiwert, C. L. Hill, I. A. Weinstock, *Inorg. Chem.* **2006**, *45*, 958–960.

[26] N. Leclerc-Laronze, J. Marrot, G. Hervé, *CR. Chimie* **2006**, *9*, 1467–1471.

[27] L. Ni, F. Hussain, B. Spingler, S. Weyeneth, G. R. Patzke, *Inorg. Chem.* **2011**, *50*, 4944–4955.

[28] R. G. Finke, M. W. Droege, *J. Am. Chem. Soc.* **1984**, *106*, 7274–7277.

[29] T. Yamase, T. Ozeki, H. Sakamoto, S. Nishya, A. Yamamoto, *B. Chem. Soc. JPN.* **1993**, *66*, 103–108.

[30] K. Nomiya, M. Takahashi, K. Ohsawa, J. A. Widegren, *J. Chem. Soc. Dalton* **2001**, 2872–2878.

[31] J. C. Wu, M. Q. Chen, M. X. Li, G. Y. Xie, S. L. Jin, *Chinese J. Chem.* **1999**, *17*, 350–355.

[32] R. Thouvenot, M. Fournier, R. Franck, C. Rocchiccioli-Deltcheff, *Inorg. Chem.* **1984**, *23*, 598–605.

[33] E. F. Wilson, H. N. Miras, M. H. Rosnes, L. Cronin, *Angew. Chem. Int. Ed.* **2011**, *50*, 3720–3724.

[34] J. J. Stracke, R. G. Finke, *J. Am. Chem. Soc.* **2011**, *133*, 14872–14875.

[35] Q. Yin, J. M. Tan, C. Besson, Y. V. Geletii, D. G. Musaev, A. E. Kuznetsov, Z. Luo, K. I. Hardcastle, C. L. Hill, *Science* **2010**, *328*, 342–345.

[36] B. Keita, Y. W. Lu, L. Nadjo, R. Contant, *Eur. J. Inorg. Chem.* **2000**, 2463–2471.

[37] M. Sadakane, E. Steckhan, *Chem. Rev.* **1998**, *98*, 219–238.

[38] J. P. Launay, *J. Inorg. Nucl. Chem.* **1976**, *38*, 807–816.

[39] B. Keita, I.-M. Mbomekallé, L. Nadjo, R. Contant, *Electrochem. Commun.* **2001**, *3*, 267–273.

[40] B. Keita, U. Kortz, L. R. Brudna Holzle, S. Brown, L. Nadjo, *Langmuir* **2007**, *23*, 9531–9534.

[41] B. Keita, S. Floquet, J.-F. Lemonnier, E. Cadot, A. Kachmar, M. Benard, M.-M. Rohmer, L. Nadjo, *J. Phys. Chem. C.* **2008**, *112*, 1109–1114.

[42] S. P. E. Smith, J. B. Christian, *Electrochim. Acta.* **2008**, *53*, 2994–3001.

[43] X. Liu, Y. Li, S. Peng, G. Lu, S. Li, *Int. J. of Hydrogen Energ.* **2012**, *37*, 12150–12157.

[44] Z. Zhang, Q. Lin, S.-T. Zheng, X. Bu, P. Feng, *Chem. Commun.* **2011**, *47*, 3918–3920.

[45] H. Lv, J. Song, Z. Haiming, Y. V. Geletii, J. Bacsa, Z. Chongchao, T. Lian, D. G. Musaev, C. L. Hill, *J. Catal.* **2013**, *307*, 48–54.

[46] N. Mizuno, K. Yamaguchi, K. Kamata, *Coord. Chem. Rev.* **2005**, *249*, 1944–1956.

[47] L. Ni, J. Patscheider, K. K. Baldridge, G. R. Patzke, *Chem. Eur. J.* **2012**, *18*, 13293–13298.

[48] R. G. Finke, M. W. Droege, P. J. Domaille, *Inorg. Chem.* **1987**, *26*, 3886–3896.

[49] W. G. Klemperer in *Inorganic Syntheses*, John Wiley & Sons, Inc, **2007**.

[50] H. Naruke, N. Kajitani, T. Konya, *J. Solid State Chem.* **2011**, *184*, 770–777.

Chapter 6

The Self-Assembly Process of Ga(III) Substituted Polyoxotungstates

6 The Self-Assembly Process of Ga(III) Substituted Polyoxotungstates

6.1.1 Introduction

The lacunary Wells-Dawson precursor $[Si_2W_{18}O_{66}]^{16-}$ was used earlier to prepare POMs with transition metal cations (V, Mn, Fe, Co Ni, Cu). Open Wells-Dawson POMs functionalized with the lanthanide cations Tb, Dy, Gd, Ho were prepared via a different synthetic strategy.[1] Furthermore, a Ni containing open Wells-Dawson POM was reported earlier, which attracted particular attention as highly active water oxidation catalyst.[2] Recently, Ga-substituted silicotungstates have been reported by our group:[3] As reported in §5.2, two new structures could be isolated in phase pure form through the reaction of the lacunary precursor $[A\text{-}\alpha\text{-}SiW_9O_{34}]^{10-}$ with Ga(III) cations. $K_8Na_2[Ga_4(H_2O)_6(Si_2W_{18}O_{66})]\cdot 19.5H_2O$ **(Ga-3)** with an embedded Ga_4 core was obtained as minor impurity in the earlier reported synthesis of the silicotungstates $K_{10}[Ga_6(H_2O)_3\{A\text{-}\alpha\text{-}SiW_9O_{35}(OH)_2\}_2]\cdot 35.5H_2O$ **(Ga-1)** and $K_{12}[Ga_4(H_2O)_2\{A\text{-}\alpha\text{-}SiW_{10}O_{38}\}_2]\cdot 30H_2O$ **(Ga-2)**.[3] Herein we report on the successful optimization of reaction conditions in order to increase the yield of the polyanion $[Ga_4(OH)_6(Si_2W_{18}O_{66})]^{10-}$ by using high resolution mass spectrometry.

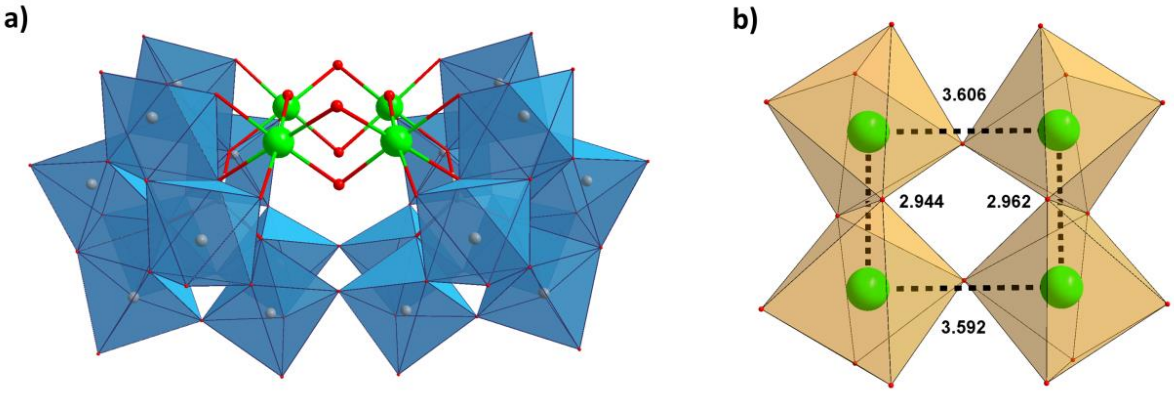

Figure 6.1. (a) Polyhedral ball and stick representation of the polyanion $[Ga_4(OH)_6(Si_2W_{18}O_{66})]^{10-}$ (**Ga-3**); **(b)** polyhedral ball and stick representation of the transition metal core of **Ga-3**, Ga-Ga interatomic distances are indicated by dashed lines.

6.1.2 Results and Discussion

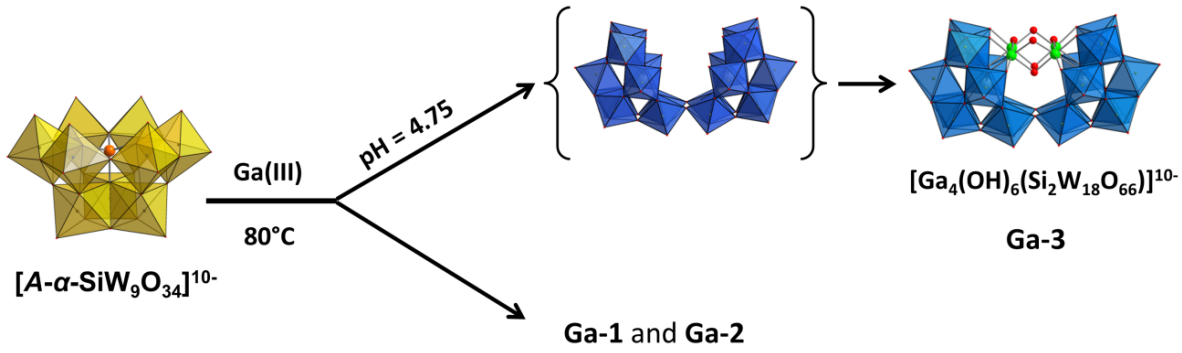

Figure 6.2. Overview of the reaction of the lacunary precursor [A-α-SiW_9O_{34}]$^{10-}$ with Ga(III) cations, resulting in the formation of $K_8Na_2[Ga_4(H_2O)_6(Si_2W_{18}O_{66})]\cdot 19.5H_2O$ **(Ga-3)**.

6.1.2.1 Synthetic Strategy

Crystals of $K_8Na_2[Ga_4(H_2O)_6(Si_2W_{18}O_{66})]\cdot 19.5H_2O$ **(Ga-3)** were obtained from the reaction of the lacunary silicotungstate [A-α-SiW_9O_{34}]$^{10-}$ with $Ga(NO_3)_2$ after heating the reaction mixture to 80 °C. Afterwards, the pH of the reaction mixture was adjusted to 4.75 with NaOH. The pH of the reaction mixture drops slowly so that further addition of NaOH is required until the pH remains stable at 4.75. The addition of solid KCl led to the formation of a white precipitate from which the desired crystals are obtained after recrystallization. This procedure is similar to the procedure reported earlier for **(Ga-1)** with the difference that NaOH was added until the pH was stable at 4.75. Although the yield of **Ga-3** crystals could be highly increased thereby, the reaction products still remained a mixture of **Ga-1** and **Ga-3**.

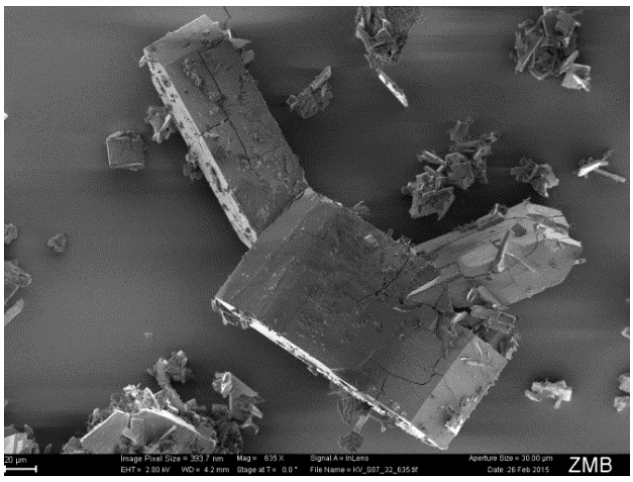

Figure 6.3. Scanning electron microscope (SEM) image of crystals of **Ga-3** (scale bar = 20 µm).

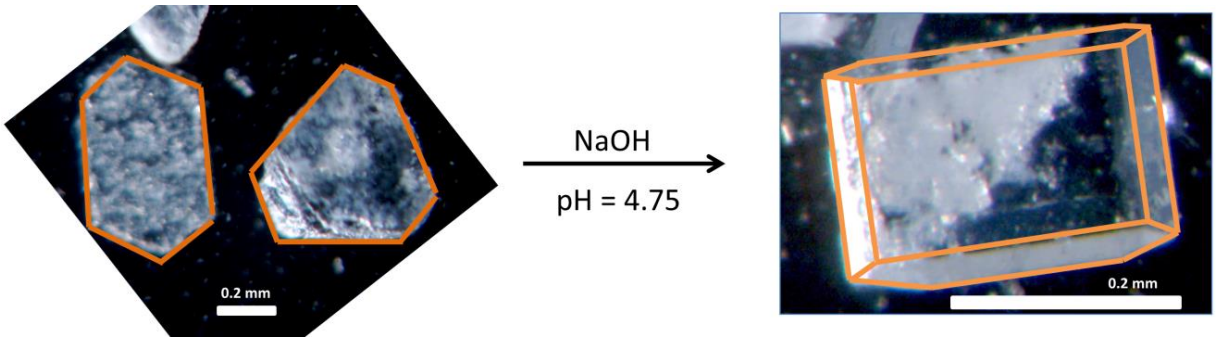

Figure 6.4. Light microscope image of crystals which were obtained from the reaction mixture. Crystal edges are highlighted in orange: **Ga-1** (left), **Ga-3** (right).

The respective crystal habitus of both compounds are very different, allowing a visual discrimination between the two compounds. This requires that the amount of $[Ga_4(OH)_6(Si_2W_{18}O_{66})]^{10-}$ is sufficiently high for crystals with properly developed faces to form (Figure 6.4 and Figure 6.3). Experimental PXRD patters are in agreement with calculated positions (Figure 6.5). The amorphous fraction is most likely due to the presence of non-crystalline $K_{10}[Ga_6(H_2O)_3\{A\text{-}\alpha\text{-}SiW_9O_{35}(OH)_2\}_2]\cdot 35.5H_2O$, **(Ga-1)**. As the ratio of the two species cannot be quantified by PXRD, visual analysis of the reaction mixture with a microscope allows a rough estimation of the distribution of the two different species.

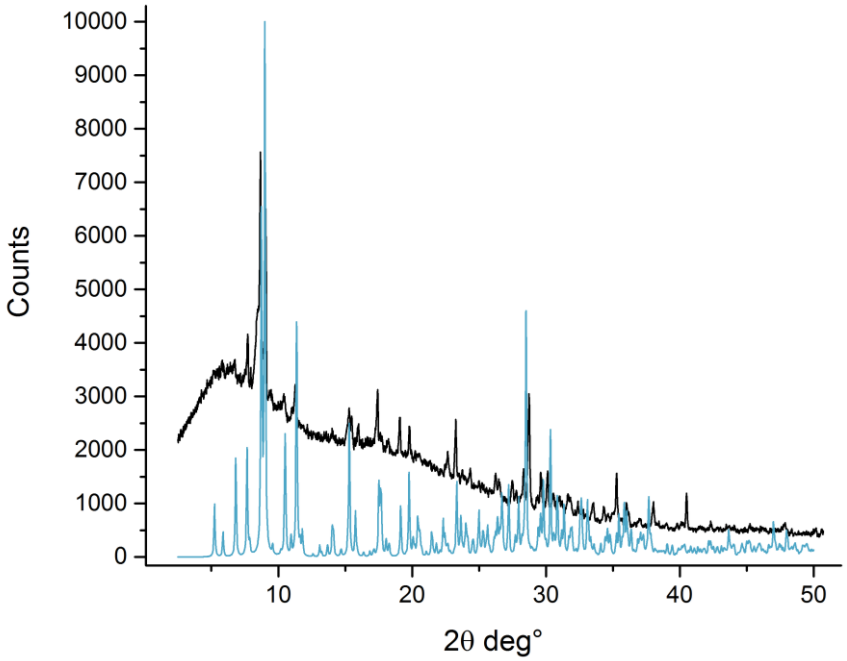

Figure 6.5. PXRD pattern of a mixture of **Ga-1** and **Ga-3** measured (black) vs. calculated (blue). (Cu $K_{\alpha 1}$ radiation1.54056 Å)

6.1.3 Spectroscopic Characterization

Raman spectroscopy could be performed on a single selected crystal of **Ga-3** whose unit cell parameters were previously determined (Figure 6.6). Raman shifts have been reported earlier for the main W-O vibration of Keggin type polyoxotungstates [α/β-$XW_{12}O_{40}$] (X = B, Si, P, Ge, As; A = H, K, Na, TBA, NH_4, Gua). Although the herein reported Ga_4 polyanion has a different structure compared to these reference compounds, the general assignment of W-O vibrations may still be viable. However, the W-O vibrations may be shifted and additional Raman bands are expected due to the presence of Ga-O bonds

The Raman band at 237.5 cm^{-1} is assigned to the symmetric tungsten-oxygen vibrations which have been reported between 209.0 and 223.0 cm^{-1}. The broad peak at 971.9 cm^{-1} has a shoulder at 960.4 cm^{-1} which may be an overlap of the symmetric and asymmetric stretching frequencies of the terminal oxygen atoms. These vibrations have been reported to appear between 951 and 1004 cm^{-1}.

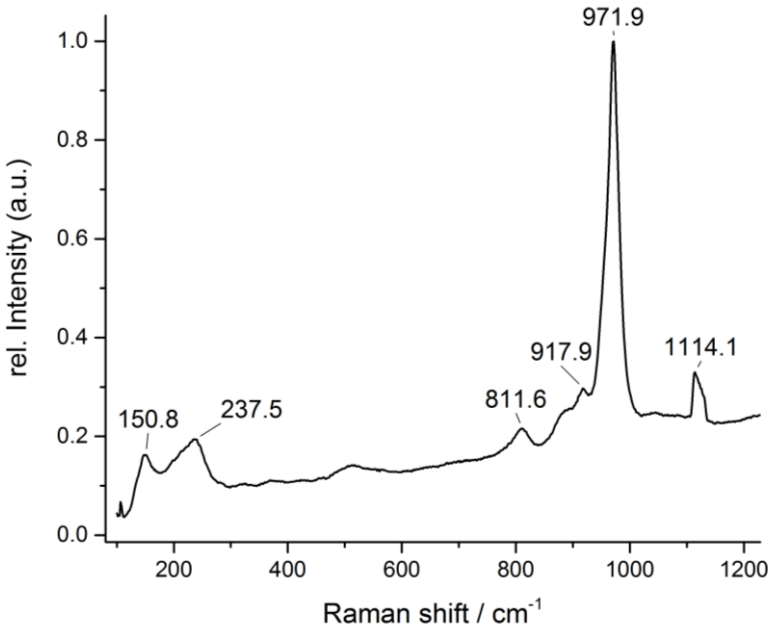

Figure 6.6. Raman spectrum of $K_8Na_2[Ga_4(H_2O)_6(Si_2W_{18}O_{66})]\cdot 19.5H_2O$ **(Ga-3)** (Ar^+-Ion, 514 nm).

Table 6.1. Crystallographic and structural refinement data for **Ga-3**.

	Ga-3
Empirical formula	$Ga_4H_{45}K_8Na_2O_{91.5}Si_2W_{18}$
Formula weight ($g \cdot mol^{-1}$)	5512.22
Temperature	183(2)
Wavelength (λ/Å)	0.71073
Crystal system	monoclinic
Space group	$P2_1/c$
a (Å)	18.1491(5)
b (Å)	20.2374(5)
c (Å)	24.1798(6)
α (°)	90
β (°)	111.731(3
γ (°)	90
V ($Å^3$)	8249.9(4)
Z	4
ρ_{calc} (g/cm^{-3})	4.438
Crystal size	0.07 x 0.11 x 0.29
Reflections collected/unique	56290/22701
Unique observed reflections	19465
θ range (°)	2.901-30.969
F(000)	9740
Data/restraints/parameters	22701/3006/1171
Goodness-of-fit	1.088
R_1[a] [I>2σ(I)]	0.0421
wR_2[b]	0.0960
R_1[a] [I>2σ(I)] (all data)	0.0524
wR_2[b] (all data)	0.1009

6.1.4 Crystal Structure of $K_8Na_2[Ga_4(OH)_6(Si_2W_{18}O_{66})]\cdot 19.5H_2O$ (Ga-3)

The polyanion $K_8Na_2[Ga_4(OH)_6(Si_2W_{18}O_{66})]\cdot 19.5\ H_2O$ **(Ga-3)** crystallizes in the monoclinic space group $P2_1/c$ with potassium and sodium as counter-cations. The model was refined with 19.5 crystal water molecules. The asymmetric unit contains an entire polyanion. **Ga-3** is constituted of the lacunary, open Wells-Dawson structure $[A\text{-}\alpha\text{-}Si_2W_{18}O_{66}]^{16-}$ with four Ga(III) cations in the outer pocket, which form the transition metal core.

BVS values of tungsten atoms between 5.89 and 6.04 Å confirm the oxidation state +VI. Tungsten oxygen bond lengths for terminal oxo groups are found in the range of 1.707(7)–1.736(7) Å for terminal oxygen atoms, between 1.799(7)-2.005(7) Å for equatorial oxygen atoms and 2.221(6)-2.421(7) Å for axial oxygen atoms. This is in agreement for W-O bond lengths in polyoxotungstates. All Ga atoms have BVS values between 2.98–3.00 which indicates an oxidation state of +III. The four Ga atoms are crystallographically independent and share one plane. Each of them is located in the corner of a rectangle with the average dimensions 3.5994(17) Å x 2.9539(16) Å (Figure 6.1). The coordination sphere of Ga(III) cations contains six oxygen atoms in the corner of a distorted octahedron. BVS values of Ga-surrounding oxygen atoms are found between 1.77 and 1.95 for oxygen atoms bridging between Ga and W. Interatomic Ga···Ga distances are found at 2.9539(16) Å between Ga atoms at the short edges of the rectangle.

They are bridged by one hydroxy group only. Ga···Ga distances between the Ga atoms at the long edge were determined as 3.5994(17) Å, and bridging occurs via two hydroxy groups.

6.1.5 Self-Assembly of $[A\text{-}\alpha\text{-}SiW_9O_{34}]^{10-}$ and Ga(III) Cations

High resolution mass spectra of a single crystal of **Ga-3** confirm the presence of the polyanion $[Ga_4(OH)_6(Si_2W_{18}O_{66})]^{10-}$ (**Figure S5.15**). Furthermore, the reaction of the lacunary precursor with $Ga(NO_3)_3$ to $[Ga_4(OH)_6(Si_2W_{18}O_{66})]^{10-}$ in aqueous solution was monitored by high resolution mass spectrometry to obtain information on the composition of the reaction mixture and on the influence of temperature and pH on the polyanion distribution. Equivalents of the lacunary precursor $[A\text{-}\alpha\text{-}SiW_9O_{34}]^{10-}$ were added subsequently to a solution of $Ga(NO_3)_3$ at room temperature. The composition of the reaction mixture was analyzed after the addition of each equivalent. A hypothetical scheme of formation has been presented earlier (**Figure 5.1**), deduced from the observed species, which crystallized subsequently from the reaction mixture. HR-ESI MS confirmed the presence these intermediates in solution.

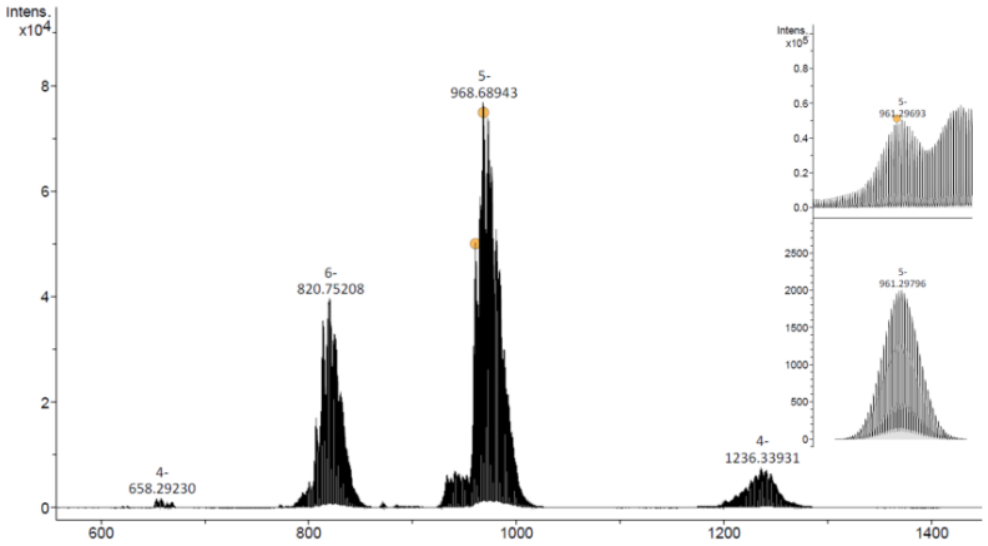

Figure 6.7. HR ESI MS of a single crystal of $K_8Na_2[Ga_4(OH)_6(Si_2W_{18}O_{66})]\cdot 19.5\ H_2O$ **(Ga-3)**. Inset: zoom of the simulated peak at m/z = 968.68943 (top) and the simulated isotope distribution (bottom).

The lacunary precursor $[A\text{-}\alpha\text{-}SiW_9O_{34}]^{10-}$ reacts quickly with Ga(III) ions at room temperature to form the Ga-substituted monomer $[Ga_3\{SiW_9O_{35}(OH)_2\}]^{5-}$ as indicated by the peaks m/z between 1240 and 1340 which correspond to the Na/K adducts (Figure 6.7). Peaks of the monomer are observed simultaneously with peaks of the dimer $[Ga_6(H_2O)_3\{\alpha\text{-}$

$SiW_9O_{35}(OH)_2\}_2]^{10-}$ (m/z = 995–1060). Mass peaks of the lacunary precursor have not been observed, which indicates that the starting material reacts completely with an excess of Ga(III) cations. According to the measured HR-ESI MS spectra heating represents a crucial step for the formation $[Ga_4(OH)_6(Si_2W_{18}O_{66})]^{10-}$ mass peaks which can be assigned to this polyanion (m/z = 1200-1250) already appear after heating the reaction mixture to 80 °C for 1h. This indicates that adjustment of the pH may not shift the equilibrium towards the formation of **Ga-3**. The pH, which was initially considered as the crucial parameter for the transformation of the dimer $[Ga_6(H_2O)_3\{A\text{-}\alpha\text{-}SiW_9O_{35}(OH)_2\}_2]^{12-}$ to the open Wells-Dawson structure $[Ga_4(OH)_6(Si_2W_{18}O_{66})]^{10-}$, in finally does not seem to influence the product distribution.

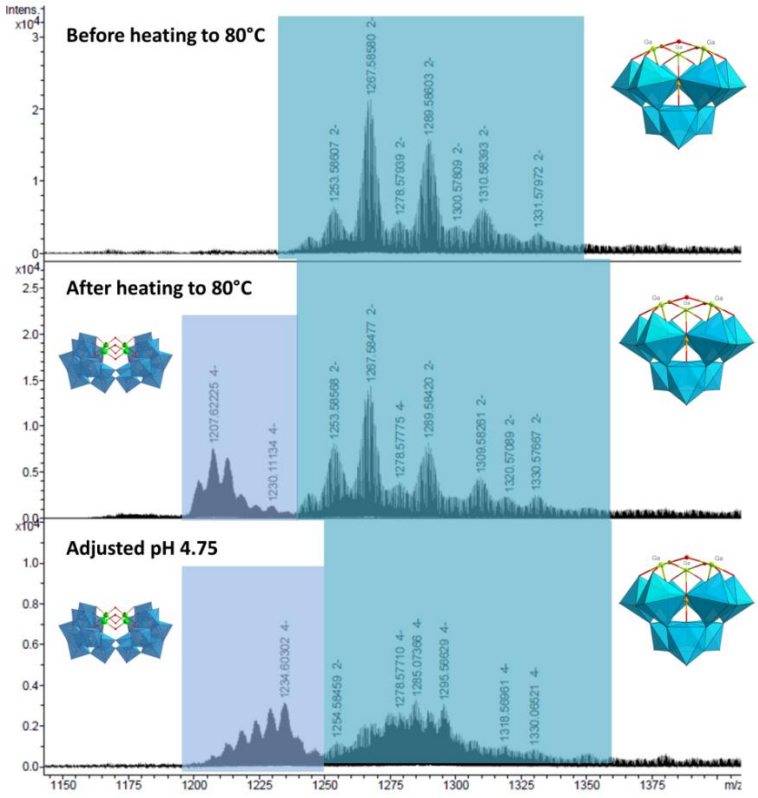

Figure 6.8. Stepwise formation of $[Ga_4(OH)_6(Si_2W_{18}O_{66})]^{10-}$: (top) after addition of 1.0 eq SiW_9. to 2.6 eq. of Ga(III), (middle) after heating of the reaction mixture to 80 °C, (bottom) after adjustment of the pH to 4.75.

6.1.5.1 Synthesis of $K_8Na_2[Ga_4(H_2O)_6(Si_2W_{18}O_{66})]\cdot 19.5H_2O$ (Ga-3)

Crystals of **Ga-3** were obtained according to a modified literature procedure.[3] A solution of $Ga(NO_3)_3\cdot 6H_2O$ (1.08 g, 4.22 mmol, 2.6 eq.) was prepared in water (10 mL). $Na_{10}[\alpha\text{-}SiW_9O_{34}]\cdot 15H_2O$ (3.90 g, 1.59 mmol, 1.0 eq.) was added in small portions to the stirred $Ga(NO_3)_3$ solution. The reaction mixture was sonicated until all of the solid precursor dissolved. The stirred reaction mixture solution was heated to 80 °C for 40 min. This was followed by the adjustment of the pH to 4.75 with NaOH (1.0 M). After addition of solid KCl (0.80 g) a white solid formed which was collected by centrifugation. Recrystallization from hot water afforded a mixture of large colorless crystals identified as $K_{10}[Ga_6(H_2O)_3\{A\text{-}\alpha\text{-}SiW_9O_{35}(OH)_2\}_2]\cdot 35.5H_2O$ **(Ga-1)** and smaller colorless crystals of $K_8Na_2[Ga_4(OH)_6(Si_2W_{18}O_{66})]\cdot 19.5H_2O$ **(Ga-3)**. The ratio of both types of crystals was estimated as 1:1.

6.2 Conclusion

The reaction of the lacunary precursor $[A\text{-}\alpha\text{-}SiW_9O_{34}]^{10-}$ with Ga(III) cations results in the formation of crystals with pronounced morphologies. Crystal structure analysis of high quality single crystals revealed the formation of two new gallium substituted polyanions $[Ga_6(H_2O)_3\{A\text{-}\alpha\text{-}SiW_9O_{35}(OH)_2\}_2]^{10-}$ **(Ga-1)** and $[Ga_4(H_2O)_2\{A\text{-}\alpha\text{-}SiW_{10}O_{38}\}_2]^{12-}$ **(Ga-2)**. Crystals of a third compound with a morphology different to that of **Ga-1** and **Ga-2** which crystallized in minor amounts from the same reaction mixture and were identified as $[Ga_4(OH)_6(Si_2W_{18}O_{66})]^{10-}$ **(Ga-3)**. This polyanion crystallizes with Na^+ and K^+ counter-cations. **Ga-3** was structurally characterized and the reaction conditions were optimized in order to increase the yield of **Ga-3**. Evolution of the reaction was monitored with high resolution mass spectrometry at crucial points of the reaction. Spectroscopic monitoring showed that polyanions of $[Ga_6(H_2O)_3\{A\text{-}\alpha\text{-}SiW_9O_{35}(OH)_2\}_2]^{10-}$ form upon addition of the precursor to the $Ga(NO_3)_3$ solution at room temperature. Heating of the reaction mixture to 80 °C is crucial for the formation of $[Ga_4(OH)_6(Si_2W_{18}O_{66})]^{10-}$. While a pH value of 4.75 first assumed to be essential for the condensation of the lacunary precursor, it probably does not influence the formation of $[Ga_4(OH)_6(Si_2W_{18}O_{66})]^{10-}$ in solution. At first glance, this is in contradiction with the observation that crystals of **Ga-3** only form in significant amounts when NaOH is added to the reaction mixture. This suggests that the crucial factor associated with NaOH addition is in fact the Na^+ counter-cation which might be essential for the formation of **Ga-3**.

6.3 Formation of New Gallium Containing Phosphotungstates

A major analytical advantage of Ga(III) cations the absence of unpaired electrons, leading to diamagnetic properties of the core. This allows monitoring the reaction of gallium nitrate with lacunary phosphotungstate precursors by ^{31}P-NMR spectroscopy. The reaction of the lacunary Wells-Dawson precursor $Na_{12}[P_2W_{15}O_{56}]\cdot 18H_2O$[4,5] with gallium nitrate resulted in the formation of four new gallium substituted phosphotungstates. Preliminary structures are shown in Figure 6.9.

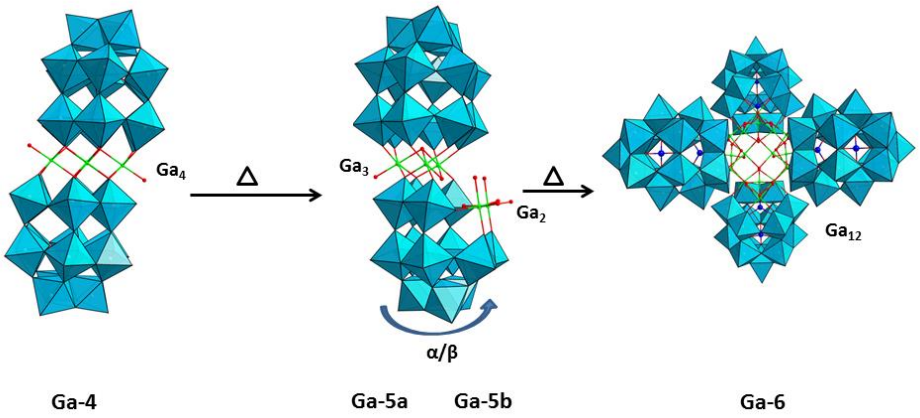

Figure 6.9 Polyhedral ball and stick representation of phosphotungstates formed by heating of $[P_2W_{15}O_{56}]^{12-}$ and Ga(III).

At room temperature single crystals of the Wells-Dawson sandwich-type structure $Na_{12}[Ga_4(H_2O)_2(P_2W_{15}O_{56})_2]\cdot 47H_2O$ **(Ga-4)** with a pure Ga_4 core were formed. After heating the reaction mixture to 80 °C for 1 h, crystals of $Na_{12}[Ga_3(H_2O)(P_2W_{15}O_{56})(\alpha\text{-}P_2W_{13}Ga_2O_{51}(H_2O)_4(OH))]\cdot 21H_2O$ **(Ga-5a)** and $Na_{12}[Ga_3(H_2O)(P_2W_{15}O_{56})(\alpha/\beta\text{-}P_2W_{13}Ga_2O_{51}(H_2O)_4(OH))]\cdot 15H_2O$ **(Ga-5b)** were obtained. This suggests the facile (α/β) isomerization of the Wells-Dawson ligand. After further heating, crystals of $[Ga_{13}P_8W_{60}O_{224}(OH)_{12}(PO_4)_4]^{33-}$ **(Ga-6)** were formed. Optimization of the reaction conditions is required to isolate these new Wells-Dawson polyanions in phase pure form. A hypothetical scheme of the self-assembly process is shown in Figure 6.10 with possible intermediates giving rise to the phosphotungstates of Figure 6.9.

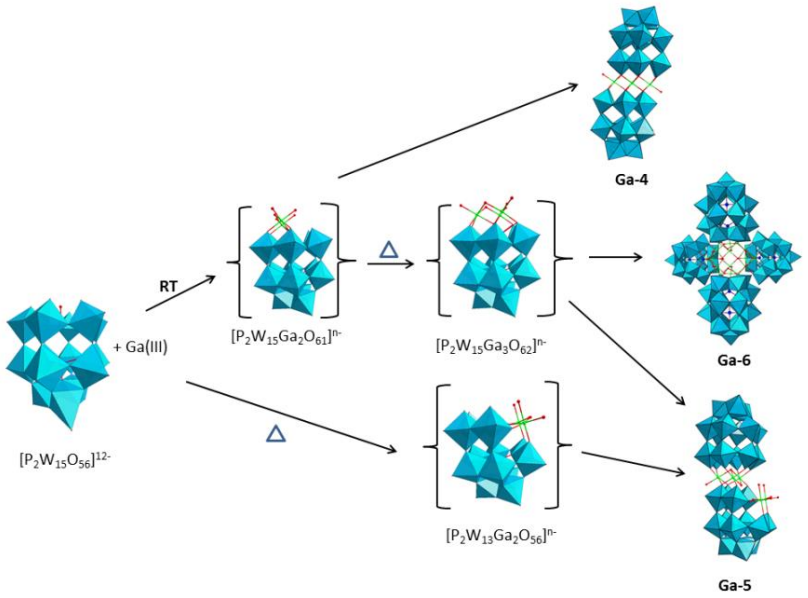

Figure 6.10. Possible formation pathways of **Ga-4-Ga-6**.

^{31}P-NMR spectroscopy can be used as rapid and convenient reaction control to quantify the amounts of the different species. The ^{31}P-NMR spectrum of the phase pure compound of (**Ga-5a**) in D_2O at RT (Figure 6.11) shows the expected 4 resonances. All in all, the combined application of ^{31}P and ^{183}W NMR spectroscopy, high resolution mass spectroscopy and single crystal structure analysis is likely to provide crucial information on the formation constants of transition metal substituted phosphotungstates and the distribution of different polyanion species. This would be a major step towards the targeted synthesis of POMs.

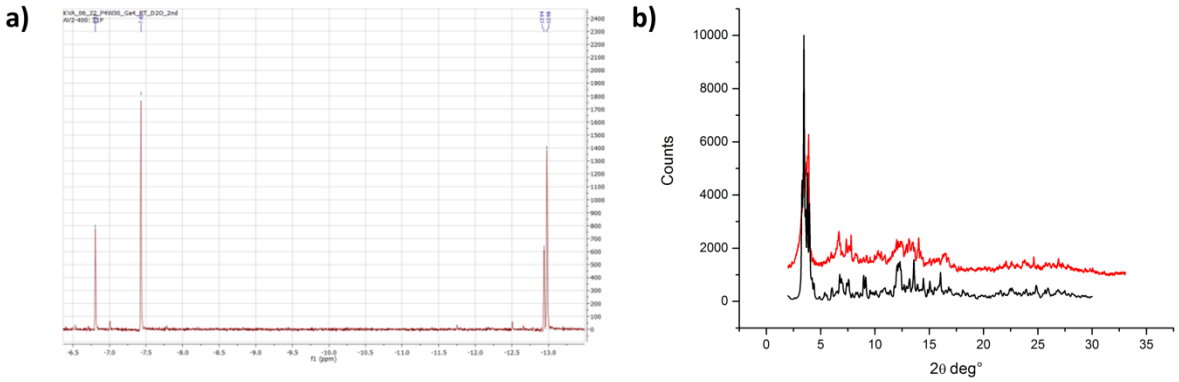

Figure 6.11. (a) ^{31}P NMR spectrum of **Ga-5a** in D_2O at RT, **(b)** PXRD pattern of **Ga-5a.**

6.4 Appendix

6.4.1 X-ray Crystallography

Crystal structure analysis was done by standard procedures, for a list of programs and instruments used see §1.16.Further details on the crystal structure investigations may be obtained from the Fachinformationszentrum Karlsruhe, D-76344 Eggenstein-Leopoldshafen, Germany (Fax: +49 7247 808 666; email crysdata@fiz-karlsruhe.de), by citing the depository number CSD-431282 (**Ga-3**).

6.4.2 Instrumentation

For a list of instruments and procedures used for the characterization of the new the new tungstobismuthates see §1.17.2.

Table S6.1. Selected bond distances $K_8Na_2[Ga_4(H_2O)_6(Si_2W_{18}O_{66})]\cdot 19.5H_2O$ **(Ga-3)**.

Bond	d / Å	Bond	d / Å	Bond	d / Å
W(1)-O(3)$_{ax.}$	2.341(7)	W(5)-O(8)$_{ax}$	2.401(7)	W(9)-O(4)$_{ax}$	2.254(6)
W(1)-O(30)$_{ter.}$	1.718(7)	W(5)-O(22)$_{ter.}$	1.736(7)	W(9)-O(10)$_{ter.}$	1.713(7)
W(1)-O(26)$_{eq.}$	1.947(7)	W(5)-O(18)$_{eq.}$	1.821(7)	W(9)-O(14)$_{eq.}$	1.961(6)
W(1)-O(2)$_{eq.}$	1.951(7)	W(5)-O(5)$_{eq.}$	1.926(7)	W(9)-O(17)$_{eq.}$	1.922(7)
W(1)-O(27)$_{eq.}$	1.859(7)	W(5)-O(19)$_{eq.}$	1.960(7)	W(9)-O(9)$_{eq.}$	1.931(7)
W(1)-O(19)$_{eq.}$	1.894(7)	W(5)-O(6)$_{eq.}$	1.910(7)	W(9)-O(7)$_{eq.}$	1.857(6)
W(2)-O(11)$_{ax.}$	2.391(6)	W(6)-O(3)$_{ax.}$	2.401(7)	W(10)-O(40)$_{ax.}$	2.263(6)
W(2)-O(28)$_{ter.}$	1.712(7)	W(6)-O(32)$_{ter.}$	1.724(8)	W(10)-O(59)$_{ter.}$	1.723(7)
W(2)-O(6)$_{eq.}$	1.910(7)	W(6)-O(12)$_{eq.}$	1.932(7)	W(10)-O(1)$_{eq.}$	1.929(7)
W(2)-O(27)$_{eq.}$	1.993(7)	W(6)-O(26)$_{eq.}$	1.935(7)	W(10)-O(35)$_{eq.}$	1.906(7)
W(2)-O(25)$_{eq.}$	1.965(7)	W(6)-O(13)$_{eq.}$	1.845(7)	W(10)-O(61)$_{eq.}$	1.950(7)
W(2)-O(29)$_{eq.}$	1.813(7)	W(6)-O(20)$_{eq.}$	1.907(7)	W(10)-O(43)$_{eq.}$	1.857(7)
W(3)-O(11)$_{ax.}$	2.357(6)	W(7)-O(3)$_{ax.}$	2.343(6)	W(11)-O(44)$_{ax.}$	2.421(7)
W(3)-O(21)$_{ter.}$	1.725(7)	W(7)-O(15)$_{ter.}$	1.720(7)	W(11)-O(57)$_{ter.}$	1.717(7)
W(3)-O(13)$_{eq.}$	2.005(7)	W(7)-O(2)$_{eq.}$	1.915(7)	W(11)-O(41)$_{eq.}$	1.924(7)
W(3)-O(24)$_{eq.}$	1.924(7)	W(7)-O(9)$_{eq.}$	1.922(7)	W(11)-O(46)$_{eq.}$	1.951(7)
W(3)-O(25)$_{eq.}$	1.916(7)	W(7)-O(12)$_{eq.}$	1.947(7)	W(11)-O(54)$_{eq.}$	1.937(7)
W(3)-O(72)$_{eq.}$	1.799(7)	W(7)-O(16)$_{eq.}$	1.853(7)	W(11)-O(55)$_{eq.}$	1.813(7)
W(4)-O(8)$_{ax.}$	2.392(6)	W(8)-O(4)$_{ax.}$	2.243(6)	W(12)-O(47)$_{ax.}$	2.345(7)
W(4)-O(23)$_{ter.}$	1.713(7)	W(8)-O(31)$_{ter.}$	1.725(7)	W(12)-O(56)$_{ter.}$	1.713(8)
W(4)-O(7)$_{eq.}$	1.946(6)	W(8)-O(1)$_{eq.}$	1.893(7)	W(12)-O(34)$_{eq.}$	1.916(7)
W(4)-O(16)$_{eq.}$	1.989(7)	W(8)-O(24)$_{eq.}$	1.898(7)	W(12)-O(48)$_{eq.}$	1.933(7)
W(4)-O(69)$_{eq.}$	1.819(7)	W(8)-O(14)$_{eq.}$	1.917(6)	W(12)-O(50)$_{eq.}$	1.865(7)
W(4)-O(5)$_{eq.}$	1.918(7)	W(8)-O(20)$_{eq.}$	1.917(6)	W(12)-O(52)$_{eq.}$	1.914(7)

Bond	d / Å	Bond	d / Å	Bond	d / Å
W(13)-O(44)$_{ax.}$	2.383(6)	W(17)-O(40)$_{ax.}$	2.221(6)	Ga(1)-O(63)$_{OH}$	1.641(7)
W(13)-O(33)$_{ter.}$	1.709(7)	W(17)-O(62)$_{ter.}$	1.719(7)	Ga(1)-O(64)$_{OH}$	1.980(7)
W(13)-O(43)$_{eq.}$	1.969(7)	W(17)-O(34)$_{eq.}$	1.944(7)	Ga(1)-O(67)$_{OH}$	1.971(7)
W(13)-O(53)$_{eq.}$	1.985(8)	W(17)-O(37)$_{eq.}$	1.878(7)	Ga(1)-O(44)$_{O}$	1.638(7)
W(13)-O(71)$_{eq.}$	1.806(8)	W(17)-O(17)$_{eq.}$	1.904(6)	Ga(1)-O(55)$_{O}$	1.976(7)
W(13)-O(54)$_{eq.}$	1.916(7)	W(17)-O(61)$_{eq.}$	1.929(7)	Ga(1)-O(71)$_{O}$	1.975(7)
W(14)-O(45)$_{ax.}$	2.418(7)	W(18)-O(47)$_{ax.}$	2.326(7)	Ga(2)-O(63)$_{OH}$	1.949(7)
W(14)-O(58)$_{ter.}$	1.710(8)	W(18)-O(49)$_{ter.}$	1.707(7)	Ga(2)-O(64)$_{OH}$	1.944(7)
W(14)-O(36)$_{eq.}$	1.957(7)	W(18)-O(39)$_{eq.}$	1.881(7)	Ga(2)-O(65)$_{OH}$	1.949(7)
W(14)-O(38)$_{eq.}$	1.820(7)	W(18)-O(46)$_{eq.}$	1.868(7)	Ga(2)-O(11)$_{O}$	2.118(6)
W(14)-O(39)$_{eq.}$	1.973(7)	W(18)-O(48)$_{eq.}$	1.955(7)	Ga(2)-O(29)$_{O}$	1.968(7)
W(14)-O(41)$_{eq.}$	1.916(7)	W(18)-O(51)$_{eq.}$	1.961(7)	Ga(2)-O(72)$_{O}$	1.966(7)
W(15)-O(45)$_{ax.}$	2.362(6)	Si(1)-O(3)	1.636(7)	Ga(3)-O(66)$_{OH}$	1.965(7)
W(15)-O(42)$_{ter.}$	1.720(7)	Si(1)-O(4)	1.609(7)	Ga(3)-O(68)$_{OH}$	1.956(7)
W(15)-O(36)$_{eq.}$	1.921(7)	Si(1)-O(8)	1.635(7)	Ga(3)-O(65)$_{OH}$	1.961(7)
W(15)-O(37)$_{eq.}$	1.946(7)	Si(1)-O(11)	1.628(7)	Ga(3)-O(18)$_{O}$	1.959(7)
W(15)-O(50)$_{eq.}$	1.969(7)			Ga(3)-O(8)$_{O}$	2.066(7)
W(15)-O(70)$_{eq.}$	1.822(7)			Ga(3)-O(69)$_{O}$	1.976(7)
W(16)-O(47)$_{ax.}$	2.368(7)	Si(2)-O(40)	1.619(7)	Ga(4)-O(66)$_{OH}$	1.960(7)
W(16)-O(60)$_{ter.}$	1.711(7)	Si(2)-O(45)	1.641(7)	Ga(4)-O(67)$_{OH}$	1.950(7)
W(16)-O(35)$_{eq.}$	1.928(7)	Si(2)-O(44)	1.638(7)	Ga(4)-O(68)$_{OH}$	1.983(7)
W(16)-O(51)$_{eq.}$	1.928(7)	Si(2)-O(47)	1.626(7)	Ga(4)-O(38)$_{O}$	1.971(7)
W(16)-O(52)$_{eq.}$	1.932(7)			Ga(4)-O(45)$_{O}$	2.066(7)
W(16)-O(53)$_{eq.}$	1.848(8)			Ga(4)-O(70)$_{O}$	1.952(7)

6.5 References

[1] L. Ni, F. Hussain, B. Spingler, S. Weyeneth, G. R. Patzke, *Inorg. Chem.* **2011**, *50*, 4944–4955.

[2] G. Zhu, E. N. Glass, C. Zhao, H. Lv, J. W. Vickers, Y. V. Geletii, D. G. Musaev, J. Song, C. L. Hill, *Dalton Trans.* **2012**, *41*, 13043–13049.

[3] K. D. von Allmen, P.-E. Car, O. Blacque, T. Fox, R. Müller, G. R. Patzke, *Z. anorg. allg. Chem.* **2014**, *640*, 781–789.

[4] W. J. Randall, M. W. Droege, N. Mizuno, K. Nomiya, T. J. R. Weakley, R. G. Finke, N. Isern, J. Salta, J. Zubieta, 167–185.

[5] R. Contant, W. G. Klemperer, O. Yaghi in *Inorganic Syntheses*, John Wiley & Sons, Inc, **2007**.

7 Summary

Artificial photosynthesis is a promising approach for light to chemical energy conversion. Using solar energy is the most sustainable way to substitute carbon based fuels and nuclear energy. Rising CO_2 levels lead to an increase of the average global temperature, which has large impacts on our society. Nuclear energy is a CO_2 free alternative. However, tragic accidents in Chernobyl (1986) and Fukushima (2011) have shown that a nuclear meltdown is a perpetual danger. Research done in context of this thesis is focused on the preparation of new visible-light-driven catalysts for O_2 and H_2 evolution. Hydrogen represents the primary fuel of the future through directly storing the energy of sunlight. Inorganic metal-oxygen clusters known as polyoxometalates (POMs) were explored as catalysts for artificial photosynthesis to produce H_2 and O_2. These metal-oxygen clusters were tested for catalytic activity in a setup which was designed to mimic the basic processes of natural photosynthesis by separating both half-reactions of the water splitting process. Special attention was paid to the Mn-containing POMs, because they can be tuned to mimic the oxygen evolving complex of photosystem II as a promising structural feature for catalytic activity. Nickel containing Keggin-type polyanions $[Ni(H_2O)(XW_{11}O_{39})]^{n-}$ (X = Si, P, Ge) were successfully investigated as catalysts for photochemical H_2 evolution. We have studied the influence of electron density on the catalytic activity of these Ni-substituted polyanions. Nickel POMs with silicon, phosphorous and germanium heteroatoms were synthesized and their potassium salts were characterized by single crystal X-ray diffraction. Structure solution and refinement was a challenging task considering the high symmetry of these structures in combination with their Ni/W disorder. The purity of all compounds was confirmed with different methods to rule out catalytically active residues. Structure-activity relationships have been established by subjecting this series of Ni POMs with different heteroatoms to photocatalytic tests and by correlating these results with the electron density on the Ni centers. The latter was studied with UV/vis and X-ray absorption near edge spectroscopy. It is highest on the Ni center of $[Ni(H_2O)(GeW_{11}O_{39})]^{4-}$. Density functional theory calculations, however, show that there is no significant contribution of the heteroatom to the lowest unoccupied orbital. Turnover numbers (TONs) and turnover frequencies (TOFs) were determined in photocatalytic tests as characteristic performance parameters of these Ni containing POM catalysts. Significant H_2 evolution activity was observed for $[Ni(H_2O)(GeW_{11}O_{39})]^{4-}$ with the highest measured TON. The results from photocatalysis could not be compared easily with redox and onset potentials determined from electrochemical experiments. Deposition of layers of heteropolyblues and -

browns on the electrode under H_2 evolution conditions do not allow a clear identification of the homogeneous POM catalyst as the active species. Therefore, photocatalytic and electrocatalytic results could not be compared. We have shown that the heteroatom significantly influences the catalytic activity in photocatalytic H_2 evolutions tests. Linking the observed differences to electron density variations on the Ni center, however, was only a partially satisfying explanation. The POM-PS complex is a solid formed by coulombic interaction of the sensitizer and complicates the explanation of observed differences. This topic opens up interesting follow-up studies, focusing on the POM-PS complex as active catalyst.

Searching for POM based WOCs, transition metal substituted polyanions based on the lacunary precursor $[BiW_9O_{33}]^{9-}$ have been investigated (lacunary POMs have a deficiency in WO_6 octahedra). Phase pure synthesis of this precursor already turned out to be demanding. Manganese, cobalt and copper cations were tested as transition metal centers to functionalize the emerging tungstobismutates. Activity was reported in our previous studies for a tungstobismutate with a W/Co disorder at the inner and outer position of the transition metal core. In contrast, its structural analogue with W/Mn disorder was inactive. In this work a detailed analysis of the reported W/Mn disorder has shown that the pure Mn_4 core is very unlikely to exist in solution, which may be the cause for the lack of activity for water oxidation. Based on this hypothesis attempts were made to prepare Mn-containing tungstobismutates with a pure transition metal core. After careful adjustments of the reaction conditions, POMs with a considerably higher percentage of the Mn_4 core could be crystallized. Structure refinement revead that the W/Mn disorder is restricted to the inner positions of the transition metal core. The outer positions are fully occupied with manganese cations. By eliminating the W/Mn disorder at the outer positions, the probability of the Mn_4 core was increased by a factor of 410. For cobalt substitution the same increase could be observed, and the W/Co disorder could be restricted to the inner positions by applying milder reaction conditions. While for the Mn-POM series a large diversity of 0D and 2D structures with distinct transition metal cores could be crystallized, only 0D structures could be isolated for the cobalt analogues. Despite the increased percentage of the Mn_4 core no water oxidation activity was observed. For a deeper understanding of the self-assembly process of the lacunary precursor $[BiW_9O_{33}]^{9-}$ with paramagnetic Mn and Co cations, the reaction process was monitored by HR-ESI MS.

Recent reports on Cu-based WOCs inspired us to investigate Cu functionalized tungstobismutates as potential catalysts for artificial photosynthesis. Six different 0D – 3D copper substituted tungstobismutates could be characterized by their single crystal X-ray structures. It turned out that very similar reaction conditions result in very different compounds. The only Cu containing tungstobismutate that could be isolated phase pure was fully characterized and studied in further detail. Although it was not active for O_2 evolution and only minor activity for H_2 evolution could be observed, the entire synthetic study on new copper substituted tungstobismutates brought forward new insights, such as the tremendous importance of countercations in POM synthesis.

Ga(III) cations are non-paramagnetic so that their bahevior in solution can be studied with ^{183}W NMR experiments. The reaction of the lacunary precursor $[SiW_9O_{34}]^{10-}$ with gallium nitrate was studied in particular, and new Ga substituted POMs could be isolated pure and were fully characterized. The reaction of the lacunary silicotungstate with Ga(III) cations shows that an equilibrium between three different polyanion species exists. Only two of these species could be isolated in phase pure form. The transformation between two species can be monitored visually, as the morphology of all three crystals is significantly different. In order to isolate the third compound in phase pure form as well, the interconversion of different polyanion species was studied by HR-ESI MS. Further investigations of the reaction of the lacunary Wells-Dawson phosphotungstate $[P_2W_{15}O_{56}]^{12-}$ with Ga(III) cations showed that different Ga substituted phosphotungstates could be accessed and characterized by single crystal X-ray diffraction. Phosphotungstate precursors enable the use of ^{31}P NMR spectroscopy as additional method to check the reaction mixture for phase purity. The structure of the isolated gallium containing phosphotungstates clearly shows that this precursor undergoes partial decomposition and α-β isomerization, followed by re-assembly into various different and unexpected phosphotungstates. This renders the above reaction an ideal platform to study the formation of phosphotungstates and to determine the formation constants for transition metal substituted phosphotungstates. A combined approach of ^{31}P and ^{183}W NMR, HR-ESI mass spectrometry and X-ray crystallography was applied to obtain crucial information on the stability of different structures and to get a step closer to the targeted synthesis of polyoxotungstates.

POMs are fascinating inorganic clusters with a broad range of applications. In the context of this thesis their potential as catalysts for artificial photosynthesis was studied. “What is the potential of Mn POMs as catalysts for water oxidation?” was the starting point of all research

done in context of this thesis. In the course of the presented work, none of the manifold Mn-based POM compounds could be successfully tested positive in established photochemical assays for water oxidation. Mn-POMs are difficult to prepare in phase pure form due to their complex multistep self-assembly processes. However, the purity of potential Mn-catalysts needs to be checked carefully as Mn(II) salts are easily oxidized to manganese oxides, which are known for their catalytic activity. The formation of the solid POM-PS complex from the positively charged photosensitizer $[Ru(bpy)_3]^{2+}$ and negatively charged polyanions further questions the use of POMs as homogeneous catalysts for artificial photosynthesis

The preparation of new transition metal substituted polyoxotungstates is a challenging task. Despite the encountered difficulties, POM chemistry has an enormous potential for structure-activity and reaction mechanism studies. They may primarily aim for a deeper understanding of the formation and crystallization of these all-inorganic metal oxygen clusters. It is crucial to understand these processes, especially in consideration of a potential scale up. Methods such as NMR, ESI MS and PXRD are powerful tools for purity and reaction course control. Follow-up studies on POM formation mechanisms are now mandatory for their successful scale-up on the way to new applications.

8 Zusammenfassung

Künstliche Photosynthese ist ein interessanter Ansatz, um Sonnenlicht in chemische Energie umzusetzen und zu speichern. Die Nutzung von Sonnenenergie ist der direkteste Weg, um fossile Brennstoffe und Kernenergie langfristig zu ersetzen. Die zunehmende CO_2 Konzentration in der Atmosphäre hat einen Anstieg der durchschnittlichen globalen Temperatur zur Folge, was schwerwiegende Auswirkungen auf unsere Gesellschaft und Umwelt hat. Kernenergie ist eine CO_2 freie Alternative. Tragische Unfälle in Tschernobyl (1986) und Fukushima (2011) haben jedoch gezeigt, dass die Gefahr einer Kernschmelze real ist. Die Forschungsprojekte, die im Rahmen dieser Arbeit durchgeführt wurden, konzentrieren sich auf die Suche nach neuen Photokatalysatoren für die Wasseroxidation. Der dabei entstehende Wasserstoff ist wichtiger alternativer Energieträger, in dem Sonnenergie zwischengespeichert werden kann. Anorganische Metall-Sauerstoff-Cluster, auch bekannt als Polyoxometallate (POMs), wurden für diesen Zweck synthetisiert. Die katalytische Aktivität dieser potenziellen Katalysatoren wurde in einem Versuchsaufbau gemessen, welcher die Prozesse der natürlichen Photosynthese in vereinfachter Weise nachahmt. POMs wurden getestet, um beide Halbreaktionen der Wasseroxidation zu katalysieren. Mangan substituierten Polyoxometallaten wurde spezielle Beachtung geschenkt, da diese als strukturelle Nachbildung des aktiven Zentrums in Photosystem II gestaltet werden können, in dem Wasser zu Sauerstoff oxidiert wird.

Nickel-substituierte Polyanionen des Keggin-Typs $[Ni(H_2O)(XW_{11}O_{39})]^{n-}$ (X = Si, P, Ge) wurden erfolgreich als Katalysatoren für photochemische H_2 Bildung getestet. Anstrengungen wurden unternommen, um den Einfluss des Heteroatoms auf die Elektronendichte am Nickel Atom einzuschätzen. Dabei wurde zunächst davon ausgegangen, dass die katalytische Aktivität vom Heteroatom stark beeinflusst wird. Eine Reihe von Ni-substituierten Keggin-POMs wurde synthetisiert, in denen das Heteroatom systematisch ausgetauscht wurde. Als Heteroatome wurden Silizium, Phosphor und Germanium eingesetzt. Die Kaliumsalze dieser POMs wurden mittels Röntgendiffraktion charakterisiert und ihre Kristallstruktur wurde bestimmt. Die Lösung dieser Strukturen und deren Verfeinerung war eine Herausforderung, in Anbetracht der hohen Symmetrie in Kombination mit W/Ni Fehlordnung. Die Reinheit aller Verbindungen wurde mit verschiedenen Methoden bestätigt, um katalytisch aktive Verunreinigungen auszuschliessen. UV/vis und XANES Spektroskopie wurden angewandt, um die Elektronendichte am Ni Atom als Funktion des Heteroatoms zu bestimmen. DFT Rechnungen sollten den Einfluss des Heteroatoms auf das LUMO aufzeigen. e XANES-

Messungen an der Ni-K-Kante zeigten, dass das Ge Heteroatom zur höchsten Elektronendichte am Nickel führt. Photokatalytische Tests wurden mit allen POMs und ausgewählten Referenzverbindungen durchgeführt und demonstrierten, dass die Ni-Funktionalisierung die katalytische Aktivität erheblich verbessert. Turnover Numbers (TONs) und Turnover Frequencies (TOFs) wurden als charakteristische Kennzahlen der POM-Katalysatoren ermittelt. Signifikante Wasserstoffbildung konnte nur für das Ge substituierte POM beobachtet werden. Leider konnten die Ergebnisse der elektrochemischen Messung von Redox- und Onset-Potentialen nicht in Einklang mit den Ergebnissen der photokatalytischen Messungen gebracht werden, da sich unter elektrokatalytischen Bedingungen Heteropolyblau- und -braunverbindungen auf der Elektrode ablagern. Dies lässt leider nur begrenzt Schlüsse über die elektrochemischen Eigenschaften der homogenen POM-Katalysatoren zu. Es konnte jedoch klar gezeigt werden, dass sich mit verschiedenen Heteroatomen die katalytische Aktivität von Nickel POMs beeinflussen lässt. Die Rolle des POM-PS Komplexes, ein Feststoff der sich durch die elektrostatische Wechselwirkung zwischen POM und Photosensitizer bildet, bleibt weiterhin unbekannt und bietet die Möglichkeit für weiterführende Untersuchungen an der Grenze zwischen homo- und heterogener Wasseroxidationskatalyse.

Auf der Suche nach neuen POM-basierten Wasseroxidations-Katalysatoren (engl. Water Oxidation Catalysts oder WOCs) wurde der lacunare Precursor $[BiW_9O_{33}]^{9-}$ detailliert untersucht (lacunar = POM mit fehlenden WO_6 Oktaedern), dessen phasenreise Synthese sich als herausfordernd erwies. Ausgehend von diesem Precursor wurden Mangan-, Kupfer- und Cobalt-funktionalisierte POMs hergestellt. Veröffentlichte Resultate unserer Forschungsgruppe hatten bereits gezeigt, dass Mangan- und Cobalt-funktionalisierte POMs, die auf dem $[BiW_9O_{33}]^{9-}$ Precursor basieren, an der äusseren und inneren Position im Übergangsmetall-Kern W/M (M = Mn, Co) fehlgeordnet sind. Während ein POM mit einem W/Co fehlgeordneten Kern als WOC aktiv war, konnte für das entsprechende analoge Polyanion mit W/Mn fehlgeordnetem Kern keine Aktivität beobachtet werden. Im Rahmen dieser Arbeit wurde diese W/Mn Fehlordung genauer untersucht. Die Wahrscheinlichkeit, dass reine Polyanionen mit einem Mn_4 Kern existieren, wurde unter den gegebenen Bedingungen als vernachlässigbar ermittelt, was die mangelnde WOC Aktivität erklären könnte. Basierend auf dieser Hypothese wurde versucht, Mn POMs mit einem reinen Mn_4 Kern herzustellen. Die Verwendung von milderen Reaktionsbedingungen konnte die W/Mn-Fehlordnung reduzieren. Waren ursprünglich die äusseren und inneren Position im

Übergangsmetall-Kern fehlgeordnet, konnte die Fehlordung durch die angepassten Reaktionsbedingungen auf die inneren Positionen beschränkt werden. Die Wahrscheinlichkeit für einen reinen Mn_4 Kern konnte dadurch um den Faktor 410 erhöht werden. Ähnliches konnte für die Synthese mit Cobalt beobachtet werden. Während für Mangan die strukturelle Vielfalt gross ist und von 0D bis hin zu 2D Strukturen reicht, konnten für Cobalt nur 0D Strukturen kristallisiert werden. Trotz des erhöhten Anteils an POMs mit einem reinem Mn_4 Kerns konnte keine katalytische Aktivität in Wasseroxidations-Tests festgestellt werden. Die Synthese dieses Precursors und alle darauf aufbauende Synthesen sind anspruchsvoll, da dieses lacunare Polyoxowolframat sehr untabil ist. Um den Einfluss der verschiedenen Reaktionsparameter auf die Bildung von bismuthaltigen Wolframaten besser zu verstehen, wurde die Reaktion des lacunaren Precursors $[BiW_9O_{33}]^{9-}$ mit Mn(II) und Co(II) mit hochaufgelöster Massenspektroskopie genauer untersucht.

Die neuesten vielversprechenden Ergebnisse von Kupfer-Komplexen als WOCs inspirierten uns, neue Tungstobismutate mit Kupfer zu funktionalisieren. Die Kristallstruktur von sechs dieser neuen Strukturen konnten bestimmt werden. Unter ähnlichen Reaktionsbedingungen lässt sich eine Fülle von verschiedenen Polyoxometalaten aus der Lösung kristallisieren. Eine Verbindung mit einem fehlgeordneten Cu/K Kern konnte phasenrein isoliert und anschliessend charakterisiert werden. Die neue Verbindung war trotz ihrere interessanten Struktur nicht als WOC aktiv und ist nur bedingt für die H_2 Katalyse geeignet. Die Synthese dieser neuen multidimensionalen Strukturen liefter jedoch neue Erkenntnisse, wie das eingesetzte Übergangsmetall den Ausgang der Reaktion beinflussen kann.

Ga(III) Kationen sind diamagnetisch. Dieser Vorteil erlaubt es, Ga-funktionalisierte Polyanionen in Lösung mittels ^{183}W NMR zu untersuchen. Die Reaktion des lacunaren Wolfram-Precursors $[SiW_9O_{34}]^{10-}$ mit Galliumnitrat ergibt eine Mischung von Kristallen mit einer sehr unterschiedlichen, charakteristischen Morphologie. Neue Ga substituierte POMs konnten isoliert und charakterisiert werden.Es stellte sich heraus, dass sich drei verschiedene Spezies im Gleichgewicht miteinander befinden, was sich unter anderem optisch an der diversen Morphologie der Kristalle deutlich äussert. Phasenreines Material konnte unter Anwendung einiger spezieller Isolationsschritte für zwei POM-Spezies gewonnen werden. Um auch die dritte POM-Spezies phasenrein isolieren zu können, wurde hochaufgelöste Massenspektrometrie zur besseren Reaktionskontrolle verwendet. In weiterführenden Untersuchungen mit dem phosphorhaltigen lacunaren Wells-Dawson Precursor $[P_2W_{15}O_{56}]^{12-}$ in Gegenwart von Ga(III) Kationen konnten Kristalle von Ga-substituierten

Phosphowolframaten isoliert und deren Struktur mittels Einkristallstrukturanalyse und ^{31}P NMR Spektroskopie ermittelt werden. Dadurch wird ersichtlich, dass dieser Precursor sich schrittweise zersetzt und dabei eine α-β Isomerisierung durchläuft. Diese Reaktion stellt somit eine ideale Plattform dar, um die Bildung von übergangsmetall-substituierten Phosphowolframaten genauer zu untersuchen und deren Bildungskonstanten zu ermitteln. Ein kombinierter Ansatz aus ^{31}P NMR, ^{183}W NMR, HR-ESI Massenspektrometrie und Röntgenkristallografie liefert dabei essentielle Informationen zur Kontrolle der Selbstorganisation von Polyoxometalaten.

POMs sind faszinierende anorganische Cluster mit einem vielfältigen Anwendungsspektrum. Im Mittelpunkt dieser Arbeit stand ihr Potential als Photokatalysatoren für beide Halbreaktionen der künstlichen Photosynthese untersucht. Die Ausgangsfrage war: „Was ist das Potential von Mangan substituierten POMs als Katalysator für Wasseroxidation?“ Obwohl eine grosse Anzahl von Mn-POMs mit Standard-Assays als WOC getestet wurden, wurde kein signifikant neuer Wasseroxidationskatalysator identifiziert. Ein Screening von Mn substituierten POMs in grossem Umfang zum Erstellen von Struktur-Aktivitäts-Beziehungen hat sich zudem als schwierig erwiesen, da die hohe erforderliche Phasenreinheit vieler Produkte generell schwierig zugänglich ist. Kontrolle über die Selbstorganisations- und Kristallisationsprozesse der POM-Bildung bleibt eine massive Herausforderung. Ein weiteres Problem stellen die POM-PS Komplexe dar, welche sich zwischen den Polyanionen und dem positiv geladenen Photosensitizer bilden. POMs können deshalb nicht als homogene Katalysatoren in Gegenwart eines positiv geladenen Photosensitizers aufgefasst werden.

Die Synthese von neuen, mit Übergangsmetallzentren funktionalisierten POMs ist daher eine Aufgabe für die Zukunft. Trotz der Probleme bei der Verwendung von POMs als Katalysatoren für künstliche Photosynthese hat die POM Chemie ein massives Potential für weiterführende Arbeiten. In ihrem Mittelpunkt sollten das Verständnis der Selbstorganisationsprozess und der gezielten Kristallisation dieser Cluster stehen. Jede potentielle Anwendung verlangt, dass sich die Synthese von POMs skalieren lässt und die Reinheit einfach und verlässlich kontrolliert werden kann. Es ist deshalb unerlässlich, dass analytische Methoden wie NMR, ESI-MS und PXRD und mechanistische Studien konsequent auch in der POM Chemie angewandt werden. Erst wenn diese Probleme gelöst sind, lässt sich das Potential von Polyoxometalaten für katalytische und andere Prozesse voll ausschöpfen.